Exploring geodynamics at different depths with shear wave splitting

Zur Erlangung des akademischen Grades eines
DOKTORS DER NATURWISSENSCHAFTEN (Dr. rer. nat.)

von der KIT-Fakultät für Physik des
Karlsruher Instituts für Technologie (KIT)
genehmigte

DISSERTATION

von

M.Sc. Michael Grund
aus Künzelsau

Tag der mündlichen Prüfung:	08. Februar 2019
Referent:	apl. Prof. Dr. Joachim Ritter
Korreferent:	Prof. Dr. Andreas Rietbrock

"Geologists have a saying - rocks remember"

-Neil Armstrong-

Abstract

Dynamic processes in the Earth's interior are the dominant driving forces behind the continuous deformation-related reworking of its surface. The characterization of deformation caused by past tectonic events near the Earth's surface as well as mapping of ongoing dynamic-driven processes deep inside the Earth are therefore major objectives to understand the dynamics of our planet. Seismic anisotropy, the direction-dependence of seismic wave speed, is directly related to deformation processes and can be "felt" by passing seismic waves. Although seismic anisotropy is a well-known phenomenon, the individual contributions from different depth ranges are still debated. However, recordings available from dense and large-aperture seismic station networks, provide the opportunity for resolving both, small-scale variations relatively close to the surface as well as so far unknown structures at greater depth.

In 2012, an international seismological field experiment, called ScanArray, was initiated. The combination of 72 temporary broadband stations with long-running national permanent stations and arrays resulted in a recording network consisting of 266 seismic stations in total that were distributed across the Fennoscandian peninsula in northern Europe. Fennoscandia opens the opportunity to study the (past) geodynamical evolution of crustal and upper mantle structures far away from currently active plate tectonics.

The main goal of this study is to characterize the anisotropic structure beneath the Fennoscandian peninsula as well as in the Earth's lowermost mantle based on a uniformly processed data set provided by the ScanArray network. For this purpose single-event shear wave splitting analysis was performed using core-refracted shear waves (*SKS*, *SKKS*, *PKS*) of around 3000 globally distributed teleseismic earthquakes (1998-2017). In order to improve the data coverage at a recording station, a new plugin (StackSplit) for a widely applied analysis software (SplitLab) is introduced allowing efficient and flexible handling of multi-event splitting measurements.

Based on the massive seismic data set, this study provides a comprehensive characterization of the distinct lateral and backazimuthal variations of the shear wave splitting pattern at individual stations and across the ScanArray network. These variations partly correlate well with different tectonic regimes related to past large-scale lithospheric deformation due to ancient collision events. Detailed forward modeling allowed to explore different anisotropic structural geometries including anisotropy with a dipping axis of symmetry. Although, the majority of the shear wave splitting observations can be explained with high reliability, for a small num-

ber of recording stations non-unique anisotropy models were found which fit the observed data equally well.

Furthermore, this study sheds light on lowermost mantle anisotropy located in the so-called D" layer just atop the core-mantle boundary in $\sim$ 2900 km depth. This unexpected discovery is based on observations of distinct splitting discrepancies between teleseismic *SKS* and *SKKS* phases for the same source-receiver configuration. The lowermost mantle anisotropy can be associated with two large-scale seismic velocity anomalies beneath the North Atlantic and northwestern Siberia. Even though the exact geometry and mechanism of the anisotropic fabrics in D" cannot be fully constrained by ScanArray recordings alone, these new observations provide important and much-needed boundary conditions for improved future geodynamic mantle modeling.

Contents

Abstract v

List of Figures xi

List of Tables xv

1 Introduction 1
- 1.1 Motivation 4
- 1.2 Outline of this thesis 5

2 Seismic anisotropy 7
- 2.1 Elasticity and anisotropy 7
- 2.2 Seismic wave propagation in anisotropic media 9
- 2.3 Shear wave splitting 15
- 2.4 Locations of anisotropy in the Earth 19
  - 2.4.1 Crustal anisotropy 20
  - 2.4.2 Anisotropy in the upper mantle and mantle transition zone 21
  - 2.4.3 Lowermost mantle anisotropy 23

3 The ScanArray experiment 25
- 3.1 ScanArray network 25
- 3.2 LITHOS-CAPP 29
  - 3.2.1 Data acquisition 29
  - 3.2.2 Data processing 37
  - 3.2.3 Data description and completeness 37
  - 3.2.4 Data quality and accuracy 38
  - 3.2.5 Data availability and access 40

4 Data processing 41
- 4.1 SplitLab 41
  - 4.1.1 Data requests 41
  - 4.1.2 Missing data or malfunctioning stations 42
  - 4.1.3 Techniques to measure shear wave splitting 42

4.1.4 Uncertainties, errors, and challenges . . . 44
4.1.5 Detection of misorientations . . . 45
4.2 Evaluation of SIMW using simple synthetic examples . . . 48

5 StackSplit - a plugin for multi-event shear wave splitting analyses in SplitLab . . . 53
5.1 Abstract . . . 53
5.2 Introduction . . . 53
5.3 Description of the program . . . 55
5.3.1 General remarks . . . 55
5.3.2 StackSplit main module . . . 56
5.3.3 Surface stacking . . . 57
5.3.4 Simultaneous Inversion of Multiple Waveforms . . . 60
5.3.5 StackSplit outputs . . . 60
5.4 Application example . . . 62
5.5 Conclusions . . . 64

6 Lowermost mantle anisotropy observed at ScanArray . . . 67
6.1 Abstract . . . 67
6.2 Introduction . . . 68
6.3 Data and methods . . . 71
6.4 Results and discussion . . . 72
6.4.1 Observation of clearly discrepant *SKS-SKKS* waveforms . . . 72
6.4.2 Geographic clusters in the lowermost mantle . . . 75
6.4.3 Nature of anisotropy below Siberia . . . 78
6.4.4 Anisotropic source beneath the Atlantic . . . 79
6.5 Conclusions . . . 83

7 Characterization of the anisotropy beneath Fennoscandia . . . 85
7.1 Introduction . . . 85
7.2 Data and methods . . . 91
7.3 Shear wave splitting results . . . 93
7.3.1 General trends and geographical variations . . . 93
7.3.2 Re-analysis of some MAGNUS station waveforms . . . 101
7.3.3 Stereoplot representation . . . 102
7.4 Modeling of complex splitting patterns . . . 107
7.4.1 General considerations . . . 107
7.4.2 Forward modeling approach . . . 108
7.4.3 Evidence for anisotropy with a dipping symmetry axis . . . 111

7.4.4 Non-uniqueness of models . . . 114
7.5 Discussion and interpretation . . . 124
7.5.1 Can the splitting patterns be associated with tectonic units and events? . 125
7.5.2 Comparison with surface wave data and absolute plate motion . . . 131
7.5.3 May lateral variations or deep anisotropy play a role? . . . 134
7.6 Summary . . . 136

8 Conclusions and outlook . . . 139

Acknowledgements . . . 145

Appendix . . . 149
A Used hardware and software . . . 151
B Station information . . . 152
C Sensor misorientations of the extended ScanArray network . . . 157
D Lowermost mantle anisotropy (*SKS-SKKS*) – Supporting content . . . 159
E Anisotropy beneath Fennoscandia – Supporting content . . . 165
F Electronic appendix . . . 187

Bibliography . . . 189

Index . . . 207

List of Figures

1.1 Studying seismic anisotropy from large to (relatively) small scale . . . 3

2.1 Sample of an ultramafic peridotite and schematic olivine crystal . . . 10
2.2 Vertical transverse isotropy (VTI) . . . 13
2.3 Horizontal transverse isotropy (HTI) and lattice-preferred orientation (LPO) . . . 14
2.4 Tilted transverse isotropy (TTI) . . . 15
2.5 Shear wave splitting . . . 16
2.6 Raypaths of core-refracted shear waves . . . 17
2.7 Traveltimes of seismic phases . . . 19
2.8 Locations of seismic anisotropy in the Earth . . . 21
2.9 Vertically coherent deformation (VCD) and simple asthenospheric flow (SAF) . . . 22

3.1 Map of the extended ScanArray network . . . 27
3.2 Record sections of the 2015 Nepal earthquake and a regional event in Sweden . . . 28
3.3 Picture from the field experiment . . . 29
3.4 Locations of LITHOS-CAPP stations in Finland . . . 30
3.5 Locations of LITHOS-CAPP stations in Sweden . . . 31
3.6 Instrument response functions of LITHOS-CAPP sensors . . . 36
3.7 Instruments to correctly align seismometers . . . 37
3.8 PSD spectra calculated at LITHOS-CAPP stations . . . 39

4.1 Exemplary splitting measurement . . . 43
4.2 Exemplary null measurement . . . 44
4.3 Misorientation analysis . . . 46
4.4 Waveform examples of misorientation analysis . . . 47
4.5 Concatenated synthetic waveforms . . . 48
4.6 Synthetic test 1 . . . 50
4.7 Synthetic test 2 . . . 51
4.8 Statistics of synthetic test 2 . . . 52

5.1 StackSplit workflow . . . 57
5.2 Graphical user interface of StackSplit . . . 58
5.3 Stacking example using the WS method . . . 61

5.4 Multiple waveform example using SIMW . . . 62
5.5 Steroplot of station VAF . . . 63
5.6 Comparison multi-event methods . . . 65

6.1 Schematic cross-section showing lowermost mantle features . . . 68
6.2 Study region, *SKS-SKKS* raypaths and earthquake distribution . . . 69
6.3 Stereoplots for permanent stations PVF and KEF . . . 70
6.4 Waveform example of a discrepant *SKS-SKKS* pair . . . 71
6.5 Fresnel zones of *SKS-SKKS* in different depths . . . 73
6.6 Distance and depth statistics of *SKS-SKKS* pairs . . . 74
6.7 Record section for an event east of the network . . . 75
6.8 Record section for an event west of the network . . . 76
6.9 D" pierce points of *SKS-SKKS* pairs atop GyPSuM tomography model . . . 77
6.10 Separations between *SKS-SKKS* pierce points . . . 77
6.11 D" pierce points of *SKS-SKKS* pairs and measured ΔSI values . . . 79
6.12 Locations of recording stations atop geological units . . . 80
6.13 D" pierce points of *SKS-SKKS* pairs atop cluster analysis (fast areas) . . . 80
6.14 D" pierce points of *SKS-SKKS* pairs atop cluster analysis (slow areas) . . . 81
6.15 Interpretation cartoon . . . 82
6.16 Overview about lowermost mantle studies . . . 82

7.1 Simplified geological/tectonic map of Fennoscandia . . . 87
7.2 Shear wave splitting in Fennoscandia: a review . . . 88
7.3 ScanArray overview map . . . 90
7.4 Distribution of teleseismic earthquakes . . . 92
7.5 Distribution of splitting measurements across ScanArray . . . 94
7.6 Histograms of splitting parameters distributions . . . 95
7.7 Distribution of splitting measurements in terms of source regions (BAZ 0°-360°) . . . 97
7.8 Distribution of splitting measurements in terms of source regions (BAZ 0°-31° and BAZ 32°-45°) . . . 98
7.9 Distribution of splitting measurements in terms of source regions (BAZ 46°-64° and BAZ 65°-84°) . . . 99
7.10 Distribution of splitting measurements in terms of source regions (BAZ 231°-260° and BAZ 261°-280°) . . . 100
7.11 Waveform examples of re-analyzed MAGNUS stations . . . 101
7.12 Exemplary stereoplots . . . 102
7.13 Distribution of stereoplots in southern Norway . . . 104
7.14 Distribution of stereoplots for NORSAR stations . . . 105

7.15 Distribution of stereoplots in southern and central Finland . . . 106
7.16 Synthetic splitting parameters for different model settings . . . 107
7.17 Parameter conventions used for modeling dipping structures . . . 109
7.18 Influence of a dipping symmetry axis . . . 110
7.19 Exemplary stereoplots showing v-shaped patterns . . . 111
7.20 Modeling of a dipping symmetry axis in limited BAZ interval . . . 112
7.21 Comparison of observed and theoretical splitting parameters for a dipping symmetry axis . . . 113
7.22 Exemplary stereoplots showing complex patterns . . . 114
7.23 Two-layer modeling at station KONO . . . 115
7.24 Parameter distribution of two-layer modeling at station KONO . . . 115
7.25 Comparison of observed and theoretical splitting parameters for two-layer modeling at station KONO (best four models) . . . 116
7.26 Modeling of a dipping symmetry axis at station KONO . . . 117
7.27 Comparison of observed and theoretical splitting parameters for models with dipping symmetry axes at station KONO . . . 117
7.28 Two-layer modeling at station KEF . . . 118
7.29 Parameter distributions of two-layer modeling at station KEF . . . 119
7.30 Two-layer modeling at station KEF in limited BAZ interval . . . 120
7.31 Parameter distributions of two-layer modeling at station KEF in limited BAZ interval 121
7.32 Comparison of observed and theoretical splitting parameters for two-layer modeling at station KEF (full and limited BAZ interval) . . . 122
7.33 Modeling of a dipping symmetry axis at station KEF . . . 122
7.34 Comparison of observed and theoretical splitting parameters for dipping and two-layer modeling at station VAF (full and limited BAZ interval) . . . 123
7.35 Modeling results in map view atop major tectonic units of Fennoscandia . . . 126
7.36 Different stages of continental growth . . . 129
7.37 Findings and interpretations of the BABEL project . . . 130
7.38 Comparison with surface-wave results . . . 132
7.39 Pierce point distributions in different depth ranges . . . 135

8.1 Potential future study areas . . . 143

D.1 Further discrepant *SKS*-*SKKS* examples . . . 159
D.2 Waveform examples of *SKS*, *SKKS* and *sSKS* . . . 161
D.3 Exemplary 3D-raypaths of *SKS* and *SKKS* . . . 163
D.4 Map showing split-split *SKS*-*SKKS* pairs atop GyPSuM tomography model . . . 164

E.1 Exemplary multi-event measurements . . . 166

E.2 Visualization of multi-event parameter definitions 167
E.3 Distribution of splitting measurements in terms of source regions (BAZ 85°-120°) . 171
E.4 Distribution of splitting measurements in terms of source regions (BAZ 180°-230°) 172
E.5 Distribution of splitting measurements in terms of source regions (BAZ 281°-320°) 173
E.6 Distribution of splitting measurements in terms of source regions (BAZ 321°-360°) 174

List of Tables

3.1 Instrumentation information 32
3.2 Properties of the LITHOS-CAPP sensors 35
3.3 Misorientations of the LITHOS-CAPP sensors 36

4.1 Data centers and network codes 41
4.2 Recording stations with poor data quality 42

5.1 Names of modified SplitLab functions 56

B.1 Seismic recording stations of the ScanArray network 152

C.1 Sensor misorientations of the extended ScanArray network 157

D.1 Subset of *SKS-SKKS* analysis results 160

E.1 Subset of shear wave splitting results 165
E.2 Multi-event shear wave splitting results 167

F.1 Content of electronic appendix 187

1 Introduction

The present-day shape of the Earth's surface is characterized by a variety of large-scale tectonic structures such as mountain belts, rift systems and underwater mid-ocean ridges. In principle, all of them can be traced back to deformation processes triggered by the motion of lithospheric plates atop the asthenosphere. As already inferred by Alfred Wegener, the collision of two continents along convergent plate boundaries ($\rightarrow \leftarrow$) can effect mountain-building processes (*Wegener*, 1920), generally accompanied by the subduction of one plate beneath the other. In contrast, divergent boundaries form as a result of plate spreading ($\leftarrow \rightarrow$), caused by locally upwelling hot material from the interior of the Earth. The relative motion of the lithospheric plates with respect to the underlying mantle mainly controls deformation in the asthenosphere underneath. The dominant driving forces behind these movements are assumed to be located deep inside the planet. In this context, an anomalous 200-300 km-thick layer just atop the core-mantle boundary in around 2700 km depth most likely plays a fundamental role for the dynamics of the overlying mantle. The inhomogeneity of this layer was already inferred by Cornelius G. Dahm in 1934 (*Dahm*, 1934) and later by Keith E. Bullen (*Bullen*, 1949) based on relatively sparse amounts of seismic data. Nowadays, the so-called D" layer has become an important research subject in global seismology. However, knowledge about the composition and geometry of D" is limited and answers to several puzzling questions are still missing (e.g. *Nowacki et al.*, 2011). The characterization of deformation caused by past tectonic events near the Earth's surface as well as mapping of current dynamic-driven processes such as mantle flow deep inside the Earth are therefore major objectives to understand the dynamics of our planet.

The most powerful tool to look into the Earth's interior are seismic waves recorded at globally distributed stations and networks. These can be used to study subsurface structure ranging from global (e.g. *Van der Hilst et al.*, 1997; *Schaeffer and Lebedev*, 2013) over regional (e.g. *Ritter et al.*, 2001; *Grund et al.*, 2016a) to local scale (e.g. *Grund et al.*, 2016b; *Zieger and Ritter*, 2018). Along the raypath from an earthquake source location to a receiver at the surface, a seismic wave generally propagates through volumes with differing elastic properties. An important property is seismic anisotropy, the direction-dependence of seismic wave velocity. In the Earth, seismic anisotropy is caused by different deformation-related mechanisms, mainly depending on depth. Layering of material with different elastic properties and fluid-filled fractures (so-called shape-preferred orientation, SPO) are mostly responsible for shallow anisotropy in the crust (e.g. *Backus*, 1962; *Crampin and Booth*, 1985). Lattice-preferred orientation (LPO)

of intrinsically anisotropic minerals like olivine by strain (e.g. *Nicolas and Christensen*, 1987; *Zhang and Karato*, 1995; *Karato et al.*, 2008) is assumed to make the largest contribution to elastic anisotropy in the upper mantle (e.g. *Silver*, 1996; *Long and Becker*, 2010). In D" high-pressure phases of different minerals like magnesium silicate (post-perovskite) most likely play a major role for the formation of seismic anisotropy (e.g. *Murakami et al.*, 2004; *Merkel et al.*, 2007). Alternatively, partial melt, aligned due to deformation, can cause SPO anisotropy in D" (e.g. *Kendall and Silver*, 1996).

A significant amount of globally detected anisotropy is based on shear wave (*S*-wave) observations. Shear waves propagating through an anisotropic fabric are split into two orthogonally polarized shear waves, each traveling with a different speed. This phenomenon is commonly known as shear wave splitting and is equivalent to optical birefringence (e.g. *Savage*, 1999). The polarization orientations of the split waves as well as the accumulated time delay between their arrivals at a recording station provide information about anisotropy along their raypaths. While early studies of Masataka Ando and co-workers only focused on shear wave splitting of direct *S*-waves beneath Japan (*Ando et al.*, 1980; *Ando and Ishikawa*, 1982), Lev P. Vinnik initially introduced the analysis technique to study the splitting with core-refracted shear waves such as *SKS*, *SKKS* and *PKS* in 1984 (*Vinnik et al.*, 1984). The most frequently applied method nowadays (also in this thesis) goes back to the work of Paul G. Silver and Winston Chan (*Silver and Chan*, 1991). Shear wave splitting measurements are used to address numerous deformation-related questions in seismology including the formation of orogens (e.g. *Barruol et al.*, 1998; *Long et al.*, 2016), the dynamics of subduction zone systems (e.g. *Matcham et al.*, 2000; *Eakin et al.*, 2016), the evolution of rift systems (e.g. *Gao et al.*, 1994; *Hammond et al.*, 2014), the dynamics in D" (e.g. *Niu and Perez*, 2004; *Long and Lynner*, 2015) and the potential of acting as a forecasting tool for volcanic eruptions (*Gerst and Savage*, 2004). There are also efforts ongoing to study shear wave splitting on the Moon using recordings of the seismometers that were installed during the Apollo missions (*Dimech et al.*, 2017).

At present, collision zones such as the Himalayas are still reworked by high deformation rates and therefore provide insights into active geodynamic processes. However, regions affected by ancient collision are also in the focus of seismologists since they provide the opportunity to understand the (past) geodynamical evolution of crustal and upper mantle structures far away from currently active plate tectonics. Even if the last tectonic events partly date back millions of years, the fossil signatures of the deforming forces can be mapped by studying seismic anisotropy. A prominent example of such a region is the Fennoscandian peninsula in northern Europe which encompasses some of the oldest parts of the European continent. Although Fennoscandia is not much tectonically active anymore, its geological history enables to test hypothesis about the formation of cratonic regions. The increasing use of dense seismological recording networks around the globe such as, for instance, USArray in North America or AlpArray in Europe (*Hetényi et al.*, 2018) allows to study current and past deformation pro-

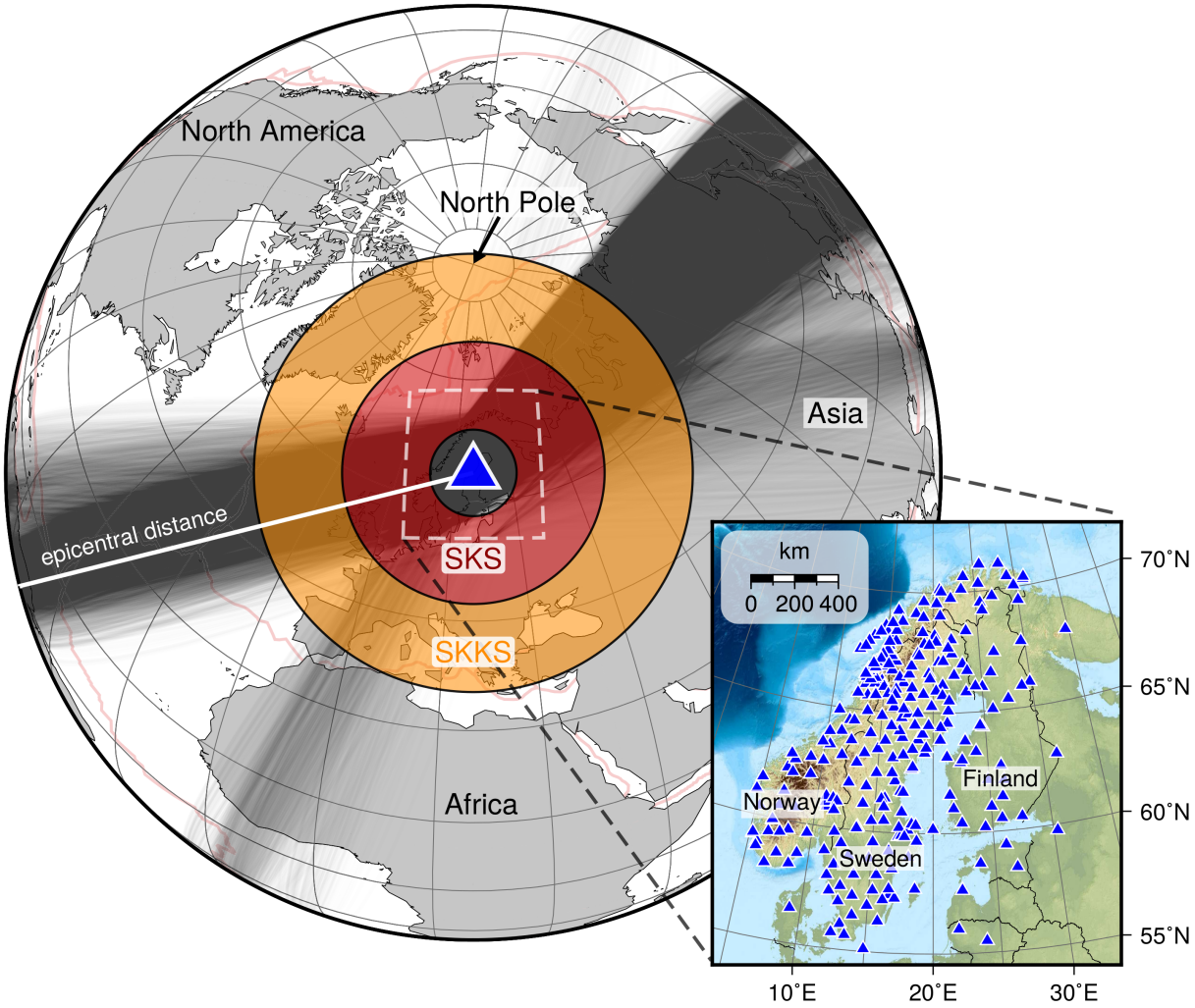

Figure 1.1: Studying seismic anisotropy from large to (relatively) small scale. Map in polar projection showing the lowermost mantle areas sampled by core-refracted seismic shear waves recorded at the ScanArray network (blue triangle). The large red ring represents D" areas which are sampled by *SKS* waves while the orange ring displays the same for the *SKKS* waves. Thin black lines highlight the raypaths of teleseismic events recorded at ScanArray. An exemplary epicentral distance is marked by the white line. Landmasses are shown in gray. Plate boundaries after *Bird* (2003) are displayed by light red lines. The smaller map on the right shows a zoom on Fennoscandia (white dashed box) and displays the individual 266 analyzed ScanArray recording stations (blue triangles).

cesses with a high lateral resolution using recordings of teleseismic earthquakes. For the same purpose, in 2012 the ScanArray project was initiated by different international research institutions. The corresponding seismic network included 72 temporary broadband stations that were operated between 2012 and 2017 in Norway, Sweden and Finland. Combined with national permanent stations and arrays, the continuous ground motion was recorded at a total of 266 seismic receivers which makes ScanArray the largest seismological field experiment conducted in northern Europe so far (Fig. 1.1).

In the last two decades the anisotropic structure beneath Fennoscandia and neighboring terranes was repeatedly subject of seismological research. Previous studies were mainly conducted in the frameworks of regional short-running temporary experiments with only few high-quality

shear wave splitting measurements (*Plomerová et al.*, 2002a; *Plomerová et al.*, 2006; *Vecsey et al.*, 2007; *Plomerová et al.*, 2011; *Vinnik et al.*, 2014). Arrivals of seismic waves from different directions, however, are essential to reliably characterize the anisotropy beneath a recording station. Therefore, the short recording periods in the past hampered an analysis only based on shear wave splitting measurements. For this purpose, splitting measurements were partly combined with traveltime residuals of compressional *P*-waves. While the former is a widely applied and robust approach (e.g. *Savage*, 1999; *Long and Silver*, 2009), the latter technique is much less used since traveltime differences caused by anisotropic contributions cannot easily be distinguished from the effects of lateral heterogeneity. With this approach, indications for sharply bounded areas, each with an individual splitting pattern and dipping geometry of anisotropy, were found. The spatial variations were interpreted as signatures of different tectonic blocks that assembled in the past due to several collision events (*Plomerová et al.*, 2002a; *Plomerová et al.*, 2006; *Vecsey et al.*, 2007; *Eken et al.*, 2010).

1.1 Motivation

The main goal of this work is to characterize the anisotropic structure beneath whole Fennoscandia based on uniformly processed shear wave splitting measurements at a dense and large-aperture seismological recording network. The ScanArray network therefore offers the opportunity to study the signatures of current and past deformation processes with a high lateral resolution across the individual tectonic units of Fennoscandia. Furthermore, for several permanent stations now ten or more years of continuous recordings are available which allows to explore and model complex anisotropy systems with high reliability. Since former studies were mainly limited to selected smaller areas of interest, potential large-scale anisotropic patterns could not be constrained. Moreover, additional anisotropy contributions not directly related to the formation of Fennoscandia have not been considered so far. However, there is growing evidence from recent studies that deep anisotropy in the Earth's lowermost mantle (D" layer), far away from the recording network itself, may distort the splitting observations. Due to limited source-receiver configurations around the globe such rare observations are urgently needed to improve future geodynamical models. Favored by its nearly perfect location with respect to the epicentral distance from earthquake sources to the receivers, ScanArray additionally enables to study relatively wide areas in D" with the same network configuration (Fig. 1.1). Based on these circumstances I focus on the following four key questions in this thesis:

1. *What can we learn from shear wave splitting measurements conducted at long-running seismic recording stations compared to short-term deployments?*

2. *Is there only a component from past lithospheric deformation included in the splitting signals or also a contribution from present-day dynamic processes and structures in the deep mantle?*

3. *Do the splitting observations correlate with geological and tectonic features across Fennoscandia?*

4. *Can complex anisotropic structure such as a dipping symmetry axis of anisotropic fabrics also be reliably constrained by splitting measurements alone?*

In the final chapter of this thesis (chapter 8), each of these questions is confronted with the findings presented in the preceding chapters and sections.

1.2 Outline of this thesis

In the following I give a brief overview how this thesis is structured. Since several parts of this work have already been published (see below), some aspects related to shear wave splitting analysis and anisotropy are included in each of the corresponding chapters.

In chapter 2, first the basics about elasticity and anisotropy relevant for seismology are presented (section 2.1). In a next step the most important aspects related to seismic wave propagation in anisotropic media are introduced (section 2.2). In section 2.3 the concepts of shear wave splitting and the analyzed seismic phases are described. Locations of anisotropy within the Earth and the underlying mechanisms are outlined in section 2.4.

Chapter 3 provides an overview of the ScanArray field experiment in which I was actively involved. First, the seismological recording network is introduced as a whole (section 3.1), followed by a more detailed description of the German contribution LITHOS-CAPP (section 3.2). Besides the site description of the individual recording stations, information is given about the installed instrumentation (seismometers, data loggers, GPS) and the acquisition and quality of the data. Difficulties during the installation process are also discussed. Most parts of this chapter are published in a technical report of the GIPP (Geophysical Instrument Pool Potsdam) Experiment and Data Archive (*Grund et al.*, 2017a).

Details of the shear wave splitting analysis procedure are described in chapter 4. Section 4.1 provides an overview of the utilized analysis toolbox SplitLab including the data requisition, the implemented single-event splitting measurement techniques and potential challenges and uncertainties. Results of testing a recently published multi-event technique with synthetic data are presented in section 4.2.

In chapter 5 I introduce a newly developed multi-event plugin for SplitLab, called StackSplit, which bundles different approaches in a single, freely available software package. The content of this chapter is published in *Computers & Geosciences* (*Grund*, 2017).

Chapter 6 focuses on D" anisotropy beneath northwestern Siberia and the Atlantic Ocean that was detected in the seismic data recorded by the ScanArray network, based on clear discrepancies between *SKS* and *SKKS* phases. The presented results are integrated in a discussion about possible sources, mechanisms and pitfalls related to the interpretation of lowermost mantle anisotropy. Most parts of this chapter are published in *Geology* (*Grund and Ritter*, 2019).

Finally, chapter 7 deals with the characterization of seismic anisotropy beneath Fennoscandia. Initially, the geological and tectonic evolution of Fennoscandia and the Baltic Shield are summarized (section 7.1), followed by a methodological part describing the data set and the applied processing steps (section 7.2). The shear wave splitting results of 266 recording stations are presented in section 7.3, with an additional focus on selected representative single station observations. The splitting measurements form the basis for a detailed modeling of the anisotropy beneath Fennoscandia. Model setups as well as modeling results are described in section 7.4. An integrative discussion and interpretation of the findings is given in the last section 7.5. A publication for the contents of this chapter is in preparation.

In chapter 8 an overall summary and a brief outlook on future regional and global tasks in shear wave splitting analysis is given.

2 Seismic anisotropy

Seismic anisotropy, the direction-dependence of seismic wave velocity is routinely estimated in most globally recorded seismological data sets using well-established techniques. Since the presence of seismic anisotropy can be linked to stress and rock deformation, the detection of corresponding signatures in recorded seismic data allows us to map current and past dynamic processes in the Earth's interior. In this context, the observation of seismic anisotropy perhaps represents the best tool available to characterize the direction of mantle flow at depths.

In the following chapter the basic theory on seismic anisotropy is outlined, beginning with the most simple relation between stress and strain to the seismological diagnostic used in this work. This overview is based on standard lecturing books (*Babuška and Cara*, 1991; *Lay and Wallace*, 1995; *Stein and Wysession*, 2009; *Clauser*, 2014) and methodology-focused papers (e.g. *Silver and Chan*, 1991; *Wüstefeld and Bokelmann*, 2007) or reviews (e.g. *Savage*, 1999; *Long and Silver*, 2009; *Nowacki et al.*, 2011) in which for several aspects presented here a more detailed description can be found.

2.1 Elasticity and anisotropy

First, we consider a medium whose particles will return to their initial position immediately after a displacement. Such a medium is called linear elastic and can be described by *Hooke's law*:

$$\sigma_{ij} = c_{ijkl}\varepsilon_{kl}, \tag{2.1}$$

with the second-order stress (σ_{ij}) and strain (ε_{kl}) tensors and the fourth-order stiffness tensor (c_{ijkl}) that describes the elastic properties of the medium. Note that the Einstein notation is used here (*Einstein*, 1916) which means that repeated indices in a term indicate a summation over this index. For three independent space coordinates, c_{ijkl} has in total 81 constants that link the applied stress to the resulting deformation (strain) of the medium. Taking into account the symmetries of σ_{ij} and ε_{kl} as well as thermodynamical considerations, the number of independent elastic coefficients in the stiffness tensor can be reduced to 21.

With these 21 constants it is possible to fully describe the relationship between stress and strain of a linear hyper-elastic medium. To simplify the visualization of the stiffness tensor we follow the convention of *Voigt* (1928):

$$C_{mn} = \begin{pmatrix} c_{1111} & c_{1122} & c_{1133} & c_{1123} & c_{1113} & c_{1112} \\ c_{2211} & c_{2222} & c_{2233} & c_{2223} & c_{2213} & c_{2212} \\ c_{3311} & c_{3322} & c_{3333} & c_{3323} & c_{3313} & c_{3312} \\ c_{2311} & c_{2322} & c_{2333} & c_{2323} & c_{2313} & c_{2312} \\ c_{1311} & c_{1322} & c_{1333} & c_{1323} & c_{1313} & c_{1312} \\ c_{1211} & c_{1222} & c_{1233} & c_{1223} & c_{1213} & c_{1212} \end{pmatrix} = \begin{pmatrix} C_{11} & C_{12} & C_{13} & C_{14} & C_{15} & C_{16} \\ C_{21} & C_{22} & C_{23} & C_{24} & C_{25} & C_{26} \\ C_{31} & C_{32} & C_{33} & C_{34} & C_{35} & C_{36} \\ C_{41} & C_{42} & C_{43} & C_{44} & C_{45} & C_{46} \\ C_{51} & C_{52} & C_{53} & C_{54} & C_{55} & C_{56} \\ C_{61} & C_{62} & C_{63} & C_{64} & C_{65} & C_{66} \end{pmatrix}. \tag{2.2}$$

Assuming the simplest case with only two independent constants the stiffness tensor becomes (*Babuška and Cara*, 1991; *Stein and Wysession*, 2009):

$$c_{ijkl} = \lambda \delta_{ij} \delta_{kl} + \mu (\delta_{ik} \delta_{jl} + \delta_{il} \delta_{jk}), \tag{2.3}$$

with the so-called *Lamé* parameters λ and μ. While the physical meaning of λ is hard to interpret, μ (also known as *shear modulus* or *rigidity*) describes the ratio of shear stress to shear strain. Therefore, (2.2) simplifies to:

$$C_{mn} = \begin{pmatrix} \lambda + 2\mu & \lambda & \lambda & 0 & 0 & 0 \\ \lambda & \lambda + 2\mu & \lambda & 0 & 0 & 0 \\ \lambda & \lambda & \lambda + 2\mu & 0 & 0 & 0 \\ 0 & 0 & 0 & \mu & 0 & 0 \\ 0 & 0 & 0 & 0 & \mu & 0 \\ 0 & 0 & 0 & 0 & 0 & \mu \end{pmatrix}. \tag{2.4}$$

This is the isotropic case and implies that the elastic properties are the same in all directions. More complex crystallic systems can only be described with an increasing number of independent elastic constants. Therefore, in these systems the properties are not equal for all directions which is also known as *anisotropy*. One of the most commonly considered cases is the hexagonal case. Anisotropic fabrics characterized by hexagonal symmetry have a single plane of isotropy that is perpendicular to the symmetry axis. This is also known as *transverse isotropy*. Hexagonal anisotropy can be fully described by five independent constants, the so-called *Love* coefficients A, C, F, L and N (*Love*, 1927):

$$C_{mn} = \begin{pmatrix} A & A-2N & F & 0 & 0 & 0 \\ A-2N & A & F & 0 & 0 & 0 \\ F & F & C & 0 & 0 & 0 \\ 0 & 0 & 0 & L & 0 & 0 \\ 0 & 0 & 0 & 0 & L & 0 \\ 0 & 0 & 0 & 0 & 0 & N \end{pmatrix}. \tag{2.5}$$

Most parts of Earth's upper mantle are assumed to consist of olivine ($\sim 70\%$, *Ismaïl and Mainprice*, 1998). A mantle rock found in the Eifel volcanic field (Germany) that consists mostly of green olivine crystals is shown in Fig. 2.1. Olivine is highly anisotropic and can be described by an orthorhombic system that has three perpendicular axes of symmetry and nine independent constants (*Babuška and Cara*, 1991):

$$C_{mn} = \begin{pmatrix} a & b & c & 0 & 0 & 0 \\ b & d & e & 0 & 0 & 0 \\ c & e & f & 0 & 0 & 0 \\ 0 & 0 & 0 & g & 0 & 0 \\ 0 & 0 & 0 & 0 & h & 0 \\ 0 & 0 & 0 & 0 & 0 & i \end{pmatrix}. \tag{2.6}$$

For horizontal alignment of the crystal a-axes, the signatures of hexagonal and orthorhombic fabrics "felt" by a nearly vertical propagating seismic wave do not differ significantly (*Savage*, 1999). Therefore, observations of seismic anisotropy can provide valuable information about mantle processes.

2.2 Seismic wave propagation in anisotropic media

In the next step we consider how the stiffness tensor affects seismic wave propagation. We start with the three-dimensional elastic equation of motion for a continuous homogeneous medium:

$$\rho \frac{\partial^2 u_i}{\partial t^2} = \frac{\partial \sigma_{ij}}{\partial x_j} \qquad i,j = 1,2,3. \tag{2.7}$$

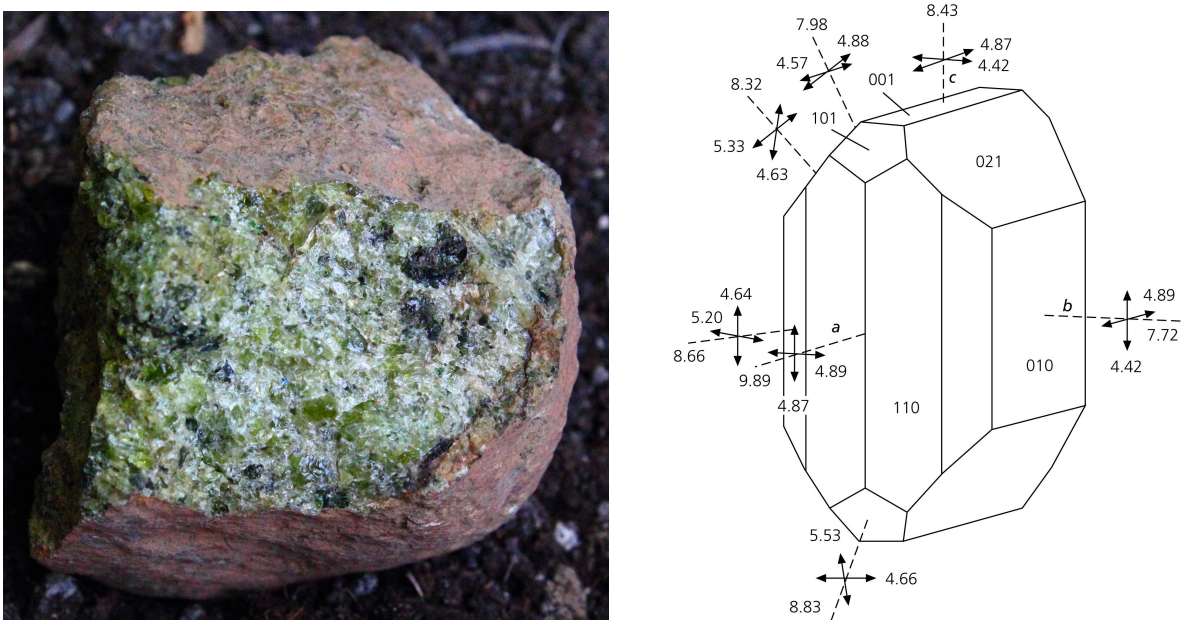

Figure 2.1: Left: Sample of an ultramafic peridotite consisting mostly of olivine crystals (greenish colors). Its original source was potentially located in the Earth's upper mantle. The sample was collected in the Eifel volcanic field, Germany (© M. Grund, 2012). Right: Schematic overview of the seismic *P*- (dashed lines) and *S*-wave (pairs of perpendicular solid lines with arrows) velocities (in km/s) of a single olivine crystal in different directions, obtained from laboratory measurements. The fastest direction corresponds to the *a* axis (or [1 0 0]) of the crystal (after *Stein and Wysession*, 2009).

Inserting Hooke's law from equation (2.1) results in:

$$\rho \frac{\partial^2 u_i}{\partial t^2} = c_{ijkl} \frac{\partial \varepsilon_{kl}}{\partial x_j}. \tag{2.8}$$

Furthermore, using the definition of small strain (*Babuška and Cara*, 1991):

$$\varepsilon_{kl} = \frac{1}{2} \left(\frac{\partial u_k}{\partial x_l} + \frac{\partial u_l}{\partial x_k} \right), \tag{2.9}$$

we can write the wave equation in a homogenous medium as

$$\rho \frac{\partial^2 u_i}{\partial t^2} = c_{ijkl} \frac{\partial^2 u_l}{\partial x_j \partial x_k}. \tag{2.10}$$

The stiffness tensor c_{ijkl} allows us to consider anisotropy in the wave equation. The propagation of a plane wave can be expressed by its displacement vector:

$$\vec{u}(\vec{x},t) = \vec{a} f \left(t - \frac{\vec{n} \cdot \vec{x}}{c} \right), \tag{2.11}$$

where $\vec{x}$ is the space coordinate of the particle, $\vec{a}$ represents a vector that describes the polarization and amplitude, function f describes the particle motion, $\vec{n}$ is a unit vector perpendicular

to the phase surface (pointing into the direction of propagation) and c is the phase velocity. Inserting the plane wave Ansatz into equation (2.10) we get for the derivatives of $\vec{u}$ with respect to time and space ($i, m = 1, 2, 3$):

$$\frac{\partial^2 u_i}{\partial t^2} = a_i f''\left(t - \frac{n_m x_m}{c}\right) \tag{2.12}$$

$$\frac{\partial^2 u_l}{\partial x_j \partial x_k} = \frac{n_j n_k}{c^2} a_l f''\left(t - \frac{n_m x_m}{c}\right) \tag{2.13}$$

and therefore:

$$c^2 a_i = \frac{1}{\rho} c_{ijkl} n_j n_k a_l. \tag{2.14}$$

The right side of (2.14) without a_l can be written as symmetric *Christoffel matrix* (*Christoffel*, 1877):

$$m_{il} = \frac{1}{\rho} c_{ijkl} n_j n_k, \tag{2.15}$$

where the components m_{il} are dependent on a specific propagation direction $\vec{n}$ (*Babuška and Cara*, 1991). With the elements of the Christoffel matrix, equation (2.14) can be expressed as:

$$m_{il} a_l = c^2 a_i. \tag{2.16}$$

(2.16) has the form of an eigenvalue problem and finding the eigenvalues (c_1^2, c_2^2, c_3^2) and eigenvectors ($\vec{a}_1, \vec{a}_2, \vec{a}_3$) of the Christoffel matrix allows us to determine the phase velocities and propagation directions of individual waves.

Considering the outcomes of section 2.1, for an isotropic case and a plane wave propagation in x_1 direction ($\vec{n} = \vec{e}_1$) the corresponding Christoffel matrix can be written as ($j, k = 1$):

$$m_{il} = \frac{1}{\rho} c_{i11l} n_1 n_1 = \frac{1}{\rho} \begin{pmatrix} c_{1111} & c_{1112} & c_{1113} \\ c_{2111} & c_{2112} & c_{2113} \\ c_{3111} & c_{3112} & c_{3113} \end{pmatrix} = \frac{1}{\rho} \begin{pmatrix} C_{11} & C_{16} & C_{15} \\ C_{61} & C_{66} & C_{65} \\ C_{51} & C_{56} & C_{55} \end{pmatrix} \tag{2.17}$$

and therefore

$$m_{il} = \frac{1}{\rho} \begin{pmatrix} \lambda + 2\mu & 0 & 0 \\ 0 & \mu & 0 \\ 0 & 0 & \mu \end{pmatrix}. \tag{2.18}$$

By solving $\det(m_{il} - c^2\delta_{il}) = 0$ we find the three eigenvalues $c_1^2 = (\lambda + 2\mu)/\rho$, $c_2^2 = \mu/\rho$ and $c_3^2 = \mu/\rho$ which correspond to the speeds of the *P*- (compressional) and *S*- (transverse) waves:

$$v_{\mathrm{P}} = \sqrt{\frac{\lambda + 2\mu}{\rho}}, \qquad v_{\mathrm{S}_1} = v_{\mathrm{S}_2} = \sqrt{\frac{\mu}{\rho}} \tag{2.19}$$

Both waves travel in a certain propagation direction (here x_1) with the *P*-wave polarized parallel to the propagation direction and the two *S*-waves (same speed) perpendicular to it (vertically and horizontally polarized *SV* and *SH* wave).

Next we consider the case of a medium with hexagonal symmetry and the symmetry axis in x_3 direction. Such a medium can be represented by a stack of thin layers with alternating elastic properties (fast and slow seismic velocities) and causes the so-called *shape-preferred orientation* (SPO) anisotropy (Fig. 2.2). Although the individual layers themselves can be isotropic, the stacked medium as a whole behaves anisotropic (*Backus*, 1962). This form of anisotropy is commonly known as *vertical transverse isotropy* (VTI), *radial anisotropy* or *polar anisotropy* (*Thomsen*, 1986) and can only be "felt" by waves that have large wavelengths compared to the thickness of the different layers (e.g. *Backus*, 1962). Inserting (2.5), for a plane wave propagating either in x_1 or x_2 direction (perpendicular to the symmetry axis) the corresponding Christoffel matrix is given by:

$$m_{il} = \frac{1}{\rho}\begin{pmatrix} A & 0 & 0 \\ 0 & N & 0 \\ 0 & 0 & L \end{pmatrix} \tag{2.20}$$

with the three eigenvalues on the diagonal elements of the matrix from which the individual wave speeds can be calculated:

$$v_{\mathrm{P}_1} = \sqrt{\frac{A}{\rho}} \tag{2.21}$$

$$v_{\mathrm{S}_1} = \sqrt{\frac{N}{\rho}}, \qquad v_{\mathrm{S}_2} = \sqrt{\frac{L}{\rho}}. \tag{2.22}$$

For anisotropy caused by horizontal layering of media with different seismic properties, $A > N > L$ (*Babuška and Cara*, 1991). The compressional wave P_1 has the highest velocity and is polarized parallel to the propagation direction x_1 (see Fig.2.2). The faster shear wave S_1 is polarized in the x_1-x_2 plane when propagating in x_1 direction while the slower shear wave S_2

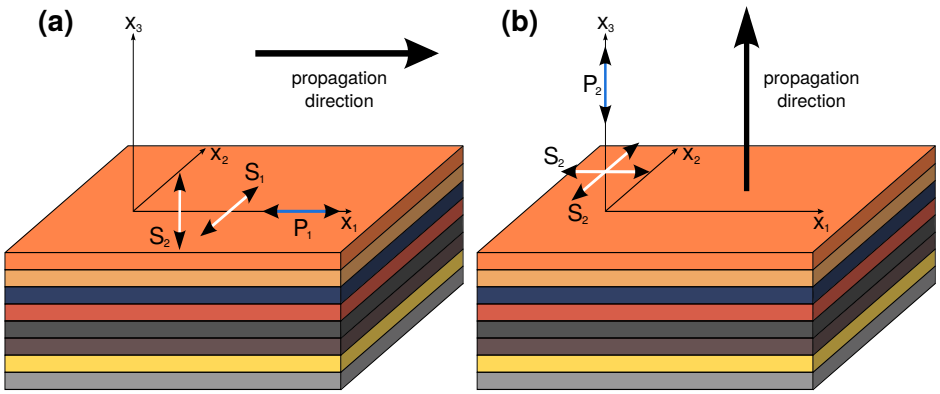

Figure 2.2: Schematic to illustrate vertical transverse isotropy (VTI) or radial anisotropy: (a) If the propagation direction of a shear wave is perpendicular to the vertical symmetry axis of a layered medium (here x_3), where the different layers have different elastic properties (wave speed, density etc.), the two waves S_1 and S_2 separate over distance (they are split) since S_1 only oscillates in one layer with one seismic wave speed. In contrast S_2 oscillates across different layers with different speeds which in general means that S_2 is traveling slower than S_1. (b) For a wave propagating parallel to the vertical symmetry axis of the medium, no separation or splitting will take place since the velocity of the shear wave is independent with respect to the polarization. Moreover, the thickness of the different layers has to be small in comparison to the studied wavelength (after *Babuška and Cara*, 1991).

has a polarization across the individual layers in the x_1-x_3 plane. Therefore, both shear waves propagate in the same direction but with different speeds which results in a time delay between fast and slow wave:

$$\delta t = H\left(\frac{1}{v_{S_2}} - \frac{1}{v_{S_1}}\right) \tag{2.23}$$

with H representing the path length through an anisotropic medium. For a wave propagation in x_3 direction we get for the Christoffel matrix:

$$m_{il} = \frac{1}{\rho}\begin{pmatrix} L & 0 & 0 \\ 0 & L & 0 \\ 0 & 0 & C \end{pmatrix} \tag{2.24}$$

and the resulting wave speeds (calculated from the eigenvalues of m_{il}) are:

$$v_{P_2} = \sqrt{\frac{C}{\rho}} \tag{2.25}$$

$$v_{S_1} = \sqrt{\frac{L}{\rho}}, \qquad v_{S_2} = \sqrt{\frac{L}{\rho}}. \tag{2.26}$$

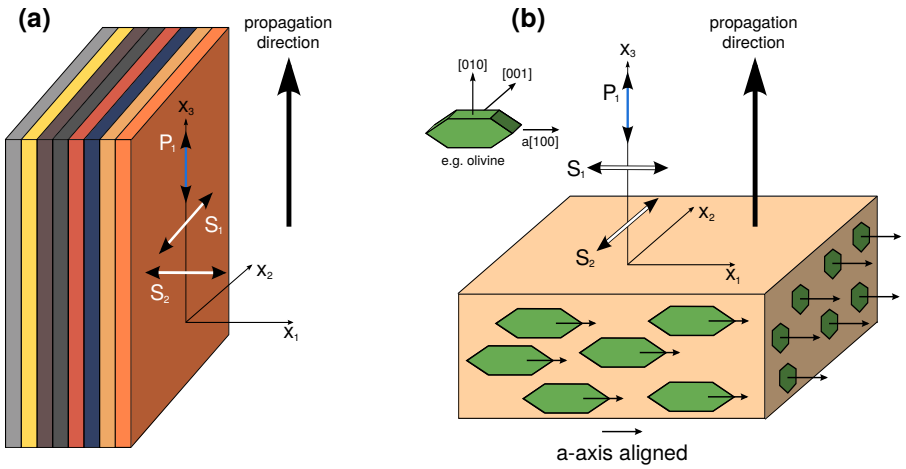

Figure 2.3: Schematic to illustrate horizontal transverse isotropy (HTI) or azimuthal anisotropy: (a) For a shear wave propagating in x_3 direction, perpendicular to the horizontal symmetry axis of a medium with vertically standing layers of different properties (here x_1), the wave will split into two separate waves. (b) Lattice-preferred orientation anisotropy (LPO) of an olivine fabric. If a seismic wave travels through such a medium it splits up and the two resulting waves separate and travel with different speeds (modified after *Bastow et al.*, 2010).

Since both shear waves S_1 and S_2 have obviously the the same velocity ($v_{S_1} = v_{S_2}$), no separation occurs and therefore no delay time δt can be measured (Fig. 2.2). Generally $v_{P_2} < v_{P_1}$ since the wave P_2 oscillates across different layers (also containing slow velocities) while P_1 preferentially travels in the fast layers in the x_1 direction (*Stein and Wysession*, 2009).

If we turn the symmetry axis into the horizontal plane the example from above changes to a medium with vertically aligned layers (Fig. 2.3). This could be decscribe e.g. a medium with vertical fluid-filled cracks or fractures. Therefore, both examples can be described by *horizontal transverse isotropy* (HTI). For shear waves with nearly vertical incidence the wave velocities in such a medium will vary with respect to the azimuth (or backazimuth) from which the waves arrive. This type of anisotropy is called *azimuthal anisotropy*. Thus it is necessary to have good backazimuthal coverage at a seismic recording station to ensure a precise determination of the affecting underlying system of anisotropy.

Besides the SPO cases described so far, azimuthal anisotropy can also result from the *lattice-preferred orientation* (LPO) of intrinsically anisotropic mantle minerals like olivine (Figs. 2.1 and 2.3). Since the *a*-axes of the olivine crystals in principal tend to align parallel to the mantle flow direction, observations of seismic anisotropy are a powerful tool to map the flow characteristics at depths (e.g. *Silver*, 1996).

The main process behind LPO-development in the mantle is called *dislocation creep* which is the motion of crystalline dislocations within a mineral (e.g. *Nicolas and Christensen*, 1987; *Karato*, 2008). In contrast, deformation in the *diffusion creep* regime does not generate LPO (*Karato and Wu*, 1993). It was inferred that the lower mantle is generally be deformed in the diffusion creep regime. However, some studies suggest that in specific regions in the lowermost mantle (D" layer) dislocation creep may also play a role. Thus, LPO development of mineral

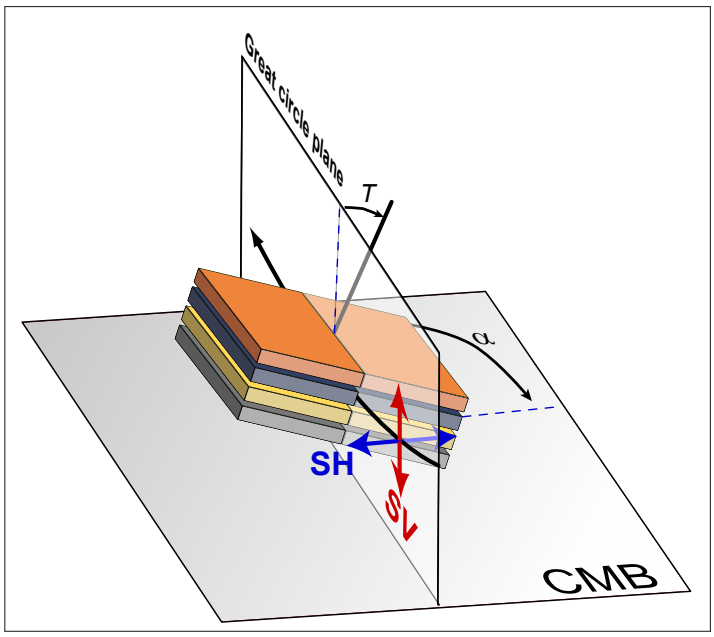

Figure 2.4: Simplified schematic to illustrate tilted transverse isotropy (TTI) located just atop the core-mantle boundary (CMB) in the D" layer caused by a stack of layers with different seismic properties (modified after Garnero, http://garnero.asu.edu/research_images/, with kind permission, last accessed 11 January 2019). The system is equivalent to VTI except that the whole stack is plunging in a specific direction (here azimuth α) with a dip angle T. The passing *SH* and *SV* waves sample different portions of the volume. The great circle plane is parallel to the direction from which the wave arrives (backazimuth).

phases such as post-perovskite potentially contributes to anisotropy in the lowermost mantle (e.g. *McNamara et al.*, 2001; *Creasy et al.*, 2017).

Another form of azimuthal anisotropy occurs for a tilted symmetry axis of VTI. Such a scenario is known as *tilted transverse isotropy* (TTI) and can be described by the dip-angle of the symmetry axis and the azimuth of the dip-direction (Fig. 2.4). TTI is another component that is assumed to be responsible for D" anisotropy (*Wookey and Kendall*, 2008; *Nowacki et al.*, 2011) and is discussed in more detail in section 2.4.3. However, for a symmetry axis that plunges towards the receiver it is not possible to distinguish between TTI and VTI in D" if observations along only one direction (backazimuth) are available (*Nowacki et al.*, 2010). Therefore, multiple azimuths are necessary to detect a tilt of the symmetry axis (e.g. *Wookey and Kendall*, 2008).

2.3 Shear wave splitting

As described in the previous section the presence of seismic anisotropy can be "felt" by seismic waves during their travel through Earth. The most significant contributions to globally detected anisotropy are coming from shear wave splitting (Fig. 2.5) observations. Shear wave splitting is the seismological analog of the well-known phenomenon of optical birefringence (*Savage*, 1999). In principal shear wave splitting can be measured from all kinds of shear waves (*S*-waves). However, detailed knowledge about the initial polarization of the wave before entering the anisotropic volume is important. In this context core-refracted *S*-waves of an earthquake represent a significant facilitation. The most commonly used wave is the *SKS* phase whose raypath to a seismic recording station can be divided into three separate legs (Fig. 2.6). First, the wave travels from the earthquake source down to the core-mantle boundary

(CMB) as an *S*-wave (***S***, for a detailed description of seismic phase name conventions see, e.g., *Storchak et al.*, 2011). By entering the Earth's liquid outer core all initial *SH* energy is reflected and the *SV* wave is converted to a compressional *P*-wave (***K***, standing for the German word *Kern* which means *Core*). Since *P*-waves only oscillate in longitudinal direction, potential shear wave splitting on the source-side of the raypath is cancelled out after the *S*-to-*P* conversion at the CMB. On the receiver-side CMB, the *P*-wave is again converted to an *S*-wave (***S***), in the following defined as $s(t)$. Other core-refracted phases like *SKKS* or *PKS* (Fig. 2.6) follow the same convention but sample partly different portions of the Earth's interior, especially in the lowermost 250 km of the mantle (D"-layer) just atop the CMB. These teleseismic phases can only be observed in limited distance ranges from the source location, namely between around 80°-140° distance (depending on the source depth, Fig. 2.7).

After the *P*-to-*S* conversion at the CMB, $s(t)$ is only polarized in the radial (*SV*) direction $s_R(t)$ or, in other words, $s(t)$ is linearly polarized in the raypath plane between source and receiver (see gray plane in Fig. 2.5). Thus, the initial polarization direction corresponds also to the backazimuth of the seismic event. On the transverse component $s_T(t)$, that is perpendicular to $s_R(t)$, no energy should be observed after the receiver-side *P*-to-*S* conversion (neglecting minor contributions from e.g. 3D scattering).

Assuming linearly polarized $s(t)$ now enters a transversely isotropic medium with a

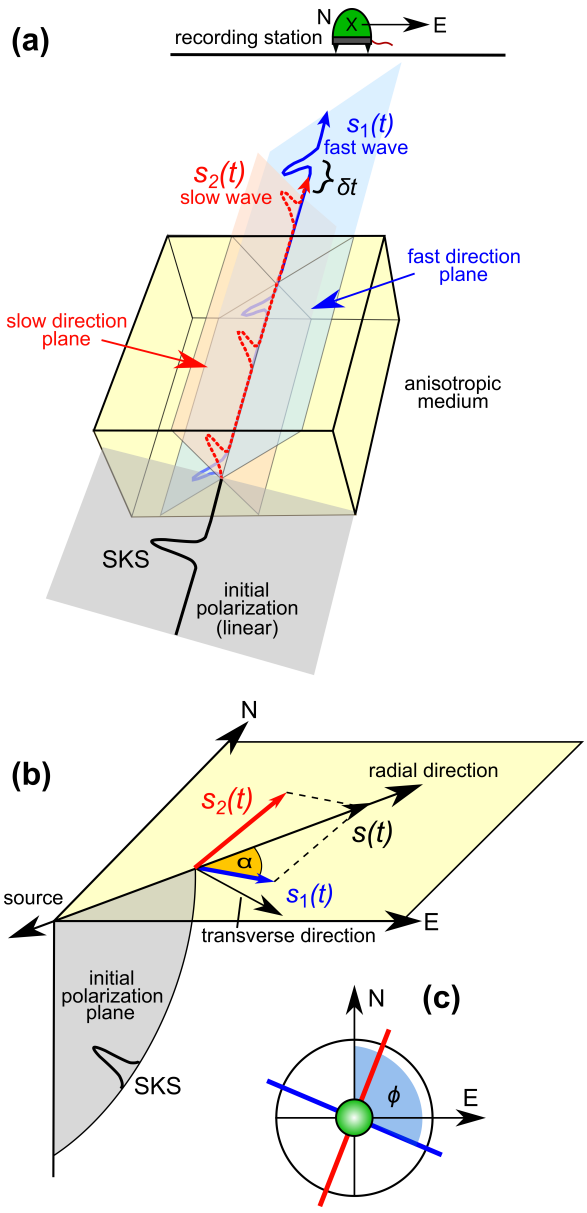

Figure 2.5: (a) Schematic of shear wave splitting (mod. after Garnero, http://garnero.asu.edu/research_images/, with kind permission, last accessed 11 January 2019). An *SKS* wave (linearly polarized parallel to the gray great circle plane) with nearly vertical incidence enters an anisotropic volume (yellow box). The wave is split into two quasi-*S*-waves, one polarized parallel to the fast axis direction (blue) and one perpendicular to it (red, slow axis). With an increasing path length, a time delay δt between the fast and slow wave accumulates that can be measured at a station on the surface (green). (b) Conventions to calculate the splitting of the incident *SKS* phase in equations 2.28 and 2.30 (after *Babuška and Cara*, 1991). (c) Top view at the seismic station. The azimuth of the fast direction (blue) corresponds to ϕ and is measured clockwise from North (here $\phi \approx 135°$ or, equivalent, $\phi \approx -45°$).

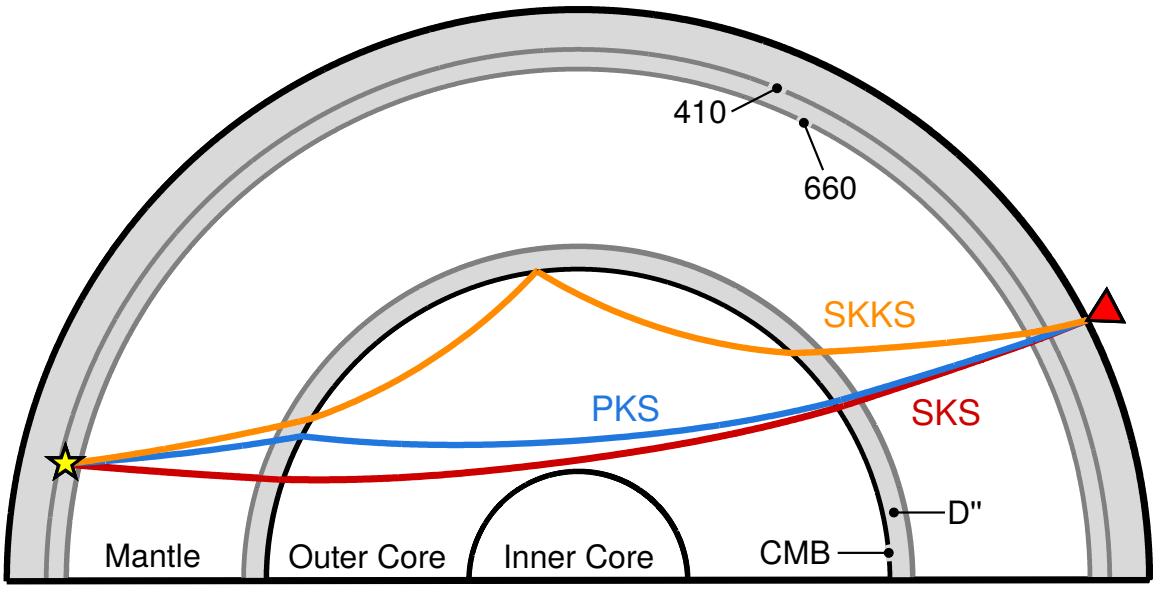

Figure 2.6: Raypaths of teleseismic phases (*SKS*, *SKKS*, *PKS*) that are used to study shear wave splitting in Scandinavia. The raypaths are computed for an event in 500 km depth and with an epicentral distance of 140° using the tauP toolkit (*Crotwell et al.*, 1999) with the standard Earth model *iasp91* (*Kennett*, 1991). Please note that all three phases are only observable in a narrow distance window (see Fig. 2.7). In most cases only *SKS* and *SKKS* were analyzed. Major seismological structures are indicated - CMB: core-mantle boundary, D": 200-300 km-thick layer atop the CMB (see section 2.4.3), 410 and 660: discontinuities in 410 and 660 km depth

horizontal symmetry axis (under nearly vertical incidence), the wave splits up into two orthogonal quasi-*S*-waves (Fig. 2.5, compare section 2.2) which then are polarized in the direction of the anisotropy fast axis and perpendicular to it (slow axis):

$$s_1(t) = s(t)\cos(\alpha), \qquad s_2(t) = s(t-\delta t)\sin(\alpha) \tag{2.27}$$

with α defining the polarization angle between the radial direction and the fast axis and δt representing the resulting delay time between the fast and slow wave (Fig. 2.5, see equation 2.23). Therefore, we get for the split wave on the radial and transverse components (*Babuška and Cara*, 1991):

$$s_R(t) = s(t)\cos^2(\alpha) + s(t-\delta t)\sin^2(\alpha) \tag{2.28}$$

$$s_T(t) = \frac{1}{2}[s(t) - s(t-\delta t)]\sin(2\alpha). \tag{2.29}$$

Following *Silver and Chan* (1991), the splitting process can be easily reversed by calculating the two-dimensional time-domain covariance matrix of the horizontal particle motion:

$$c_{ij}(\alpha,\delta t) = \int_{-\infty}^{\infty} s_i(\alpha,t)s_j(\alpha,t-\delta t)\,\mathrm{d}t \qquad i,j = \mathrm{R},\mathrm{T}. \tag{2.30}$$

The two eigenvalues of c_{ij}, λ_1 and λ_2 (not to be confused with the Lamé parameter λ), may be used as a measure of linearity and therefore enable to determine if a wave was split or not. For the cases that the medium is isotropic or the initial polarization is equal to the medium's fast (or slow) axis, c_{ij} will only have one non-zero eigenvalue. This implies no splitting and is commonly known as a so-called null measurement (e.g. *Savage*, 1999; *Wüstefeld and Bokelmann*, 2007).

For the anisotropic case, both eigenvalues of c_{ij} are non-zero, unless $\alpha = n\pi/2$ (with $n =$ 0, 1, 2...) or δt is zero (*Silver and Chan*, 1991). The parameter pair α-δt that best describes the splitting process and therefore removes the signal on $s_T(t)$ can be determined by finding the most singular covariance matrix c_{ij} calculated from the systematically rotated and time-shifted split waveforms. The reason that c_{ij} in general cannot become fully singular is mainly caused by seismic noise in the recordings. The approach of minimizing λ_2 is also known as the Eigenvalue method (hereinafter EV, see e.g. *Silver and Chan*, 1991). For known initial polarizations (as for *SKS*, *SKKS* or *PKS*), the energy on the transverse component

$$E_{trans} = \int_{-\infty}^{\infty} s_T^2(t)\,\mathrm{d}t \tag{2.31}$$

after correcting the splitting can be minimized, instead of minimizing λ_2. This is the most widely applied approach in the seismological community and is commonly known as the energy minimization method (or Silver & Chan method, hereinafter SC), although slightly varying names can be found in the literature. Another approach is the so-called rotation-correlation method (RC, *Bowman and Ando*, 1987) that uses cross-correlation to find the pair of α-δt for which the systematically rotated and time-shifted split waveforms reach a maximum correlation coefficient.

In general, instead of α, the fast axis direction is declared as ϕ which is measured clockwise between geographic North and the direction of $s_1(t)$ (projected onto the Earth's surface). Alternatively, ϕ can be declared as angle relative to North in an interval between $-90°$ and $+90°$ (also in this thesis). Since for core-refracted *S*-waves the radial direction corresponds to the backazimuth $\pm 180°$, ϕ can easily be determined. The two parameters, fast axis direction ϕ and delay time δt, are commonly known as the splitting parameters (e.g. *Savage*, 1999; *Long and Silver*, 2009).

For delay times that are small compared to the dominant period of the studied seismic phase, the radial and transverse components of the split waves can also be written as (*Silver and Chan*, 1988; *Chevrot*, 2000):

$$R(t) \approx s(t) \tag{2.32}$$

$$T(t) \approx -\frac{1}{2}[\delta t \sin(2\alpha)]R'(t) \tag{2.33}$$

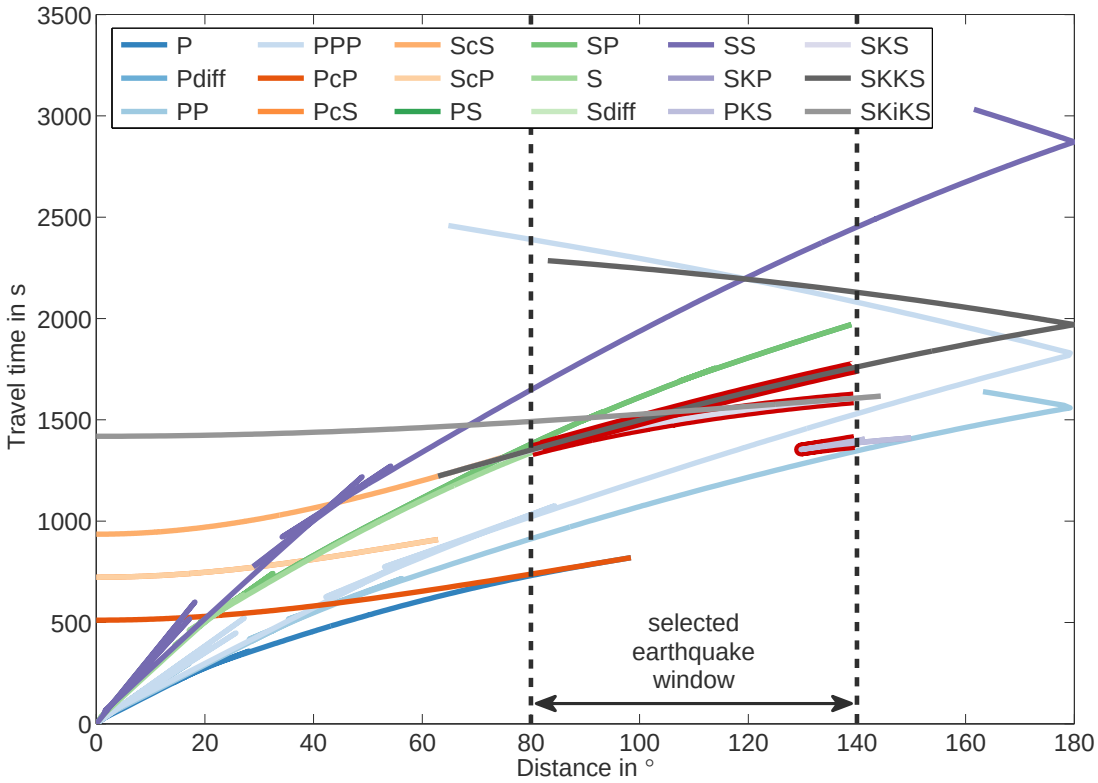

Figure 2.7: Traveltimes of seismic phases for an event depth of 0 km generated with the tauP toolkit (*Crotwell et al.*, 1999) and the standard Earth model *iasp91* (*Kennett*, 1991). The three phases *SKS*, *SKKS* and *PKS* are additionally highlighted in dark red within the 80°-140° distance window (dashed black lines) that was used to select appropriate earthquakes for the shear wave splitting analysis.

where $R'(t)$ is the time derivative of $R(t)$. Thus, $T(t)$ is simply the time derivative of the radial component multiplied by a sinusoidal factor whose amplitude depends on the delay time δt and whose phase depends on the fast axis orientation. The term in square brackets is defined as the splitting intensity (SI, *Chevrot*, 2000). The SI is a measure of the amplitude of the transverse component $T(t)$ relative to the time derivative of the radial component $R'(t)$ and can be determined by simple projection of the components within the analysis window that includes the phase onset (*Chevrot*, 2000; *Monteiller and Chevrot*, 2010; *Deng et al.*, 2017):

$$\mathrm{SI} = -2\frac{\int T(t)R'(t)\,\mathrm{d}t}{\int R'(t)^2\,\mathrm{d}t}. \tag{2.34}$$

Therefore the amount of energy on the transverse component can be easily determined and it serves as a proxy for shear wave splitting.

2.4 Locations of anisotropy in the Earth

All analysis methods described in the previous section have in common that if a clear signal on the transverse component of a recording station is observed, this is a typical indicator for

seismic anisotropy somewhere between the CMB and the surface. Due to the nearly vertical incidence of the phase at the Earth's surface (e.g. *SKS*, *SKKS*, *PKS*), shear wave splitting delivers very good lateral resolution and, therefore, it is a powerful tool to map changes in the fast axis direction ϕ and delay time δt beneath a target region. However, this requires dense station networks, preferably with long recording periods. In contrast, the depth estimation of the anisotropic volume is more complicated and can only be constrained using different approaches (e.g. using surface wave dispersion) that sample the anisotropic structure in different ways than core-refracted waves (e.g. *Long and Becker*, 2010). Nevertheless, supported by dense networks, shear wave splitting observations can at least be used to estimate the potential depth of an anisotropic source using finite-frequency assumptions (Fresnel-zone estimates) for the recorded signals (e.g. *Alsina and Snieder*, 1995; *Rümpker and Ryberg*, 2000; *Favier and Chevrot*, 2003).

In the last few decades the combination of different seismological approaches and techniques allowed to characterize seismic anisotropy in settings like subduction zones (e.g. *Hicks et al.*, 2012; *Eakin et al.*, 2016; *Lynner et al.*, 2017), cratons (e.g. *Fouch and Rondenay*, 2006; *Vecsey et al.*, 2007; *Wüstefeld et al.*, 2010), plumes (e.g. *Walker et al.*, 2005), volcanoes (e.g. *Gerst and Savage*, 2004), mid-ocean ridges (e.g. *Eakin et al.*, 2018) or in the vicinity of geothermal powerplants (e.g. *Frietsch et al.*, 2015). Globally, the presence of seismic anisotropy was inferred for the Earth's crust, upper mantle (lithosphere and asthenosphere), mantle transition zone, the 200-300 km-thick D" layer in the lowermost mantle just atop the CMB in around 2700 km depth and the solid inner core (Fig. 2.8). With the exception of the inner core, potentially all depths ranges above the CMB can contribute to the overall anisotropic signals analyzed in this thesis. Therefore in the following I will only focus on these volumes. Further details and information about anisotropy in the inner core can be found in *Woodhouse et al.* (1986), *Su and Dziewonski* (1995), *Wookey and Helffrich* (2008), *Deuss* (2014) and *Frost and Romanowicz* (2017).

2.4.1 Crustal anisotropy

Crustal anisotropy is assumed to occur in the upper 10 km to 15 km of the Earth's crust and is mainly SPO anisotropy caused by two primary sources: The first are small micro-cracks and fractures, in general randomly oriented and filled with water or other fluids. Fractures are mostly aligned perpendicular to the minimum horizontal stress direction. The alternating changes of the elastic properties result in seismic anisotropy with the fast axis direction ϕ parallel to the maximum horizontal stress component (e.g. *Crampin*, 1984; *Crampin and Lovell*, 1991; *Crampin and Chastin*, 2003). The strength of anisotropy (δt) is controlled by the amount of cracks and fractures as well as their dimensions and contents (e.g. water, air, hydrocarbons). The second source for crustal anisotropy are media consisting of fine-layered material with alternating fast and slow velocities (see section 2.2). Even if the individual layer materials are

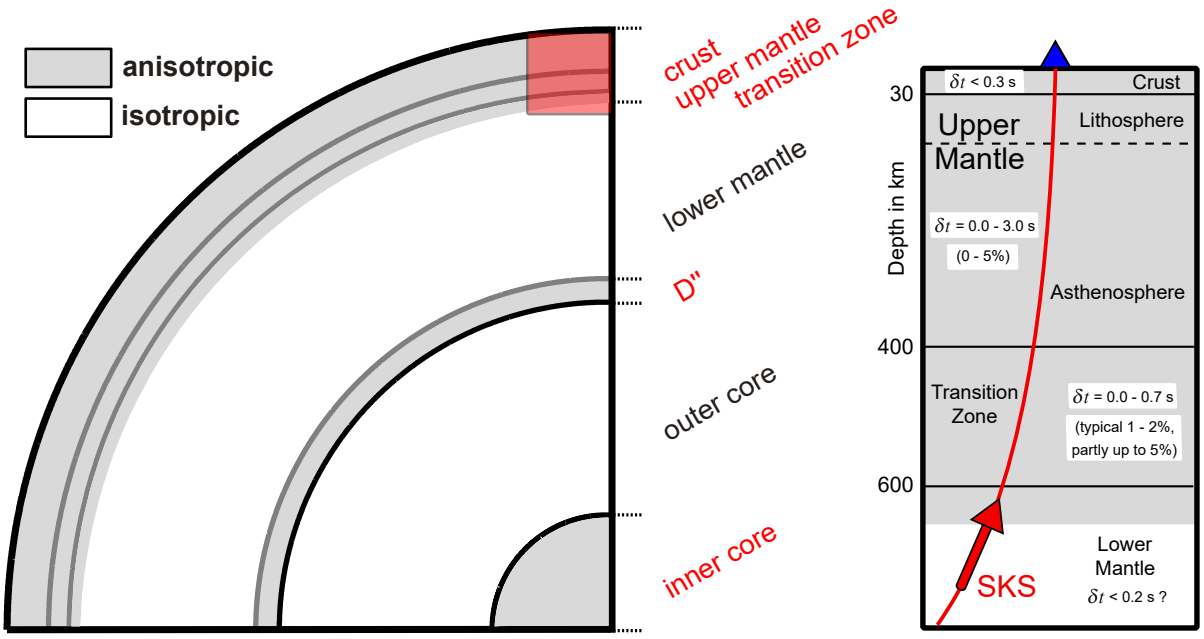

Figure 2.8: Left: Schematic view of the Earth (modified after Garnero, http://garnero.asu.edu/research_images/, with kind permission, last accessed 11 January 2019), indicating areas where seismic anisotropy was detected in general using seismology (e.g. by shear wave splitting and surface wave dispersion analysis). Areas marked in gray are indicated as anisotropic (crust, upper mantle, transition zone, D", inner core). White zones are generally assumed to be nearly isotropic (e.g. *Meade et al.*, 1995). Right: Zoom into the shallower part (red box in left figure) of the Earth (modified after *Savage*, 1999). Typically observed values for the delay times δt in different depth ranges and the percentage of anisotropy are indicated. The red line marks a typical *SKS* raypath to a seismic recording station at the surface (blue triangle).

isotropic themselves, the resulting stack of layers as a whole can act as an anisotropic volume (e.g. *Backus*, 1962). Both cases can be described by a hexagonal symmetry system with the symmetry axis orthogonal to the cracks or the layers, respectively. Typical delay times for crustal anisotropy are assumed to be in the order of < 0.3 s (Fig. 2.8, e.g. *Crampin and Booth*, 1985; *Silver and Chan*, 1988; *Barruol and Mainprice*, 1993; *Savage*, 1999). However, some studies suggest slightly larger values for specific regions around the globe (*McNamara et al.*, 1994; *Kong et al.*, 2016; *Latifi et al.*, 2018).

2.4.2 Anisotropy in the upper mantle and mantle transition zone

The sources for observed delay times > 0.5 s (Fig. 2.8) most likely are located in the upper mantle (*Savage*, 1999). However, the depth range to which anisotropy is reaching down is still under debate although several studies suggest little to negligible contributions below 400 km to 600 km depth (e.g. *Vinnik et al.*, 1992; *Barruol and Mainprice*, 1993; *Yuan and Beghein*, 2013). Especially for surface waves, anisotropy vanishes with increasing wavelength (e.g. *Debayle et al.*, 2005) and therefore indicates a decreasing strength with increasing depth. The following assumptions and conclusions are mainly based on laboratory experiments (e.g. *Is-*

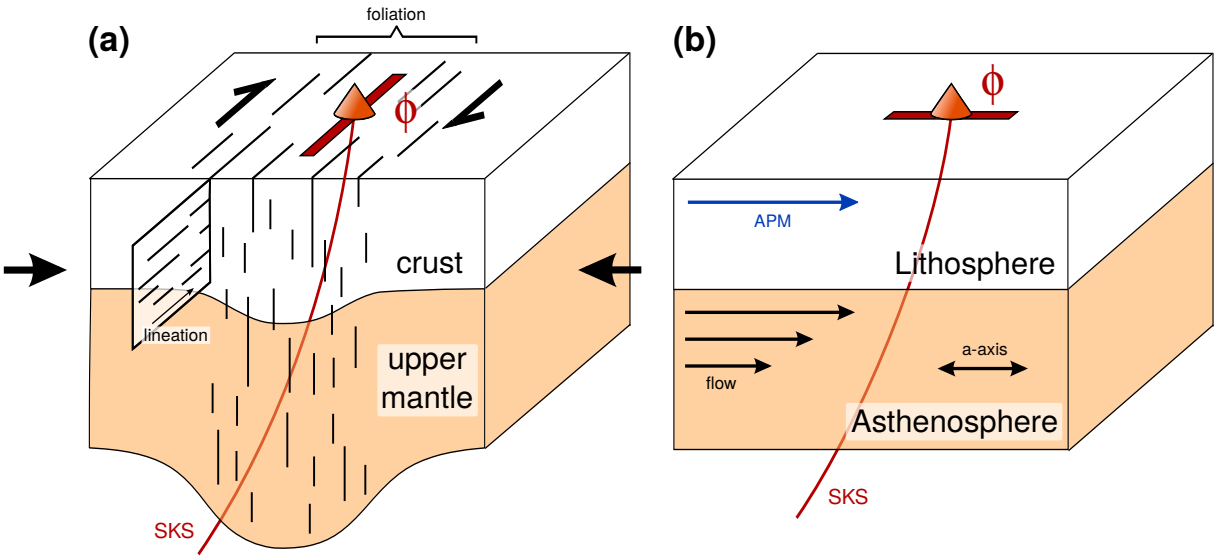

Figure 2.9: Interpretations of shear wave splitting observations (modified after *Silver*, 1996; *Savage*, 1999). Left: *vertically coherent deformation* (VCD) caused by transpressional motion. Large black arrows on the left and right indicate the direction in which most deformation is accumulated. The foliation planes are assumed to be vertical with the lineation sub-horizontal in the foliation plane and therefore the fast axis direction ϕ (red bar) is parallel to the lineation direction. Right: *simple asthenospheric flow* (SAF). The absolute plate motion (APM) of the lithosphere is parallel to the anisotropy fast axis ϕ as measured at a recording station (orange cone). This can be directly linked to the underlying mantle flow direction. In both cases the anisotropy is caused by LPO development (compare Fig. 2.3).

maïl and Mainprice, 1998; *Karato et al.*, 2008) in which different ambient conditions of the mantle material (temperature, density, fluid content) are tested. In the lithospheric part of the mantle, the LPO of intrinsically anisotropic mantle minerals like olivine (about 70% of the mantle, *Ismaïl and Mainprice*, 1998) is assumed to play a key role for the development of seismic anisotropy. Due to so-called *vertically coherent deformation* (Fig. 2.9) the crust and the subcontinental mantle undergo coherent deformation within tectonically active periods which can result in the development of an LPO fabric. A cool-down effect is that the major deformation trend of the latest reworking is frozen into the lithosphere (e.g. *Silver*, 1996; *Long and Becker*, 2010; *Long et al.*, 2016). Therefore, in the simplest case, for vertically coherent deformation caused by transpressional and/or transcurrent motion (Fig. 2.9), the fast axis direction ϕ mirrors the large-scale structural trend of the last tectonic event in a studied region. Descriptively, for large-scale continental collision, ϕ is assumed to be parallel to the formed mountain belts (*Silver*, 1996). In contrast, for extensional motion (e.g. in rifting environments), ϕ aligns with the extension direction (e.g. *Gao et al.*, 1994). Observed delay times of up to 1 s would typically require about 150 km wave propagation paths in anisotropic lithosphere (*Mainprice and Silver*, 1993).

In the asthenospheric part of the mantle the fast axis of the anisotropic crystals tend to align with the maximum shear direction. Therefore, measured orientations of ϕ can be used to indirectly constrain the direction of, e.g., horizontal asthenospheric mantle flow (*simple astheno-*

spheric flow, Fig. 2.9) that (in a hot spot reference frame like HS3-NUVEL 1A, *Gripp and Gordon*, 2002) is parallel to the absolute plate motion (APM) direction of the plate (e.g. *Silver*, 1996; *Long and Becker*, 2010). Vertical mantle flow sampled by shear waves with steep incidence will consequently result in a null measurement (e.g. *Wolfe and Solomon*, 1998; *Lynner and Bodmer*, 2017) since vertically aligned *a*-axes only cause negligible weak anisotropy (see Fig. 2.1). If only smooth variations of ϕ across different tectonic or geological borders are observed, asthenospheric mantle flow is one of the most plausible explanations (e.g. *Yang et al.*, 2014). In contrast, frozen-in anisotropy in the lithosphere may reflect these borders by abrupt changes or significant variations in the splitting parameters within short length scales (e.g. *Vecsey et al.*, 2007). All these interpretations are valid for typical upper mantle conditions. However, specific variations in physical and chemical parameters like water content or temperature changes can have an influence on the type of LPO that develops (e.g. *Katayama et al.*, 2004; *Jung et al.*, 2006).

Mantle anisotropy caused by SPO is assumed to mainly result from melt-filled cracks or lenses and layered sheets of melt (e.g. *Kendall*, 1994; *Braun et al.*, 2000; *Moore et al.*, 2004). There is much evidence that such structures (at least in parts) are responsible for the development of anisotropy beneath mid-ocean ridges (e.g. *Wolfe and Solomon*, 1998; *Eakin et al.*, 2018) and continental rift-zones (e.g. *Gao et al.*, 1997; *Hammond et al.*, 2014).

Although most studies assume the mantle transition zone (Fig. 2.8) to be generally isotropic, some work based on surface wave and normal mode observations infers a contribution from this depth range (e.g. *Trampert and van Heijst*, 2002; *Beghein et al.*, 2008). Evidence from shear wave splitting is rare (e.g. *Fouch and Fischer*, 1996) since in most cases no significant splitting differences were found for comparisons between teleseismic phases like *SKS* and *S* phases of deep local earthquakes.

2.4.3 Lowermost mantle anisotropy

Originally the Earth's lower mantle (Fig. 2.8) was defined as the so-called *D* layer (*Bullen*, 1940). However, it was quickly noted that the lowermost part of the D layer ($\approx$ 200-300 km) is seismically distinct from the overlying lower mantle volume. Therefore, the lower mantle was divided into the (upper) *D'* and (lower) *D''* layer (*Bullen*, 1949). Only the latter designation is still in use in global seismology to refer to the corresponding layer, the others are generally replaced by more modern name conventions (*Nowacki et al.*, 2011). However, at this point it has to be mentioned that this anomalous layer was already described by Cornelius G. Dahm in 1934 (*Dahm*, 1934). Unfortunately, his name and findings fell partly into oblivion over the years (*Howell Jr. and Kisslinger*, 2000).

While the lower mantle in general is assumed to be nearly isotropic (e.g. *Meade et al.*, 1995; *Panning and Romanowicz*, 2006), it was found that D" contains regions of significant anisotropy

(e.g. *Kendall and Silver*, 1996; *Garnero et al.*, 2004; *Maupin et al.*, 2005). It is widely accepted that this is mainly caused by a change in material composition due to a thermal boundary layer between the hot outer core and the colder mantle (e.g. *Nowacki et al.*, 2011, and references therein). Potential sources behind D" anisotropy are assumed to be SPO or LPO or a combination of both, maybe from melt lenses or layers of melt material and mantle flow (e.g *Weber*, 1994; *Moore et al.*, 2004; *Nowacki et al.*, 2011; *Cottaar and Romanowicz*, 2013). Simple vertical transverse isotropy was assumed to make the major contribution to D" anisotropy based on splitting measurements of *S*-waves that sample these volumes in a nearly horizontal way (e.g. *ScS* phases). However, using seismic waves arriving from different directions, more recently it was shown that in some areas also a type of TTI most likely plays an important role (e.g. *Wookey and Kendall*, 2008; *Nowacki et al.*, 2010, 2011). Further evidence for (azimuthal) anisotropy in D" is coming from clear splitting discrepancies of *SKS* and *SKKS* phases for the same source-receiver pair (e.g. *He and Long*, 2011; *Long*, 2009; *Lynner and Long*, 2012, 2014; *Long and Lynner*, 2015; *Deng et al.*, 2017). The *SKS-SKKS* technique is used in this thesis (see chapter 6) to probe so far unexplored volumes in the lowermost mantle with data recorded at the dense station network in Scandinavia. Such networks are required to get further insights into Earth's deep structures. However, the globally sampled D" regions are also limited by specific source-receiver paths that are controlled by the station locations (so far mainly on landmasses) as well as the natural seismicity along (preferentially) deep subduction zones (*Nowacki et al.*, 2011).

3 The ScanArray experiment

This chapter switches from the theoretical background to the practical component of my doctoral research and focuses on the ScanArray field experiment in which existing temporary and permanent networks were extended with broadband sensors in Finland and Sweden. First a brief overview of the ScanArray seismic network is given, followed by a more detailed description of the German contribution LITHOS-CAPP, in which I was actively involved. Most parts of this chapter have been published in:

> *Grund, M., Mauerberger, A., Ritter, J.R.R. & Tilmann, F.* (2017), **Broadband Recordings for LITHOS-CAPP: Lithospheric Structure of Caledonian, Archean and Proterozoic Provinces, Sep. 2014 – Oct. 2016, Sweden and Finland**, Scientific Technical Report STR – Data 17/02, GIPP Experiment and Data Archive, Potsdam: GFZ German Research Centre for Geosciences, http://doi.org/10.2312/GFZ.b103-17029.

3.1 ScanArray network

The deep structure and the evolution of the Baltic (or Fennoscandian) Shield and the Caledonian Scandinavian Mountains (Scandes) are the focus of an international team of geoscientists (Fig. 3.1). The western rim of Scandinavia with the Scandes mountain range has elevations of up to 2500 m. Since this region lacks recent compressional tectonic forces, it provides a great opportunity to understand the geodynamical evolution of crustal and upper mantle structures at passive continental margins. In the central part of Scandinavia the Baltic Shield grew during several collisional phases whose present deep structure is only poorly understood.

In order to clarify open questions in this context, the joint international seismological experiment **ScanArray** was established which covers the whole area for the first time (Fig. 3.1). ScanArray is a consortium including Helmholtz-Centre Potsdam GFZ German Research Centre for Geosciences, Karlsruhe Institute of Technology (KIT), NORSAR[1], NGU[2] (both Norway) as well as the Universities of Copenhagen, Oslo, Leicester, Uppsala, Bergen, Aarhus and Oulu (*Thybo et al.*, 2012). In fall 2014, 97 broadband stations were deployed by the project partners

[1] NORSAR, http://www.norsardata.no/, last accessed 11 January 2019
[2] NGU, http://www.ngu.no/en/node, last accessed 11 January 2019

covering central and northern Norway and Sweden and the western margin of Finland. Twenty broadband seismic stations were provided by the Geophysical Instrument Pool Potsdam (GIPP) and Section 2.4 Seismology of GFZ and operated for two years (see next section 3.2, *LITHOSCAPP*). Furthermore, the temporary networks SCANLIPS3D (University of Leicester, *England et al.*, 2015) and Neonor2[3] (University of Bergen) as well as about 115 permanent stations of different national network operators in Scandinavia (Norway, Sweden, Finland, Denmark) and neighboring countries (Russia, Latvia, Estonia, Lithuania) contributed to the (extended) ScanArray network (Fig. 3.1). In general, inter-station distances within the ScanArray network are approximately 50 km to 60 km. A record section of the 2015 M_W 7.8 Nepal earthquake[4] is shown in the top panel of Fig. 3.2. Waveforms for a local/regional earthquake that occurred off the coast of northern Sweden[5] are shown in the bottom panel of Fig. 3.2. For both types of events the data quality is satisfactory with respect to the signal-to-noise ratios (SNR) and therefore allows to apply different seismological approaches. Please note that the *P*- and *S*-phase onsets for the local/regional event are only visible up to around 3° epicentral distance (or ≈ 333 km) before they are masked by the background noise. However, the Rayleigh wave is seen across the whole network also several hundred kilometers away from the hypocenter.

The ScanArray project links to former studies which mainly covered the southern regions of Scandinavia (Fig. 3.1, open gray triangles). An unusually shallow crust and lithosphere-asthenosphere boundary have been found beneath the high-topography Scandes mountain range of western Norway, where a clear crustal mountain root seems to be absent. However, the lower topography regions of eastern Norway and Sweden reveal a thicker crust, which contrasts with the principles of Airy isostasy. Lower seismic velocities than expected for a tectonically stable region have been found for southern Norway with a sharp transition to higher seismic *P*-wave and *S*-wave velocities beneath Sweden. To obtain a high-resolution (lithospheric) shear wave model, it was planned to combine tomographic and waveform inversions of surface waves and ambient noise subsequently producing 3D velocity models, including both isotropic and anisotropic analyses. The focus was on the variation of crustal and lithospheric structure as well as seismic velocity across the Scandes mountain range and western (Phanerozoic) and eastern (Proterozoic) Scandinavia. The spatial variation of anisotropic structures should give a hint at the tectonic formation since anisotropy might differ between the tectonic units or could be consistent over larger regions.

[3] Neonor2, for further details see https://www.ngu.no/en/neonor2, last accessed 11 January 2019
[4] USGS, https://earthquake.usgs.gov/earthquakes/eventpage/us20002926, last accessed 11 January 2019
[5] Institute of Seismology, University of Helsinki, http://www.seismo.helsinki.fi/bulletin/list/catalog/earthquakes.html, last accessed 11 January 2019

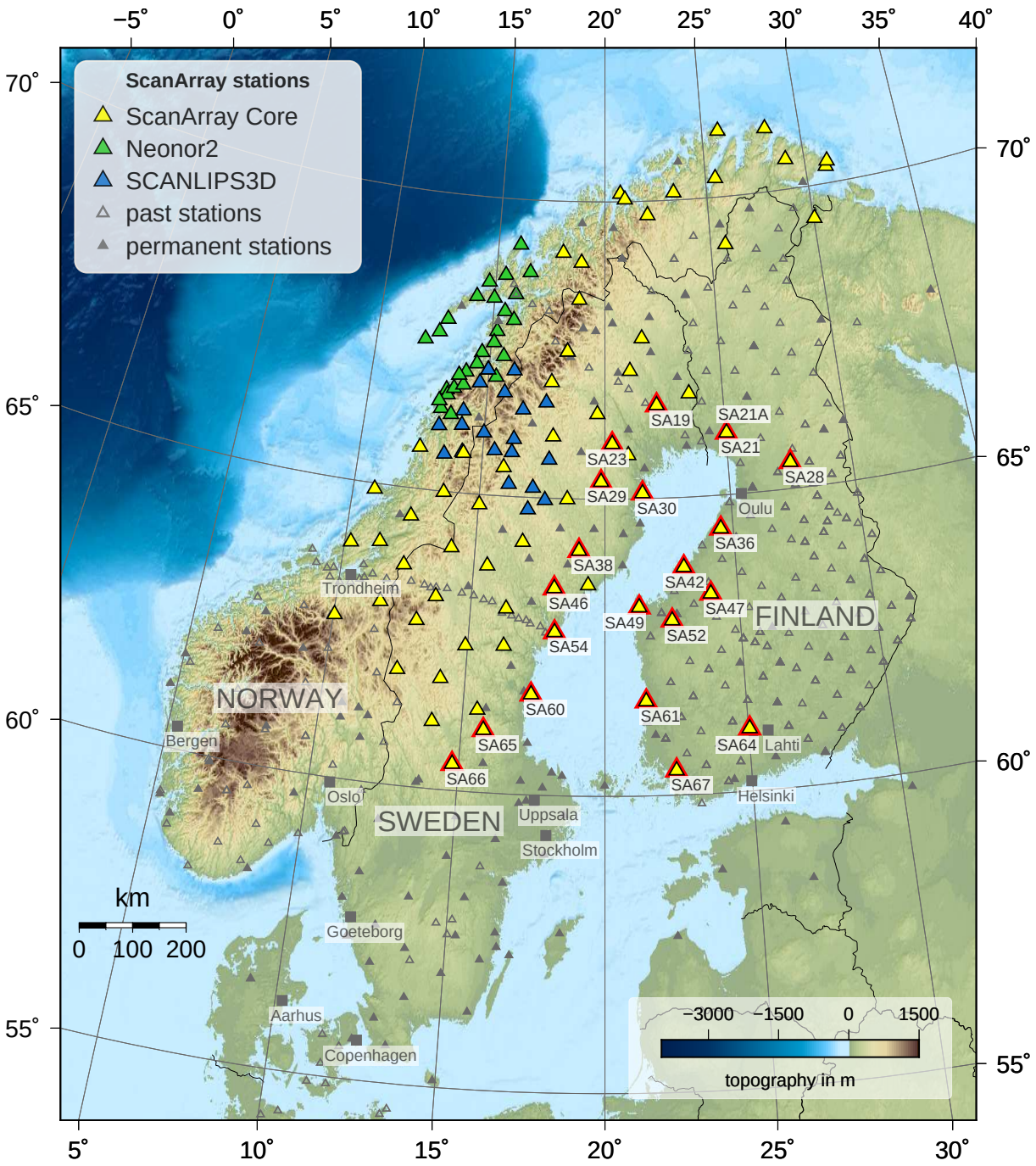

Figure 3.1: Map of the extended ScanArray network (*Thybo et al.*, 2012). Yellow triangles indicate the major contributing temporary stations, the so-called ScanArray Core network. Red edges mark the German contribution LITHOS-CAPP (LC), operated by KIT and GFZ Potsdam (*Grund et al.*, 2017a). Names of LC stations are also indicated (SA*). Images of the individual sites are shown in Figs. 3.4 and 3.5. Green triangles display station locations of the temporary Neonor2 network mainly operated by University of Bergen. Blue triangles show stations of the SCANLIPS3D project operated by University of Leicester (*England et al.*, 2015). The high number of permanent stations (runtimes partly $>$ 10 years) are indicated as filled gray triangles. Open gray triangles mark stations of past temporary experiments. Topography and bathymetry of the region are given as background color.

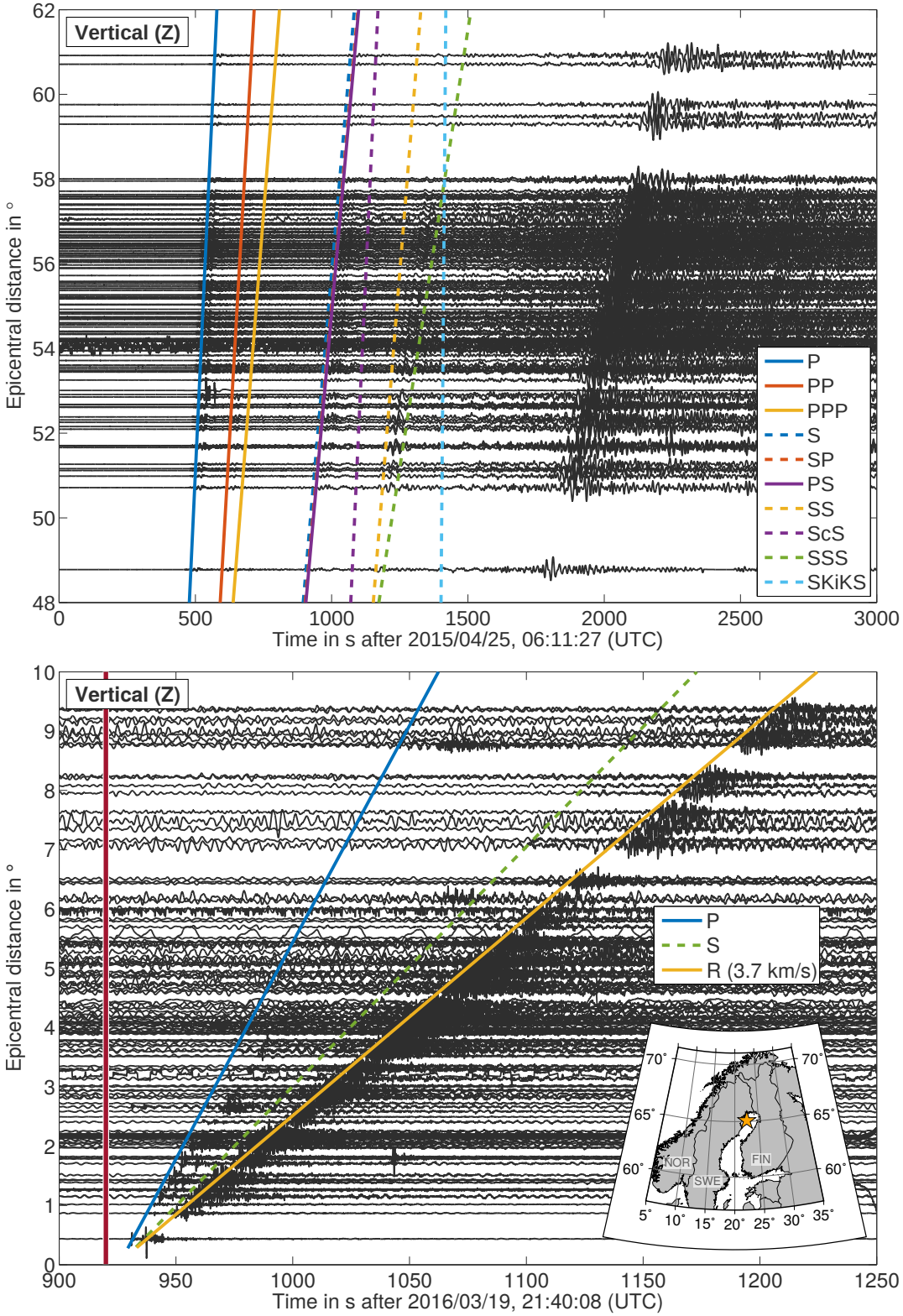

Figure 3.2: Top: Record section of the 2015 Nepal earthquake (M_W 7.8) across the ScanArray network. Shown are all stations for which data were available on 25 April 2015. Waveforms are bandpass-filtered between 0.01 Hz and 0.5 Hz. Bottom: Local and regional waves (bandpass-filtered between 0.04 Hz and 2 Hz) of an M_L 4.1 earthquake which occurred in the Bothnian Bay region off the coast of Sweden (see orange star in inset map). Shown are all stations for which data were available on 19 March 2016. Theoretical arrival times based on the iasp91 Earth model (*Kennett*, 1991) are shown as colored lines. For the regional earthquake *R* stands for the Rayleigh-wave with a phase velocity of around 3.7 km/s and the vertical red line marks the origin time of the event.

Figure 3.3: Picture from the field experiment while dismantling of station SA42 (Palmantie, Finland) beneath a hut close to a lake in October 2016 (© W. Scherer, 2016, with kind permission). The inset map shows the exact location of the station.

3.2 LITHOS-CAPP

The LITHOS-CAPP project (**LITHO**spheric **S**tructure of **C**aledonian, **A**rchaean and **P**roterozoic **P**rovinces) is the German contribution to the ScanArray initiative (Helmholtz-Centre Potsdam GFZ German Research Centre for Geosciences and Karlsruhe Institute of Technology, KIT).

3.2.1 Data acquisition

Experiment design and schedule

Within the framework of LITHOS-CAPP, 20 temporary seismic broadband stations were deployed and operated by KIT and GFZ in Finland and Sweden to record teleseismic earthquakes and local seismicity in the period September 2014 to October 2016 (Fig. 3.1). Depending on the individual site conditions, sensors were installed on bedrock, concrete floors or concrete plates close to or within residential as well as governmental buildings. Power supply was mostly contributed by the individual site owners. After the installation in September/October 2014, service trips were undertaken to check the technical components as well as change and save the hard drives with the data (in May 2015, September 2015 and May 2016). Finally, stations were removed in September/October 2016 (Fig. 3.3), after two years of continuous recording.

Figure 3.4: Station locations for the LITHOS-CAPP stations in Finland (see also Fig. 3.1). In two cases red arrows mark the location of the sensor when it is not clearly visible.

Figure 3.5: Station locations for the LITHOS-CAPP stations in Sweden (see also Fig. 3.1). In four cases red arrows mark the location of the sensor when it is not clearly visible.

Network geometry and location

The seismic stations were installed close to or within buildings (Figs. 3.4 and 3.5) to ensure a continuous power supply over the long-lasting winter periods. Depending on the individual site, most sensors were directly installed on concrete floor or bedrock. To establish a consistent nomenclature, station names were generated for the whole ScanArray network. Thus, the LITHOS-CAPP station names listed in Table 3.1 are part of this superordinated naming system and are not labeled with consecutive numbers from 1 to 20. Please note that station SA21 was removed in May 2015 due to flooding caused by snow melt water. In September 2015, this station was reinstalled at the same property a few hundred meters away as station SA21A. If more than one data logger is listed for a station, this indicates a replacement due to technical problems. Besides all station names, Table 3.1 lists the locations, elevations, and sensor and data logger types with serial numbers as well as runtime periods of the individual data loggers.

Table 3.1: Instrumentation information including serial numbers of the used sensors and data loggers for each recording station. Note the replacement of station SA21 as SA21A. Note that the deployment period reflects the time the station was deployed in the field, not the data holdings. There is a discrepancy at some stations because of station outages due to technical failures.

Station	Location	Alt. /m	Sensor, ID	Logger, ID	Deployment period
SA19	66.5654N	178	Trillium 120 PA	EDL-PR6	2014/09/18-
(Ertsjärv)	22.1788E		003	3226	2016/09/23
SA21	66.0406N	79	CMG-3ESPC	EDL-PR6	2014/09/30-
(Tervola)	25.0304E		008	3250	2015/05/12
SA21A	66.0405N	79	CMG-3ESPC	EDL-PR6	2015/09/19-
(Tervola, replaced)	25.0295E		008	3397	2016/10/06
SA23	65.9262N	115	CMG-3ESPC	EDL-PR6	2014/09/20-
(Bredsel)	20.3008E		005	3219	2016/09/22
SA28	65.4469N	172	Trillium 240	EDL-PR6	2014/09/29-
(Pudasjaervi)	27.5106E		632	3247	2016/05/10
				EDL-PR6	2016/05/10-
				3028	2016/10/06
SA29	65.2879N	346	Trillium 240	EDL-PR6	2014/09/20-
(Lilltraesk)	19.8452E		631	3241	2016/09/24
SA30	65.0923N	6	CMG-3ESPC	EDL-PR6	2014/09/21-
(Jaevrebodarna)	21.4977E		007	3220	2016/09/24

continued on next page ...

Station	Location	Alt. /m	Sensor, ID	Logger, ID	Deployment period
SA36	64.4402N	51	Trillium 120 PA	EDL-PR6	2014/10/01-
(Pyhajoki)	24.5172E		004	3246	2015/07/06
				EDL-PR6	2015/07/06-
				3070	2016/10/05
SA38	64.1291N	236	CMG-3ESPC	EDL-PR6	2014/09/15-
(Oertraesk)	19.0003E		004	3218	2016/09/24
SA42	63.8265N	1	CMG-3ESPC	EDL-PR6	2014/10/04-
(Palmantie)	23.0079E		013	3245	2016/05/10
				EDL-PR6	2016/05/10-
				3401	2016/10/05
SA46	63.4896N	140	Trillium 120 PA	EDL-PR6	2014/09/15-
(Bredbyn)	18.0945E		002	3222	2016/09/25
SA47	63.3596N	106	CMG-3ESPC	EDL-PR6	2014/10/04-
(Pulkkinen)	23.9733E		010	3240	2015/05/17
				EDL-PR6	2015/05/17-
				3163	2016/10/04
SA49	63.1749N	6	CMG-3ESPC	EDL-PR6	2014/10/09-
(Soedra Vallgrund)	21.2788E		011	3254	2016/10/03
SA52	62.9381N	20	Trillium 240	EDL-PR6	2014/10/05-
(Pelmaa)	22.4878E		634	3253	2016/10/04
SA54	62.7504N	13	Trillium 240	EDL-PR6	2014/09/14-
(Hemsoen)	18.1489E		630	3224	2016/09/26
SA60	61.6930N	15	CMG-3ESPC	EDL-PR6	2014/09/13-
(Arnevikon)	17.3793E		002	3216	2016/09/21
SA61	61.5934N	2	Trillium 120 PA	EDL-PR6	2014/10/06-
(Maentykallo)	21.4622E		005	3249	2016/05/09
				EDL-PR6	2016/05/09-
				3403	2016/10/03
SA64	61.0537N	123	Trillium 240	EDL-PR6	2014/10/08-
(Lammi)	25.0399E		633	3252	2016/10/02

continued on next page ...

Station	Location	Alt. /m	Sensor, ID	Logger, ID	Deployment period
SA65	61.0535N	99	CMG-3ESPC	EDL-PR6	2014/09/11-
(Svabensverk)	15.7698E		001	3215	2016/09/22
SA66	60.4468N	239	Trillium 120 PA	EDL-PR6	2014/09/10-
(Bjoerbo)	14.7806E		001	3244	2016/09/21
SA67	60.4158N	45	CMG-3ESPC	EDL-PR6	2014/10/07-
(Tuorla)	22.4439E		009	3251	2016/10/02

Instrumentation

All sensors and data loggers were kindly provided by GIPP and GFZ section 2.4. Ancillary equipment (batteries, GPS antennas, etc.) was purchased with DFG funding, or on loan from the GIPP and KArlsruhe BroadBand Array (KABBA) at KIT. All stations recorded data with three components (vertical, N-S, E-W) and a sampling rate of 100 Hz. Table 3.1 lists the individual instrumentation configurations at each recording station. In total we installed five Nanometrics Trillium 240 seismometers (eigenperiod 240 s), five Nanometrics Trillium 120 PA (120 s) and ten Güralp CMG-3ESPC seismometers (60 s)[6].

All seismic stations were equipped with EarthData PR6-24 recorders as data loggers (EDL)[7]. The data were stored on exchangeable hard disks (36.6 GB) which were replaced during each station service. The EDL recorded continuously at 100 samples per second and pre-amplification was set to 0.4. Logger settings and sensor characteristics to deconvolve time series to true ground velocity from the raw data are listed in Table 3.2. Instrument response functions for the used sensors based on the values of Table 3.2 are displayed in Fig. 3.6.

Orientations of sensors

During the installation of the Swedish stations, the sensors were oriented to true north using a fiberoptic gyroscope of type iXblue OCTANS (Fig. 3.7, typical uncertainty of 0.1°[8]). For the installations in Finland the GIPP gyroscope was not available and orientations were obtained using an Azimuth Pointing System (APS, Fig. 3.7), kindly supplied by University of Oulu (Finland). Similar to the gyroscope this system is unaffected by local magnetic interference. However, good GPS reception is required and thus measurements in most cases had to be con-

[6] for details see http://www.gfz-potsdam.de/en/section/geophysical-deepsounding/infrastructure/geophysical-instrument-pool-potsdam-gipp/instruments/seismic-pool/, last accessed 11 January 2019

[7] for details see http://www.gfz-potsdam.de/en/section/geophysical-deep-sounding/infrastructure/geophysical-instrument-pool-potsdam-gipp/instruments/seismic-pool/recorder-earthdata-pr6-24/, last accessed 11 January 2019

[8] iXblue OCTANS, https://www.ixblue.com/products/octans, last accessed 11 January 2019

Table 3.2: Properties of the used sensors (Trillium 240, Trillium 120 PA and Güralp CMG-3ESPC, small pictures) and data loggers (EDL-PR6). Instrument response functions based on the listed values are displayed in Fig. 3.6.

Sensor	AD conversion in counts/V	Sensitivity in V/(m/s)	Norm. factor	Poles	Zeros
Trillium 240 	400000	1200	451700	-1.7700E-02 + 1.7600E-02i -1.7700E-02 - 1.7600E-02i -1.2670E+02 + 0.0000E+00i -1.9200E+02 + 2.5900E+02i -1.9200E+02 - 2.5900E+02i -5.5770E+02 + 1.1430E+03i -5.5770E+02 - 1.1430E+03i	0 0 -9.1660E+01 -1.6010E+02 -3.2070E+03
Trillium 120 PA 	400000	1200	1.70369E+09	-3.8590E-02 + 3.6490E-02i -3.8590E-02 - 3.6490E-02i -1.9000E+02 + 0.0000E+00i -1.5800E+02 + 1.9300E+02i -1.5800E+02 - 1.9300E+02i -6.3900E+02 + 1.4180E+03i -6.3900E+02 - 1.4180E+03i	0 0 -1.0600E+02 -1.5800E+02
Güralp CMG-3ESPC 	400000	2000	5.715E+08	-7.4000E-02 + 7.4000E-02i -7.4000E-02 - 7.4000E-02i -1130.97 -1005.31 -502.655	0 0

ducted outside the buildings. Afterwards, measured directions to true North (accuracy < 0.2°, depending on GPS integrity[9]) were transferred to the position of the sensors via laser. Before station removal in October 2016, all sensor orientations in Finland were checked with the GIPP gyroscope directly at the sensor to detect possible misorientations. In general, misorientations are smaller than 5° at most sites (Table 3.2). However, for three stations deviations of $> 5°$ were measured (SA21A, SA52, SA36). Station SA36 was wrongly oriented towards West instead of North ($\Delta \approx 90°$). Data for the correct ZNE-system can be recovered by rotating the corresponding station components N-S and E-W using the equations by *Plesinger et al.* (1986) (see also stationXML files for the misorientations when using the waveforms). The subsequent determi-

[9] Azimuth Pointing System, https://www.lasertech.com/Azimuth-Pointing-System.aspx, last accessed 11 January 2019

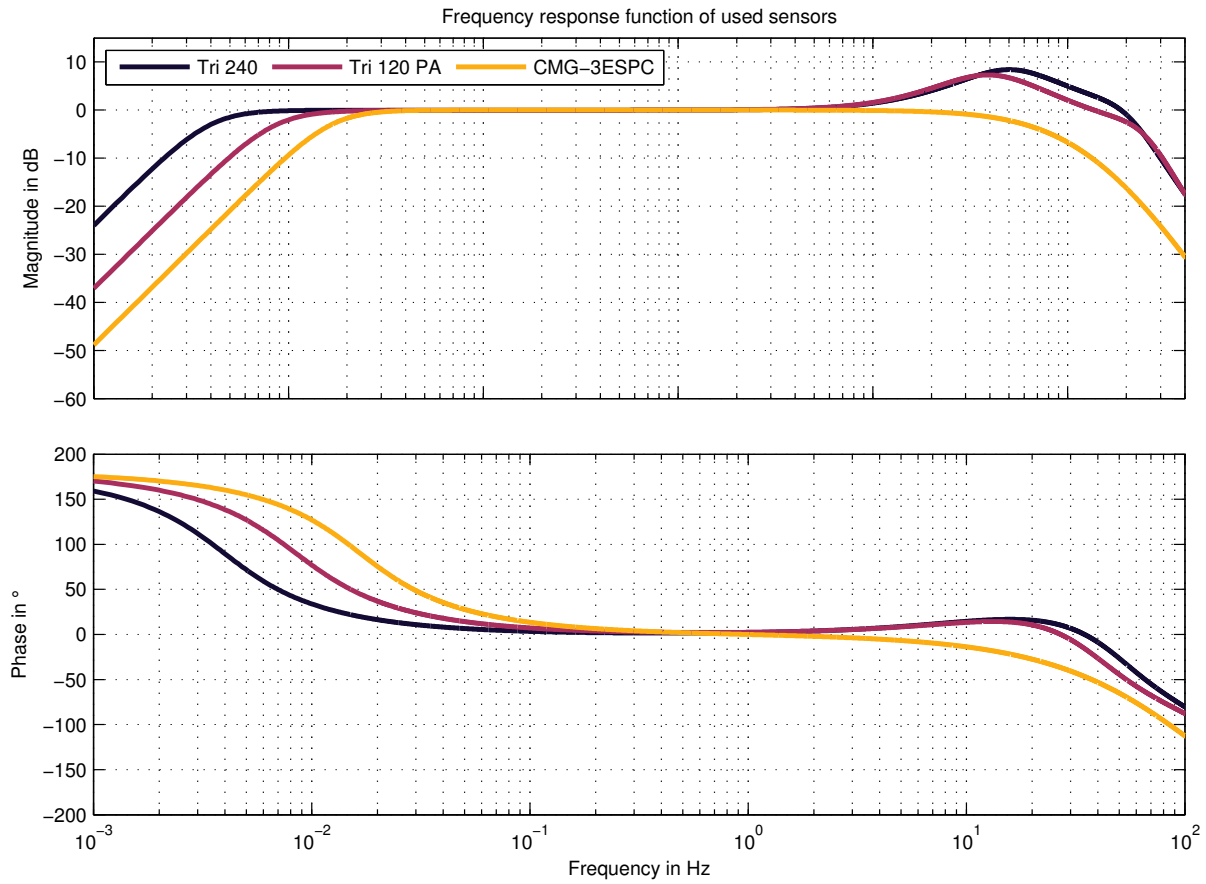

Figure 3.6: Instrument response functions of the three used sensors Nanometrics Trillium 120 PA, Trillium 240 and Güralp CMG-3ESPC, computed with the values given in Table 3.2.

Table 3.3: Determined misorientations of the sensors installed in Finland. Absolute measured orientations are listed in the second column, orientations relative to true North in the third column.

Station	Measured absolute orientation in °	Orientation relative to true north in °
SA21 (Tervola)	3.4	+3.4
SA21A (Tervola)	15.4	+15.4
SA28 (Pudasjaervi)	356.1	-3.9
SA36(Pyhajoki)	272.0	-88
SA42 (Palmantie)	358.6	-1.4
SA47 (Pulkkinen)	2.9	+2.9
SA49 (Soedra Vallgrund)	355.8	-4.2
SA52 (Pelmaa)	353.6	-6.4
SA61 (Maentykallo)	1.9	+1.9
SA64 (Lammi)	0.3	+0.3
SA67 (Tuorla)	359.7	-0.3

Figure 3.7: Azimuth Pointing System (APS) of the University of Oulu (left) and GIPP gyroscope of type iXblue OCTANS (right). Both instruments were used to correctly align the seismometers to true North during the installation or dismantling, respectively.

nation of sensor misorientations based on recorded data and shear wave splitting measurements is discussed in section 4.1.5.

3.2.2 Data processing

The data set was preprocessed at GFZ in Potsdam and converted from the raw EDL MSEED files (*.pri[012]) to standard MSEED files using the *mseed2mseed* tool provided by the GIPP. The digital MSEED data with a sampling rate of 100 samples per second were originally stored in day files. After conversion, channels were renamed to HHZ, HHN, HHE. Only for station SA36 the channels were labeled as HHZ, HH1, HH2 indicating the misorientation described above. All measured misorientations of the Finnish stations have been included in the stationXML metadata files.

3.2.3 Data description and completeness

Recording at each station started as described in Table 3.1. As mentioned above, due to the long winter periods, especially in the northern part of the network, only three service trips were conducted to save the data and check the instruments. During the first service trip in May 2015, besides several technical problems with some data loggers (see Table 3.1), station SA21 was removed since the site was flooded and the sensor did not work anymore. After maintenance and repair, during the second service trip in September 2015, the sensor was reinstalled in the

same area, but approximately 50 m away from the old site (new station code SA21A). Technical problems occurred also at station SA36 caused by an incorrect installation in September 2014. Data are corrupted by bit noise and hence useless until 18/09/2015. Therefore, these data were not transferred to the GEOFON archive. After fixing this problem, station SA36 ran for only 5 days before switching off again until the next service trip in May 2016. Hence, data exist mainly from 10/05/2016 onwards. A detailed description of all problems and component changes is given in the Appendix (Service Trips Summary Table) of *Grund et al.* (2017a). For most stations data coverage is 100% but at some sites we only have up to 50% due to unforeseen technical problems during the long periods between the individual service trips.

3.2.4 Data quality and accuracy

GPS signals were regularly lost at many stations, but for most of the stations GPS timing was logged at least once per day to synchronize the recordings. However, at stations SA46, SA54 (old military bunker) and SA64 the GPS signals were completely lost for several months. Hence, their recorded times should be considered unreliable during these periods. Regarding all other stations, to our best knowledge GPS timing problems can be neglected. Detailed GPS information is shown in the appendix of *Grund et al.* (2017a). Here, the AVR (automatic voltage regulator) flag labels indicate times where the EDL shut down either automatically (red dot) or manually by technicians (green dot). GPS signal which was lost for more than 60 seconds is indicated by red bars. Bad timing accuracy with a larger misfit of 5 ms is shown as purple bar. We provide the complete log files (*msg and pll files) for all 20 stations if detailed GPS information is necessary. Data is structured in the following directory trees: */logs_yyyy/station/day of year/*msg* and */logs_yyyy/station/day of year/*pll*. Data quality is in general high but depends on the local noise conditions (water pumps, etc.). Since most stations were placed within buildings (cellars etc., see Figs. 3.4 and 3.5) temperature changes for the sensors are small. However, some sensors were installed outside (close to buildings) only protected by insulation material against environmental influences. To give an overview, in Fig. 3.8 we display the power spectral density (PSD) of all stations separated in two-week periods of recording in summer and winter. Since stored data are in counts, we processed the corresponding time series for the PSD calculations.

First, data were converted to true ground velocity in m/s, followed by removal of mean, trend and instrument response (deconvolution), tapering and bandpass filtering between 240 s or 120 s and 50 Hz. Depending on the sensor orientation, the recordings were rotated to account for the misorientations given in Table 3.3. For the PSD calculation we use a single-taper method with 24-hour long time windows that are finally stacked to get an overall averaged PSD for the two-week period. For the summer period we used data from 11/07/2016 to 24/07/2016 at all stations, except SA21 and SA28 for which data was taken from 11/04/2015 to 24/04/2015.

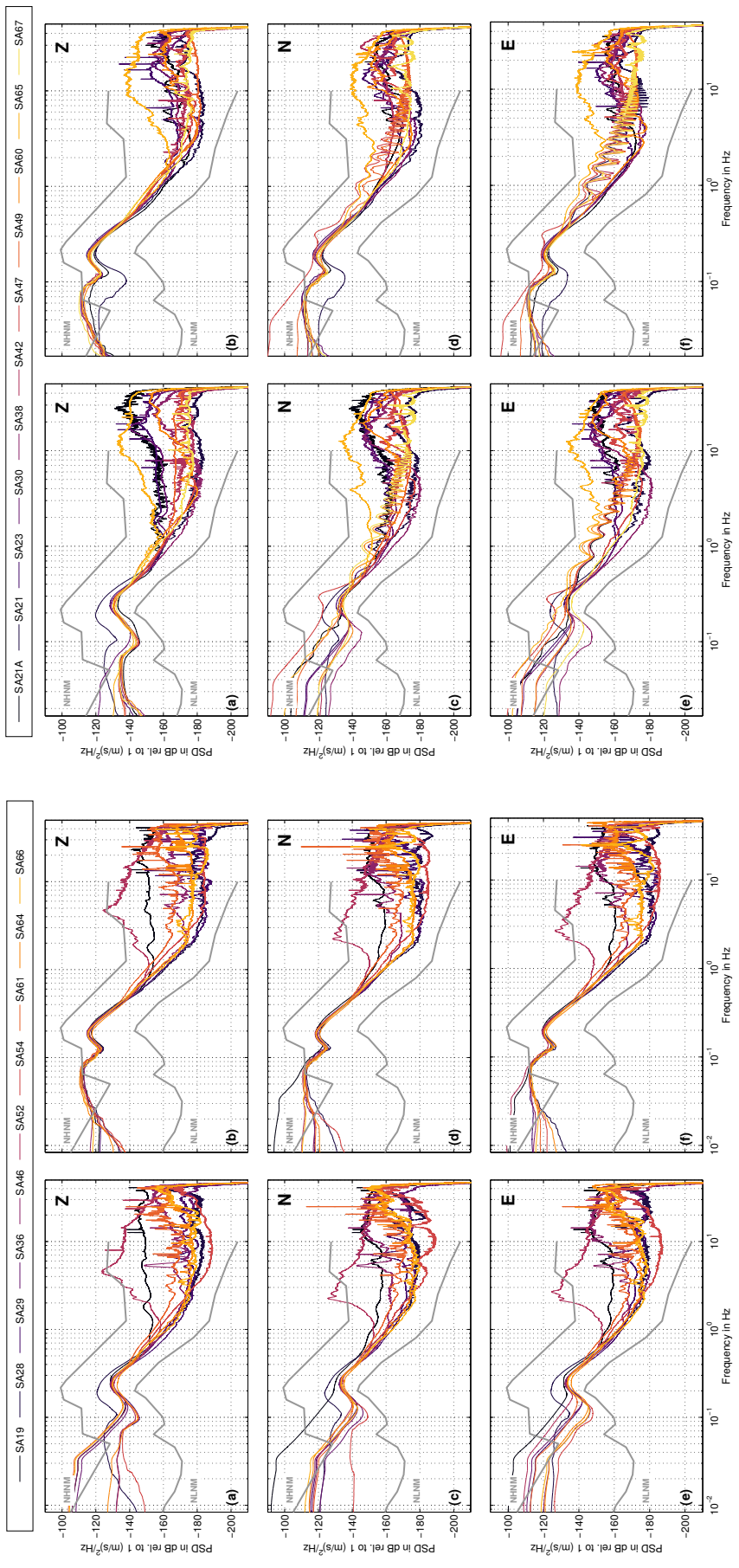

Figure 3.8: PSD spectra for stations with Nanometrics Trillium sensors calculated for a two-week period in summer (first column), and winter (second column). The new low-noise model (NLNM) and new high-noise model (NHNM) after *Peterson* (1993) are indicated as gray lines. The third and fourth column show the same for the stations equipped with Güralp sensors.

The winter period covers data from 02/11/2015 to 15/11/2015 at all stations, except station SA21 for which we used data from 02/11/2014 to 15/11/2014. For station SA36 no PSD was calculated for the winter period due to missing data. In general, the long period recordings ($<$ 20 s) show a low SNR where some stations exceed the new high-noise model (NHNM) by *Peterson* (1993). For several stations located in or close to buildings, the high frequency range above 2 Hz is dominated by several high amplitude peaks mainly caused by human activity or machinery. Furthermore, during winter time the low frequency bands between 0.04 Hz and 1 Hz are highly affected by the oceanic microseism. In the new low-noise model (NLNM), the two peaks between 0.06 Hz and 0.07 Hz and at around 0.2 Hz correspond to the primary and secondary oceanic microseism, respectively. At a few stations we also see potentially increased noise levels (2-7 Hz) due to wind turbines that are located at distances between 5 km and 10 km from our recording sites (compare, e.g., *Zieger and Ritter*, 2018).

3.2.5 Data availability and access

The data are archived in the GFZ Seismological Data Archive (GEOFON) with the network code 1G where it will be made freely available to the scientific community in October 2019. Metadata is stored in stationXML inventory files. Both data sets can be accessed via http://geofon.gfz-potsdam.de/waveform/. The log files with the GPS information are archived in the GIPP Experiment and Data Archive and can be requested via http://doi.org/10.5880/GIPP.201417.1 (*Grund et al.*, 2017b).

4 Data processing

In this chapter I give a summary of the standard data processing applied within my thesis work. For all single-event shear wave splitting measurements I used the SplitLab package (*Wüstefeld et al.*, 2008). Furthermore, I briefly discuss potential challenges and uncertainties in shear wave splitting measurements. Finally, I validate a recently published multi-event technique, called SIMW (*Roy et al.*, 2017), with simple synthetic models.

4.1 SplitLab

In order to perform the single-event shear wave splitting measurements I used the freely available and well-established SplitLab toolbox for MATLAB (*Wüstefeld et al.*, 2008). This toolbox enables to fully request data, perform the splitting measurements as well as set simple models up directly during the analysis procedure.

4.1.1 Data requests

Seismic data were requested from different institutions in most cases directly from within SplitLab. Table 4.1 lists a summary of the network codes for which data were ordered from the individual data centers. For the networks ScanArray Core (Copenhagen, GFZ, KIT, Aarhus) and Neonor2 data were located at GFZ's GEOFON platform (*GEOFON Data Centre*, 1993; *Hanka and Kind*, 1994) and requested via `FDSN Web Services` and `breq_fast`. SCANLIPS3D data are stored at the SEIS-UK server of the University of Leicester (*Brisbourne*, 2012) and was requested via different tools directly from the server. Data of the permanent networks are partly stored at GEOFON, ORFEUS (*Dost*, 1994), the Incorporated Research Institutions for Seismology (IRIS) or on local ftp servers (NNSN, NORSAR). Restricted data of the Swedish National Seismic Network (*SNSN*, 1904) were provided for the years 2012-2016 directly via GEOFON. Additional data of the Finnish

Table 4.1: Data centers and individual network codes for which data were requested.

Data center	Network code(s)
GEOFON	1G, 2D, DK, EE, GE, FN, HE
ORFEUS	NO, NS, UP, HF
IRIS	II, IU
SEIS-UK	ZR
Uni Helsinki	HE
KABBA	Z6

Table 4.2: Information about nine seismic recording stations for which no reliable split or null measurement are available. *Country* indicates the location and *Operator* the institution that was responsible for installation and station service.

Station	Lat	Lon	Country	Operator	Issue
ARNU	61.6920	17.3780	Sweden	Uppsala	technical problem
N1304	66.8761	14.6548	Norway	Leicester	no high quality data (no splits/nulls)
NBB13	66.6275	13.3272	Norway	Bergen	no high quality data (no splits/nulls)
ONSU	57.3965	11.9259	Sweden	Uppsala	less data (only few days)
SA15A	67.4746	18.3647	Sweden	Aarhus	no high quality data (no splits/nulls)
SA21A	66.0405	25.0295	Finland	KIT/GFZ	done together with SA21 (only few meters away)
SA22	66.0382	17.8591	Sweden	Aarhus	technical problem
SA26	65.6992	12.4383	Norway	Copenhagen	no high quality data (no splits/nulls)
SA55A	63.2978	10.0584	Norway	Copenhagen	no high quality data (no splits/nulls)

network were requested directly from the University of Helsinki. Re-analyzed MAGNUS data were provided by the KABBA data center of KIT-GPI.

4.1.2 Missing data or malfunctioning stations

In total seismic data of 275 recording stations (temporary and permanent) located across whole Fennoscandia and neighboring countries were analyzed (for details see appendix B, Table B.1). However, due to technical problems or strong noise, for several stations it was not possible to detect at least one reliable split or null measurement. The corresponding stations and their issues are listed in Table 4.2. Therefore, results of 266 stations are shown in the following sections and chapters.

4.1.3 Techniques to measure shear wave splitting

SplitLab incorporates three different methods which are applied simultaneously for each selected teleseismic shear wave phase: the rotation-correlation method (hereinafter RC, e.g. *Fukao*, 1984; *Bowman and Ando*, 1987), the energy minimization method (SC, *Silver and Chan*, 1991) and the eigenvalue method (EV, e.g. *Silver and Chan*, 1991). Each of these methods performs a grid search to find the pair of parameters (fast polarization axis direction ϕ and delay time δt) that best removes the effect of splitting from the recorded waveforms under the assumption of a single anisotropic layer with a horizontal symmetry axis (see section 2.3). For this purpose the recorded waveforms on the Z, N and E components are rotated into the ray-coordinate LQT system. Besides the backazimuth (BAZ), the LQT system also considers the incidence angle of the arriving wave. For perfectly vertical incidence, the LQT system is equivalent to the vertical-radial-transverse (ZRT) coordinate system (*Plesinger et al.*, 1986).

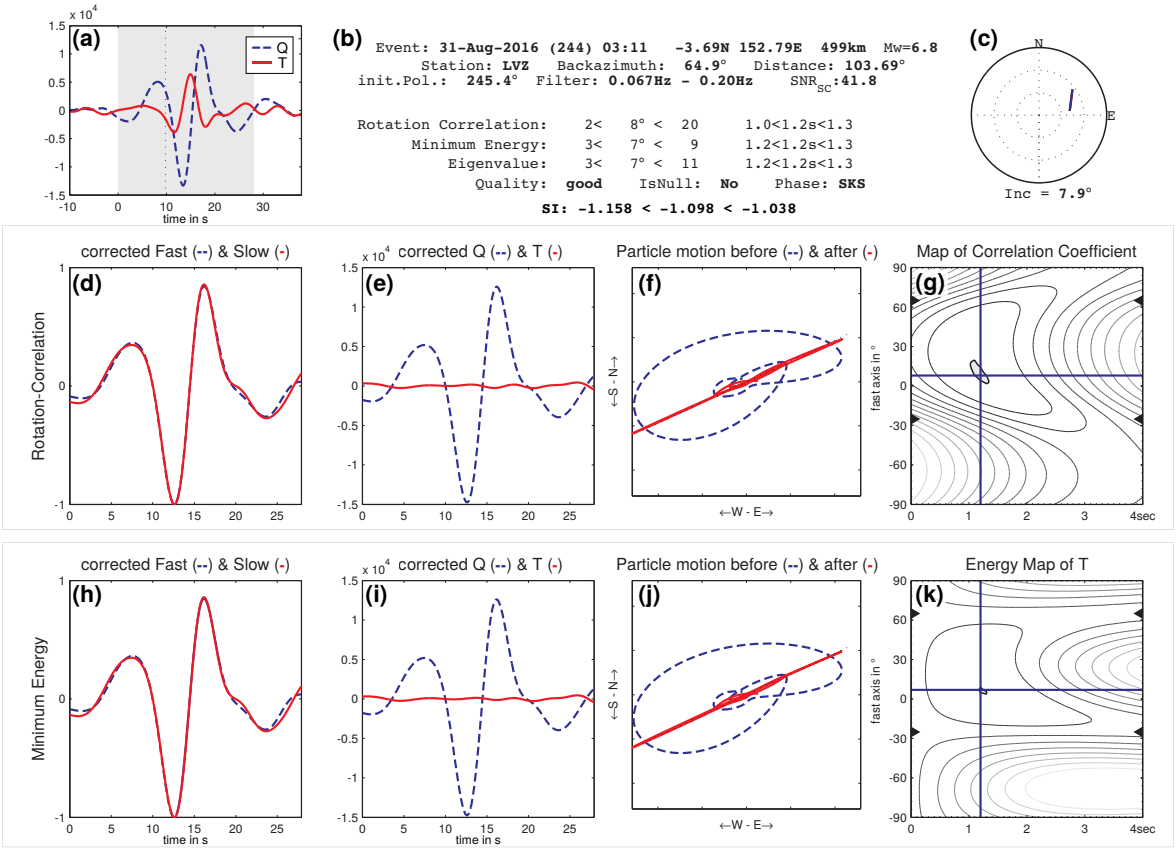

Figure 4.1: Diagnostic plot of a shear wave splitting measurement with SplitLab at the Russian permanent station LVZ on the Kola peninsula. (a) Original (uncorrected) radial (Q, blue dashed) and transverse (T, solid red) component seismograms. Gray area indicates the analysis window. Thin dotted line displays the theoretical arrival of the *SKS* phase based on the iasp91 Earth model (*Kennett*, 1991). (b) Station, event and processing information (filter, SNR, etc.) as well as splitting parameters (ϕ, δt) (with uncertainties, 95% confidence interval) resulting from the rotation-correlation method (RC, e.g. *Fukao*, 1984; *Bowman and Ando*, 1987), the energy minimization method (SC, *Silver and Chan*, 1991) and the eigenvalue method (EV, e.g. *Silver and Chan*, 1991). Quality of the measurement, null case (yes or no) and the phase name are also shown. The splitting intensity (SI, *Chevrot*, 2000) is displayed in the lowermost row (with uncertainties, 95% confidence interval). (c) Stereoplot showing the splitting measurement as a function of backazimuth (clockwise direction from North) and incidence angle (radial axis). Results of two methods (RC and SC) are also visually shown. (d)-(g) Diagnostics for the RC method showing the (d) corrected fast (blue dashed) and slow (solid red) components (normalized), (e) the corrected radial (blue dashed) and transverse (solid red) components (not normalized), (f) the initial (blue dashed) and splitting-corrected (solid red) particle motion and (g) the contour plot of the correlation coefficients with the best-fitting splitting parameters (blue lines) and the 95% confidence region (gray area). (h)-(k) Same content for the SC method. All three methods (RC, SC and EV) show nearly identical results indicating a robust measurement.

Afterwards the waveforms are systematically rotated and time-shifted to remove the observed shear wave splitting. A comparison of the individual results of the three methods can be used to automatically classify the quality of the measurement (*Wüstefeld and Bokelmann*, 2007). To measure potential contributions from lowermost mantle anisotropy in the D" layer, additionally I implemented the splitting intensity (SI) method after *Chevrot* (2000) in SplitLab following *Deng et al.* (2017). For further details see sections 2.3 and 6.3.

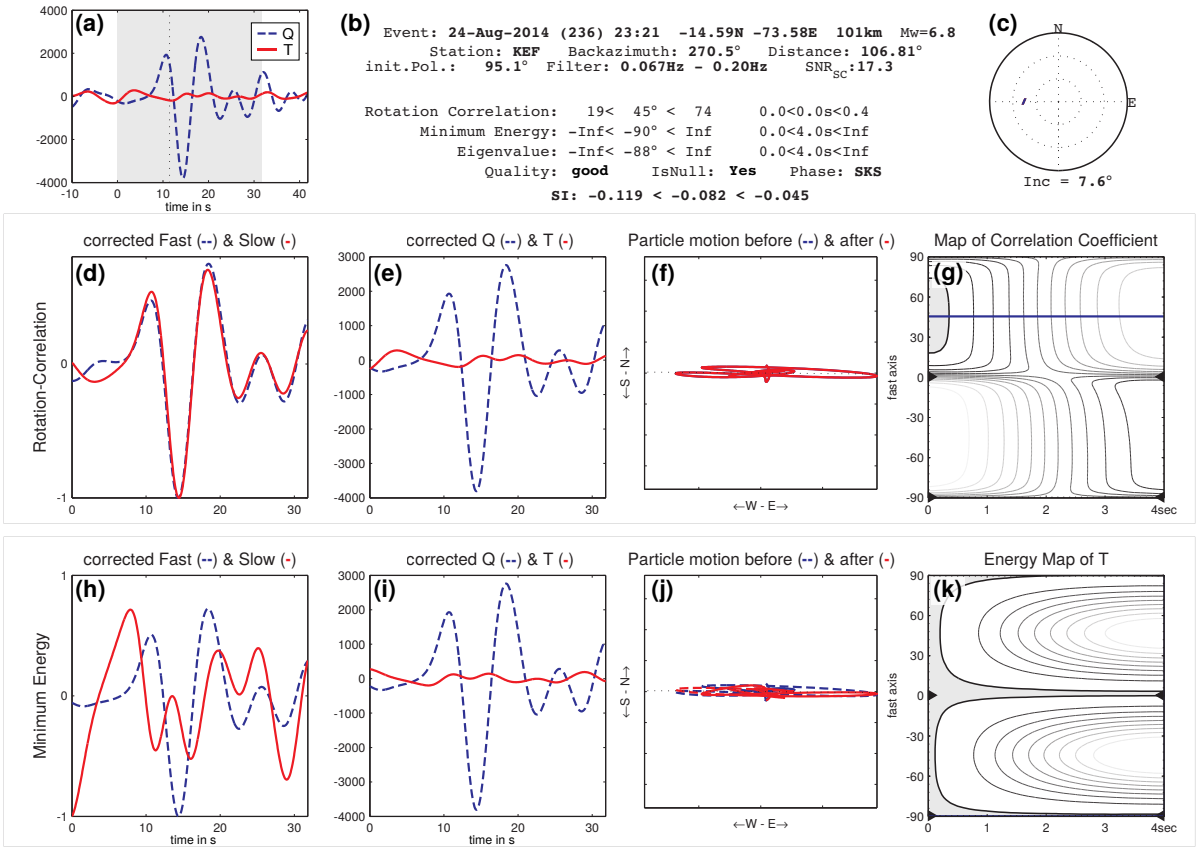

Figure 4.2: Diagnostic plot of a typical null measurement performed with SplitLab at the Finnish permanent station KEF. Panels are the same as in Fig. 4.1. Linear particle motions before and after the correction for splitting as well as partly striking differences for ϕ and δt (RC, SC and EV) indicate a clear null case.

Fig. 4.1 displays a typical high-quality measurement of a split *SKS* phase recorded at the Russian permanent station LVZ on the Kola peninsula. The comparative high signal-to-noise ratio (SNR) allows to identify a clear signal on both, the radial and transverse components. In contrast, the absence of a clear signal on the transverse component (except the seismic background noise) indicates a so-called null measurement (Fig. 4.2). The simultaneous splitting inversion with three different methods allows to directly check the reliability of the splitting measurement.

4.1.4 Uncertainties, errors, and challenges

Shear wave splitting measurements should be handled with care to avoid bias and artifacts from processing which can lead (in the worst case) to misleading interpretations and conclusions (e.g. *Restivo and Helffrich*, 1999; *Vecsey et al.*, 2008; *Monteiller and Chevrot*, 2010; *Liu and Gao*, 2013). The effect of strong variations in the splitting parameters due to high noise levels in the analysis windows can be compensated by applying appropriate (bandpass-) filters that reduce the influence of frequencies outside of the dominant periods of teleseismic arrivals (e.g. *Vecsey et al.*, 2008). Also the filter itself can have an effect on the calculated splitting parameters

especially in the case of frequency-dependent anisotropy (e.g. *Marson-Pidgeon and Savage*, 1997; *Özalaybey and Chen*, 1999; *Wirth and Long*, 2010; *Long*, 2010). In the ScanArray data set such effects were not observed within the uncertainties. However, to check for frequency-dependencies different filter schemes were applied. These resulted in consistent splitting results for the different frequency bands. Furthermore, the length of the analysis window can have an influence on the inversion result since phases with similar arrival times (and therefore overlapping waveforms) included in this window (in parts or in full) can disturb the typical elliptical particle motion and causes a non-stable and weak linearization. Depending on the hypocenter depths, overlapping arrivals are often seen for events with epicentral distances of 80° to 84° (compare Fig. 2.7 in section 2.3). Here, the *SKS* phase partly arrives close to the direct *S*-wave which is in general not only polarized in the radial direction before it enters the anisotropic medium on the receiver-side. As mentioned in the previous section, the comparison of different analysis methods allows to assign a quality rank and can help to minimize potential bias effects (*Wüstefeld and Bokelmann*, 2007).

For error calculation a statistical *F*-Test was applied to estimate the 95% confidence interval of the corresponding SC method measurement. The errors for the RC method are computed using a Fisher transformation formulation (*Wüstefeld et al.*, 2008). The original error formulation for the SC method (*Silver and Chan*, 1991) was used in numerous studies (primarily in the last three decades and still in recently published papers) to calculate the formal errors of the splitting measurements. Recently it was found that the errors are underestimated (*Walsh et al.*, 2013). For all the analysis done in the framework of this thesis the corrected equations for error estimation after *Walsh et al.* (2013) were applied. Furthermore, large errors or confidence regions can be stabilized using different stacking schemes (for more details see chapter 5).

Finally, it should be mentioned that errors are already included in the source locations of the earthquakes used for shear wave splitting analysis (e.g. *Billings et al.*, 1994). Therefore, the backazimuth calculated for an event from the station location is biased (little) due to the earthquake location error. Since this BAZ value is the angle which is used for the rotation of the single component waveforms into the LQT system, slight uncertainties cannot be fully ruled out.

4.1.5 Detection of misorientations

Besides processing pitfalls, errors may already occur during the installation of the seismic sensors. Depending on the installation locations and conditions (variations of the magnetic declination) and the accuracy and diligence throughout the installation itself (e.g. measuring the orientation with a standard compass within buildings), a seismic sensor can be wrongly aligned with its components ZNE (Vertical, North-South, East-West) pointing not in the corresponding direction (Fig. 4.3). While the alignment with the vertical Z axis can be easily adjusted

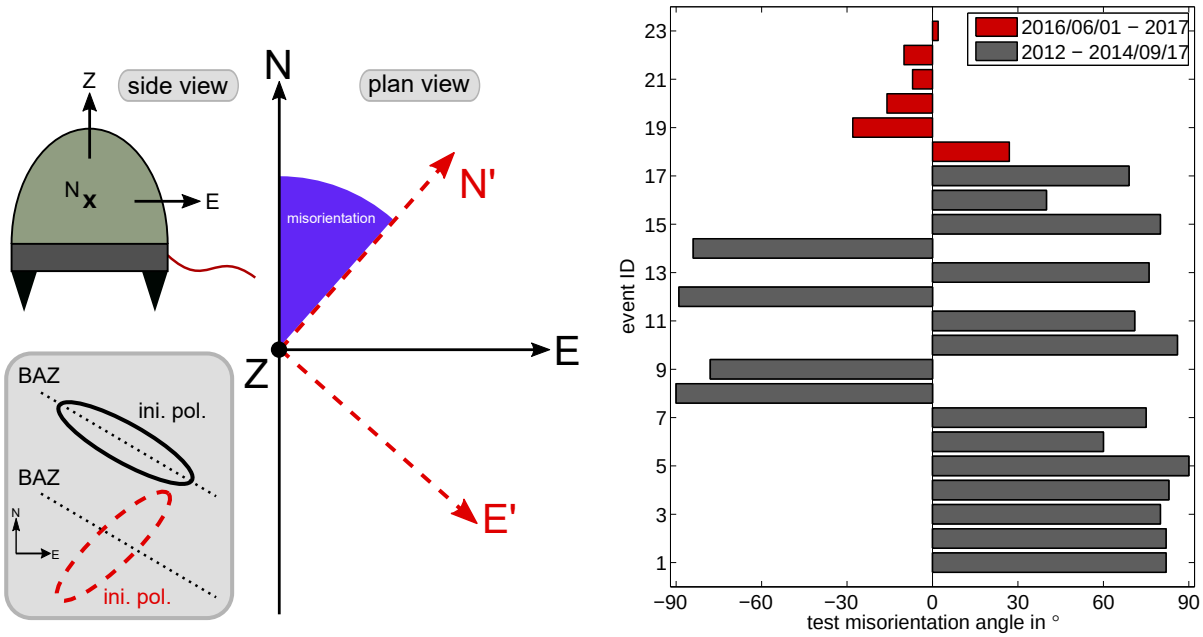

Figure 4.3: Left: schematic overview of misorientations. The three (correct) seismometer components are shown in black indicated by Z, N and E (side and plan view). Misaligned components N' and E' are shown as red dashed lines (plan view). Simplified particle motion plots (gray box) show correct and erroneous initial polarizations (ellipses) along with the BAZ of the event (dotted black line). Right: misorientation analysis for temporary station SA41 running between 2012 and 2017. While measuring shear wave splitting an offset between the initial polarization estimated by SplitLab and the backazimuth was observed for *good/fair* split and null observations, with the last event on 2014/09/17 (gray bars). For the next *good/fair* measurement the offset (nearly) disappeared (red bars), indicating that the seismometer was rotated correctly towards true North sometime between these two events. Thus, the recordings were rotated systematically between -90° and 90° and the difference between initial polarization and the backazimuth was calculated. In the figure the test misorientation angle for each event is shown for which the minimum difference was observed. It is obvious that between 2012 and 2016 for most events the difference tends toward ± 90°, indicating that the sensor was wrongly installed with the North component in east-west direction and the East component in north-south direction. Since the installed sensor was an STS2, where the marking point for correct orientation is in E-W direction, it is understandable that the intuitive orientation in N-S direction was used and thus the sensor misoriented by 90°.

and checked via a spirit level on top of the instrument, the horizontal components N and E are often misaligned (see also section 3.2.1, *Orientations of sensors*). Such misorientations of seismic sensors, including temporary (*Lynner and Long*, 2012) as well as long running permanent deployments (e.g. *Liu et al.*, 2008; *Tian et al.*, 2011), can strongly affect the conducted shear wave splitting measurements. Subsequent interpretations may therefore be biased significantly. In previous works it was shown that the misorientations can be seen in the analyses depending on the method that was used (*Tian et al.*, 2011; *Hanna and Long*, 2012). Furthermore, it was demonstrated that the true instrument orientation (if not documented or reconstructible as in several cases for temporary experiements) can be estimated directly from the shear wave splitting measurements themselves (e.g. *Lynner and Long*, 2012) by comparing the initial polarization of the seismic phase (measured from the recorded particle motion in SplitLab) with the backazimuth of the event. For typical deviations of e.g. $> 10°$ from the backazimuth (*Lynner*

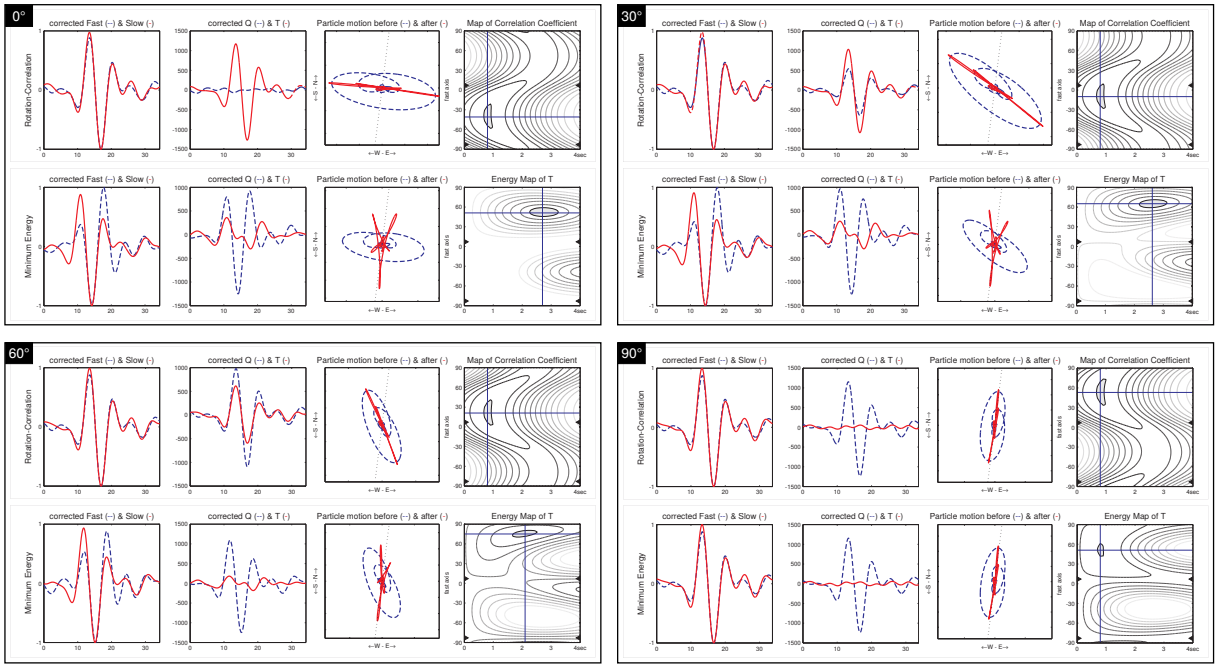

Figure 4.4: Diagnostics for four different test misorientations (original, 30°, 60°, 90°, see top left corner of each block) applied at station SA41 for event 2013/11/05 (see also Fig. 4.3). Obviously, for an angle of 90° the initial polarization (fit through the ellipse's semi-major-axis) is parallel to the backazimuth direction (black dotted line). A further proxy for correct orientation is the agreement between the RC (top panels in each block) and SC method (bottom panels) for a test rotation of 90° (lower right block). For both methods the energy on the transverse component is nearly removed (except the background noise) and the waveforms for the fast and slow waves show good agreement.

and Long, 2012) one can systematically test for different rotation angles to fit the backazimuth with the estimated initial polarization.

For some stations of the extended ScanArray network significant misorientations were detected during the shear wave splitting analysis. As described in section 3.2.1, misorientations of LITHOS-CAPP stations were already known prior to the splitting analysis and considered accordingly (Table 3.3). An example of a systematic misorientation analysis using SplitLab is shown in Figs. 4.3 and 4.4 for temporary station SA41 that was installed in Norway by University of Copenhagen. Based on the different test rotations a potential misorientation of $\pm$ 90° relative to true North was found for the time period 2012-2016. This indicates that the sensor was wrongly installed with the North component in east-west direction and the East component in north-south direction. Besides the polarization, the erroneous orientation can be clearly seen from the deviations for ϕ and δt based on the SC and RC methods. Only for a $\pm$ 90° rotation of the records, the SC and RC results coincide (ϕ-δt surfaces), the corrected linear particle motion is parallel to the backazimuth direction and the energy on the transverse component (SC and RC) is nearly removed (Fig. 4.4). Determined misorientations based on comparing the SC and RC splitting methods for stations of the extended ScanArray network (except LITHOS-CAPP stations) are listed in appendix C, Table C.1.

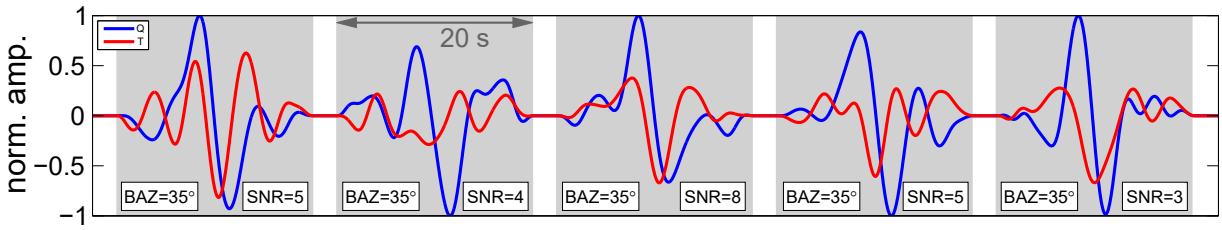

Figure 4.5: SIMW example based on five concatenated synthetic split waveforms. Each of the five time windows has a length of 20 s (gray boxes). Single waveforms have dominant periods of 8 s and were computed for a single, horizontal anisotropic layer ($\phi = 0°$, $\delta t = 1.3$ s) and a backazimuth (BAZ) of 35°. Gaussian noise was added on both, the radial (Q, blue) and transverse (T, red) components to simulate more realistic signals. Signal-to-noise ratios (SNR) are given in the lower right corner of each gray box. The individual traces were bandpass-filtered between 0.02 Hz and 0.3 Hz as well as tapered to prevent steps in the concatenated timeseries.

4.2 Evaluation of SIMW using simple synthetic examples

To tackle the problem of unstable results with partly large error bounds (e.g. caused by low SNRs, see section 4.1.4), several multi-event shear wave splitting approaches were developed (for a detailed review, see next chapter). The Simultaneous Inversion of Multiple Waveforms (SIMW, *Roy et al.*, 2017) is a new waveform-based approach and was developed recently before this thesis work started, only tested with real data though. Briefly, this method allows to invert simultaneously the concatenated radial and transverse component waveforms of individual events in limited source regions to determine the ϕ-δt pair that best describes the splitting of all waveforms. To evaluate the performance of this method, some simple tests were accomplished using synthetic models. The robustness was tested in terms of recovering the model input parameters. A comparison with other stacking approaches is given in section 5.4 of the next chapter.

The first test is based on a simple one-layer model with a fast axis fixed at $\phi = 0°$. The effective delay times (δt) for the layer were varied between 0.5 s and 2 s with a 0.5 s step size. Synthetic radial and transverse component waveforms were generated for backazimuths of 10°, 20°, and 35° assuming vertically propagating shear waves (incidence angle is 0°). Thus, for the first case the separation between BAZ and ϕ is only 10° which is a typical near-null scenario (*Wüstefeld and Bokelmann*, 2007). Gaussian noise was added on the computed synthetic waveforms at levels corresponding to different SNRs between 3 and 15 to simulate more realistic signals. Fig. 4.5 shows an example of five concatenated synthetic waveforms. For each backazimuth the inversion was done for a single phase (standard) as well as three, five, ten and 15 concatenated phases (SIMW) using the SC method. This procedure was repeated 250 times for each parameter setting. The final splitting parameters were calculated as average of the 250 computed ϕ-δt pairs. The results of the systematic testings with different parameter settings are presented in Fig. 4.6 similar to the work of *Restivo and Helffrich* (1999).

For a BAZ separation of 10° from the input fast axis, low SNR and small δt (Fig. 4.6a), the recovered results for a single phase strongly deviate from the inputs (ϕ and δt). Furthermore, the errors are quite large. Including several phases from the same BAZ direction leads to more stable outputs for δt while the deviation of ϕ from the model input fast axis is still significant. An increase in delay time, BAZ separation (20° and 30°) and SNR results in an improved input fitting for one phase (e.g. *Restivo and Helffrich*, 1999; *Wüstefeld and Bokelmann*, 2007) and very similar for increasing phase numbers (Fig. 4.6b-l). Thus, high-SNR records of a single phase will lead to very similar results like the inversion of several low-SNR phases of a common source region using SIMW.

To give an overview of the improvements over a wider BAZ range, a second test was conducted using $\phi = 0°$ and $\delta t = 1.3$ s as model setup. Synthetic waveforms (each with an SNR of 10) were computed for backazimuths between 0° and 360° with a 1° step size. Similar to the first test for each backazimuth the splitting parameters were determined for different numbers of phases. In Fig. 4.7 an example for one single phase and five concatenated phases is presented. Based on the null criterion of *Wüstefeld and Bokelmann* (2007) the individual measurements are ranked in different qualities (*good*, *fair*, *poor* splitting and *good/fair* null). The availability of five phases from earthquakes of similar source regions is a possible scenario also for relatively short temporary deployments. For most BAZ regions with high event density, often also a few well-recorded phases with high SNR are available. Nevertheless, some regions only offer low-magnitude events with a low repeating rate which often leads to unstable single-event splitting parameters.

For one phase (top panels in Fig. 4.7) scattering is observed for ϕ and δt for almost all backazimuths although for this example the effective model delay time is large ($\delta t = 1.3$ s) and the SNR with a value of 10 is comparatively high. Although some measurements are ranked as *good* and *fair* they deviate significantly from the input parameters that are shown as horizontal lines. The histograms on the right indicate the distribution of the values and the red lines the 2σ bounds of the measurements that were automatically ranked as *good* and *fair* splits (red and orange filling). For one phase they are very large for both methods, RC ($2\sigma_\phi \pm 35°$, $2\sigma_{\delta t} \pm 0.87$ s) and SC ($2\sigma_\phi \pm 36.2°$, $2\sigma_{\delta t} \pm 0.83$ s). The typical differing trends over BAZ which depend on the used method are discussed in detail in *Wüstefeld and Bokelmann* (2007). In contrast, for 15 phases the input parameters (ϕ and δt) are recovered over a wide backazimuthal range. The corresponding 2σ bounds of SIMW results are significantly decreased compared to the single-phase results. As already demonstrated in Fig. 4.6, with an increasing number of phases the confidence into the inversion result increases. Besides the 2σ bounds for 1 and 5 phases, in Fig. 4.8 these are also plotted for 10, 15 and 25 phases (computed with the same anisotropic model). It clearly shows that for 25 and more concatenated waveforms the results for different SNRs seem to reach nearly the same level, except for the ϕ determination using the RC method.

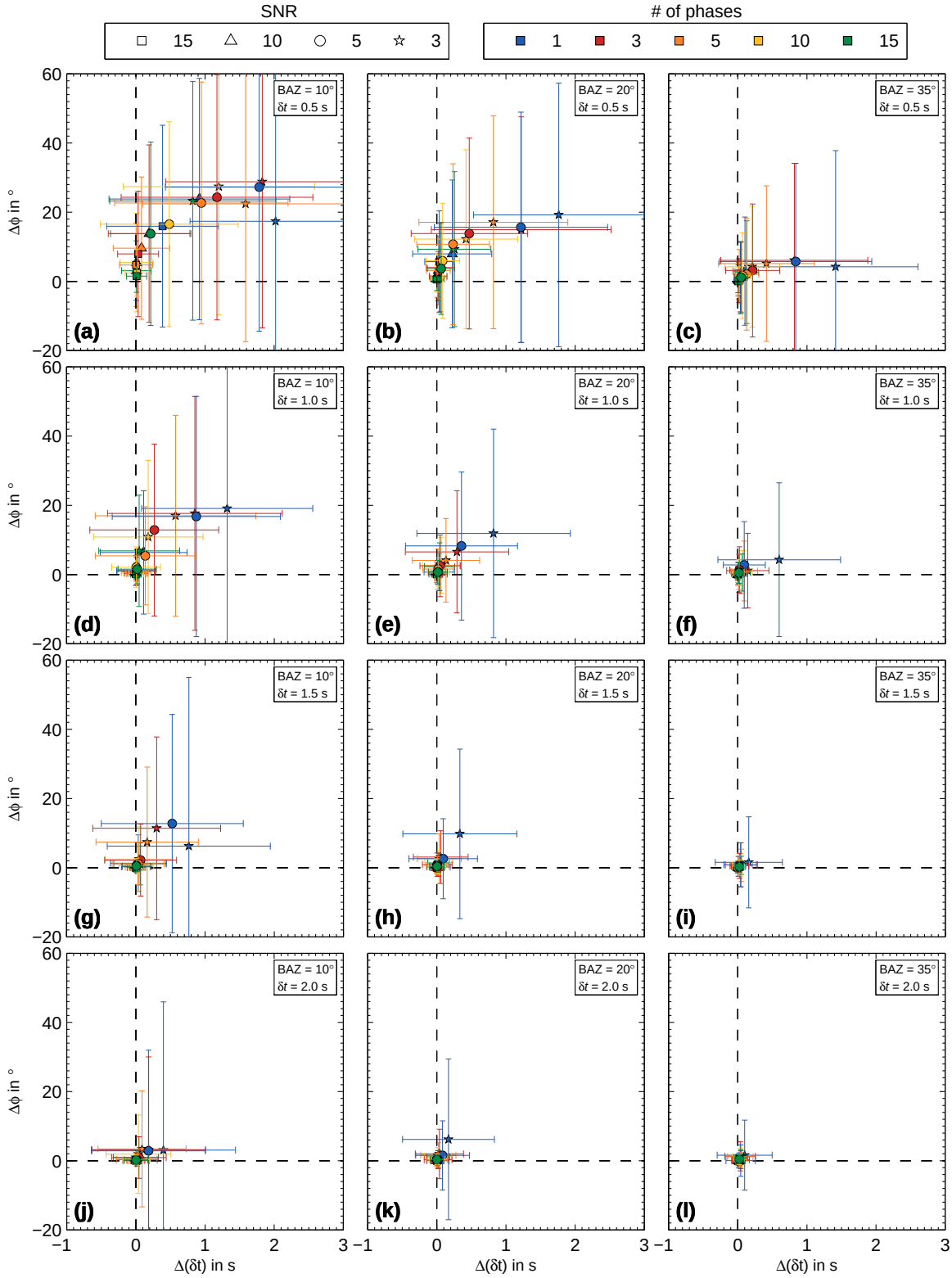

Figure 4.6: Results of the systematic synthetic tests for the SIMW method with a one-layer model with $\phi = 0°$. Effective delay times δt increase from top to bottom panels (0.5 s, 1.0 s, 1.5 s and 2.0 s) and the backazimuth separation from left to right (10°, 20°, and 35°). Different symbols indicate the varying SNRs of the used synthetic waveforms and color the number of (concatenated) phases used for the individual inversions. For each measurement the absolute deviation of ϕ and δt from the input parameters is shown ($\Delta\phi$ and $\Delta(\delta t)$, vertical and horizontal dashed lines). Error bars represent the standard deviations (1σ) calculated of the 250 ϕ-δt pairs for each parameter setting (see text for details).

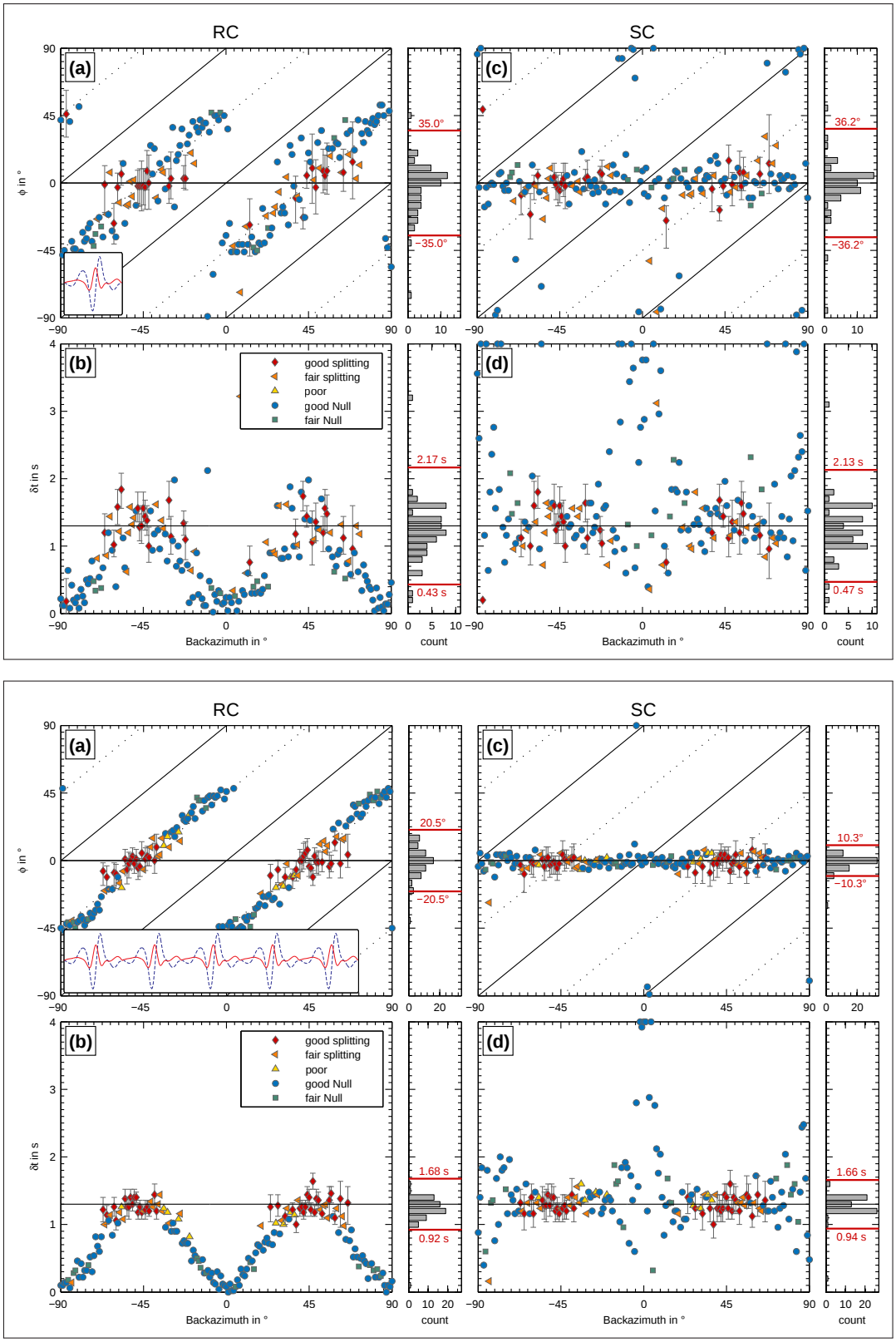

Figure 4.7: Results of the synthetic tests for a one-layer model with $\phi = 0°$ and an effective delay time of $\delta t = 1.3$ s (horizonal black lines in each panel) over the whole backazimuthal range between 0° and 360°. Top box: Distribution of the recovered splitting parameters for a single phase. (a) and (b): fast axis ϕ and delay time δt for the RC method. (c) and (d): same for the SC method. The histograms on the right indicate the distribution of the values and the red lines the 2σ bounds of the measurements that were automatically ranked as *good* and *fair* splits (red and orange filling). Bottom box: Same content but for 5 concatenated phases.

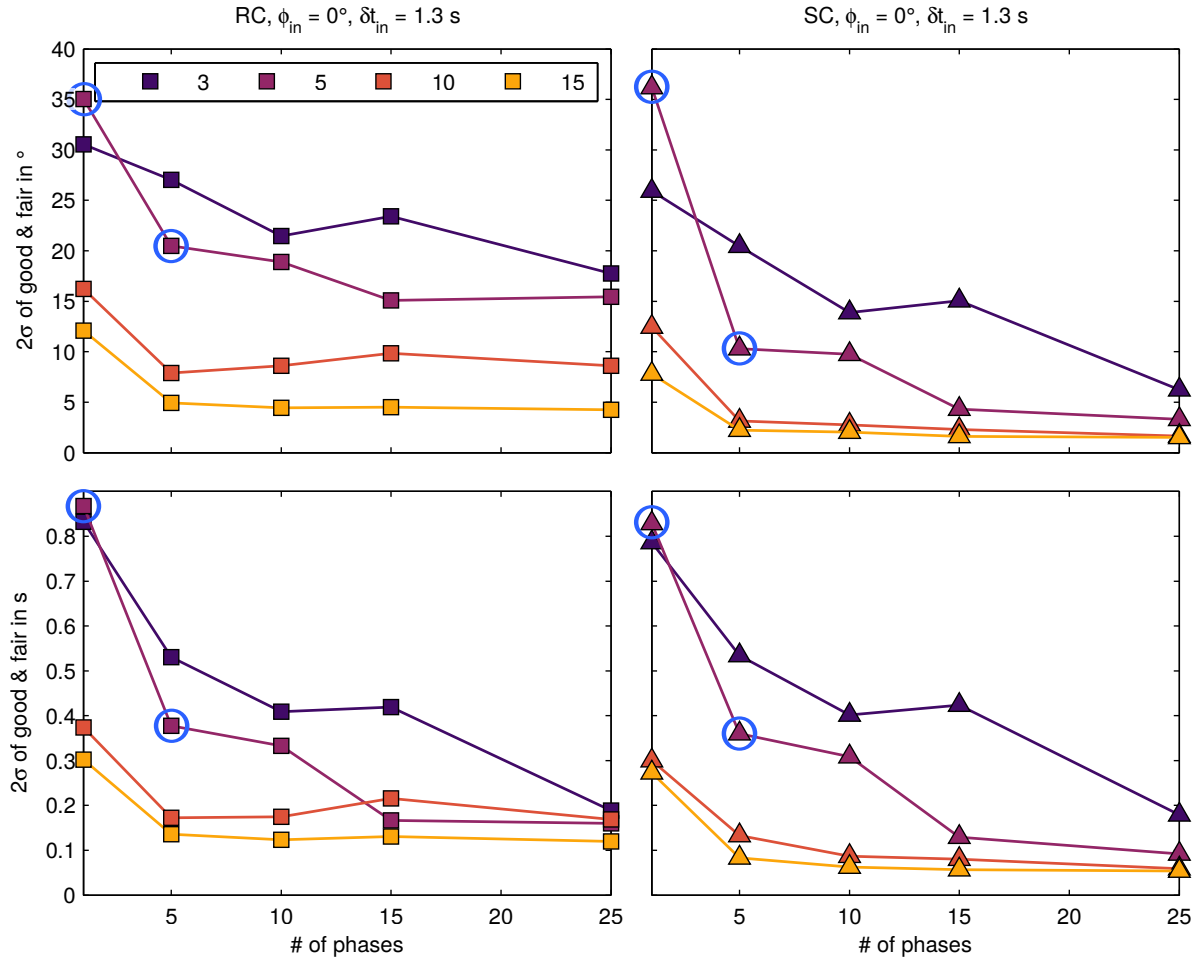

Figure 4.8: 2σ bounds of the splitting measurements that were automatically ranked as *good* and *fair* (*Wüstefeld and Bokelmann*, 2007) for a one-layer model with $\phi = 0°$ and an effective delay time of $\delta t = 1.3$ s over the whole BAZ range between 0° and 360°. Different SNRs are shown in color and the number of inverted phases in each panel increases from left to right. The example shown in Fig. 4.7 corresponds to the curve of an SNR 5 and phase numbers 1 and 5 (marked by the blue circles in each panel).

Although these synthetic tests are based on simplified models, they show that the more phases of a common source region are available the better the SIMW results can constrain the true underlying anisotropic model. However, this also depends on the deviation of the fast polarization axis ϕ from the corresponding backazimuth and therefore from the initial polarization direction. For near-null cases (backazimuth separation $< 10°$) both, high SNR single phase waveforms or concatenated low-SNR waveforms are not able to constrain the splitting parameters very well.

5 StackSplit - a plugin for multi-event shear wave splitting analyses in SplitLab

In order to bundle all conventional shear wave splitting stacking procedures (including SIMW), I wrote a plugin for the SplitLab toolbox called StackSplit. The plugin allows a flexible and easy application for single measurements already done (see section 4.1.3). The following chapter has been published in:

Grund, M. (2017), **StackSplit - a plugin for multi-event shear wave splitting analyses in SplitLab,**
Computers and Geosciences, 105, 43-50,
https://doi.org/10.1016/j.cageo.2017.04.015.

5.1 Abstract

SplitLab is a powerful and widely used tool for analyzing seismological shear wave splitting of single event measurements. However, in many cases, especially temporary station deployments close to the noisy seaside, ocean bottom or for recordings affected by strong anthropogenic noise, only multi-event approaches provide stable and reliable splitting results. In order to extend the original SplitLab environment for such analyses, I present the StackSplit plugin that can easily be implemented within the well accepted main program. StackSplit grants easy access to several different analysis approaches within SplitLab, including a new multiple waveform based inversion method as well as the most established standard stacking procedures. The possibility to switch between different analysis approaches at any time allows the user for the most flexible processing of individual multi-event splitting measurements for a single recording station. Besides the provided functions of the plugin, no other external program is needed for the multi-event analyses since StackSplit performs within the available SplitLab structure which is based on MATLAB. The effectiveness and use of this plugin is demonstrated with data examples of a long-running seismological recording station in Finland.

5.2 Introduction

Seismic shear wave splitting analysis has become an important tool to study Earth's anisotropic behavior in the upper mantle as well as the crust and lowermost mantle (D" layer). For this

purpose several methods were developed to measure the parameters that best describe the orientation and strength of an anisotropic region in Earth's interior. These parameters are commonly the fast polarization axis direction ϕ of the split shear wave and the delay time δt, measured between the arrival times of the two split waves. For a detailed overview on applications and interpretations of shear wave splitting measurements I refer to the review papers published by *Savage* (1999) and *Long and Silver* (2009).

One of the mostly used and widely accepted analysis programs in the world-wide seismological community is the SplitLab environment (*Wüstefeld et al.*, 2008) written in MATLAB ($>$ 200 citations until end of 2018[10]). This software package contains all functionality for shear wave splitting analysis starting with requesting data for a selected recording station from different data centers, measuring the splitting parameters ϕ and δt simultaneously with three different methods and finally visualizing and saving the measured results for further analyses and modelling. In summary, SplitLab allows to perform shear wave splitting measurements in a comfortable and user-friendly way and without any need for advanced programming skills.

However, the original SplitLab environment is mainly designed for teleseismic shear wave splitting analysis and only allows to perform single event measurements. Here three different approaches are applied simultaneously: the rotation-correlation method (hereinafter RC, e.g. *Bowman and Ando*, 1987), the energy minimization method (SC, *Silver and Chan*, 1991) and the eigenvalue method (EV, e.g. *Silver and Chan*, 1991). Each of these methods performs a grid search to find the pair of parameters (ϕ, δt) that best removes the effect of splitting from the recorded waveforms (see *Wüstefeld et al.*, 2008). A comparison of the individual results of the three methods can be used to automatically classify the quality of the measurement (*Wüstefeld and Bokelmann*, 2007).

The observation of suitable *S*-wave phases for splitting analyses is limited by the specific global epicenter distribution around a station location (distance and backazimuth of events). The typically uneven source distribution leads to large backazimuthal gaps which then limit the estimation of anisotropy models. Furthermore, in many cases the recordings only have low signal amplitudes on the transverse component which can lead to unstable results (e.g. *Restivo and Helffrich*, 1999; *Vecsey et al.*, 2008; *Monteiller and Chevrot*, 2010). Thus in the past several stacking techniques were outlined to determine an overall result for ϕ and δt by stacking the individual error surfaces of the single event measurements obtained from the grid search procedure (*Wolfe and Silver*, 1998; *Restivo and Helffrich*, 1999). Recently a waveform based inversion technique was published by *Roy et al.* (2017) that utilizes the similarity of waveforms from a limited source region and concatenates the individual recordings. Especially temporary recording networks as well as stations located in noisy environments like close to the sea or even on the sea floor can benefit from such stacking techniques (e.g. *Restivo and Helffrich*, 1999).

[10] after Google Scholar, https://scholar.google.com/

Kong et al. (2015) tested the applicability of multi-event techniques and showed problems, solutions, and potential pitfalls during the interpretation of stacked results.

A look at published studies, which used SplitLab for analysis in recent years, shows that multi-event methods for stacking are widely applied by the community (e.g. *Eakin et al.*, 2010; *Zietlow et al.*, 2013; *Martin-Short et al.*, 2015; *Bodmer et al.*, 2015). Nevertheless, the outputs of SplitLab often are processed with unpublished and poorly documented code snippets and scripts. Their usage makes efficient postprocessing quite difficult for users without advanced programming skills.

Here I present the StackSplit plugin that can easily be implemented in the existing and familiar SplitLab environment without big efforts on the one hand but maximum efficiency for multi-event analyses on the other hand. Additionally, users can henceforth apply the same analysis program to their data but now also have the opportunity to directly use their single event measurements for multi-event processing. In order to perform different measurements with individual splitting methods, I provide a graphical user interface (GUI) that allows to easily switch between the single approaches at any time. Thus, the main aim of StackSplit is to ease the application of multi-event analyses for the wide audience of users that already use SplitLab or potentially want to apply it in future.

5.3 Description of the program

5.3.1 General remarks

Besides the original SplitLab package released by *Wüstefeld et al.* (2008), a slightly modified version is available from *Porritt* (2014) for which several improvements and extensions were introduced. In the latter also a new output variable was implemented which stores and saves the complete content of a calculated error surface for the selected event for further analysis outside of SplitLab. At this point I extended the parameters and values which are saved in that output variable by saving also the individually cut seismogram traces (raw or optionally filtered) used for the inversion, the estimated degrees of freedom used for error calculation and several other parameters. These different variables are essential to ensure full functionality of StackSplit. Hence the application of multi-event measurements is only possible for new SplitLab projects created after the installation of StackSplit. The original SplitLab functions that were slightly modified to successfully implement StackSplit are listed in Table 5.1.

However, in the StackSplit package provided for download, the installer file checks which of both versions is currently stored on a user's system. Thus, it is not required to change a running SplitLab version if one only wants to run StackSplit without changing the settings of the main program. For details see the user guide that is included in the download package.

Table 5.1: Names of modified SplitLab functions, new outputs and brief description of main modifications. Abbreviation *ndf* stands for number of degrees of freedom.

function name	new outputs	remark
`splitlab.m`	-	adjustments for implementation of StackSplit
`geterrorbars.m`	ndf	fixed taper and ndf calculation (*Walsh et al.*, 2013)
`geterrorbarsRC.m`	ndf	fixed taper and ndf calculation (*Walsh et al.*, 2013)
`preSplit.m`	-	adjustments to save new outputs temporary
`splitdiagnosticplot.m`	-	adjustments to save new outputs temporary
`saveresult.m`	-	adjustments to save new outputs finally
`database_editResults.m`	-	adjustments to avoid database conflicts
`seisfigbuttons.m`	-	adjustments to avoid database conflicts

Independently of the used SplitLab version, after installing the plugin, a new button called "Stacking" is available for selection at the lowermost position on the sidebar of the main SplitLab window (Fig. 5.1). Furthermore, StackSplit makes use of SplitLab's global variable `config` to store adjusted settings for a future call of the current project. Since all StackSplit function names begin with `SS_` interested users can easily take a look into the source code of the corresponding routine.

For the sake of completeness, I also implemented the modified equations by *Walsh et al.* (2013) to correctly calculate the degrees of freedom needed for error estimation (see Table 5.1). It was found that the original equations published by *Silver and Chan* (1991) will overestimate the degrees of freedom by a factor of 4/3 and thus the calculated standard errors are too small (*Walsh et al.*, 2013).

5.3.2 StackSplit main module

The StackSplit workflow (Fig. 5.1) is organised in a GUI (Fig. 5.2) from which the user can easily apply and test different methods for multi-event processing based on previously carried out single event measurements. To run StackSplit at least two saved single event measurements are necessary for a SplitLab project. Within the GUI the user has different choices how the data should be processed. Optionally, independent of the selected method, the user can define limits for the multi-event application regarding the selection ranges of event backazimuths, epicentral distances and initial polarizations. The latter can find application especially when the initial polarization direction does not equate with the backazimuth like for direct *S*-waves from local events (e.g. *Gerst and Savage*, 2004; *Eakin et al.*, 2016) or source-side splitting measurements (e.g. *Wookey and Kendall*, 2004; *Eakin and Long*, 2013). By default a limit of 5° is set for all three parameters when StackSplit is run the first time for a project. Overall the

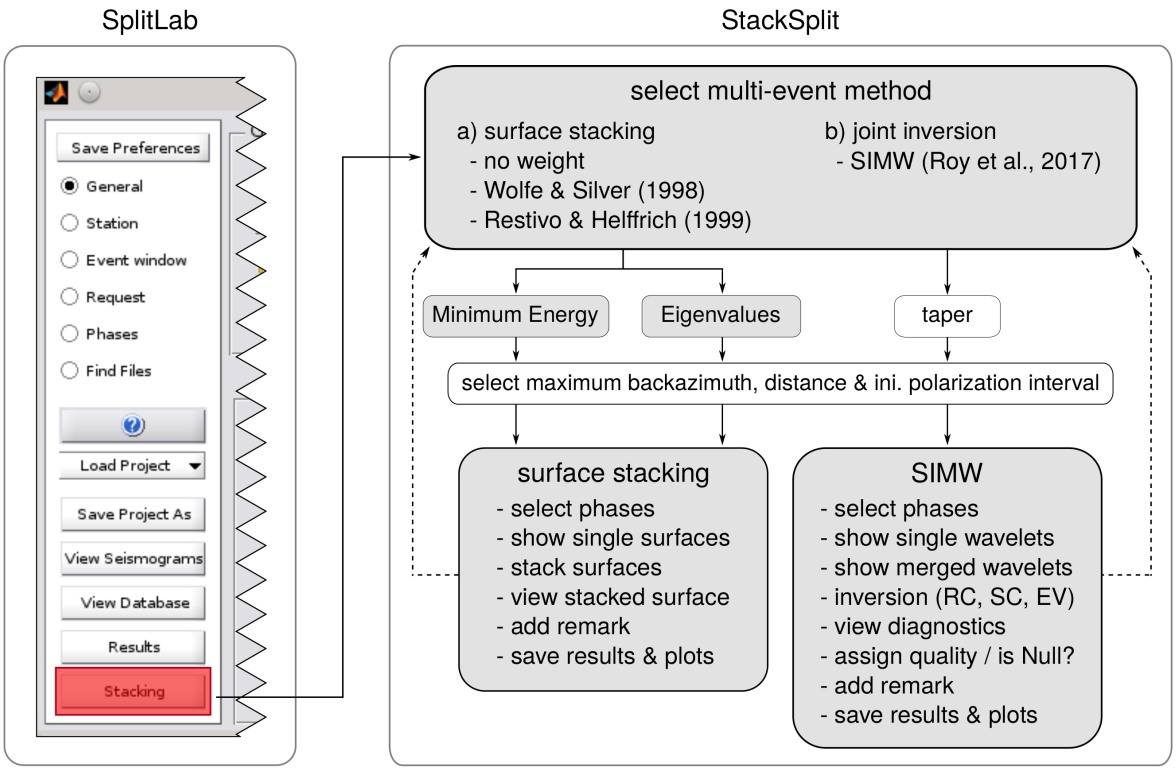

Figure 5.1: StackSplit workflow with main features/processing steps. Boxes colored in gray are essential, white ones indicate optional settings. For details see text.

StackSplit features can roughly be divided into two different multi-event approaches that are briefly described in the following.

5.3.3 Surface stacking

To calculate robust shear wave splitting parameters, firstly the user can select one of the standard stacking approaches that are applied on the output error surfaces of the single event measurements (Fig. 5.2).

In StackSplit I implemented the most common three surface stacking approaches which in general only differ in their relation to the used weight and normalization (see below). At this point the user can also choose between two different surface inputs that were saved within the framework of the single event measurements. The first is the minimum energy surface that is generated using the SC method (*Silver and Chan*, 1991). In this context the error surface represents the energy on the corrected transverse component calculated by grid-searching in the ϕ-δt parameter space. As second input the user can select the eigenvalue surface (e.g. *Silver and Chan*, 1991) whose computation depends on the previously selected eigenvalue-based option for the grid-search (maximizing λ_1 or λ_1/λ_2, minimizing λ_2 or $\lambda_1\lambda_2$, see *Silver and Chan*, 1991; *Wüstefeld et al.*, 2008). Both methods lead to very similar results but can be applied to different

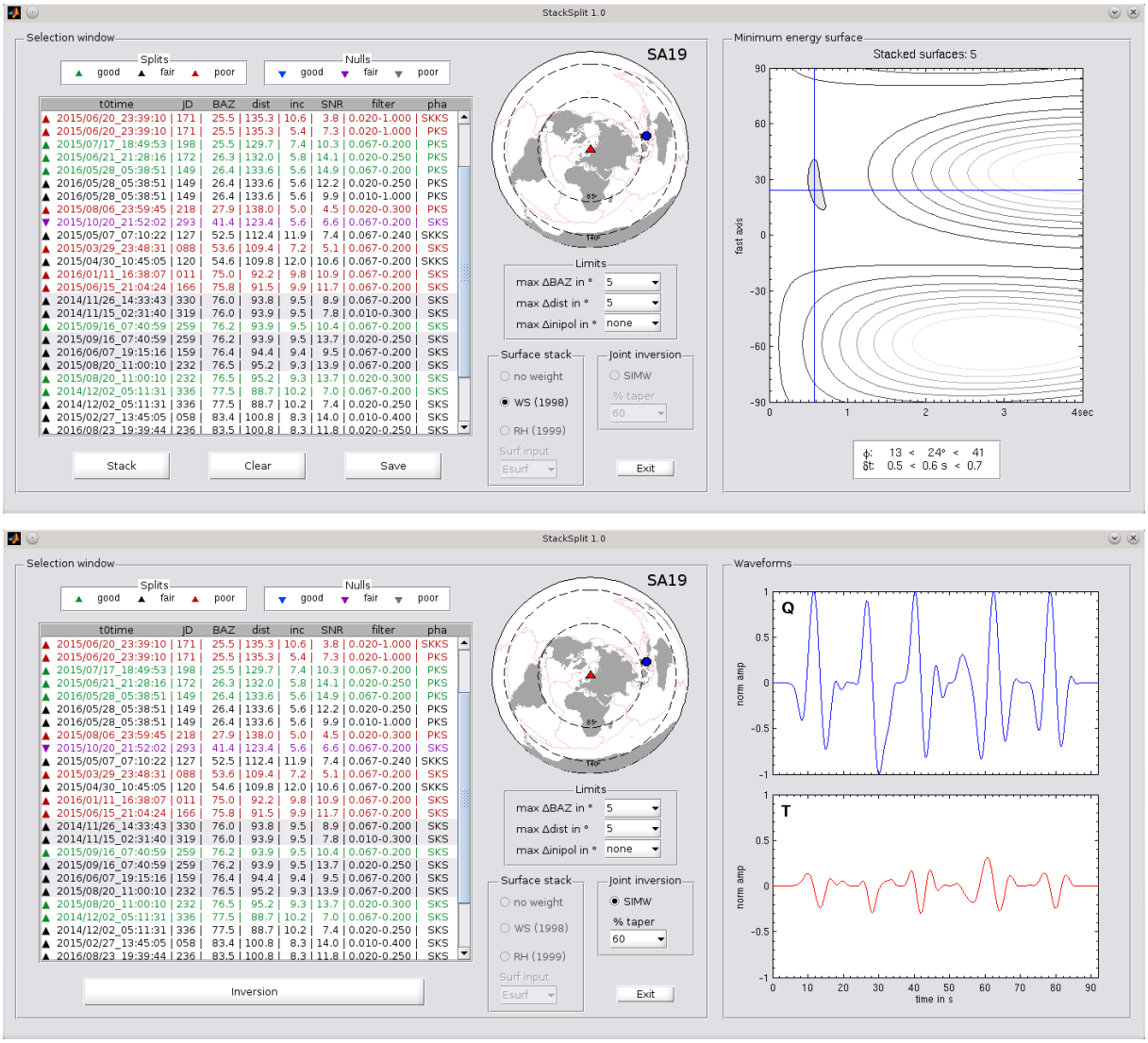

Figure 5.2: Graphical user interface of StackSplit for two different approaches. Top panel shows an example of five stacked minimum energy surfaces using the WS method (*Wolfe and Silver*, 1998). The result corresponds to the diagnostic plot displayed in Fig. 5.3a. Bottom panel shows the concatenated waveforms for the same five events when SIMW is selected. The corresponding inversion result is displayed in the exemplary diagnostic plot in Fig. 5.4. The listbox on the left side in both panels lists the individual entries of seismic phases for which a single event measurement was done and saved in SplitLab, the equidistant azimuth plot displays the distribution of the used events.

input data depending on the knowledge about the initial polarization (see e.g. descriptions in *Long and Silver*, 2009).

If several seismic phases (e.g. *SKS*, *SKKS* or *PKS*) were analyzed for an event, the user can also stack these phase results separately. This could help to stabilize the overall result especially when discrepant splitting parameters are observed for different phases of an event. Such characteristics were found for *SKS* and *SKKS* phases which often are interpreted as indicator for an anisotropic source in the lower mantle (e.g. *Wang and Wen*, 2007; *Lynner and Long*, 2014).

For an overview the user can browse through the individually saved single event measurements made with SplitLab that are listed in the listbox on the left hand side of the GUI (Fig. 5.2). Additionally, the error surface of the corresponding single-event measurement is displayed in the panel on the right. This setting allows the user to easily go through the whole available event list entries and check the error surfaces, especially for varying splitting parameters ϕ and δt regarding the different available backazimuth regions. The selection of more than one event list entry enables the user to compute a stacked surface with the currently selected method. The individual stacking approaches can easily be accessed by the different radio buttons in the "Surface stack" panel (Fig. 5.2). Furthermore, at any time the analyst is able to switch between the different methods, check the results, save them or restart the analysis with adjusted settings.

Stacking raw surfaces

This option (no weight) applies the stacking on the raw surfaces without any further consideration of the quality in terms of a weight or normalization. However, the true topography of each single error surface and thus the signal-to-noise ratio (SNR) directly influences the overall stacking result. This option is a good selection if, for example, one would like to calculate a total event surface using single measurements of the same event but different frequency filters (e.g. *Wüstefeld*, 2007). By this, the analyst can test the robustness of a measurement or detect possible frequency dependencies. As for the two following options, the standard errors for the stacked surface are calculated by assuming a χ^2 distribution for an underlying Gaussian noise process (e.g. *Wolfe and Silver*, 1998). Finally for each single error surface the estimated degrees of freedom are summed to get an overall value.

It has been noted that, if a clear backazimuthal dependency of the splitting parameters is observed, the stacking will not provide reliable results anymore. Instead of a single layer with horizontal anisotropy such characteristics point toward more complex anisotropic structures (*Silver and Savage*, 1994; *Rümpker and Silver*, 1998). Thus stacking would generate a smoothed error surface that erroneously indicates a single horizontal anisotropic layer beneath the station.

Method after Wolfe & Silver

As another option the user can select the widely applied method proposed by *Wolfe and Silver* (1998) referred to as WS in the following. Depending on the used input each single error surface is normalized before stacking, either to its absolute minimum (for λ_2, $\lambda_1\lambda_2$ and minimum energy) or maximum (λ_1 and λ_1/λ_2).

Method after Restivo & Helffrich

The final option of the surface stacking approach is the procedure initially introduced by *Restivo and Helffrich* (1999), in the following RH, that is a small extension of the WS approach. Here

each surface firstly undergoes a weighting depending on the measured SNR and secondly a normalization which reduces a high impact of overrepresented backazimuth directions (see *Restivo and Helffrich*, 1999).

5.3.4 Simultaneous Inversion of Multiple Waveforms

The second stacking approach is a waveform based multi-event inversion recently published by *Roy et al.* (2017) called SIMW (Simultaneous Inversion of Multiple Waveforms). In contrast to the surface stacking methods outlined in the previous section, SIMW directly works on the time series and not on the already calculated error surfaces. First, all events of a preferred region with similar backazimuth and epicentral distance are selected and the corresponding waveforms of the radial Q and transverse T components are concatenated in the time domain. Within StackSplit all single waveforms are normalized to the maximum of their corresponding Q components before concatenation to avoid a bias due to large amplitude recordings. Optionally a taper can be applied on each single wavelet before merging all of them together to reduce influences of potential noise sequences included in the time window used for the single-event measurement. The default taper in total influences 20% of the corresponding Q and T waveforms, so 10% at both the start and end. Then the whole generated waveform is inverted simultaneously using the three different methods implemented in SplitLab (RC, SC and EV) to remove the effect of splitting by performing a grid search (see section 5.2). The corresponding backazimuth for the concatenated waveform is calculated as a simple mean of all used single event backazimuths. This is the only limitation of SIMW, and thus the window limits for considered backazimuths and epicentral distances should be selected with care (Fig. 5.2). On the other hand, the application of SIMW, equal to the single-event measurements, enables the user to assign

a quality rank to the calculated multi-event result as proposed by *Wüstefeld and Bokelmann* (2007). The resulting splitting parameters are the best joint solution for all used waveforms. For a detailed description of SIMW including the application to two long running seismic networks, see *Roy et al.* (2017).

Within the "Waveforms window" (Fig. 5.2), the corresponding waveforms for the radial and transverse components of the currently selected single measurement are displayed. If more than one entry is selected, the corresponding concatenated waveform appears in that window (see example in Fig. 5.2).

5.3.5 StackSplit outputs

Depending on the used multi-event method, StackSplit generates different output files which can be used for further analysis and modelling outside of SplitLab (e.g. using MSAT, the MATLAB Seismic Anisotropy Toolkit by *Walker and Wookey*, 2012) or to visualize the results (e.g. using GMT, the Generic Mapping Tools by *Wessel et al.*, 2013). Firstly, independent of the

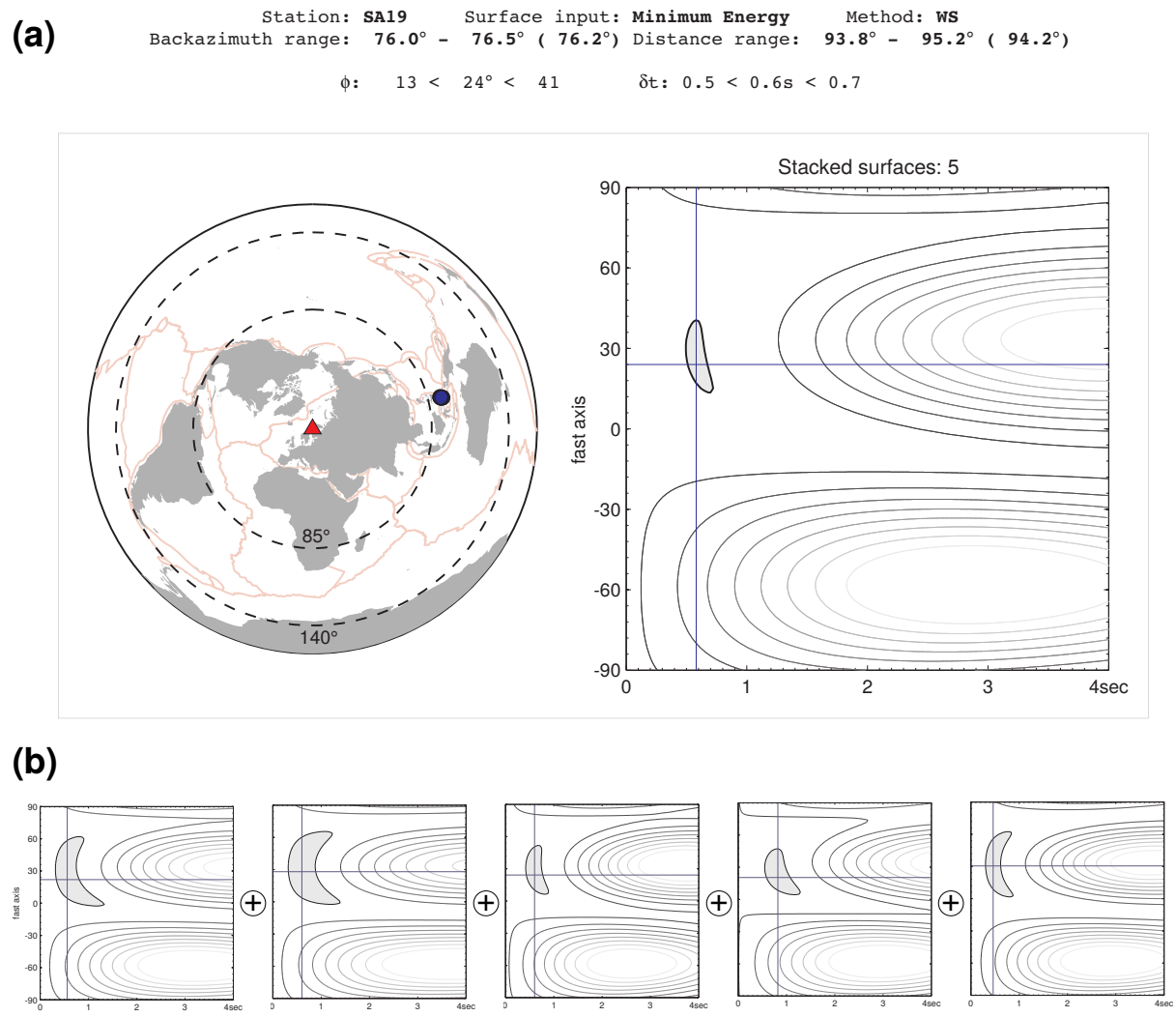

Figure 5.3: **(a)** Exemplary diagnostic plot for the WS surface stacking approach with five used single minimum energy (SC) surfaces. The corresponding single event surfaces are displayed in **(b)**. Please note that, for the sake of clarity, for each measurement the single surfaces are not included in the saved diagnostic plot. The 95% confidence region in each surface is indicated by the gray shaded area.

method, each saved measurement (surface stack or SIMW) is stored in the global MATLAB structure variable `eqstack` that is automatically generated when StackSplit is run the first time for a project. Similar to SplitLab's `eq` variable this structure contains information about each conducted multi-event measurement including the computed values for ϕ and δt as well as the whole content of the used input events/phases.

Besides this main storing variable, each saved result will appear in a plain text file that contains the whole information about the measurement like station name, considered backazimuth and distance ranges as well as the results of the multi-event measurement. Separately for both approaches, surface stack and SIMW, a text file is compiled in the folder of the set result path. Additionally, diagnostic plots are automatically saved in the preferred file format for each measurement. For the surface stack the diagnostics show the final stacked surface (same as in the

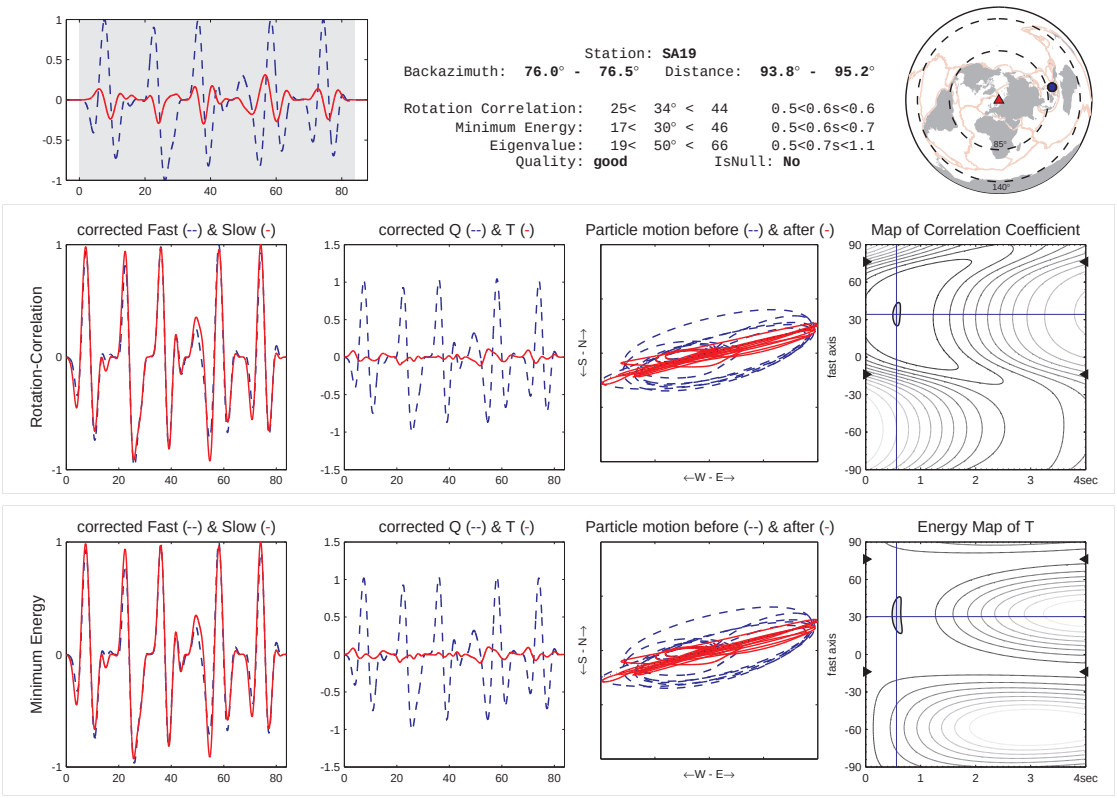

Figure 5.4: SIMW diagnostic plot for five exemplary phase records from earthquakes (top left panel) that occurred in the South-East Asia region between fall 2014 and fall 2016. Displayed are the standard SplitLab panels for the RC and SC methods (see *Wüstefeld et al.*, 2008) except the world map in the upper right corner that displays all the used events. The header gives additional information about the measurement and the input data.

GUI panel) as well as the event distribution of the selected events used for the current stacking (Fig. 5.3). On top, information about the settings as well as the final result is given. A diagnostic plot for measurements conducted with SIMW looks similar to the original SplitLab diagnostics (Fig. 5.4). Besides the corresponding information about the multi-event measurement, in addition the distribution of the used events/phases is displayed in the upper right corner.

5.4 Application example

To demonstrate the performance of StackSplit with a real data example, I present measurements of the seismic permanent station VAF of the Finnish National Seismic Network for which recordings of around ten years (2007-2016) are freely available (Fig. 5.5). In the past shear wave splitting was also partly studied within the SVEKALAPKO project at this station (*Vecsey et al.*, 2007).

First, the data were analyzed with the standard single event analysis in SplitLab which yielded in total 163 measurements that include non-null and null measurements of all qualities (ranked as *good*, *fair* and *poor* following *Barruol et al.*, 1997; *Wüstefeld and Bokelmann*, 2007). All

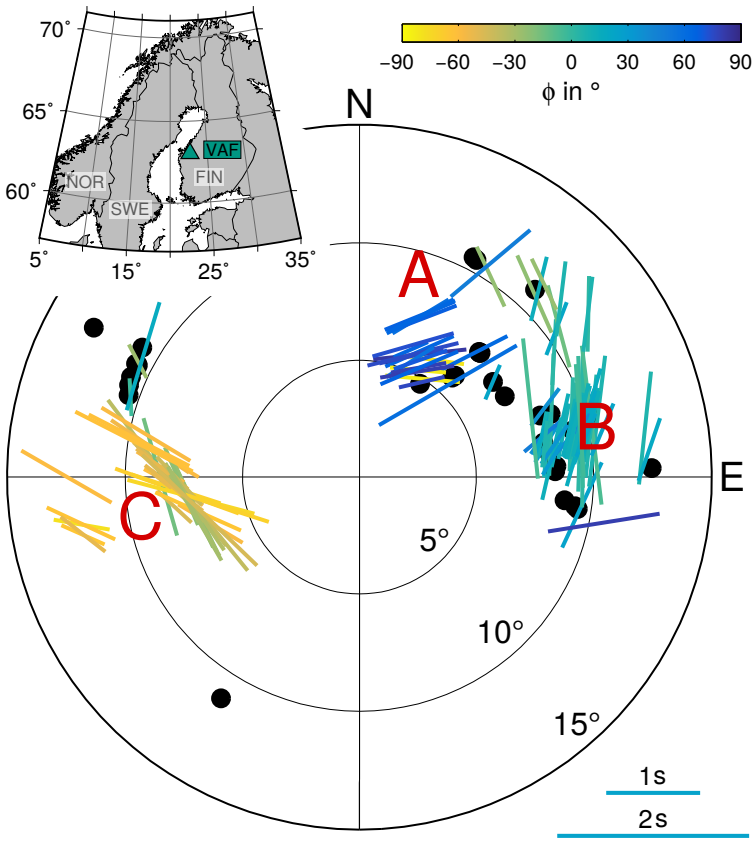

Figure 5.5: Location and determined single-event splitting parameters of all qualities (*good*, *fair* and *poor*) at permanent station VAF as a function of backazimuth and incidence angle (radial axis from center to outside). To highlight the observed variation of the fast polarization axis with backazimuth the single bars additionally are color-coded. Black filled circles represent null measurements.

waveforms were processed using a bandpass filter with corner periods mainly between 5 s and 15 s. In order to improve the SNR of the single phase arrivals, partly the corner periods were slightly adjusted as done in other studies (e.g. *Eakin et al.*, 2016).

In Fig. 5.5 the results of the single event measurements are presented that indicate complex anisotropy beneath the station due to strong variations of the splitting parameters with backazimuth. Thus for this station multi-event procedures without a preselection of backazimuths and incidence angles are not suitable to generate a single set of averaged splitting parameters; otherwise the backazimuthal characteristics would be smoothed out in the overall result. However, this station is a good example to compare the different approaches implemented in StackSplit for a multi-event analysis within limited backazimuth regions. Please note, that for the RH method in this case the backazimuthal normalization has minor influence on the stacked result.

The single event results can roughly be divided into three regions with average backazimuths (BAZ) of 21°, 75°, and 259° (regions A-C, Fig. 5.5). For each group I selected a set of 7-10 representative low-quality measurements that were mostly ranked as *poor* with SNRs between 4 to 10 to test the stacking procedures. However, some results which were ranked as *fair* but with similar SNR, were also included. The backazimuth and epicentral distance range for the used events within each group is less than 4° (Fig. 5.6).

Subsequently, for each of the four methods implemented in StackSplit, splitting parameters were computed for the three selected backazimuth regions (Fig. 5.6). Since for the surface

stacking procedures the selectable inputs are the minimum energy (SC) and eigenvalue surfaces (EV), a direct comparison with SIMW is only possible for these two methods. For the sake of clarity, in Fig. 5.6 only results based on the SC method are presented. However, the results based on the EV method reveal a very similar behavior.

In general the determined multi-event results show similar values for the fast axis ϕ and delay times δt separately for each of the selected backazimuth regions. For region A (BAZ $\sim 21°$, 7 *PKS* phases) the observed difference of the absolute values is 3° for the fast axis and 0.1 s for the delay time. The results for region B (BAZ $\sim 75°$, 10 *SKS* phases) have a wider scatter for ϕ with a maximum difference of around 6° between the different methods but also a small variation of 0.1 s for δt. The splitting parameters obtained for region C (BAZ $\sim 259°$, 7 *SKS* phases) show similar characteristics with maximum differences of around 6° for the fast axis and slightly larger variations of 0.3 s for δt.

As expected, overall the errorbounds (that represent the 95% confidence level for each measurement) of the results from stacking are essentially smaller compared to the single-event measurements whose error bars partly span across the whole parameter space (Fig. 5.6). Thus, independently of the applied method, the confidence into the obtained multi-event splitting parameters has been raised for all three backazimuth regions A-C.

5.5 Conclusions

I have introduced StackSplit, which is a flexible and easy to use plugin for the widely applied shear wave splitting environment SplitLab. StackSplit was mainly designed to allow performing multi-event analyses without big efforts for all seismologists that already use SplitLab for single event measurements or plan to use it in future. Besides the commonly already used standard stacking techniques, this package provides also a new waveform based inversion approach (*Roy et al.*, 2017) that delivers similar results for limited backazimuth regions. The flexible graphical user interface allows to switch between the different methods and to compare the corresponding outputs to receive high-quality measurements for ongoing interpretations. However, the standard analysis can be done as in the past with the exception that now directly a multi-event processing interface is available for efficient analysis within a familiar program environment.

Code availability

The StackSplit code and a detailed documentation is available at GitHub[11] and MathWorks File Exchange platform[12]. The code was tested with MATLAB versions between 2012a and 2014a

[11] GitHub: https://github.com/michaelgrund/stacksplit, last accessed 11 January 2019
[12] MathWorks File Exchange: https://de.mathworks.com/matlabcentral/fileexchange/62402, last accessed 11 January 2019

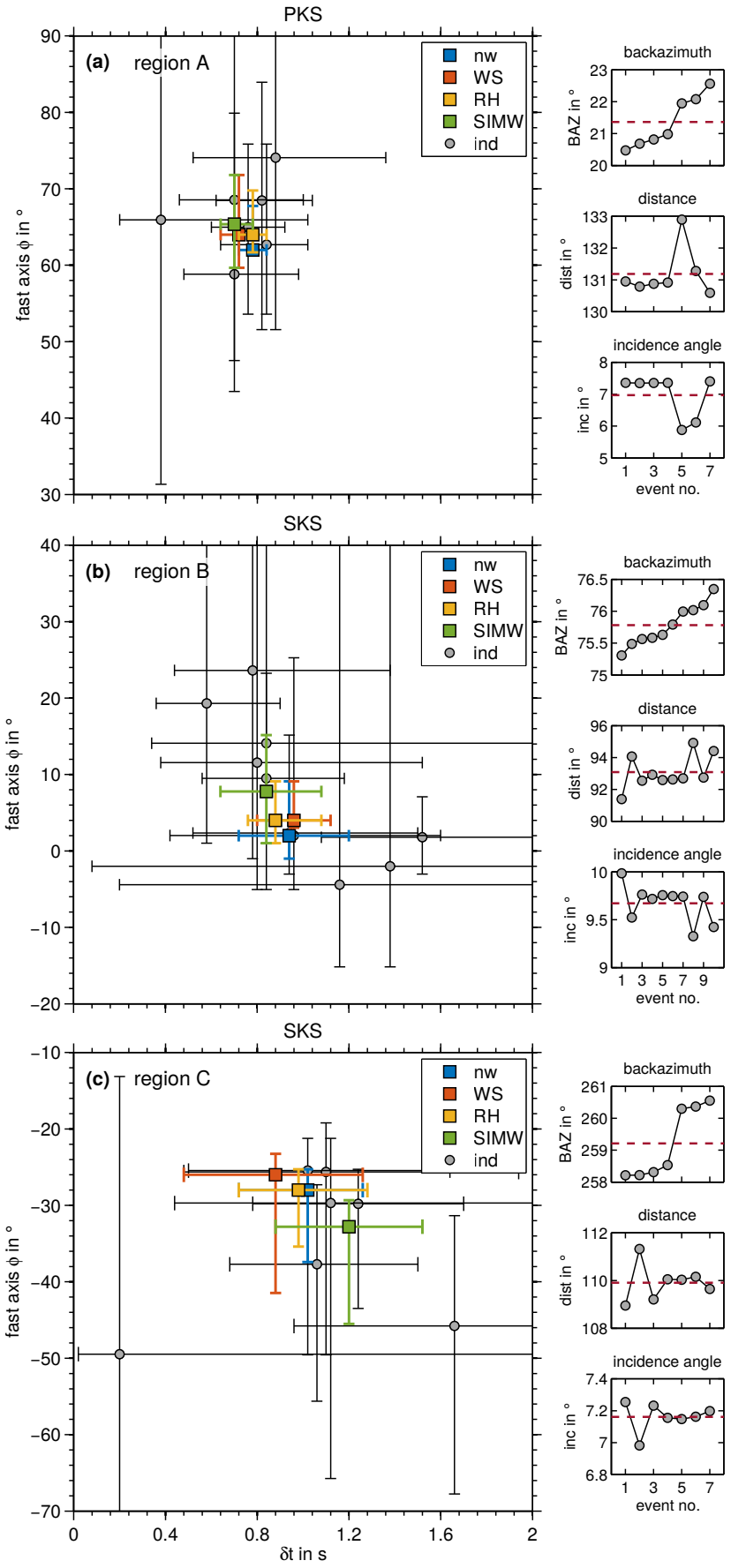

Figure 5.6: Distribution of determined splitting parameters for the individual single (gray circles, *ind*) and multi-event (colored, *nw*: no weight; *WS*: Wolfe & Silver, 1998; *RH*: Restivo & Helffrich, 1999; *SIMW*: Roy et al., 2017) measurements at permanent station VAF. For all methods only the SC results are shown. The small panels on the right-hand side give information about the backazimuth, epicentral distance and incidence angle (from top to bottom) of the used event/phase. The horizonal dashed red line indicates the calculated mean for each parameter. The shown error bounds represent the minimum and maximum range of the calculated confidence regions (see *Wüstefeld et al.*, 2008). Please note the different axis scales for the fast axis ϕ.

operating on Linux and Windows systems. However, in general no issues are expected for other versions. If a user's version is MATLAB 2014b or newer I recommend to use the SplitLab version provided by *Porritt* (2014). StackSplit automatically checks for the available version on a system.

Acknowledgements

I am grateful to all the persons that gave me the motiviation and opportunity to continue working on that package, particulary Joachim Ritter. Furthermore, I thank Yasmin Sanz Alonso for intensive testing the code with additional data from other seismic stations which helped to eliminate some bugs in an earlier version. I am thankful to three anonymous reviewers for their helpful and very constructive suggestions and comments on the manuscript and the code. This work has received funding from the Deutsche Forschungsgemeinschaft (DFG) under the LITHOS-CAPP project (RI1133/11-1).

Data for station VAF were requested from GEOFON at GFZ Potsdam where they are freely available for download. The examples in section 5.3 were generated with data of a temporary station (SA19) that is part of the ScanArray network (see *Grund et al.*, 2017a).

6 Lowermost mantle anisotropy observed at ScanArray

In this chapter I focus on a study which developed during the routine shear wave splitting analysis at the individual recording stations. Clear discrepancies of the splitting parameters between *SKS* and *SKKS* phases for the same source-receiver configuration were discovered which hint at deeply located sources of anisotropy in the Earth's lowermost mantle far away from the station network in Fennoscandia and surrounding areas. Most parts of this chapter have been published in:

> *Grund, M. & Ritter, J.R.R.* (2019), **Widespread seismic anisotropy in Earth's lowermost mantle beneath the Atlantic and Siberia**, Geology, 47(2), 123-126, https://doi.org/10.1130/G45514.1[13].

6.1 Abstract

Deep inside the Earth, just above the core-mantle boundary at around 2700 km depth, large-scale mantle structures are assumed to play a key role for global geodynamic processes. While unusual hot regions are attributed with feeding rising mantle plumes and volcanic hotspots, the accumulation of subducted lithospheric plates is associated with colder than average features. In both environments the appearance of dynamic-driven processes such as deformation and mantle flow can directly be inferred by the presence of seismic anisotropy. However, the geometries as well as the interactions of these massive anomalous structures with the surrounding mantle material are still under debate. Based on new seismic data from a dense and large-aperture recording network in Scandinavia we characterize the anisotropic signatures of two so far unexplored regions in the lowermost mantle by using observations of clearly discrepant *SKS-SKKS* shear wave splitting measurements. Thereby we can demonstrate that anisotropy is located along the northern edges of the large low-shear-velocity province beneath Africa. Furthermore, we recover an anisotropic structure in a region of fast seismic velocity underneath Siberia which provides additional evidence for widespread deformation caused by a deeply subducted slab.

[13]

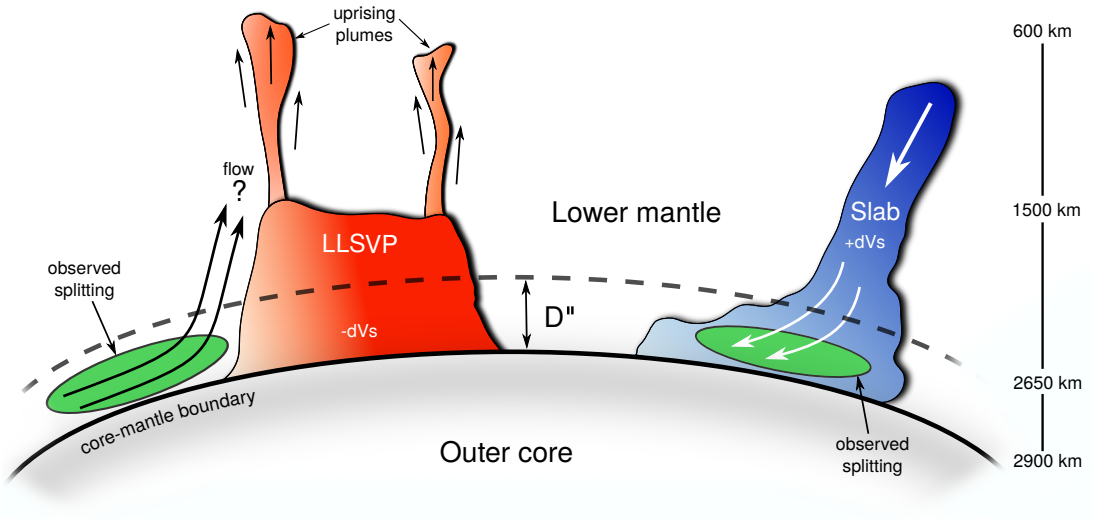

Figure 6.1: Schematic showing the most dominant lowermost mantle structures. Large low-shear-velocity provinces (LLSVPs) are located beneath Africa and the Pacific. Downgoing slab material was located in several regions of the D" region in around 2700 km depth based on seismic tomography studies (e.g. *Lekic et al.*, 2012; *Cottaar and Lekic*, 2016). On the flanks of the LLSVPs the origin of uprising plumes is assumed (e.g. *Steinberger and Torsvik*, 2012). Lowermost mantle anisotropy was found in few regions around the globe close to the edges of the LLSVPs as well as in areas where subducted slab material impinges on the core-mantle boundary (green patches). Approximate depth indications are displayed on the right. Please note that the cartoon is not to scale.

6.2 Introduction

Some regions in the Earth's lowermost mantle (Fig. 6.1) exhibit significant deviations from global reference models with regard to seismic velocities. In this context two large low-shear-velocity provinces (LLSVPs) beneath Africa and the Pacific appear as most prominent features in seismic tomography models (e.g. *Kustowski et al.*, 2008; *Simmons et al.*, 2010). These are assumed to play a key role in the dynamics of the mantle (e.g. *Garnero and McNamara*, 2008; *Garnero et al.*, 2016) as well as acting as sources of uprising plumes (e.g. *Thorne et al.*, 2004; *Burke et al.*, 2008; *Steinberger and Torsvik*, 2012). In contrast, for other areas faster than average seismic velocities are consistently observed in various global tomography models (*Shepard et al.*, 2017). Such seismic high-velocity anomalies are often interpreted as remnants of paleo-subducted slabs that reach down to the core-mantle boundary region (CMB) in 2700-2891 km depth (*Van der Voo et al.*, 1999; *McNamara et al.*, 2001; *Hutko et al.*, 2006; *Simmons et al.*, 2015). In addition, more isolated and meso-scale low-velocity structures were recently detected beneath Russia and Iceland (*Lekic et al.*, 2012; *Cottaar and Lekic*, 2016).

While several open questions regarding the origin, composition and role in global mantle dynamics (e.g. *Flament et al.*, 2017) remain for these structures, there is evidence for strong seismic anisotropy in all environments from shear wave splitting analyses (Fig. 6.1, e.g. *Niu and Perez*, 2004; *Wang and Wen*, 2007; *Long*, 2009; *Cottaar and Romanowicz*, 2013; *Lynner and Long*, 2014; *Long and Lynner*, 2015; *Ford et al.*, 2015; *Deng et al.*, 2017; *Creasy et al.*, 2017).

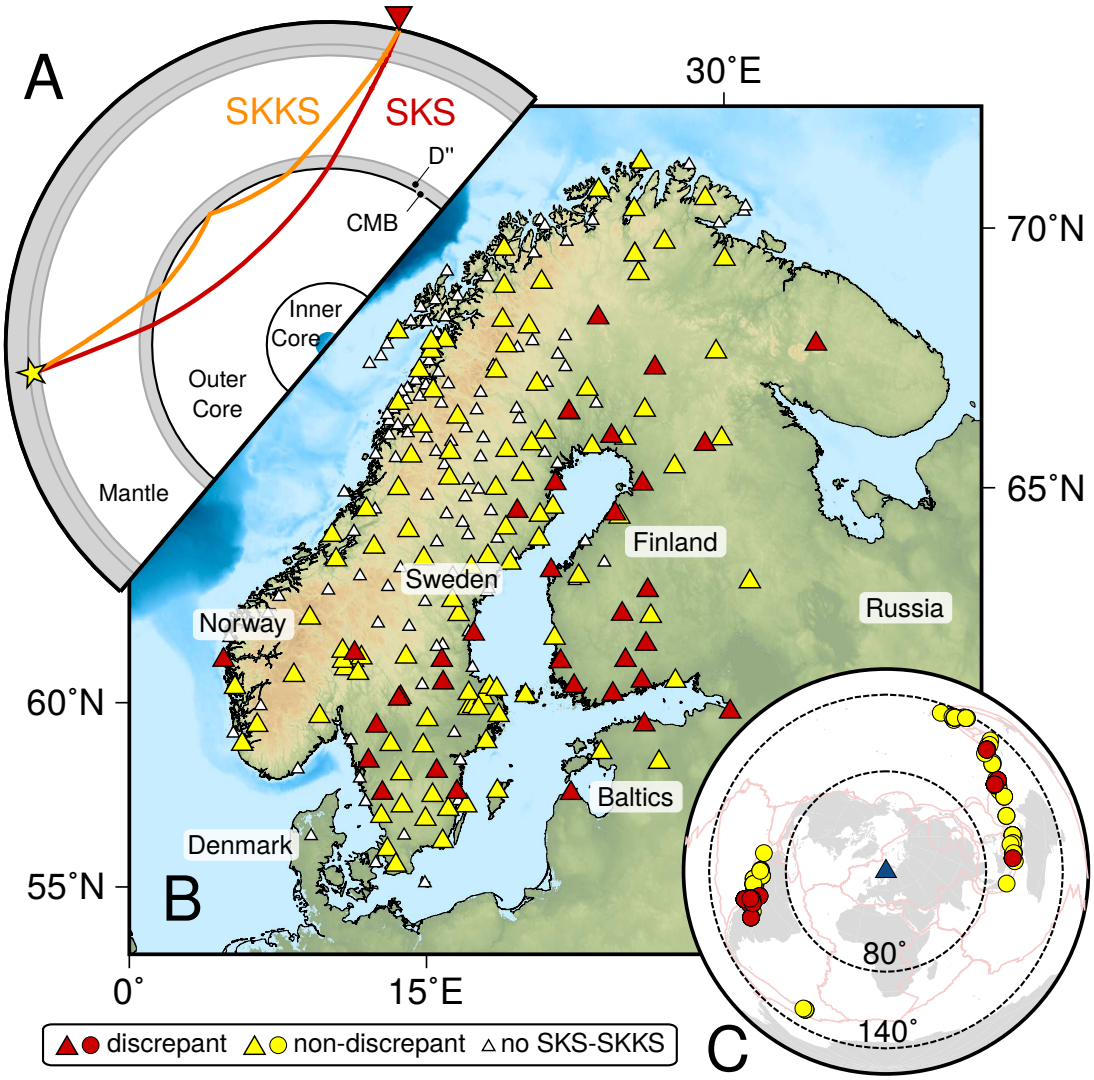

Figure 6.2: A: *SKS-SKKS* raypaths from hypocenter (star) to receiver (500 km depth, 100°). B: Seismic stations used in this study (triangles). Color fill represents the observation of *SKS-SKKS* waveforms, with red for at least one discrepant pair and yellow for only non-discrepant recordings. White triangles display sites at which no *SKS-SKKS* pairs were observed. C: Distribution of earthquakes that yielded at least one discrepant (red) or non-discrepant (yellow) *SKS-SKKS* pair.

In the presence of anisotropy a propagating shear wave is split into two orthogonal components that are polarized in the fast and slow directions. The two waves travel with different velocities and separate with distance. The orientation of the fast axis (ϕ) and the delay time (δt) between the fast and slow wave can provide valuable information about deformation processes and the strength and thickness of the anisotropic material (*Silver and Chan*, 1991; *Savage*, 1999; *Long and Silver*, 2009).

Teleseismic core-refracted shear waves such as *SKS* and *SKKS* sample nearly the same volumes in the upper 500 km of the Earth's mantle for the same source-receiver pair. In contrast, their raypaths differ significantly in the lower mantle (Fig. 6.2). With the exception of the 200-

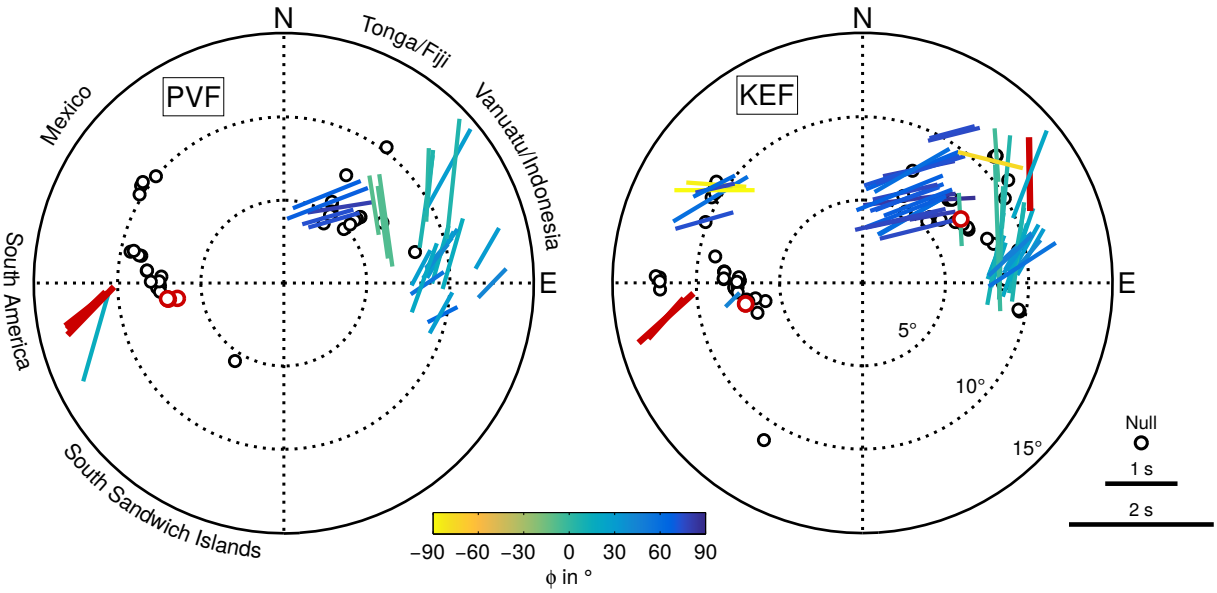

Figure 6.3: Exemplary stereoplots for the two long-running permanent stations PVF and KEF at which a strong backazimuthal variation for ϕ and δt is observed. Splitting parameters are shown as a function of backazimuth (clockwise direction from north) and incidence angle (radial axis, 5°-15°). To highlight variations of ϕ with backazimuth the single bars are also color-coded. Black open circles represent null measurements. Discrepant pairs for *SKS* and *SKKS* splitting are shown in red.

300 km-thick D" layer just atop the CMB the lower mantle is generally assumed to be nearly isotropic (e.g. *Meade et al.*, 1995).

Therefore, distinct discrepancies in *SKS-SKKS* shear wave splitting are a powerful tool to map depth-dependent anisotropic anomalies in D" (e.g. *Hall et al.*, 2004; *Lynner and Long*, 2014; *He and Long*, 2011; *Deng et al.*, 2017). Recently the observations of discrepant *SKS-SKKS* splitting pairs have increased, especially for areas along the edges of the LLSVPs beneath Africa and the Pacific (e.g. *Niu and Perez*, 2004; *Lynner and Long*, 2014; *Deng et al.*, 2017) or the Perm anomaly beneath Russia (*Long and Lynner*, 2015). It has been inferred that variations of complex and strong anisotropy are located near the boundaries of LLSVPs, which are potentially associated with deformation due to mantle flow (e.g. *Cottaar and Romanowicz*, 2013). Although only few studies exist, there is also evidence from *SKS-SKKS* splitting for anisotropy in D" caused by remnants of paleo-subducted slab material that induces high shear deformation atop the CMB (e.g. *Long*, 2009).

The sampling of potential target areas in D" substantially relies on suitable propagation paths that are controlled by the locations of receivers and the sources of earthquakes. However, only limited source-receiver configurations allow to study lowermost mantle anisotropy using pairs of *SKS-SKKS* phases around the globe. Thus, many blank spots still appear in the global image of lowermost mantle anisotropy (*Nowacki et al.*, 2011).

Here we present striking new observations of discrepant *SKS-SKKS* splitting pairs that were recorded across a large-aperture seismic network in Scandinavia and surrounding countries.

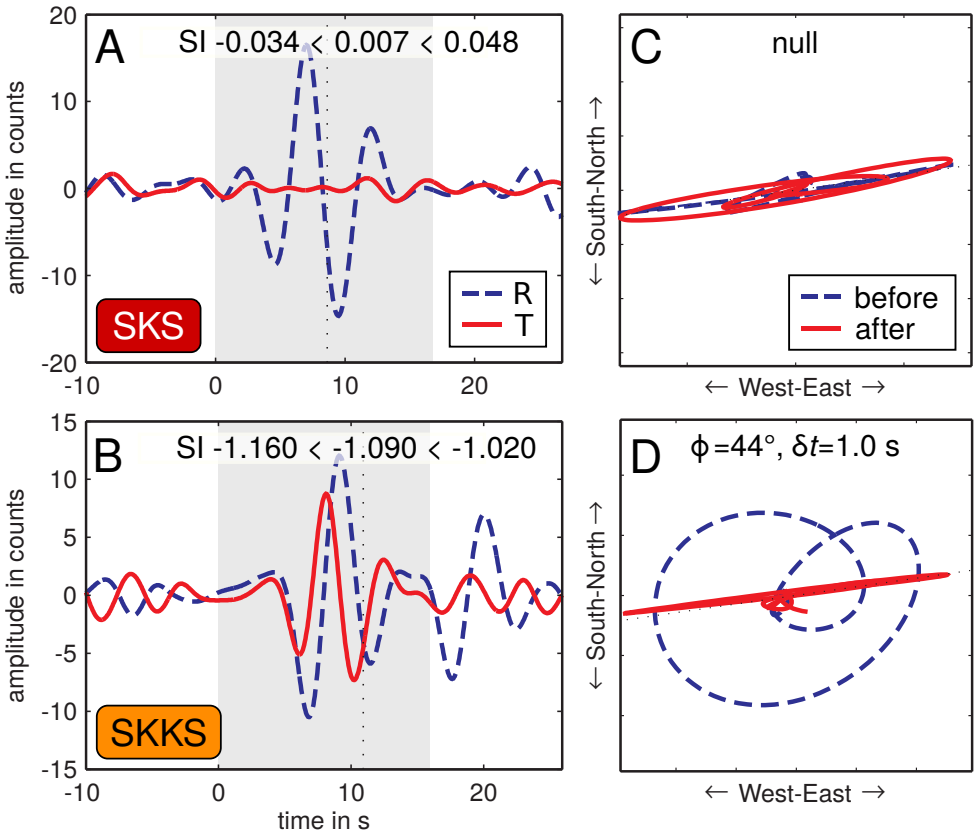

Figure 6.4: A and B: Original (uncorrected) radial (R, blue dashed) and transverse (T, solid red) component seismograms at station PVF for *SKS* (top) and *SKKS* (bottom) of the same event on 25 July 2016. At the top the splitting intensity (SI) value along with its uncertainty (95% confidence interval) is shown. C and D: Particle motions before (blue dashed) and after (solid red) correcting the splitting using the *Silver and Chan* (1991) method. Splitting parameters ϕ and δt or null are indicated at the top of each panel.

With our findings we can shed light on two widespread and so far poorly sampled or fully unexplored anomalous regions in D" that are located along the northern edges of the African LLSVP and beneath northwestern Siberia in an area of consistent fast seismic shear wave velocity (v_S). Knowledge about such anomalies provides rare constraints for improved modeling and understanding of mantle dynamics.

6.3 Data and methods

We analyzed seismic data of more than 250 temporary and permanent stations (Fig. 6.2) that are mainly part of the ScanArray network (*Thybo et al.*, 2012; *Grund et al.*, 2017a). Earthquakes with $M_W > 5.8$ at distances of 80°-140° were selected for the routine shear wave splitting analysis. Here we only focus on a subset of the whole analyzed data set, namely events for which it was possible to identify both clear *SKS* and *SKKS* arrivals on the same seismogram (see appendix D.1, Table D.1). Shear wave splitting (fast axis ϕ and delay time δt) was measured with the SplitLab package (*Wüstefeld et al.*, 2008), using simultaneously the rotation correla-

tion method (RC, *Bowman and Ando*, 1987) and the energy minimization method (SC, *Silver and Chan*, 1991).

Prior to the measurements we checked the sensor orientations (see section 3.2.1, Table 3.3 and appendix C, Table C.1) and processed the waveforms using a zero-phase bandpass filter (5-15 s). For some recordings the corner periods were slightly adjusted to improve the signal-to-noise ratio (SNR) as done in previous studies (e.g. *Long*, 2009; *Grund*, 2017). We only consider measurements that agreed for both methods (RC and SC) within their error bounds (95% confidence region) and which have an SNR ≥ 5. All splitting measurements (Table D.1) have typical errors of $< \pm 25°$ for ϕ (average: $\pm 15.5°$) and $< \pm 0.5$ s for δt (± 0.32 s). For error estimation we applied the corrected equations by *Walsh et al.* (2013) as implemented in the StackSplit plugin (*Grund*, 2017, see chapter 5). Phase arrivals with a clear signal on the radial component, SNR ≥ 5, and (nearly) linear particle motion before the correction for splitting were classified as so-called nulls (no splitting). In our data set we classified a pair of *SKS-SKKS* as discrepant if one phase was null and the other phase was clearly split. If both phases were split (similar ϕ and δt) or both were null, the pair was considered as non-discrepant (e.g. *Long and Lynner*, 2015).

In order to characterize contributions from lowermost mantle anisotropy at stations with complex splitting characteristics (Fig. 6.3), we followed the approach of *Deng et al.* (2017) by measuring the splitting intensity (SI) as decribed by *Chevrot* (2000). Based on this approach null arrivals in our data set have to fulfill the condition of an absolute SI value that is < 0.2 and for a discrepant *SKS-SKKS* pair the absolute SI-difference (ΔSI) including the errors has to be ≥ 0.2. For a potential contribution from lowermost mantle anisotropy, ΔSI between *SKS* and *SKKS* is expected to be ≥ 0.4 (*Deng et al.*, 2017).

6.4 Results and discussion

6.4.1 Observation of clearly discrepant *SKS-SKKS* waveforms

Using shear wave splitting analysis, in total we received 332 pronounced *SKS-SKKS* pairs. (Table D.1). Out of these, 49 pairs show clear discrepancies and 283 pairs offer no anomalous pattern. Figure 6.4 presents a waveform example of a discrepant *SKS-SKKS* pair. Further recordings are shown in appendix D, Fig. D.1. Where possible we cross-checked the *SKS* results by measuring splitting also for *sSKS*. Both phases sample nearly the same volumes along their raypaths and, as expected, the splitting parameters reveal consistency within the limits of uncertainty (appendix D, Fig. D.2).

Taking into account finite-frequency effects (e.g. *Favier and Chevrot*, 2003), it is quite unlikely that such waveform discrepancies originate only from shallow anisotropy directly beneath the station. With dominant periods of 6-10 s, the Fresnel zones for *SKS* and *SKKS* overlap sig-

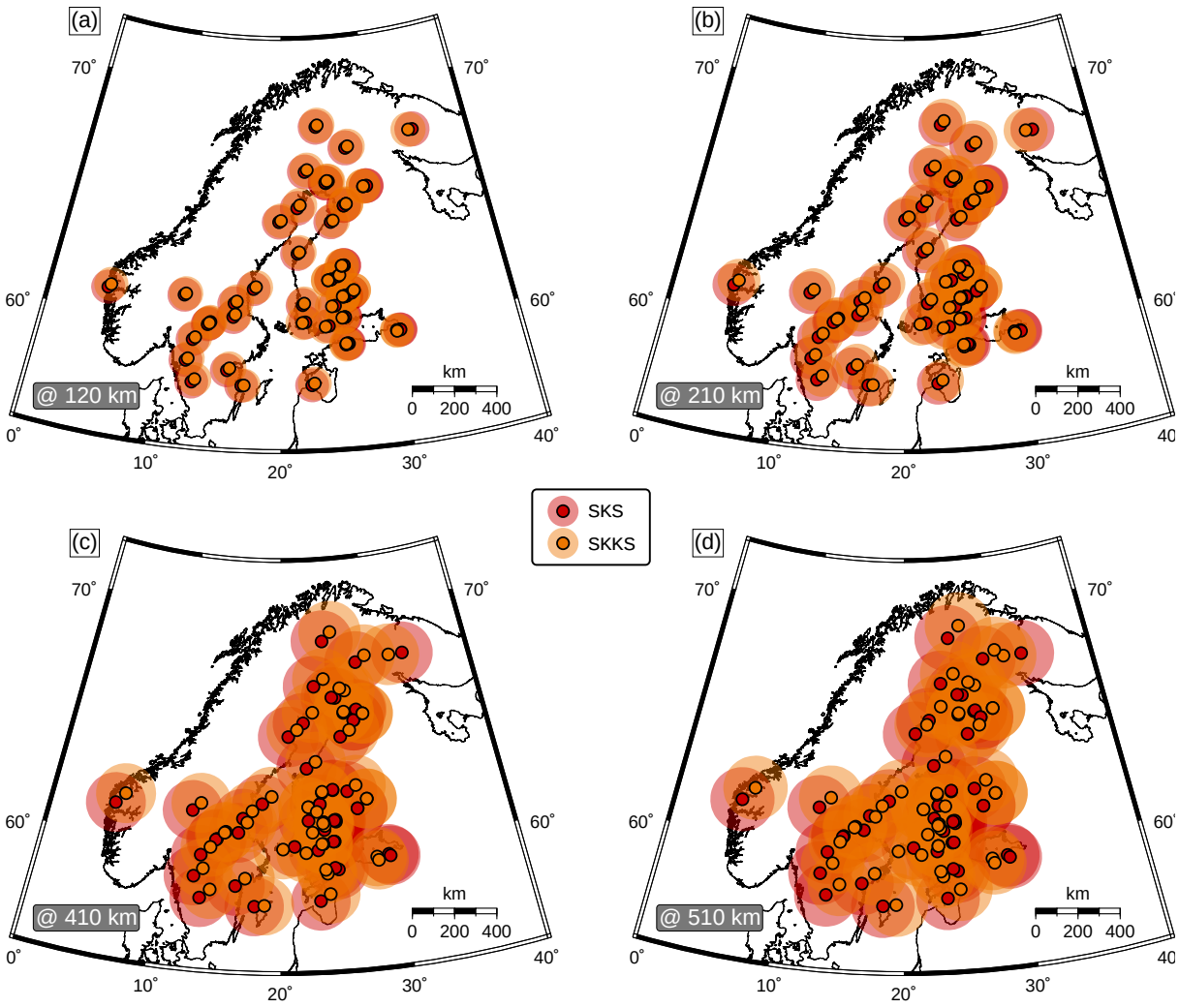

Figure 6.5: (a)-(d) Fresnel zone estimates of the 49 discrepant *SKS-SKKS* pairs (transparent large circles) for a dominant period of 8 s following *Favier and Chevrot* (2003) in four different depths (120 km, 210 km, 410 km, and 510 km). The centers of the Fresnel zones correspond to the pierce points (small black bordered circles) calculated with the tauP toolkit (*Crotwell et al.*, 1999) and the iasp91 Earth model (*Kennett*, 1991).

nificantly in the mantle transition zone and uppermost lower mantle (Fig. 6.5). For this reason both phases of a pair are sensitive to the same volume and we would expect the same ϕ-δt characteristics. A 3D visualization of exemplary *SKS-SKKS* raypaths is shown in appendix D, Fig. D.3.

Furthermore, we rule out major influences due to waveform interference between phases arriving at the stations within short time periods (*Lin et al.*, 2014). The observed discrepancies occur for distances of 100°-130° and event depths $>$ 20 km (Fig. 6.6). This was assumed to be sufficient to avoid dominant interference effects (*Deng et al.*, 2017, see also Figs. 6.7 and 6.8). Hence, our observed *SKS-SKKS* discrepancies are first-order indicators that a component of lowermost mantle anisotropy plays a key role in this context. However, for observations of non-discrepant pairs (Fig. D.2) a contribution of lowermost mantle anisotropy cannot necessarily be ruled out (e.g. *Long and Lynner*, 2015). Depending on the raypaths and the dimension of an

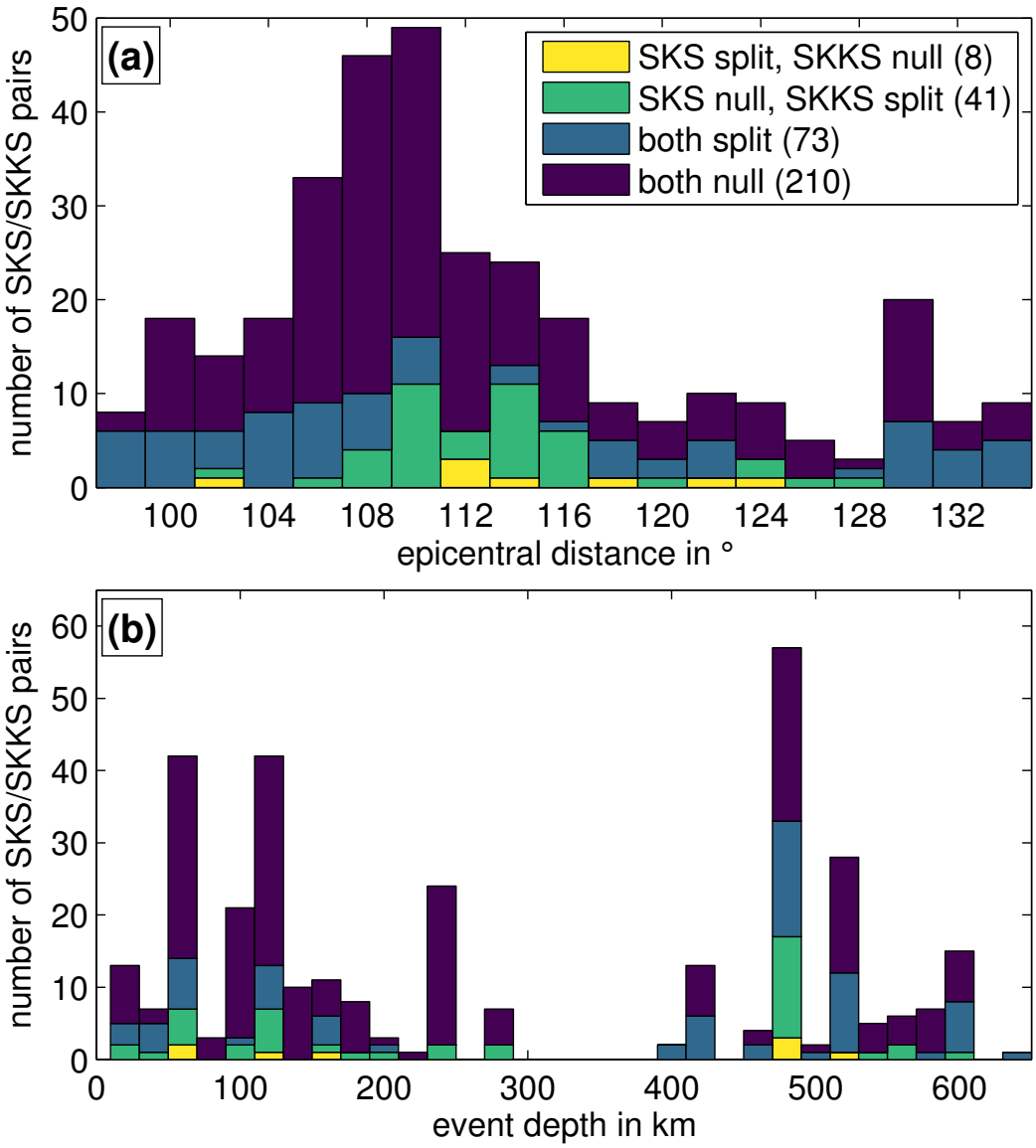

Figure 6.6: (a) Distribution of epicentral distances for all *SKS-SKKS* pairs based on the distance between epicenter and receiver. (b) Distribution of event depths for all *SKS-SKKS* pairs.

anomaly with consistent anisotropic properties (ϕ,δt), both phases could be equally split or not split (appendix D, Fig. D.4).

In order to detect any geographical correlation between the splitting discrepancies and large-scale lowermost mantle features, we summarize our results in Fig. 6.9 along with the GyPSuM global v_S tomography model (*Simmons et al.*, 2010) and the pierce points of the *SKS-SKKS* raypaths at 2700 km depth. Due to contributions from shallower anisotropy in the upper mantle, at most stations in our network the splitting pattern is not well-constrained or it indicates a non-simple nature of anisotropy (Fig. 6.3). Thus, we explicitly cannot correct for likely upper mantle contributions here as done in previous studies with more simple splitting characteristics (e.g. *Lynner and Long*, 2014). Nevertheless, the evaluation of measured ΔSI allows us to explore

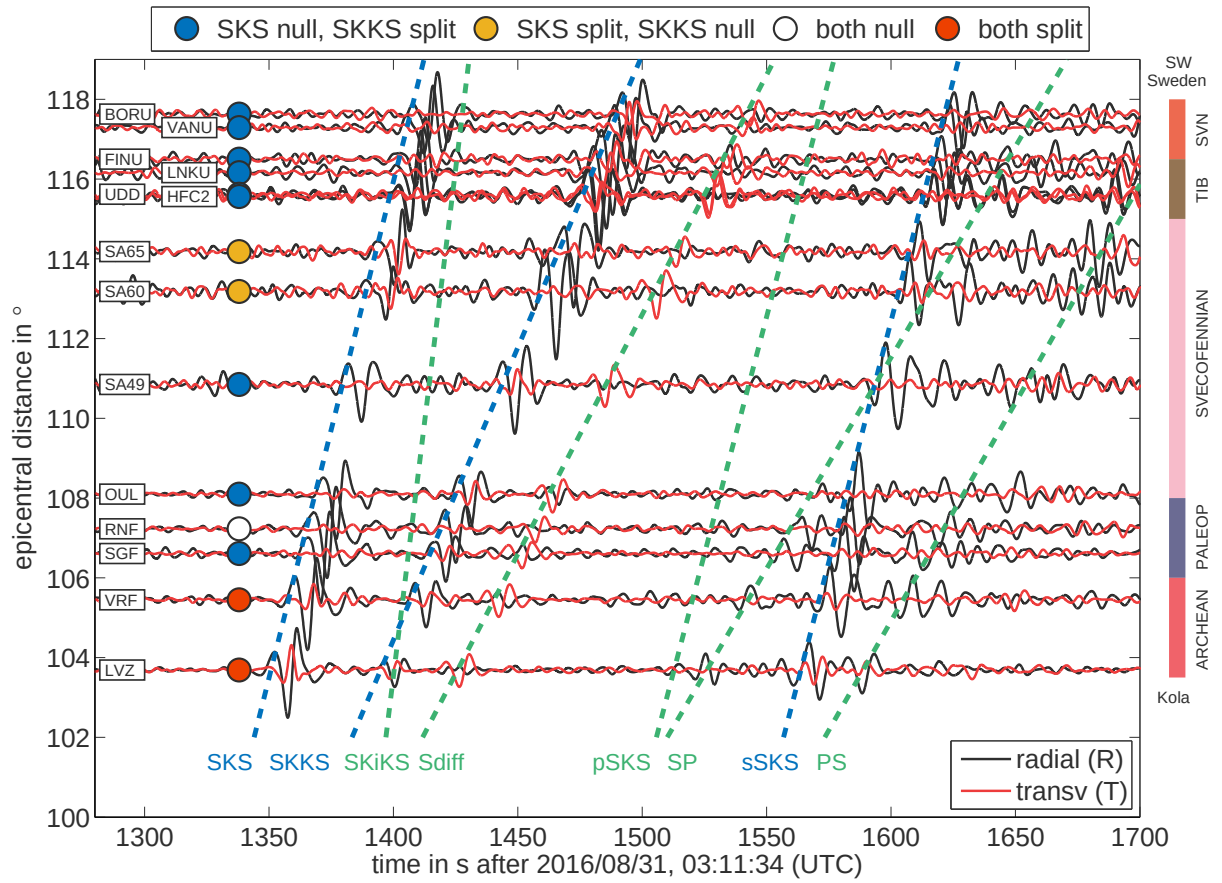

Figure 6.7: Record section with seismograms of the radial (black) and transverse (red) components of a Papua New Guinea event on 2016/08/31. Theoretical arrivals of different phases based on the iasp91 Earth model (*Kennett*, 1991) are shown as dashed lines. Blue indicates phases that were used in this study to probe lowermost mantle anisotropy (*SKS*, *SKKS* and *sSKS*) and green for phases that have similar arrival times. It is obvious that there is no major wave interference between different phases as the *SKS-SKKS* pairs have different arrivals that are well separated in time for the whole distance range. Colored circles display the characteristics for the *SKS-SKKS* pairs in the corresponding seismograms (null-split, split-null, null-null, split-split). On the right the geological units (*Gaál and Gorbatschev*, 1987; *Gorbatchev*, 2004) are shown at which the corresponding stations are sited. It is obvious that discrepant pairs are recorded across different units from southwestern Sweden (Sveconorwegian domain) up to northern Finland (Paleoproterozoic domain). As seen in more detail in appendix D, Fig. D.2 for *SKS* and *sSKS* the same pattern is observed. A map view of the stations and raypaths is shown in Fig. 6.12.

potential contributions of lowermost mantle anisotropy to the overall splitting signals (*Deng et al.*, 2017).

6.4.2 Geographic clusters in the lowermost mantle

From the locations of the D" pierce points, the anomalous pairs can be divided into a western and eastern region relative to the area of our station network (Fig. 6.9). As observed in previous *SKS-SKKS* studies, the pierce points of discrepant pairs are interleaved with non-discrepant ones that are mostly null/null observations (especially for phase arrivals from west). A possible explanation is that small-scale heterogeneity of anisotropic structure is located along the slightly varying raypaths in the lowermost mantle (e.g. *Long*, 2009; *Long and Lynner*, 2015). This

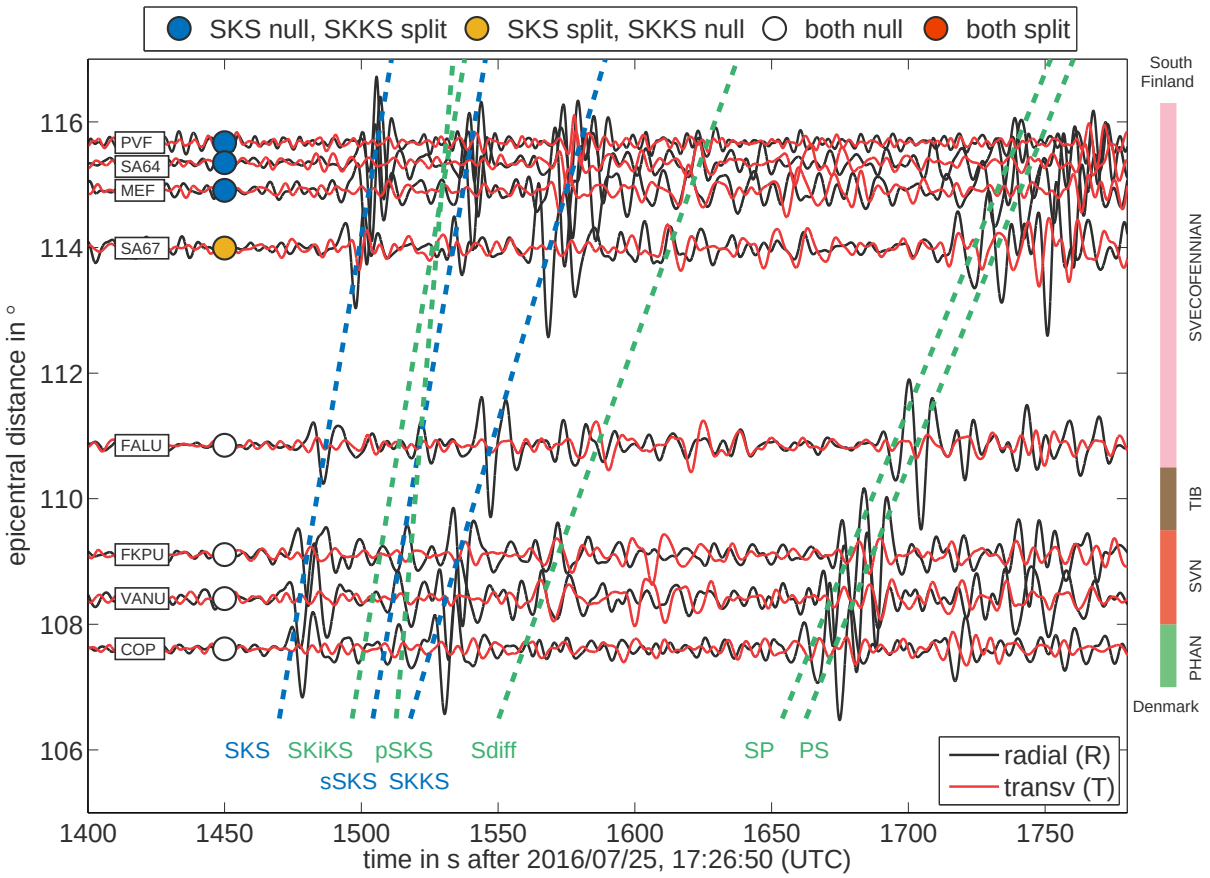

Figure 6.8: Record section with seismograms of the radial (black) and transverse (red) components of a Chile event on 2016/07/25. Theoretical arrivals of different phases based on the iasp91 Earth model (*Kennett*, 1991) are shown as dashed lines. Blue indicates phases that were used in this study to probe lowermost mantle anisotropy (*SKS*, *SKKS* and *sSKS*) and green for phases that have similar arrival times. It is obvious that there is no major wave interference expected for the *SKS-SKKS* pairs since the different arrivals are well separated for the whole distance range. Colored circles display the characteristics for the *SKS-SKKS* pairs in the corresponding seismograms (null-split, split-null, null-null, split-split). On the right the geological units (*Gaál and Gorbatschev*, 1987; *Gorbatchev*, 2004) are shown at which the corresponding stations are located. A map view of the stations and raypaths is shown in Fig. 6.12.

assumption is supported by findings of velocity changes in D" within very short length scales (e.g. *Weber and Körnig*, 1992; *Weber*, 1993). However, although the *SKS* and *SKKS* pierce points of each individual pair are separated by more than 800 km from each other (Fig. 6.10) the Fresnel zones of *SKS* and *SKKS* in the lowermost mantle also encompass areas of several hundred kilometers and therefore overlap for neighboring discrepant and non-discrepant pairs. This is one of the most puzzling points in almost all *SKS-SKKS* studies published so far and a plausible explanation is still missing. Future work should be concentrated on the synthetic reconstruction of *SKS-SKKS* discrepancies using full waveform modeling techniques to also consider finite-frequency effects (*Tesoniero et al.*, 2017).

For the eastern region we observe two types of discrepant splitting pairs. The first, is a set of 22 pairs with split *SKKS* phases and clear nulls for *SKS*. The split *SKKS* phases sample the lowermost mantle roughly along an east-west transect (65°N, 60°-92°E) near the edges of a

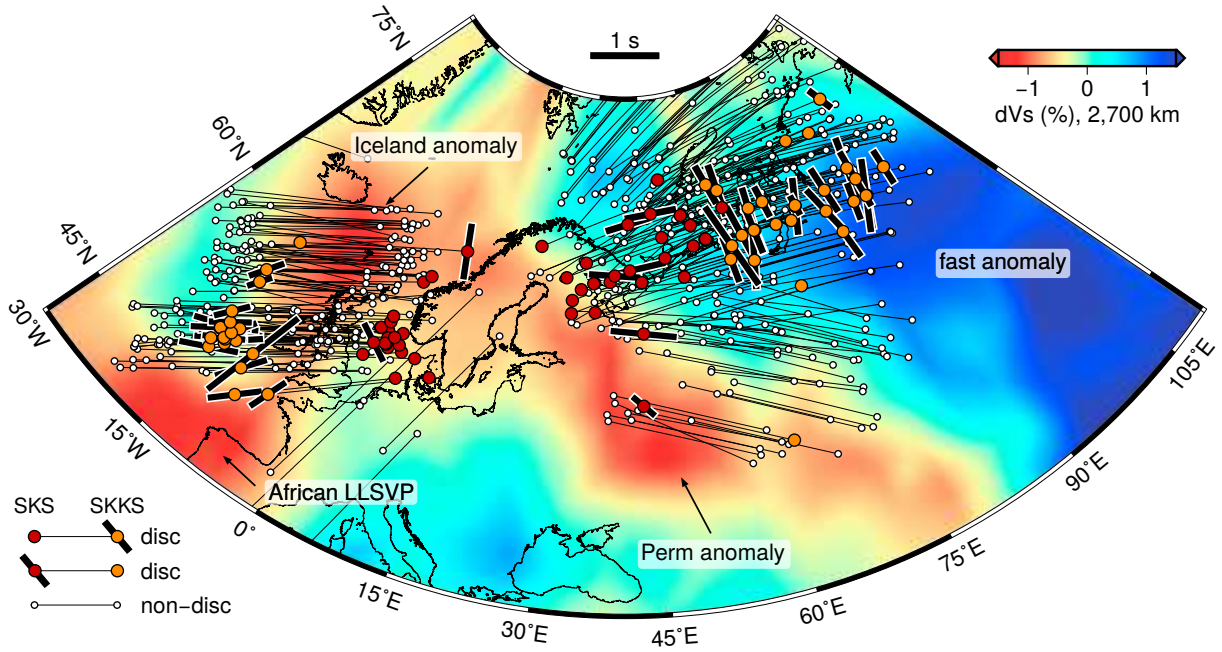

Figure 6.9: D" pierce points of *SKS-SKKS* pairs calculated with the tauP toolkit based on the iasp91 Earth model (*Crotwell et al.*, 1999) atop the GyPSuM global v_S tomography model at 2700 km depth (*Simmons et al.*, 2010). Discrepant pairs are marked with red (*SKS*) and orange (*SKKS*) dots, the split phase is indicated with a black bar oriented in the direction of ϕ and scaled by δt (as observed at the station). Related pierce points are connected by thin black lines. White dots indicate non-discrepant pairs.

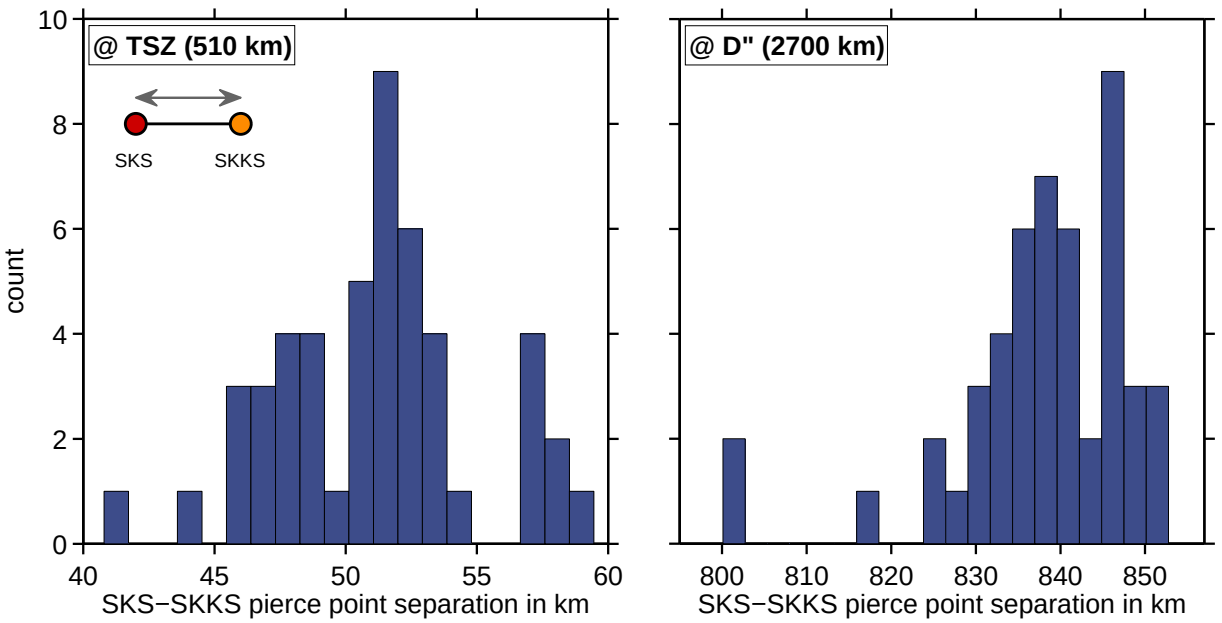

Figure 6.10: Separation distances between *SKS-SKKS* pierce points in the transition zone (TSZ, left panel) and in 2700 km depth (D", right panel) calculated on a sphere with the corresponding radius (see also Figs. 6.5 and 6.9).

major fast-v_S anomaly in D" beneath northwestern Siberia (Fig. 6.9). Besides having nearly consistent orientations for ϕ (average 5.3°), the majority of pairs have

ΔSI is > 0.4 (Fig. 6.11). Moreover, these pairs were recorded at stations that are located on different geological units from southwest Sweden up to northern Finland (Figs. 6.7, 6.8 and 6.12). Therefore, such a consistent splitting pattern indicates a large-scale feature of uniform lowermost mantle anisotropy beneath northwestern Siberia that is observed independently from structures directly underneath the network. In contrast, the second group in the east consists of six pairs with split *SKS* and nulls for *SKKS*. Beyond that, the orientations for with nearly east-west alignments differ significantly compared to the first group. The *SKS* pierce points in D" are located within a narrow north-south swath (60°-72°N, 45°E) that encompasses areas with strong variations in v_S. The two split *SKS* phases in the south fall into a region of anomalously low v_S that is known as Perm anomaly (Fig. 6.9).

Within the western cluster most pierce points of the split *SKKS* phases cover a nearly north-south oriented area in the lowermost mantle beneath the Atlantic west of UK and northwest of France. For the orientations of ϕ (only split *SKKS*) we also determined consistent directions (average of 39°) whereas δt varies with values ranging from 0.7 s up to 2.1 s. As in the eastern cluster, ΔSI values, which are mostly > 0.4, provide evidence for a contribution from lowermost mantle anisotropy (Fig. 6.11). Most non-discrepant pairs show clear nulls for both phases. A considerable number of the corresponding pierce points are located close to or within the slow-v_S anomaly beneath Iceland.

6.4.3 Nature of anisotropy below Siberia

Below Siberia several global tomography models (including GyPSuM) agree in terms of showing relatively fast v_S (*Shepard et al.*, 2017, Fig. 6.13). This anomaly was interpreted as a remnant of paleo-subducted slab material that is reaching down to the CMB (*Van der Voo et al.*, 1999). This hypothesis is supported by previous (source- and receiver-side corrected) *S-ScS* splitting that revealed a dipping symmetry axis for the anisotropic fabric in a neighboring area (*Wookey and Kendall*, 2008). Furthermore, in a common geographical reference frame, the estimated orientation for ϕ is similar to ours for a nearly east-west raypath (Fig. 6.11). From geodynamic modeling it has been shown that sinking slab material can imprint strong strain-induced anisotropy at the base of the lower mantle (e.g. *McNamara et al.*, 2002; *Nowacki et al.*, 2010; *Cottaar et al.*, 2014). Such a scenario is mainly controlled by the lattice-preferred orientation (LPO) of lower-mantle minerals such as post-perovskite (e.g. *Merkel et al.*, 2007; *Nowacki et al.*, 2010). Therefore, we infer that our discrepant *SKS-SKKS* observations indicate a widespread, so far unsampled region of coherent LPO-induced anisotropy in D", caused by downwelling slab material that impinges on the CMB beneath Siberia (Fig. 6.15).

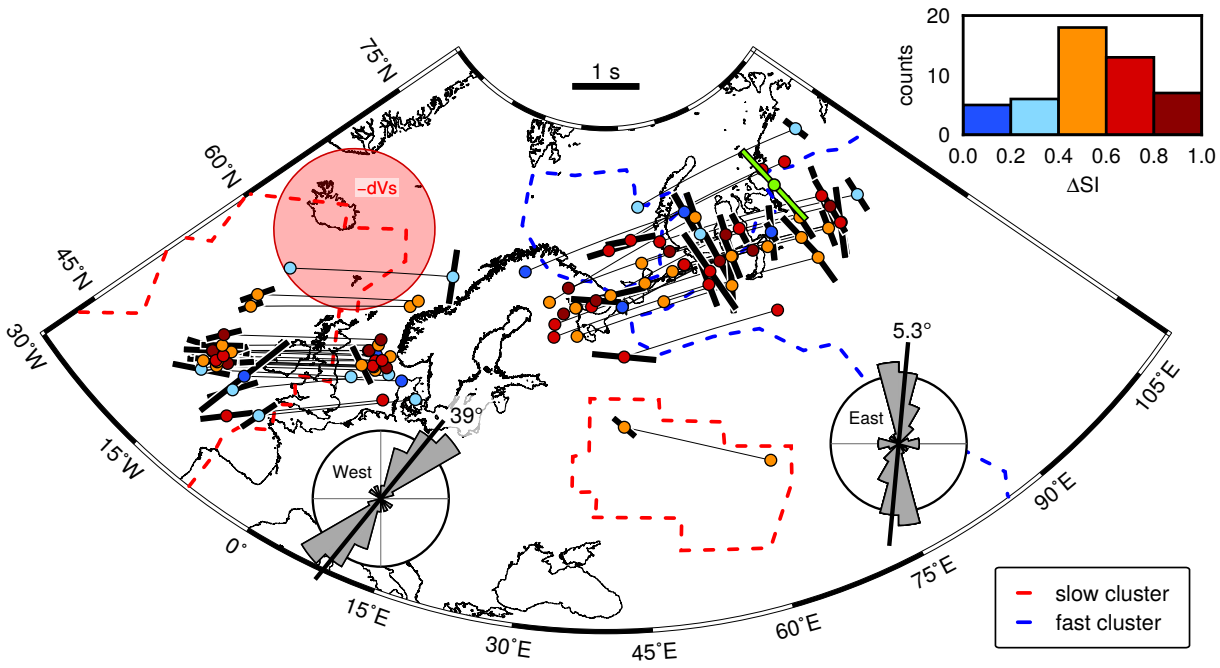

Figure 6.11: D" pierce points of the discrepant *SKS-SKKS* pairs along with the measured ΔSI values (filling of dots). The histogram highlights the number of observations binned in steps of 0.2. Rose plots indicate the distribution of ϕ for the split phases, separated into western and eastern cluster. The averages of the split *SKKS* phases for east and west are shown as black bars with ϕ_{mean} = 5.3° (east) and ϕ_{mean} = 39° (west) The green bar displays observed ScS splitting after *Wookey and Kendall* (2008). Red and blue dotted lines encompass regions of model agreement regarding slow (*Lekic et al.*, 2012, see also Fig. 6.14) and fast v_S (*Shepard et al.*, 2017, see also Fig. 6.13). The dimension of the indicated slow-v_S zone beneath Iceland (*He et al.*, 2015) is shown as red circle.

However, so far we cannot fully constrain the geometry of the anisotropic region due to limited ray coverage (except for events from the South Pacific area) and the observed ϕ-δt variations at most of our stations (Fig. 6.3). Moreover, it remains unclear whether a change in the geometry or the mechanism of anisotropy is responsible for the significant difference in ϕ between the split *SKS* and *SKKS* phases. Nevertheless, based on significant ΔSI values (Fig. 6.11), we can demonstrate that a component of lowermost mantle anisotropy contributes to the overall splitting signal.

6.4.4 Anisotropic source beneath the Atlantic

Different global tomography models (including GyPSuM) consistently show anomalously low v_S and strong lateral velocity gradients from fast to slow seismic velocities along the northern edges of the African LLSVP beneath the Atlantic (*Lekic et al.*, 2012, Fig. 6.14). Beyond that, for some models also a potential connection between the African LLSVP and a 250-650 km-wide region of heavily reduced v_S ($\sim$ -6% to -10%, Fig. 6.11) in D" below Iceland is detectable (e.g. *Helmberger et al.*, 1998; *He et al.*, 2015). The connection is located in the so-far poorly sampled area of our 19 split *SKKS* observations as far north as $\sim$ 50°N (Fig. 6.9). These splitting observations are in good agreement with results of previous studies, suggesting strong

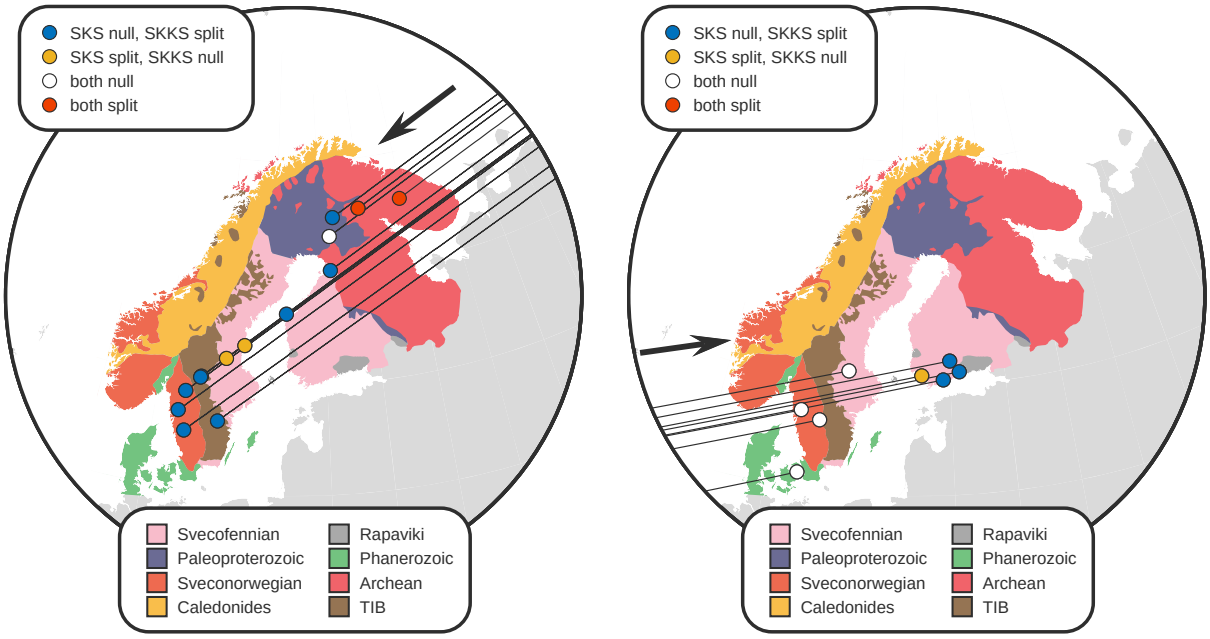

Figure 6.12: Locations of recording stations shown in Figs. 6.7 and 6.8 atop the simplified geological units of Fennoscandia (*Gaál and Gorbatschev*, 1987; *Gorbatchev*, 2004). The raypaths (thin black lines) for the events below Papua New Guinea on 2016/08/31 (left) and Chile on 2016/07/25 (right) as well as the directions of the arriving wavefronts (black arrows) are shown.

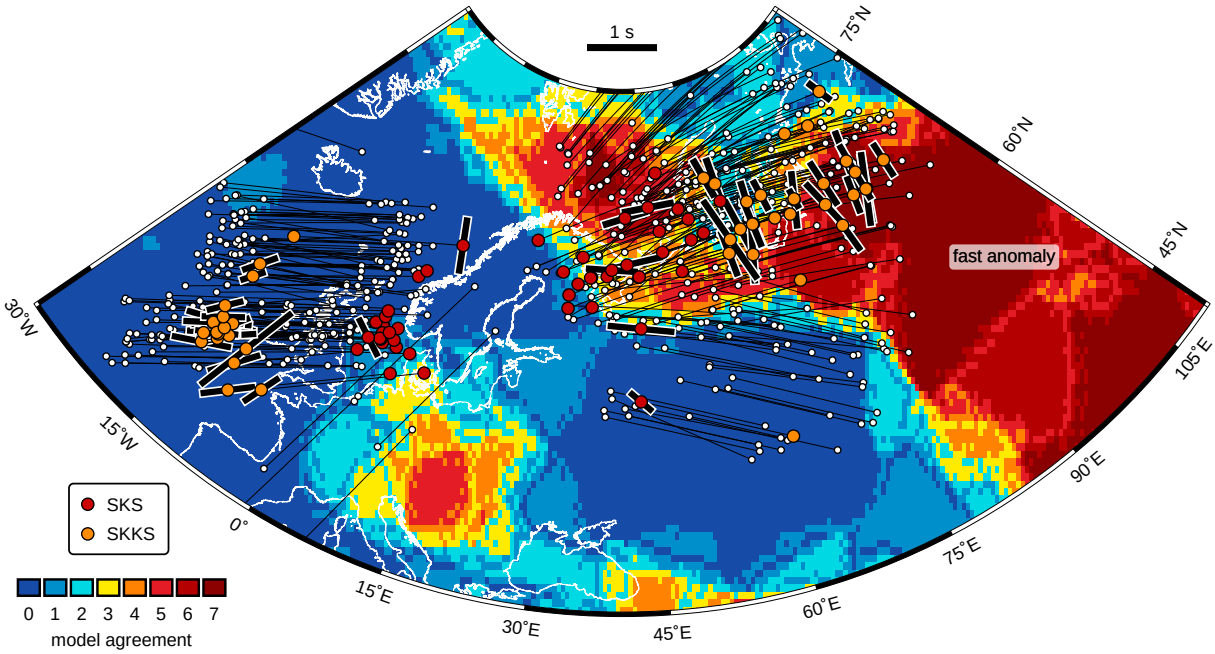

Figure 6.13: *SKS-SKKS* pierce points at 2700 km depth, calculated with the tauP toolkit (*Crotwell et al.*, 1999) and the iasp91 Earth model (*Kennett*, 1991), atop of the vote map analysis of *Shepard et al.* (2017). This vote map displays agreement between different global tomography models with respect to faster than average seismic shear wave velocities (for details see *Shepard et al.*, 2017). Discrepant pairs are marked with red (*SKS*) and orange (*SKKS*) dots, the split phase is indicated with a white bordered black bar oriented in the direction of the fast axis ϕ and scaled by the delay time δt (as observed at the station). Related pierce points are connected by thin black lines. White dots indicate non-discrepant pairs (either both are split or both are null). This figure implies that anisotropy in the lowermost mantle beneath northwestern Siberia is located along the edges of a fast anomaly that is observed in all seven tomography models.

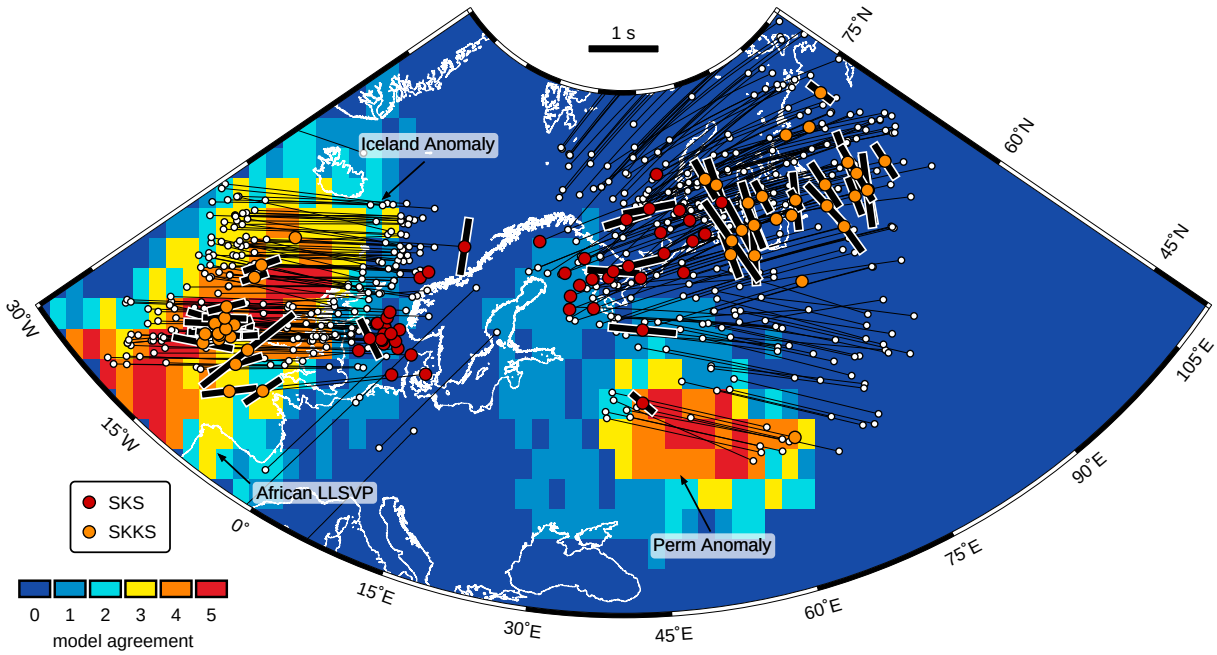

Figure 6.14: *SKS-SKKS* pierce points at 2700 km depth, calculated with the tauP toolkit (*Crotwell et al.*, 1999) and the iasp91 Earth model (*Kennett*, 1991), atop of the cluster analysis of *Lekic et al.* (2012) in the lower mantle. The cluster analysis displays agreement between different global tomography models with respect to slower than average seismic shear wave velocities (for details see *Lekic et al.*, 2012). Discrepant pairs are marked with red (*SKS*) and orange (*SKKS*) dots, the split phase is indicated with a white bordered black bar oriented in the direction of the fast axis ϕ and scaled by the delay time δt (as observed at the station). Related pierce points are connected by thin black lines. White dots indicate non-discrepant pairs (either both are split or both are null). This figure implies that anisotropy in the lowermost mantle is located along the edges of a connection between the northern extension of the African LLSVP and a slow velocity anomaly below Iceland.

and complex anisotropy along the edges of LLSVPs and of meso-scale structures of similar character (e.g. *Long and Lynner*, 2015; *Deng et al.*, 2017). In general, this anisotropy is assumed to be induced by complex mantle flow toward the boundaries of the low-v_S zones (e.g. *Cottaar and Romanowicz*, 2013). The absence of splitting within these zones, however, may indicate vertical mantle flow that feeds the upwelling hot mantle plume beneath Iceland (Fig. 6.15, *Helmberger et al.*, 1998; *He et al.*, 2015). Taking into account the overall splitting pattern at our long-running permanent stations (Fig. 6.3), for most *SKS* phases from South American earthquakes we received clear nulls indicating no contributions from upper mantle anisotropy for these raypaths. In contrast, the *SKKS* phases of the same events exhibit consistent splitting with nearly the same orientation for ϕ. Such a scenario allows us to suppose that the orientation of ϕ (measured at the stations) mirrors the true direction of the anisotropy fast axis in the lowermost mantle without further influence from the upper mantle. Therefore, our striking observations of mainly $\Delta SI > 0.4$ in this area (Fig. 6.11) support the idea that anisotropy is also located along the edges of the northern extensions of the African LLSVP towards the low-v_S anomaly beneath Iceland.

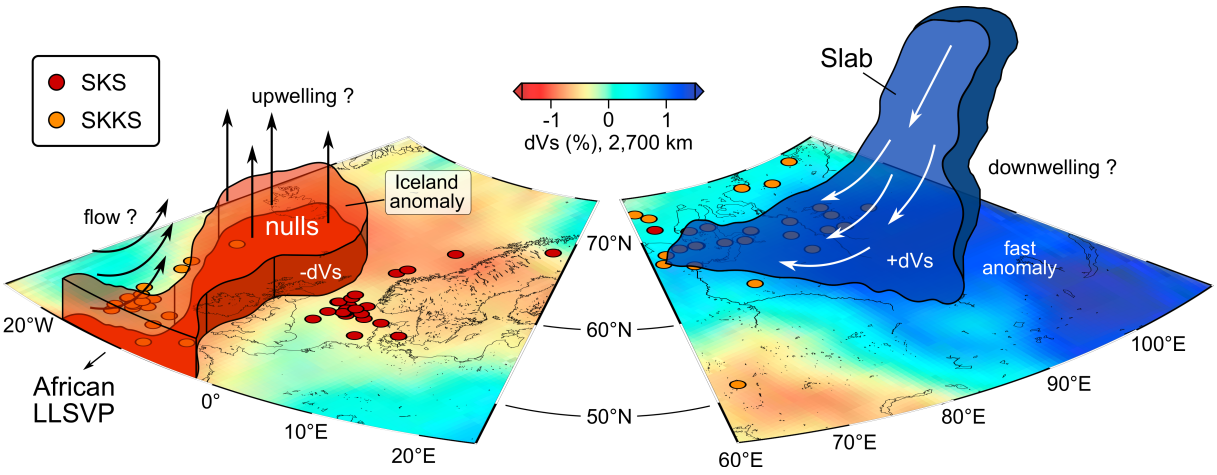

Figure 6.15: Interpretation of our findings based on two of the most plausible sources of D" anisotropy. Beneath the Atlantic, nearly horizontal mantle flow potentially induces anisotropy along the northern extensions of the African large low-shear-velocity province (LLSVP) toward the Iceland anomaly. Absence of splitting (null) is observed for the majority of measurements that correspond to pierce points located within the Iceland anomaly and potentially indicates vertical flow. Beneath Siberia downwelling (colder than average) material of a subducted slab imprints anisotropy in a widespread area atop the core-mantle boundary.

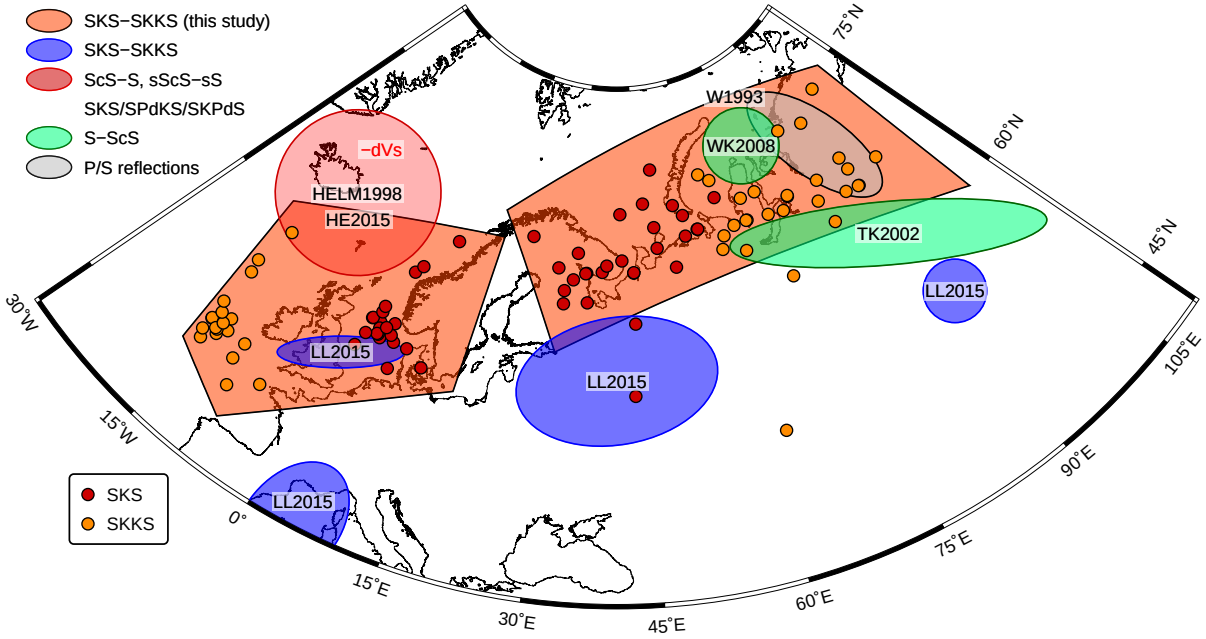

Figure 6.16: Overview about areas in which anomalous lowermost mantle structure was observed based on different seismic phase types. The two large patches colored in orange encompass the regions identified in this study based on *SKS-SKKS* splitting discrepancies. Red and orange circles indicate the *SKS-SKKS* pierce points at 2700 km depth, calculated with the tauP toolkit (*Crotwell et al.*, 1999) and the iasp91 Earth model (*Kennett*, 1991). Blue areas show regions of discrepant *SKS-SKKS* observations that were attributed to lowermost mantle anisotropy after a correction for (known) shallower anisotropy (*Long and Lynner*, 2015). The red circle shows the estimated dimension of the indicated slow shear velocity zone beneath Iceland based on *SKS/SPdKS/SKPdS* waveform interference analysis (*Helmberger et al.*, 1998) and *ScS-S* and *sScS-sS* differential traveltime residuals (*He et al.*, 2015). Green patches indicate areas where *ScS-S* splitting was used to constrain D" anisotropy that was associated with paleo-subduction (*Thomas and Kendall*, 2002; *Wookey and Kendall*, 2008). An area of anomalous *P*- and *S*-wave reflections at the D" is shown as gray ellipse (*Weber*, 1993)

6.5 Conclusions

Benefiting from a dense and large-aperture recording network in Scandinavia, we are able to explore two widespread areas on the fragmentary global map of lowermost mantle anisotropy beneath the Atlantic and northwestern Siberia. While previous studies sampled several smaller, partly overlapping patches of the lowermost mantle, with our observations of clearly discrepant *SKS-SKKS* splitting pairs we can draw a more complete picture of the whole area (Fig. 6.16) although the geometry and mechanism of the anisotropic D" fabrics cannot be fully derived from our results alone. Nevertheless, this demonstrates that the ongoing deployment of dense and large-aperture seismic networks not only helps in understanding the anisotropic structure directly beneath a station itself but can also reveal valuable and sorely needed information about extensive and dynamically active regions in D" relatively far away from the receiver.

Especially the lowermost mantle area beneath Siberia might be explored in much more detail in future. Seismic data of other large-aperture networks such as AlpArray (*Hetényi et al.*, 2018) or the Transportable Array deployment in Alaska and western Canada are partly already available or will be accessible in the near future. Depending on the source-receiver distances, *SKS* and *SKKS* phases recorded at these networks are not able to sample the D" layer beneath Siberia. Therefore, the focus should lie on differential *S-ScS* splitting analysis. For events in the Hindu-Kush region the CMB bounce points of *ScS* are roughly located in the target region beneath Siberia, halfway between the earthquake locations and the AlpArray station network. Similarly, *ScS* phases of events along the Kuril Arc that are recorded in Alaska have their CMB bounce points in nearly the same area. According to the previously conducted *S-ScS* study of *Wookey and Kendall* (2008) this would allow to explore two crossing raypath directions which might help to improve the knowledge about the geometry of this anomaly.

Acknowledgements

This work has received funding from DFG (Deutsche Forschungsgemeinschaft) via LITHOSCAPP (RI1133/11-1 and -2). Seismic data were obtained from the data centers GeoForschungsNetz (GEOFON), Observatories and Research Facilities for European Seismology (ORFEUS), Incorporated Research Institutions for Seismology (IRIS, USA), and SEIS-UK as well as University of Helsinki and the Swedish National Seismic Network (SNSN). Devices for the German contribution to ScanArray were provided by the German Research Centre for Geosciences (GFZ) Geophysical Instrument Pool Potsdam (GIPP). Maps were prepared using Generic Mapping Tools (GMT *Wessel et al.*, 2013). Abundant helpful comments on the manuscript by T. Hertweck and three anonymous reviewers are acknowledged.

7 Characterization of the anisotropy beneath Fennoscandia

In this chapter I present the main part of the analysis and modeling work conducted for characterizing seismic anisotropy beneath Fennoscandia. First, an overview about the tectonic evolution of Fennoscandia and previous shear wave splitting studies in this area is given, followed by a detailed splitting analysis of the 266 seismic stations described and shown in chapter 3. Finally, anisotropic models for most of the stations are determined which best could describe the data, integrated within a discussion in which previous work and the tectonic setting is highlighted. A publication for the contents of this chapter is in preparation.

7.1 Introduction

Seismic anisotropy is one of the key tools to investigate dynamic-driven processes in the Earth's interior. In this context the anisotropic signatures can provide valuable information about current and past deformation processes or mantle flow in the Earth's crust as well as the upper and lowermost mantle (e.g. *Babuška and Cara*, 1991; *Savage*, 1999; *Fouch and Rondenay*, 2006; *Long and Silver*, 2009). The development of seismic anisotropy can be caused by different mechanisms which are mainly depth-dependent. While layering of material with different elastic properties and fluid-filled fractures (so-called shape-preferred orientation, SPO) are mostly responsible for shallow-depth anisotropy in the crust (e.g. *Backus*, 1962; *Crampin and Booth*, 1985), the lattice-preferred orientation (LPO) of intrinsically anisotropic minerals like olivine (e.g. *Zhang and Karato*, 1995; *Karato et al.*, 2008) is assumed to make the largest contributions in the upper mantle (e.g. *Silver*, 1996; *Long and Becker*, 2010). Similarly, in the lowermost 200-300 km of the mantle (D" layer), just atop the core-mantle boundary (CMB), high-pressure phases of different minerals like magnesium silicate (post-perovskite) most likely play a major role for the formation of seismic anisotropy (e.g. *Murakami et al.*, 2004; *Merkel et al.*, 2007). Alternatively, partial melt, aligned due to deformation, can cause SPO anisotropy in D" (e.g. *Kendall and Silver*, 1996). In contrast, most parts of the lower mantle in general are assumed to be nearly isotropic (e.g. *Meade et al.*, 1995).

A shear wave that propagates through a volume of anisotropic material is split into two orthogonally polarized shear waves that travel with different speeds, polarized in the fast and slow directions of the medium (*Silver and Chan*, 1991; *Savage*, 1999; *Long and Silver*, 2009).

The orientation of the fast polarization axis direction (ϕ) and the delay time (δt), accumulated between the two split waves, are known as the splitting parameters. They can be measured at a seismic recording station at the Earth's surface. Commonly core-refracted shear waves like *SKS*, *SKKS* or *PKS* are used to constrain the anisotropy. Their radial polarization after the *P*-to-*S* conversion at the CMB ensures that the splitting, if observed, appeared on the receiver side of the travel path. Furthermore, the initial polarization of core-refracted phases coincides with the event backazimuth (BAZ) and is therefore a known quantity (e.g. *Savage*, 1999). Due to their nearly vertical propagation paths, splitting measurements of these phases made at dense recording networks provide very good lateral resolution. In contrast, the depth location of the anisotropic medium between CMB and surface cannot be determined from individual splitting observations alone. Comparisons with estimates from surface wave data (e.g. *Yuan and Beghein*, 2014; *Zhu and Tromp*, 2013) as well as discrepancies between phases measured in the same seismogram (e.g. *SKS* and *SKKS*), however, can give us a hint toward the depth range of the anisotropy (e.g. *Hall et al.*, 2004; *Lynner and Long*, 2012; *Grund and Ritter*, 2019). Although splitting measurements are often associated with only a single, horizontal layer of anisotropy, variations of ϕ and δt with respect to the backazimuth and incidence angle indicate more complex structures (e.g. *Silver and Savage*, 1994; *Hartog and Schwartz*, 2000; *Marson-Pidgeon and Savage*, 2004). Depending on the complexity, characteristic patterns of measured apparent splitting parameters allow to identify the underlying anisotropy.

The present-day shape of the Fennoscandian peninsula (Fig. 7.1) was formed during several collision and rifting events within the last 3 Ga, each affecting comprehensive reworkings of the lithosphere and the surface. A major tectonic episode, the Caledonian orogeny, was initiated around 500 Ma ago by the closing of the Iapetus Ocean. In the following, the Caledonian mountain belt was formed due to the collision of the paleo-continents Laurentia and Baltica/Avalonia 430-410 Ma ago (e.g. *McKerrow et al.*, 2000; *Roberts*, 2003; *Torsvik and Cocks*, 2005). Furthermore, it is well accepted that Baltica was partially westward subducted beneath Laurentia during the orogenesis (e.g. *Krogh*, 1977; *Roberts*, 2003; *Gee et al.*, 2008). Finally, the opening of the North Atlantic Ocean around 55 Ma ago separated the Caledonides whose fragments in present are located along the western rim of Fennoscandia as well as in North America, Greenland and Scotland. Remnants of the mostly eroded Caledonides form part of the Scandinavian Mountains (Scandes) with large nappes covering the western edge of Baltica (Fig. 7.1, e.g. *Gaál*, 1986; *Gaál and Gorbatschev*, 1987). The Scandes are located at a passive continental margin which spans along the western rim of Fennoscandia, far away from active plate tectonics. However, the topography of the mountain chain with elevations of up to 2000-2500 m (especially in the south) is still higher than expected for such an old orogen (e.g. *Nielsen et al.*, 2009) and therefore processes within the Earth's mantle most likely play an important role in explaining the current shape of the Scandes (for a review see e.g. *Maupin et al.*, 2013). Prior to the Caledonian orogeny, the Baltic Shield with its Archean, Svecofennian and Sveconorwegian provinces

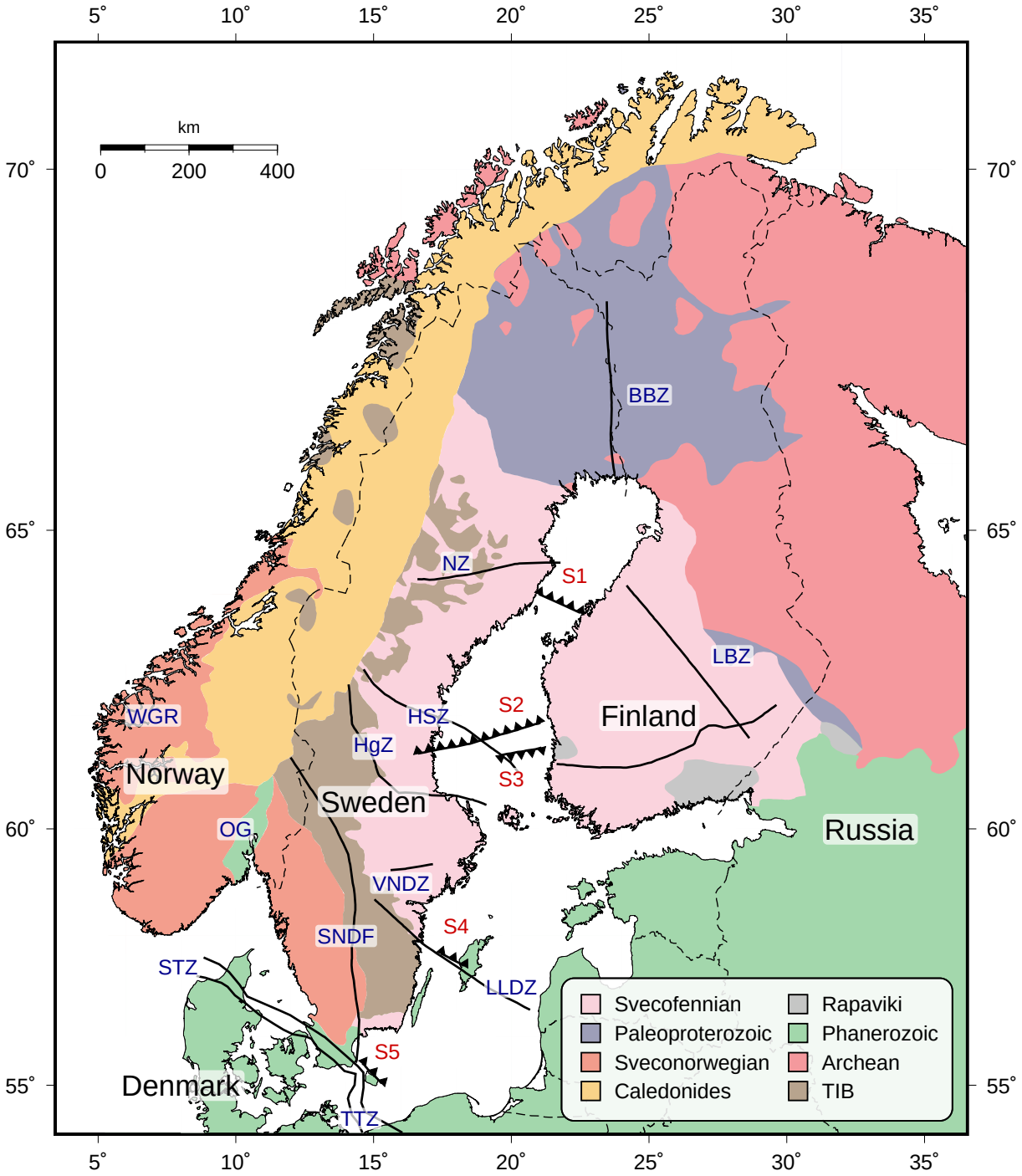

Figure 7.1: Simplified geological/tectonic map of Fennoscandia and surrounding areas after *Gorbatchev* (2004) and *Korja and Heikkinen* (2005). Locations of deformation zones (sutures, shear zones) are shown as black lines, inferred subduction zones are indicated by black "sawtooth" lines with the pike pointing into the assumed subduction direction. Abbreviations (blue and red labels): *BBZ*, Baltic Bothnian megashear zone; *HgZ*, Hagsta deformation zone; *HSZ*, Hassela shear zone; *LBZ*, Ladoga-Bothnian Bay zone; *LLDZ*, Loftahammar, Linköping deformation zone; *NZ*, Nickel zone; *OG*, Oslo Graben; *S1-S5*, inferred subduction zones; *STZ*, Sorgenfrei-Tornquist Zone; *SNDF*, Sveconorwegian deformation zone; *TTZ*, Teisseyre-Tornquist Zone; *VNDZ*, Vingåker-Nyköping deformation zone; *WGR*, Western Gneiss Region. *TIB* stands for Transscandinavian Igneous Belt. Dashed black lines indicate national borders.

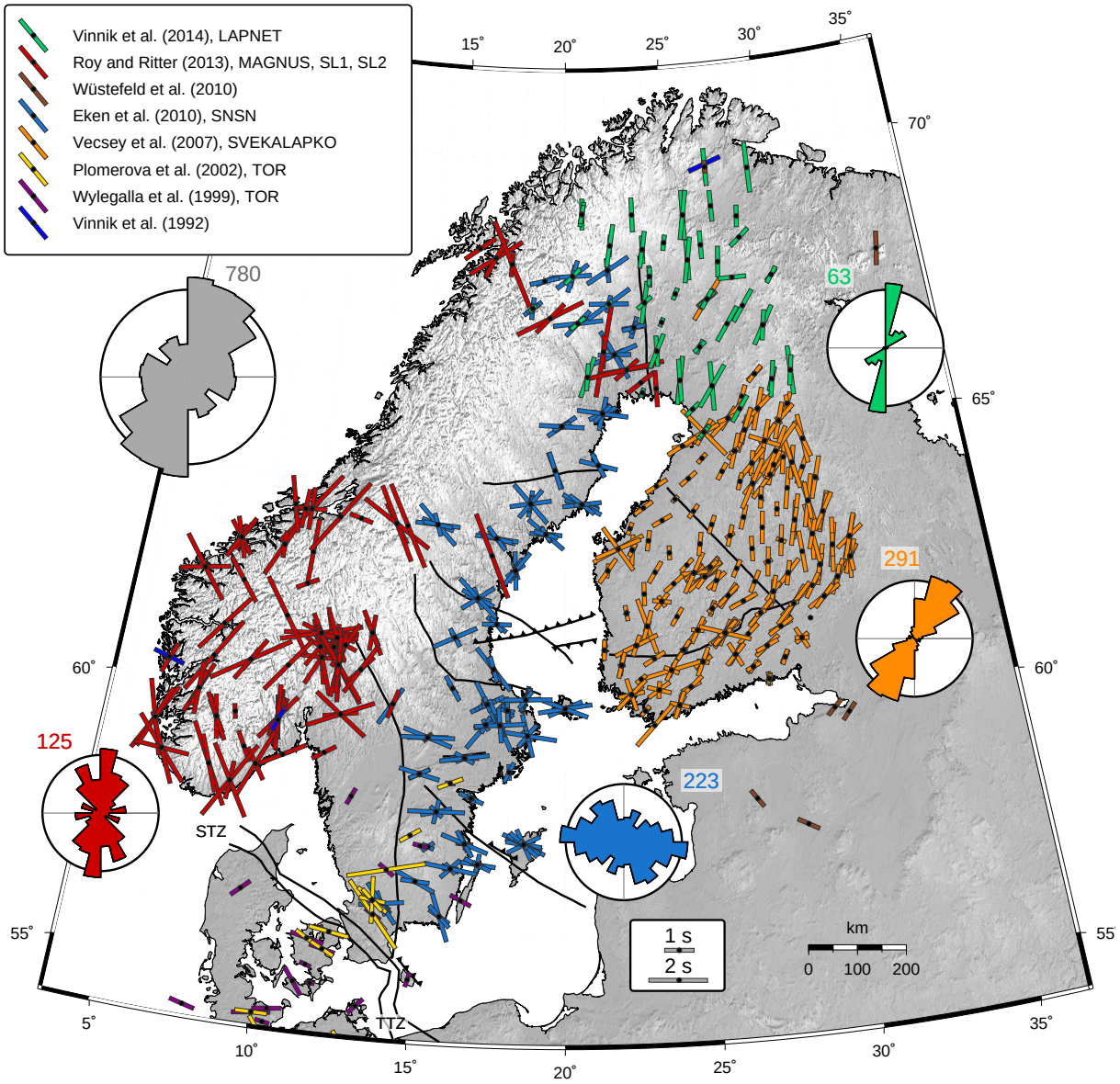

Figure 7.2: Overview of previous shear wave splitting studies in Scandinavia and surrounding areas: 1) LAPNET data in northern Finland (*Vinnik et al.*, 2014). 2) MAGNUS, SCANLIPS and SCANLIPS2 (*Roy and Ritter*, 2013). 3) Single measurements while studying the East European Craton (*Wüstefeld et al.*, 2010). 4) Detailed analysis of the SNSN data from 2002 to 2008 (*Eken et al.*, 2010). 5) SVEKALAPKO project in central and southern Finland. Data coverage is partly limited to a few month and some permanent seismic stations were included (*Vecsey et al.*, 2007). 6) TOR data were analyzed, only results for stations in Scandinavia are shown (*Plomerová et al.*, 2002a). 7) Also TOR data were analyzed, only results for stations in Scandinavia are shown (*Wylegalla et al.*, 1999). 8) Single measurements from early global seismic network (*Vinnik et al.*, 1992). The total number of splitting measurements as well as the overall splitting trends for the fast axis ϕ are shown in the gray colored roseplot. Additional roseplots indicate the trends of the four largest studies. Note the different projections of the map and the roseplots. Delay time information is given per seismic station since the bars for the individual measurements are scaled by δt (lengths of gray bars in legend are valid for all shown measurements). Null measurements (if available) are not included in this figure since in most of the studies they were not considered for modeling or interpretation. *STZ* stands for Sorgenfrei-Tornquist Zone and *TTZ* for Teisseyre-Tornquist Zone.

(Fig. 7.1) grew during several collisional phases including the accretion of individual microplates and oceanic arcs (e.g. *Gaál and Gorbatschev*, 1987; *Lahtinen et al.*, 2005; *Korja et al.*, 2006). Dipping reflectors observed in data of reflection seismic profiles were partly interpreted as relicts of paleo-subduction (e.g. *BABEL Working Group*, 1990; *Balling*, 2000). In the southwest the Sorgenfrei-Tornquist Zone (STZ) separates the Precambrian Baltic Shield from the Phanerozoic terranes of central Europe (e.g. *Berthelsen*, 1992; *Zielhuis and Nolet*, 1994). The generally NW-SE oriented STZ represents the northwestern extension of the Trans-European Suture Zone (TESZ) that resulted from the collision of Baltica with Avalonia slightly before the Caledonian orogeny started (e.g. *Pharaoh*, 1999; *Torsvik and Rehnström*, 2003). Each of these events caused a characteristic signature of deformation in the presence of compressional or extensional regimes. Seismic anisotropy can therefore be used to better understand past (and current) episodes of deformation within the different provinces of Fennoscandia.

The anisotropic structure beneath Fennoscandia and neighboring terranes, including the most western parts of the East European Craton (EEC) and the STZ suture zone, were repeatedly a subject of research in the last two decades. In this context shear wave splitting studies were mostly conducted in specific tectonically and geologically interesting areas with data of temporary seismological experiments. Fig. 7.2 gives an overview of past shear wave splitting studies in Scandinavia including the projects SVEKALAPKO in southern and central Svecofennia/Finland (*Vecsey et al.*, 2007), LAPNET in northern Finland (*Vinnik et al.*, 2014), MAGNUS, SCANLIPS, SCANLIPS2 (*Roy and Ritter*, 2013) and TOR (*Wylegalla et al.*, 1999; *Plomerová et al.*, 2002a) as well as measurements at seismic stations of the Swedish National Seismic Network (SNSN, *Eken et al.*, 2010) and single measurements from some other stations (*Vinnik et al.*, 1992; *Wüstefeld et al.*, 2010) of the early Global Digital Seismograph Network (GDSN)[14]. Besides shear wave splitting, partly also *P*-wave analysis and surface wave data were used to constrain the anisotropic pattern (e.g. *Plomerová et al.*, 2002b; *Pedersen et al.*, 2006). For larger scales, the measured shear wave splitting parameters can be compared with anisotropy models that cover most parts of Europe (e.g. *Zhu and Tromp*, 2013; *Zhu et al.*, 2015). Partly contradictory explanations were found for the anisotropy, ranging from the mostly preferred theory of fossil frozen-in anisotropy, represented by spatially varying signatures across the different accreted terranes of Fennoscandia (*Plomerová et al.*, 2001; *Plomerová et al.*, 2002a; *Plomerová et al.*, 2006; *Vecsey et al.*, 2007; *Eken et al.*, 2010; *Plomerová et al.*, 2011; *Munzarová et al.*, 2018), to multi-layered anisotropy with contributions also from asthenospheric mantle flow in northern Finland (*Vinnik et al.*, 2014). For southern Norway complex and deeply located anisotropy was inferred (*Roy and Ritter*, 2013) based on large delay times and fast axis orientation variations. Measurements at temporary stations along or close to the STZ mostly offered

[14] Data were taken from publications and the IRIS splitting database (*Wüstefeld et al.*, 2009; *IRIS DMC*, 2012; *Trabant et al.*, 2012), https://ds.iris.edu/ds/products/sws-dbs/, last accessed 11 January 2019

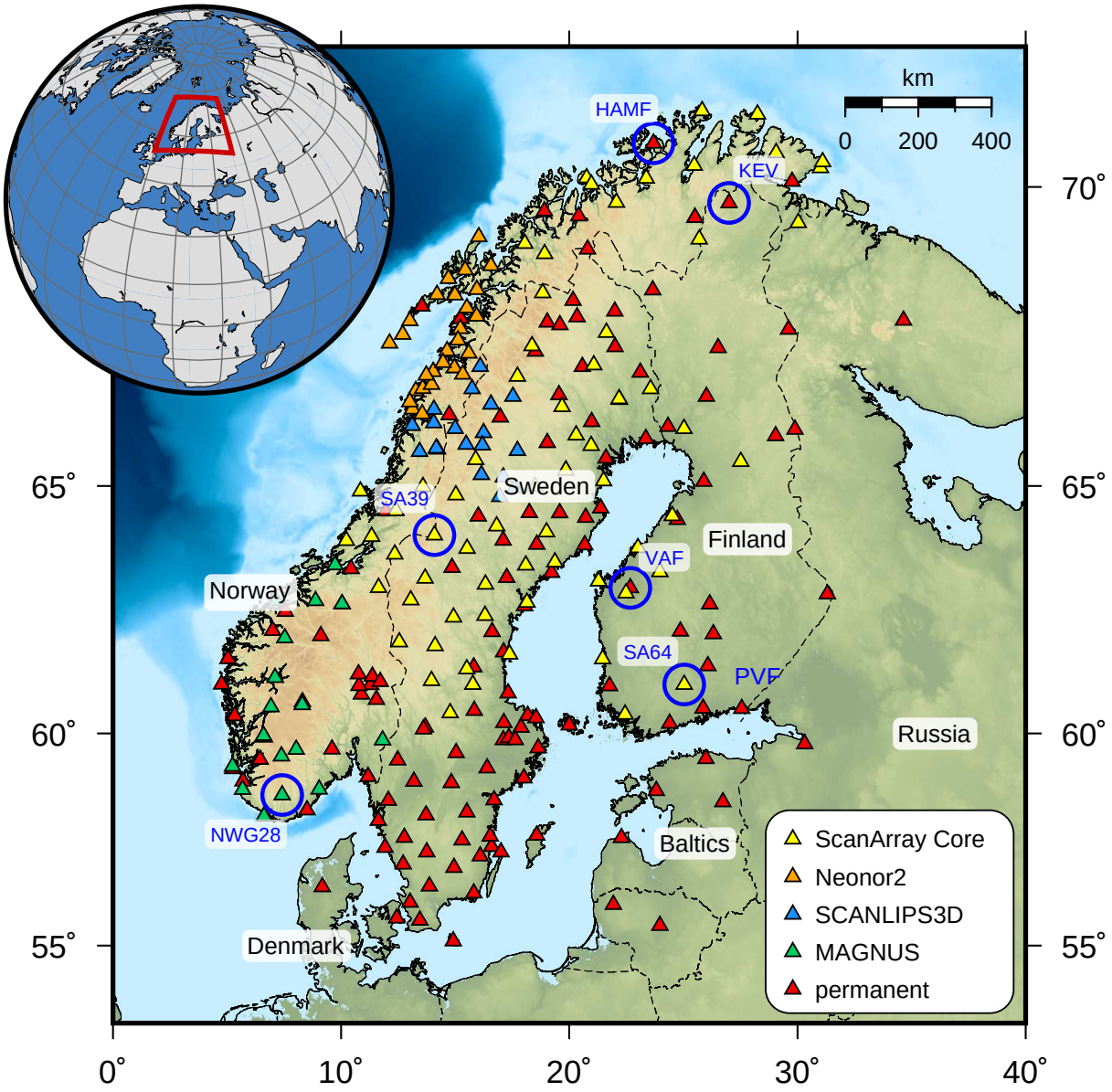

Figure 7.3: Distribution of seismic recording stations used in the shear wave splitting analysis. Color fill of the triangles indicates the different temporary (*Weidle et al.*, 2010; *Thybo et al.*, 2012; *Gradmann et al.*, 2014; *England et al.*, 2015; *Grund et al.*, 2017a) and permanent seismic station deployments that form the extended ScanArray network. Dashed lines indicate national borders. The six recording stations marked with blue circles (HAMF, KEV, NWG28, SA39, SA64 and VAF) are shown in detail in Fig. 7.12.

fast axis orientations parallel to the strike of the suture (*Wylegalla et al.*, 1999) which may be related to the collision between Avalonia and Baltica.

However, several open questions remain, related to the complexity and the spatial variability of seismic anisotropy beneath the different terranes of Fennoscandia. Based on a massive seismological data set acquired within the framework of the ScanArray initiative (Fig. 7.3) I conducted a systematic shear wave splitting analysis at 266 seismic broadband stations located across whole Fennoscandia and surrounding countries. For permanent stations that were previously analyzed, now additional 10 more years of continuous data are available in some cases.

With 6467 uniformly processed single-event shear wave splitting measurements (1772 splits and 4695 nulls) and 154 multi-event measurements I am able to constrain so far poorly or fully unresolved features related to deformation in this area. Furthermore, some blank spots along the northern Scandes are explored. At several stations (mostly long-running permanent ones) I can clearly model the observations with a dipping anisotropic fabric (only based on shear wave splitting measurements). Strong indicators for laterally varying anisotropy around the single stations are also found for individual areas. Some of the stations also show characteristics of a two-layer system. However, I cannot fully resolve a unique model that could explain both, the fast axis and delay times simultaneously. Together with new constraints from other methodologies based on ScanArray data, these observations will allow to answer open questions regarding the tectonic evolution of Fennoscandia.

7.2 Data and methods

I analyzed data of in total 266 seismic broadband recording stations for shear wave splitting (Fig. 7.3). Most stations were part of the international ScanArray initiative which includes the temporary deployments ScanArray Core (*Thybo et al.*, 2012; *Grund et al.*, 2017a), Neonor2 (*Gradmann et al.*, 2014) and SCANLIPS3D (*England et al.*, 2015). Inter-station distances were partly smaller than 50 km. Besides these three newly recorded data sets, I re-examined some stations of the temporary MAGNUS project (*Weidle et al.*, 2010) to ensure a consistent data processing for later comparison. At MAGNUS stations shear wave splitting was previously studied by *Roy and Ritter* (2013). Furthermore, high-quality data of several permanent networks in Fennoscandia and surrounding countries were analyzed (136 stations). At permanent stations that were also studied in the past the analysis was continued with more recent recordings. Data coverage ranges from only a few months (some temporary deployments) up to more than 15 years at permanent stations, especially in Finland and Norway. For most stations of ScanArray Core the recording times ranged between two and four years. From the Swedish National Seismic Network (*SNSN*, 1904) a limited subset of four years of restricted data was examined (2012-2016), however, some open stations available from ORFEUS were analyzed for longer periods. This represents a continuation of the work done by *Eken et al.* (2010) for the period 2002-2008, however, in the meanwhile several new recording stations were installed within the SNSN network.

Based on the Global CMT catalog[15] (*Dziewoński et al.*, 1981; *Ekström et al.*, 2012) I selected around 3000 teleseismic earthquakes with moment magnitude M_w 5.5 or greater at epicentral distances between 80° and 140°. All events have hypocenter depths $>$ 20 km and occurred between March 1998 and October 2017. After applying strict quality criteria (see below), the recordings of 541 events allowed to make at least one reliable splitting measurement at any of

[15] The Global CMT Project: https://www.globalcmt.org/, last accessed 11 January 2019

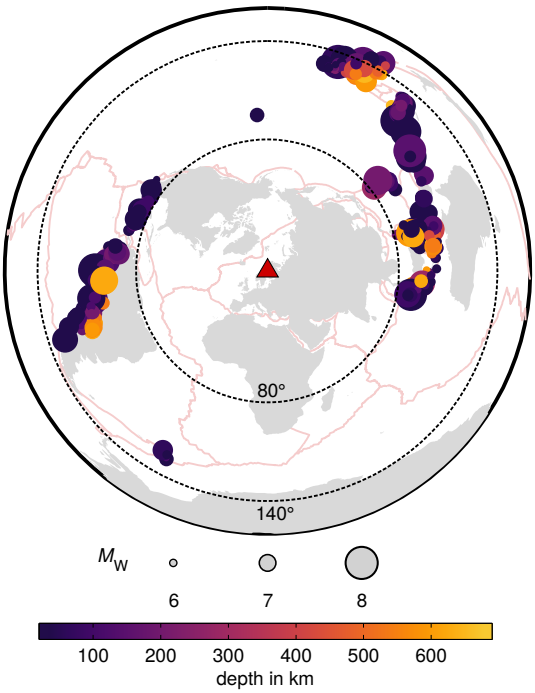

Figure 7.4: Distribution of 541 teleseismic earthquakes based on the Global CMT catalog (*Dziewoński et al.*, 1981; *Ekström et al.*, 2012) that yielded at least one *good/fair* split or null measurement. Color fill of the individual circles indicates the event depth and the size of the circles scales with the moment magnitude M_W. The epicentral distance window between 80° and 140° is displayed by the two dashed circles centered at the location of the ScanArray network (red triangle). Landmasses are shown in gray and light red lines indicate plate boundaries after *Bird* (2003).

the studied seismic stations (Fig. 7.4). In Fennoscandia the data coverage in general is dominated by events located between Indonesia and the Eastern Pacific region as well as South and Central America. Depending on the recording periods of some stations also data of a few events are available from the South Sandwich Island area as well as one event (with in total four reliable measurements) from beneath Big Island (Hawai'i) in 2006. For backazimuthal directions in between, no data for the selected criteria are available which is mainly caused by the distribution of global seismicity preferentially located along deep subduction zone systems and plate boundaries. The largest backazimuthal gap ranges from around 110° to 200° (Fig. 7.4).

Prior to the splitting analysis I applied a zero-phase butterworth band-pass filter (5 s – 15 s) to remove noise and frequencies of no interest from the waveforms. Partly the corner periods were slightly adjusted to improve the signal-to-noise ratio (SNR) and improve the waveform clarity as done in previous work (e.g. *Eakin et al.*, 2016; *Grund*, 2017; *Grund and Ritter*, 2019). Measurements for which a clear discrepancy between *SKS* and *SKKS* for the same source-receiver configuration was observed were removed from the data set since they are assumed to be contaminated by contributions from anisotropy in the lowermost mantle beneath Siberia and the Atlantic (*Grund and Ritter*, 2019, see also chapter 6).

Splitting measurements of single-phase arrivals (*SKS*, *SKKS*, *PKS*, *sSKS*) were conducted with the SplitLab toolbox (*Wüstefeld et al.*, 2008). I simultaneously applied two different analysis approaches, namely the rotation-correlation method (hereinafter RC, e.g. *Bowman and Ando*, 1987) and the energy minimization method (SC, *Silver and Chan*, 1991) to determine the two splitting parameters, fast direction ϕ and delay time δt (see section 4.1.3). Possible sensor misorientations were corrected by comparing the SC and RC outputs (e.g. *Tian et al.*, 2011;

Lynner and Long, 2012; *Grund and Ritter*, 2019, see also section 4.1.5). Determined misorientations for ScanArray stations can be found in *Grund et al.* (2017a) and appendix C. For the analyzed MAGNUS stations I considered the previously identified sensor misalignments listed in *Wawerzinek* (2012).

Only measurements for which both methods agreed within their error bounds (95% confidence region, corresponding to 2σ) and which have SNRs larger than 5 were considered (e.g. *Long and Silver*, 2009). Depending on the errors, I ranked measurements of clearly split phases as *good* (95% confidence region of up to $\pm$ 15° in ϕ and $\pm$ 0.2 s in δt) or *fair* ($\pm$ 25° in ϕ and $\pm$ 0.5 s in δt). Phase arrivals with an SNR of greater than 5 on the radial component, nearly no signal (except the background noise) on the transverse component and (nearly) linear particle motion before the correction for splitting are indicative for the absence of splitting. According to the split phases I classified these so-called null measurements as *good* or *fair* (*Wüstefeld and Bokelmann*, 2007), depending on the noise level on the transverse component and the linearity of the particle motion. The uncertainties were calculated using the corrected and updated formulation of *Walsh et al.* (2013) as implemented in the SplitLab plugin StackSplit (*Grund*, 2017, see chapter 5). The latter was also used to calculate in total 154 multi-event splitting results from low-quality measurements at several stations using the energy surface stacking technique (WS, *Wolfe and Silver*, 1998). However, due to partly strong directional variations of the splitting parameters, I only stacked measurements (if enough were available) within 5° bins with respect to backazimuth and epicentral distance (see appendix E.2, Fig.E.2). By this it was possible to increase the number of measurements at some stations. Although it was inferred that simple averaging gives similar results if ϕ and δt are invariant with respect to the backazimuth (*Kong et al.*, 2015), the WS method further allows to directly calculate formal errors from the stacking procedure. Exemplary diagnostic plots of multi-event measurements can be found in appendix E.2, Fig. E.1. In the following only the SC (single splits) and WS results are shown. All measurements are reported in appendix E, Tables E.1 and E.2. However, from the single event-results only a subset is shown, the remaining results are available from the electronic appendix (see F).

7.3 Shear wave splitting results

7.3.1 General trends and geographical variations

From the systematic shear wave splitting analysis in total I received 1772 measurements of clearly split phases and almost two and a half times more null observations (4695). As mentioned before, discrepant pairs are not included (see chapter 6, *Grund and Ritter*, 2019) in this data set. The individual splitting measurements are summarized in Fig. 7.5. The average fast direction has roughly a NE-SW orientation for this data set. However, in a histogram represen-

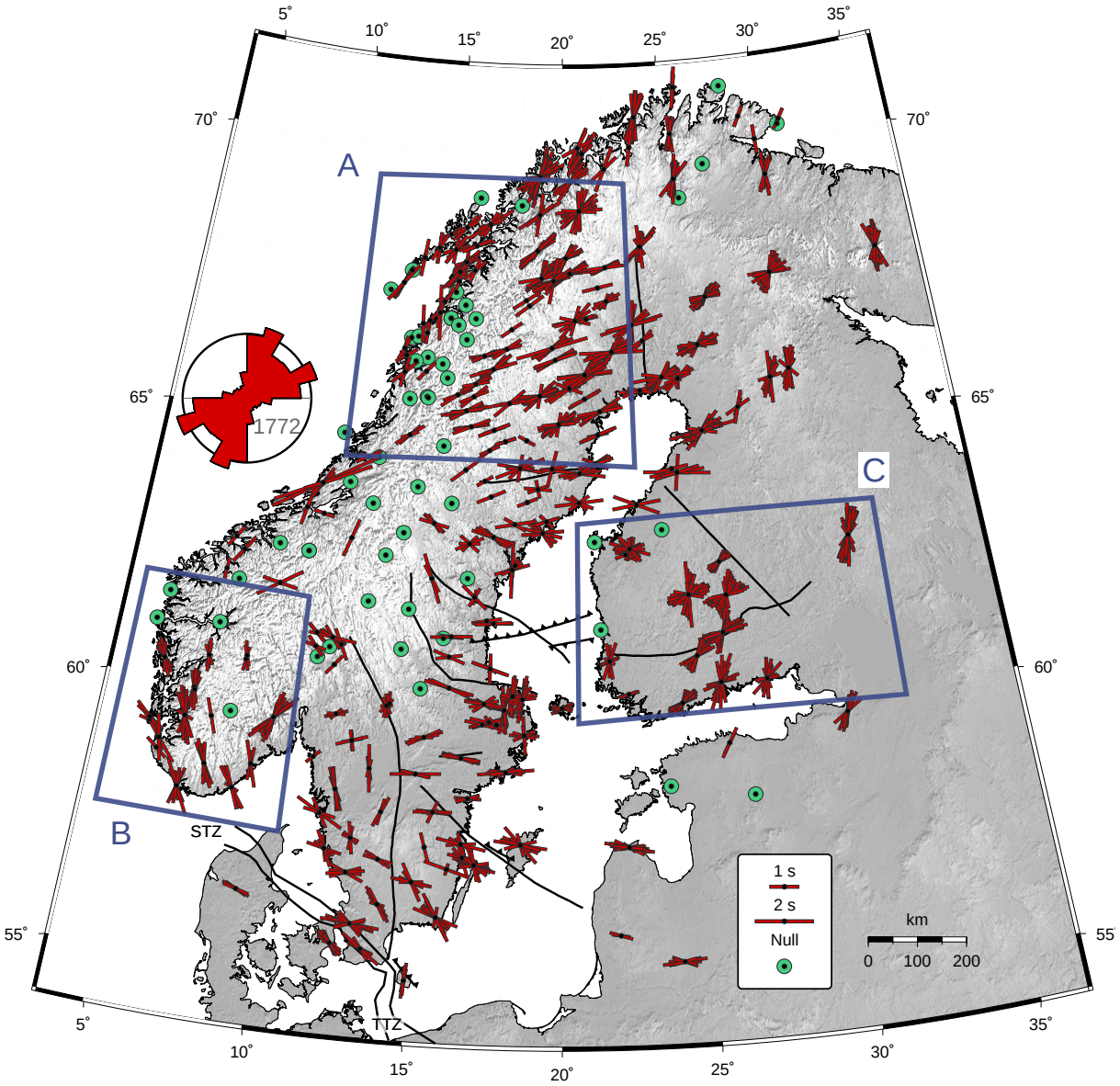

Figure 7.5: Summary of the 1772 individual single-phase shear wave splitting measurements conducted at the analyzed ScanArray stations. Each split phase is represented by a red bar with the orientation indicating the fast axis ϕ relative to North and the length of each bar is scaled by the delay time δt. The overall trends for ϕ across the whole network are displayed in the rose diagram. However, in this visualization it is not possible to distinguish between different backazimuthal/incoming directions of the seismic wave. Stations at which only nulls were observed are indicated by green circles. Nulls observed at the other stations are shown in Fig. 7.7. Blue boxes (A, B and C) indicate the regions for which histograms of the splitting parameters are displayed in Fig. 7.6.

tation the data reveals a clear trimodal distribution (Fig 7.6) for the fast axis ϕ with the three peaks at around $-75°$ (WNW-ESE), 22° (NNE-SSW) and 75° (ENE-WSW). In contrast, the delay times δt are almost evenly distributed around the average of 1.04 s with a slight trend to larger values (Fig 7.6). This is consistent with the globally observed average delay times of around 1 s for continental regions (e.g. *Silver*, 1996; *Fouch and Rondenay*, 2006).

If only results of stations in specific geographic areas are considered, clear lateral variations become obvious (especially for ϕ). For instance, in central and northern Norway/Sweden the

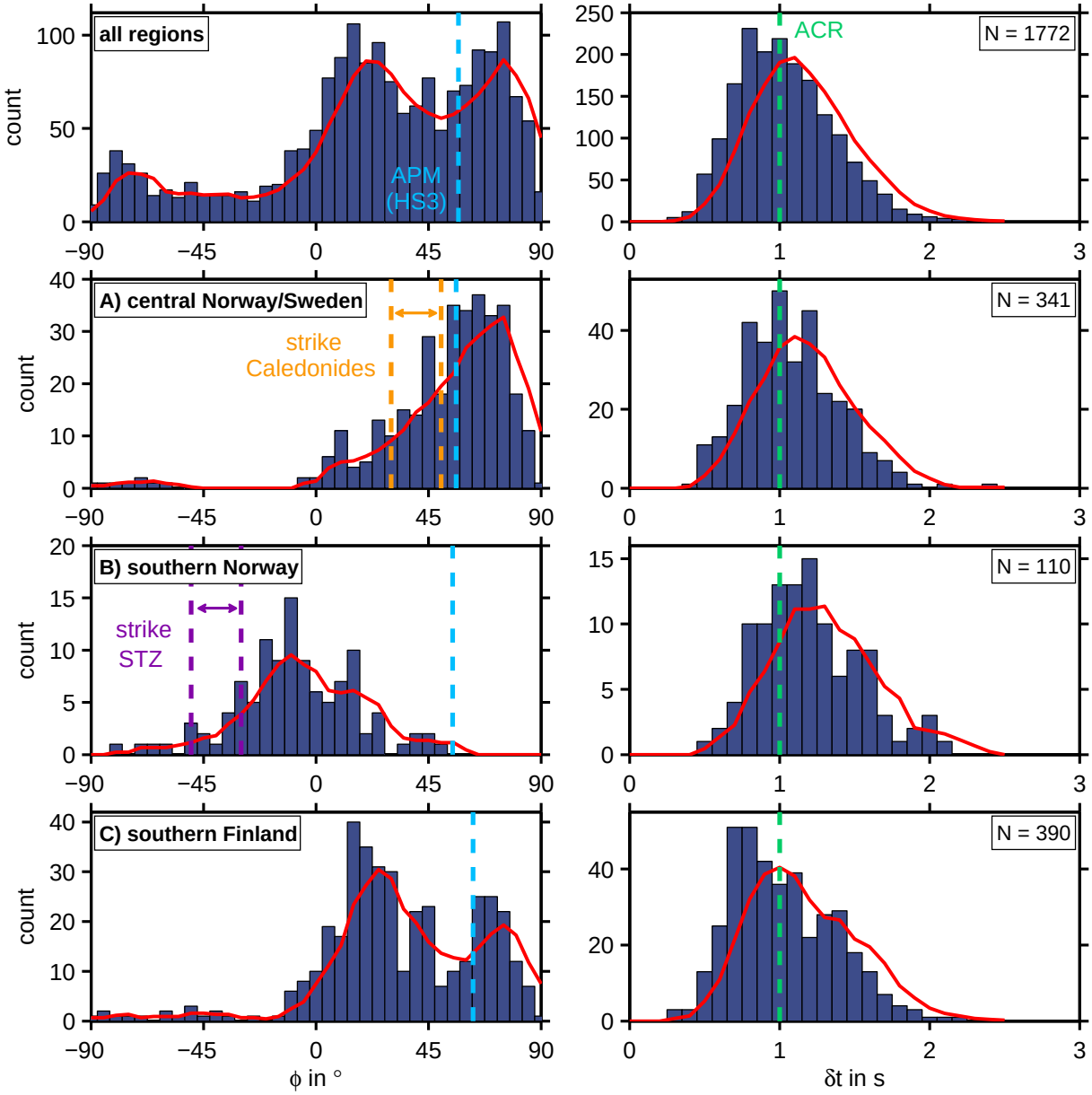

Figure 7.6: Histograms of the distribution of splitting parameters, separated into fast axis ϕ (left column panels) and delay time δt (right column panels). Top row shows distributions for the whole data set. The red curve represents a moving average of the values and highlights the trimodal distribution with peaks at around $-75°$, $22°$ and $75°$ relative to North. The average absolute plate motion directions (APM) in a hotspot reference frame (HS3) shown in the left panels (dashed blue line) were calculated with the HS3-NUVEL 1A plate motion model (*Gripp and Gordon*, 2002). The green dashed line in the right panels indicates the typical average value of around 1 s for continental regions (ACR, e.g. *Silver*, 1996; *Fouch and Rondenay*, 2006). The following rows display the distributions for specific areas across the study region as indicated in Fig. 7.5. Second row: central Norway and Sweden. The dashed orange lines indicate the range of the dominant strike direction of the Caledonian collision. Third row: southern Norway. The dashed purple lines indicate the range of the dominant strike of the Sorgenfrei-Tornquist Zone. Fourth row: southern Finland. Note the varying axis scales of the ordinates in each panel. N (upper right corners) indicates row-wise the number of values included in the histograms.

dominant directions of ϕ with 55°-75° are close to the strike of the Scandinavian mountains. The average for stations located in the area with the highest topography of the Scandes in southern Norway, however, shows a trend of around $-10°$ for ϕ. In contrast, southern Finland seems to be a more complex area with a clear bimodal distribution for ϕ (Fig 7.6). The delay times for all regions show only slight variations and contribute similarly to the overall (unimodal) trend of the whole data set presented in the top row of Fig 7.6.

At several recording stations, both temporary as well as long-running permanent ones, only nulls are observed for all phase arrivals (Fig. 7.5). However, this does not necessarily mean that the structure beneath the corresponding station is purely isotropic. Nulls can also be indicative for scenarios in which the initial polarization of the shear wave is parallel to the fast axis ϕ of the anisotropic medium (or perpendicular to it) or that the splitting is cancelled out due to multiple layers of anisotropy (e.g. *Barruol and Hoffmann*, 1999). Furthermore, it could be possible that the results obtained from waveforms with some energy on the transverse component did not meet the appropriate quality criteria I applied during the pre-processing. However, it is not possible to clearly identify regions with only null observations. Most of them are distributed across central and northern Sweden and Norway (Fig. 7.5).

Besides the clear lateral variations of ϕ between different areas in the study region (Fig 7.6), variations at several stations themselves can be observed in Fig. 7.5. To study station-specific backazimuthal dependencies of the splitting parameters in detail, first I color-coded each measurement with respect to the source region of the corresponding event (Fig. 7.7). The consideration of limited backazimuthal ranges therefore allows not only to quantify lateral variations of ϕ with respect to the initial polarization across the whole network but also at each single station. For a source region between backazimuths of 0° and 31° (Tonga and Samoa, Fig. 7.8, left) ϕ is dominantly aligned in ENE-WSW direction (around 65°), except for (north) eastern Finland, the Kola peninsula and southern Norway where the orientations differ significantly from this trend. At the two Finnish stations VJF and KAF also two different directions can be clearly distinguished which correspond to the two peaks observed in the bimodal distribution for this region (Fig 7.6).

Proceeding in clockwise direction, the dominant trends of the splitting parameters obtained from events in the individual backazimuthal ranges partly differ significantly. While for the source region between 32° and 45° (Fiji) the distribution is dominated by two nearly perpendicular directions with E-W and N-S orientation (Fig. 7.8, right), the patterns for the following two ranges (Fig. 7.9) show dominant N-S (BAZ 46°-64°, Vanuatu and Solomon Islands) and NNE-SSW (BAZ 65°-84°, eastern New Guinea and Molucca Sea) orientations, respectively. Fast axis directions measured from waveforms of South American events have a dominant NNW-SSE trend (Fig. 7.10). This orientation can consistently be observed at stations located east and west of the Baltic Sea in central Finland and Sweden as well as parallel to the STZ. Furthermore, at some stations N-S and NE-SW orientations are observed. At a large number of

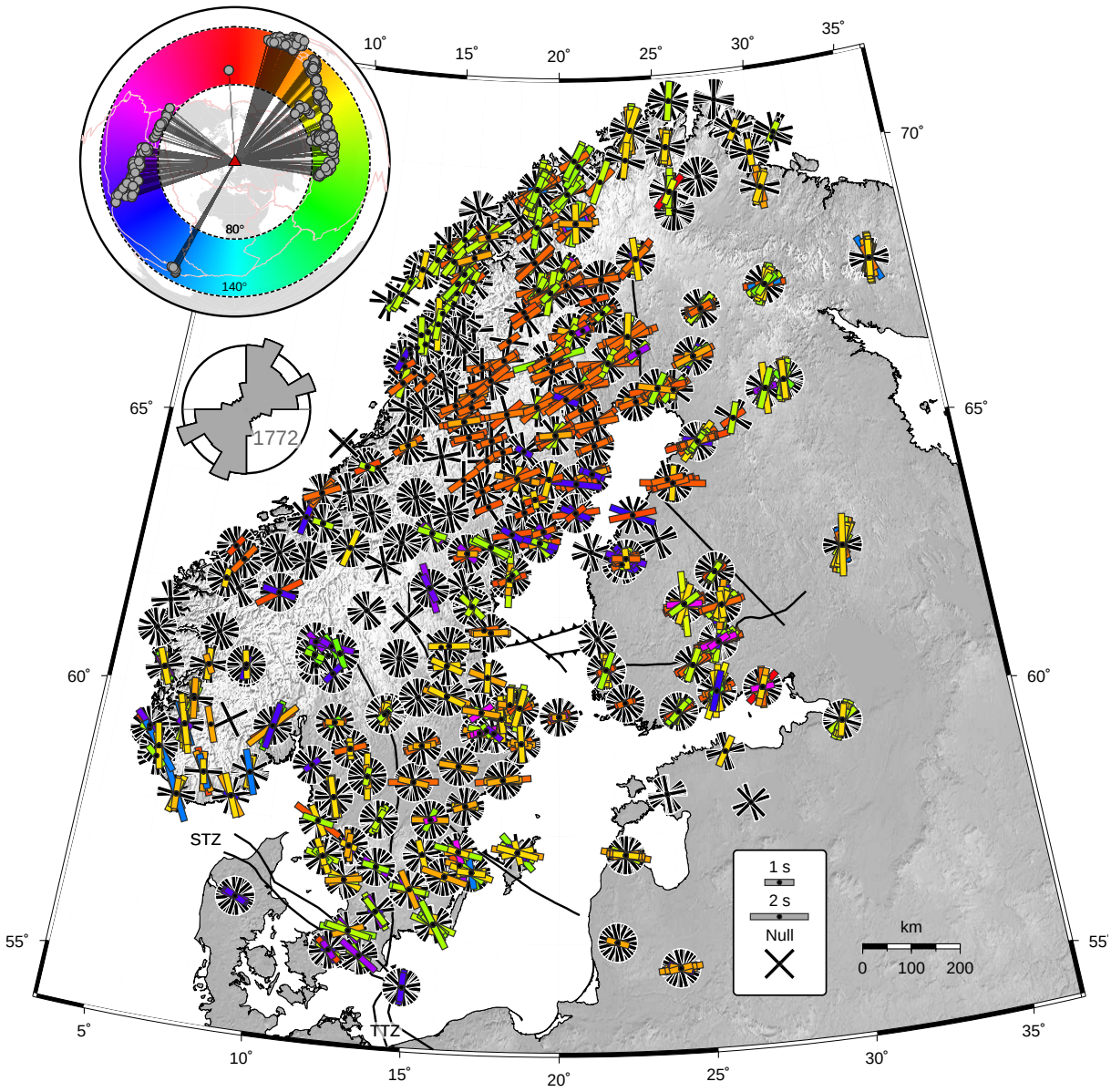

Figure 7.7: Summary of the individual 1772 shear wave splitting measurements (as in Fig. 7.5) color-coded with respect to the source region of the corresponding seismic event (see color-wheel). Individual null measurements are shown with black bars parallel and perpendicular to the backazimuth of the event.

stations (62%) I only measured nulls for events of this backazimuthal range. A similar characteristic was previously reported for stations located on the East European Craton (*Wüstefeld*, 2007) east of the study region. However, a unique explanation for this is still missing. Distributions of the remaining backazimuth regions, for which also strong variations with backazimuth can be observed, are shown in appendix E.3, Figs. E.3-E.6.

The comparison of Figs. 7.8 and 7.9 also clearly indicates that, for example, the splitting direction of ϕ ($\sim 65°$), observed for the first backazimuthal range in northern Sweden and Norway, aligns fairly well with the backazimuths shown in Fig. 7.9 (left). Here, mostly nulls are observed in the area, indicating that the fast axis polarization of the medium falls into the

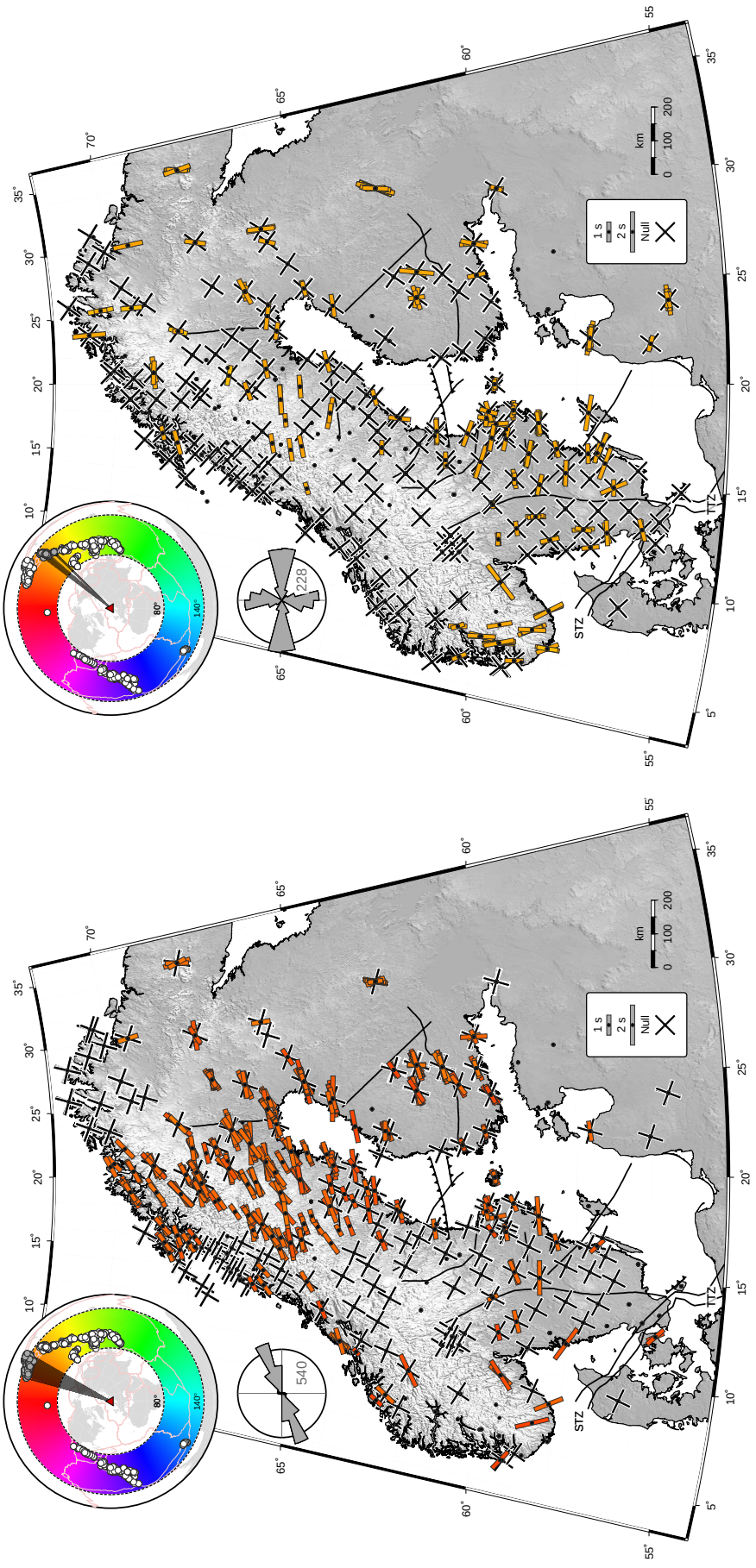

Figure 7.8: Backazimuth-dependent individual shear wave splitting measurements color-coded with respect to the source regions between backazimuths of 0°-31° (left) and 32°-45° (right). The overall trends for ϕ are displayed in the roseplots. Individual null measurements are shown with black bars parallel and perpendicular to the backazimuth of the event.

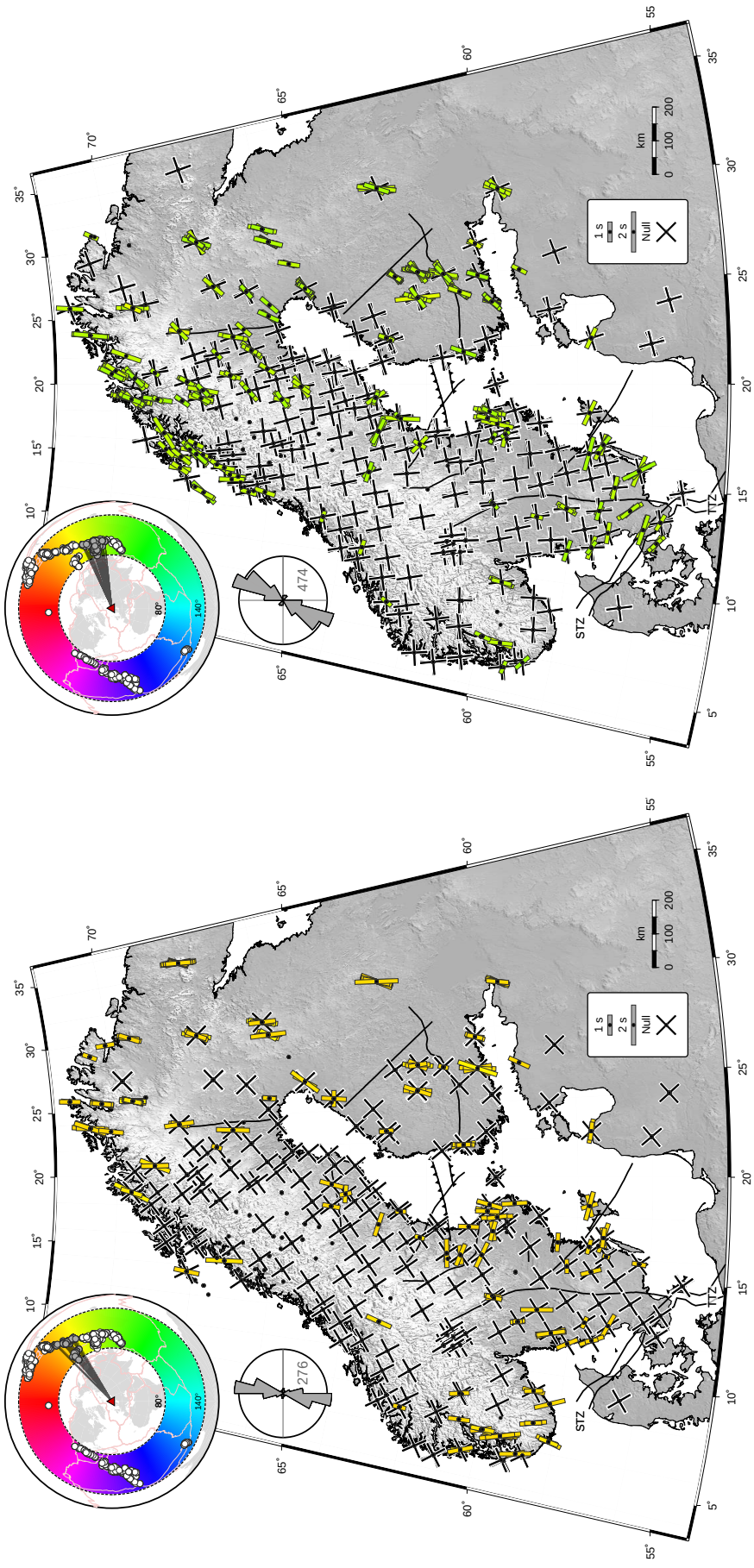

Figure 7.9: Backazimuth-dependent individual shear wave splitting measurements color-coded with respect to the source regions between backazimuths of 46°-64° (left) and 65°-84° (right). The overall trends for ϕ are displayed in the roseplots. Individual null measurements are shown with black bars parallel and perpendicular to the backazimuth of the event.

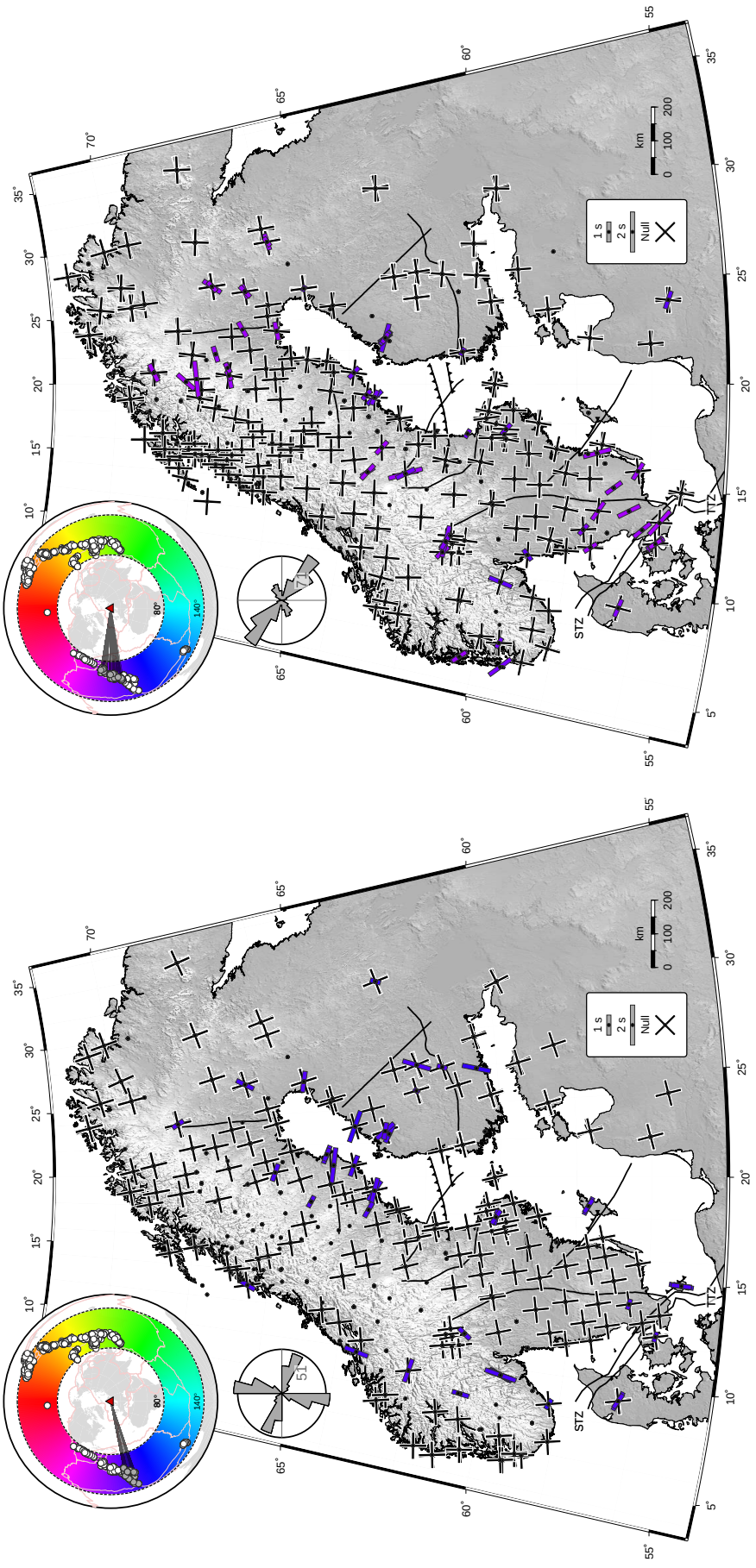

Figure 7.10: Backazimuth-dependent individual shear wave splitting measurements color-coded with respect to the source regions between backazimuths of 231°-260° (left) and 261°-280° (right). The overall trends for ϕ are displayed in the roseplots. Individual null measurements are shown with black bars parallel and perpendicular to the backazimuth of the event.

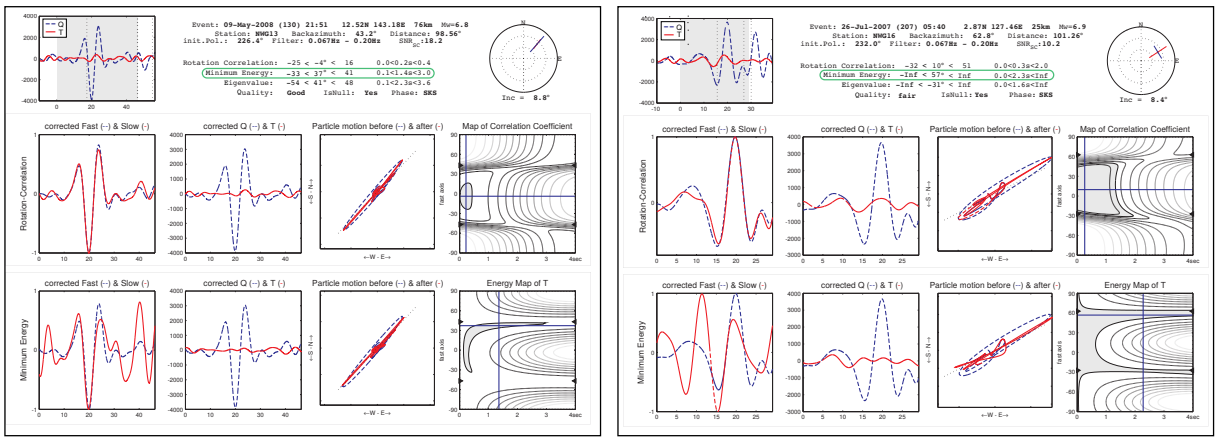

Figure 7.11: Waveform examples of the re-analyzed MAGNUS stations NWG13 (left) and NWG16 (right) for which large delay times (2.4 s and 3 s) were observed by *Roy and Ritter* (2013) only determined with the SC method though. Applied filter settings (bandpass 5 s – 15 s) are identical. The re-analysis delivered the same fast axes of 37° and 57° and only slightly smaller delay times (1.4 s and 2.3 s) using the SC method (green boxes). However, considering also the significantly different RC results (ϕ and δt) and the large uncertainties allows to conclude that these are near-null observations rather than clear splits. Therefore, the energy on the transverse component may also be recorded background noise.

direction of the initial polarization of the incoming waves. For events of the subsequent back-azimuthal range (46°-64°) in Fig. 7.9 (right) in the same area non-nulls were measured with an average fast axis direction of around 30°.

7.3.2 Re-analysis of some MAGNUS station waveforms

Data of the temporary deployment MAGNUS (*Weidle et al.*, 2010) and the long-running permanent Norwegian Seismic Array (NORSAR, located in southern Norway) were previously analyzed for shear wave splitting by *Roy and Ritter* (2013). In order to improve the lateral resolution of the splitting pattern around the available permanent recording stations, I re-analyzed some of the MAGNUS and all NORSAR stations. While the overall trend for ϕ is similar, especially for the NORSAR stations I observed many more null measurements, compared to the observations of *Roy and Ritter* (2013) with often large delay times of $\delta t > 2$ s. It seems this could be a result of the analysis approach itself, since *Roy and Ritter* (2013) only applied the SC method to measure splitting. In contrast, I simultaneously applied the SC and RC methods and only used measurements for which both methods agreed within the error bounds. As shown by *Wüstefeld and Bokelmann* (2007) large δt and strong variations of ϕ between SC and RC often are a result of a null/near-null case where the fast axis is close to the corresponding backazimuth of the event. Using both methods, the identification of nulls is more straightforward, compared to measurements with only one method. In Fig. 7.11 I present two re-evaluated examples which were rated as splits by *Roy and Ritter* (2013). While the original SC values for ϕ and δt agree with my findings, I classified these two measurements as (near-) null cases since the RC values show a significant deviation from the SC estimates. Furthermore, there are almost no significant

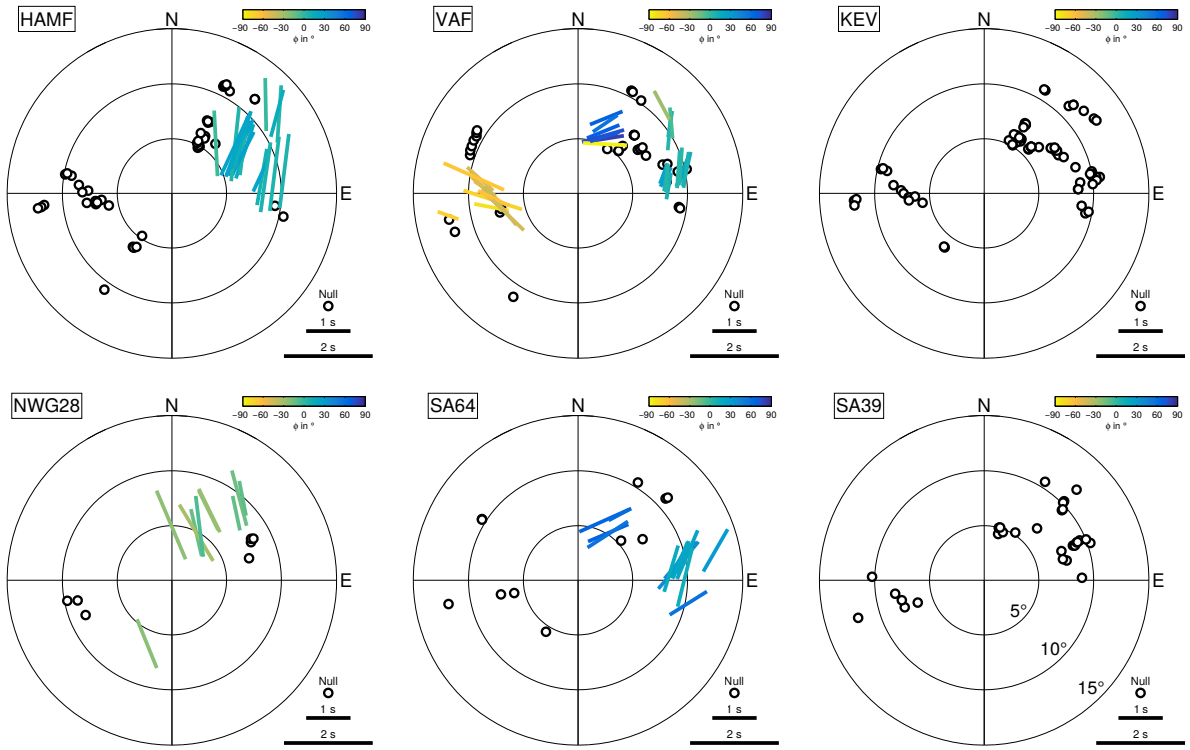

Figure 7.12: Exemplary stereoplots of stations with different splitting patterns. Splitting parameters ϕ and δt are shown as function of backazimuth (clockwise direction from north) and incidence angle (radial axis). The orientation of ϕ is additionally color-coded. Delay time δt scales with the length of the single bars. Null measurements are shown as black open circles. Top row: Observations at long-running permanent stations. Bottom row: Splitting patterns of temporary stations with observation times of around two years. Left column: Typical examples for which the assumption of a single horizontal layer of anisotropy is valid. Although the consistent split observations (ϕ and δt) are only available for limited directions, clear nulls can be observed for the backazimuths corresponding to the fast axis direction and/or perpendicular to it. Center column: Strong variations for the splitting parameters with backazimuth (especially for ϕ) are observed. Right column: Stations at which only nulls were observed for several backazimuths.

signals on the transverse components which could indicate a splitting. Therefore, I infer that the previously published splitting values (especially δt) are slightly overestimated at some stations.

7.3.3 Stereoplot representation

Another way to represent direction-dependencies at each individual station separately are so-called stereoplots in which the splitting parameters are plotted as a function of backazimuth (clockwise direction from north) and incidence angle (radial axis). For core-refracted shear waves observed in the ranges between 80° and 140° epicentral distance (*SKS*, *SKKS* or *PKS*) the incidence angles at the station are nearly vertical (mostly $< 10°$).

Based on their stereoplot characteristics I divided the 266 analyzed stations into four different classes:

1. simple (no or only negligible backazimuthal variations), **109** stations

2. complex (strong variations of ϕ and/or δt with backazimuth), **53** stations

3. null (dominated by nulls), **63** stations

4. poor (less than five *good*/*fair* split or null measurements are available), **41** stations.

In Fig. 7.12 I present exemplary stereoplots of six different recording stations located across the study region that were classified into the first three categories (see annotations in Fig. 7.3). Stereoplots for all analyzed stations (including stations ranked *poor*) can be found in appendix E.4. The left column shows two examples of the first class with relatively simple splitting characteristics and negligible azimuthal variability. At permanent station HAMF I observe a bunch of consistent splits (similar ϕ and δt) for phase arrivals in the northeastern quadrant (backazimuths of 0° to 90°). Although no splits were measured in the other quadrants, the locations of nulls along the orientation of ϕ and nearly perpendicular to it, allow to characterize the anisotropy beneath the station by a single horizontal layer (e.g. *Silver and Savage*, 1994). A similar pattern (but with different ϕ and δt) was observed at temporary station NWG28 (MAGNUS project) that was installed in southern Norway. However, one further split with consistent ϕ and δt was measured in the southwestern quadrant. In contrast, nulls were only found for the direction perpendicular to the dominant orientation of ϕ in the northeastern and southwestern quadrants. The middle column of Fig. 7.12 displays two stations at which I observe complex splitting patterns with mostly significant azimuthal variability. While the orientations of ϕ at permanent station VAF can be clearly divided into three backazimuthal domains, each with an individual dominant direction ($\sim 70°$: bluish color, $\sim 5°$: greenish and $\sim -60°$: orange), the corresponding delay times are nearly constant except for the waves from western directions with slightly larger values. In between several nulls are located without a clear first-order trend. At temporary station SA64 (ScanArray project) the variation is not as significant as at station VAF, however, the color-coding indicates a slight rotation of ϕ towards $\sim 30°$ for backazimuths around 90°. The delay times show no significant variability. Besides the robust v-shaped pattern formed by the two groups of splits, measured nulls are mostly located between them and in the southwestern quadrant.

The stereoplots shown in the last column of Fig. 7.12 represent two stations at which I did not observe any splitting. This means that for all shear wave splitting measurements clear nulls were received. However, as mentioned before this does not necessarily mean that the sampled structures beneath the station are of isotropic character.

Showing the different stereoplots in map view allows to identify stations of similar character and therefore abrupt or smooth lateral inter-station variations. For southern Norway, Sweden and northern Denmark I can clearly divide the stations into two groups, each with almost self-consistent splitting patterns (Fig 7.13). While southern Norway on average is dominated by a fast axis direction of around 0° to −20° (greenish area), south-east of this group towards south-

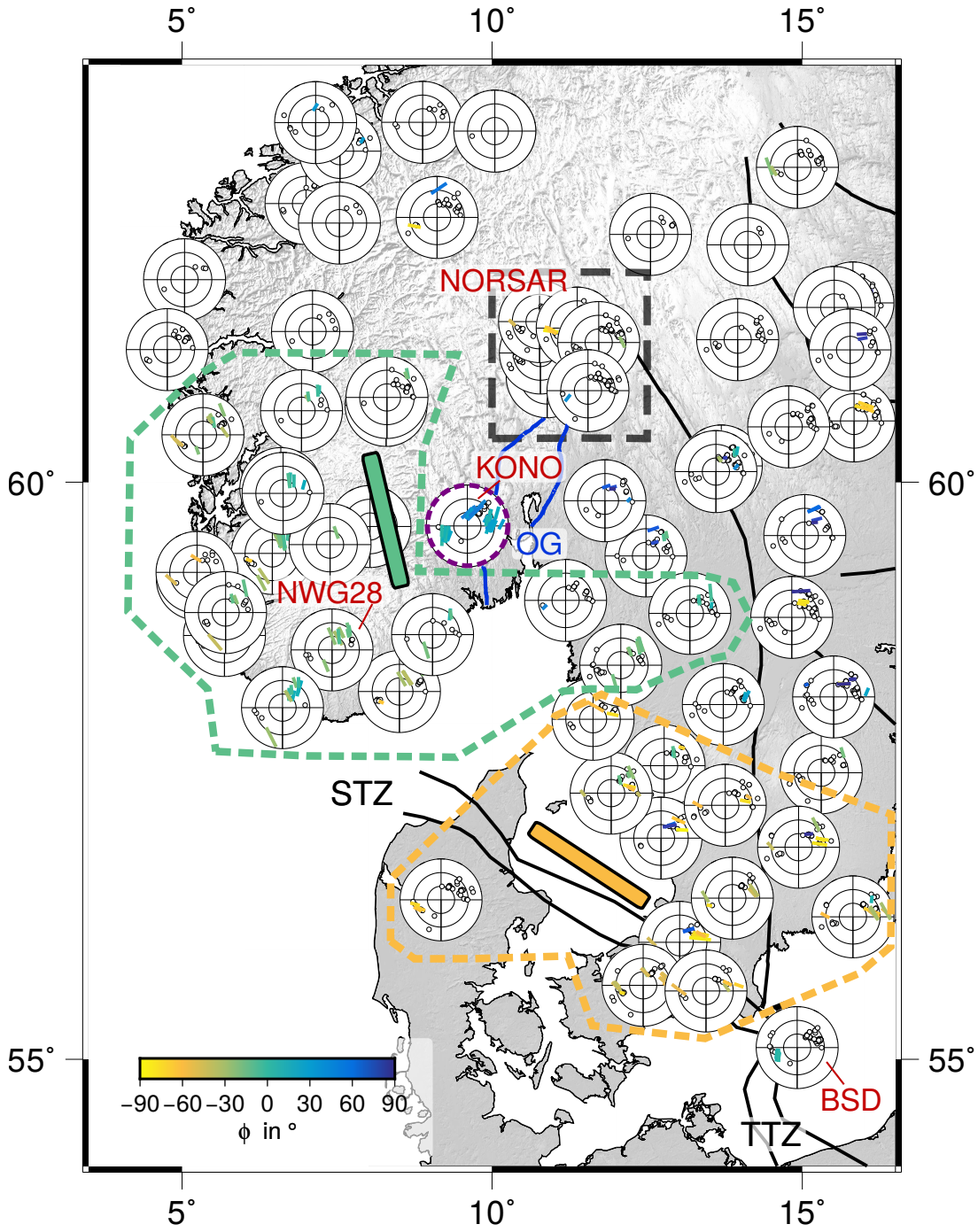

Figure 7.13: Distribution of stereoplots in southern Norway, Sweden and northern Denmark. Stations of the Norwegian Seismic Array (NORSAR, black dashed box) are shown separately in Fig. 7.14. The blue line indicates the contours of the Oslo Graben (OG). The purple dashed circle highlights station KONO at which different models are able to explain the splitting observations (see text). For plotting conventions see Fig. 7.12.

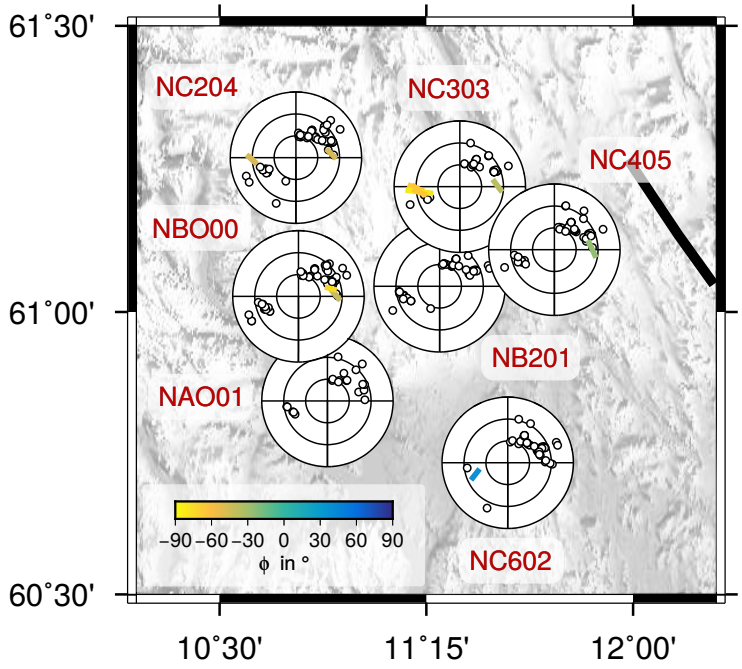

Figure 7.14: Distribution of stereoplots for NORSAR (see Fig. 7.13). Station names are shown in red. Depending on the installation date of the stations, seismic data of the period 1998-2017 were analyzed. Therefore, the patterns in general are well constrained. For plotting conventions see Fig. 7.12.

western Sweden the orientation of ϕ slightly rotates toward $-60°$ (orange area). In general, this orientation matches quite well with the strike of the STZ. A significant change can be observed for station BSD where the orientation of ϕ is aligned in almost N-S direction. This is very similar to the findings of *Wylegalla et al.* (1999) and therefore confirms that the orientation of ϕ is most probably related to the N-S striking segment of the STZ in this area (Fig 7.13). The observations at the stations of NORSAR (Fig. 7.14) are mostly dominated by null measurements from different directions. Partly consistent splits can only be observed at stations NC204, NBO00, NC303 and NC405. However, for NC204 and NC303 the majority of nulls correspond to backazimuth directions which are nearly perpendicular to the measured fast axis orientation. This allows to assume that a simple horizontal layer of anisotropy is responsible for the observed splitting. The pattern at the long-running permanent station KONO, located southwest of NORSAR at the western rim of the Oslo Graben (Fig 7.13), partly differs significantly in comparison to the surrounding stations. The dominant fast axis orientations vary between $10°$ and $45°$. Nevertheless, these are consistent within narrow backazimuthal ranges.

As indicated in the histogram distributions (Fig. 7.6), in southern and central Finland the orientations of ϕ vary significantly when switching between different source regions (Figs. 7.8-7.10). This aspect becomes more obvious when comparing the stereoplots of the recording stations in this area (Fig. 7.15). While the observations at the most eastern station JOF shows a relatively simple pattern with consistent ϕ ($\sim 10°$) and δt (~ 1.3 s) for different backazimuths, at stations KEF, KAF, RAF, PVF and VAF (purple dashed circles) the fast axes rotate consistently from $\sim 60°$ (large blue bar) to $\sim 5°$ (greenish) in the northeastern quadrant of the stereoplots. Furthermore, at VAF a third dominant direction ($\sim -60°$, orange) is observed for

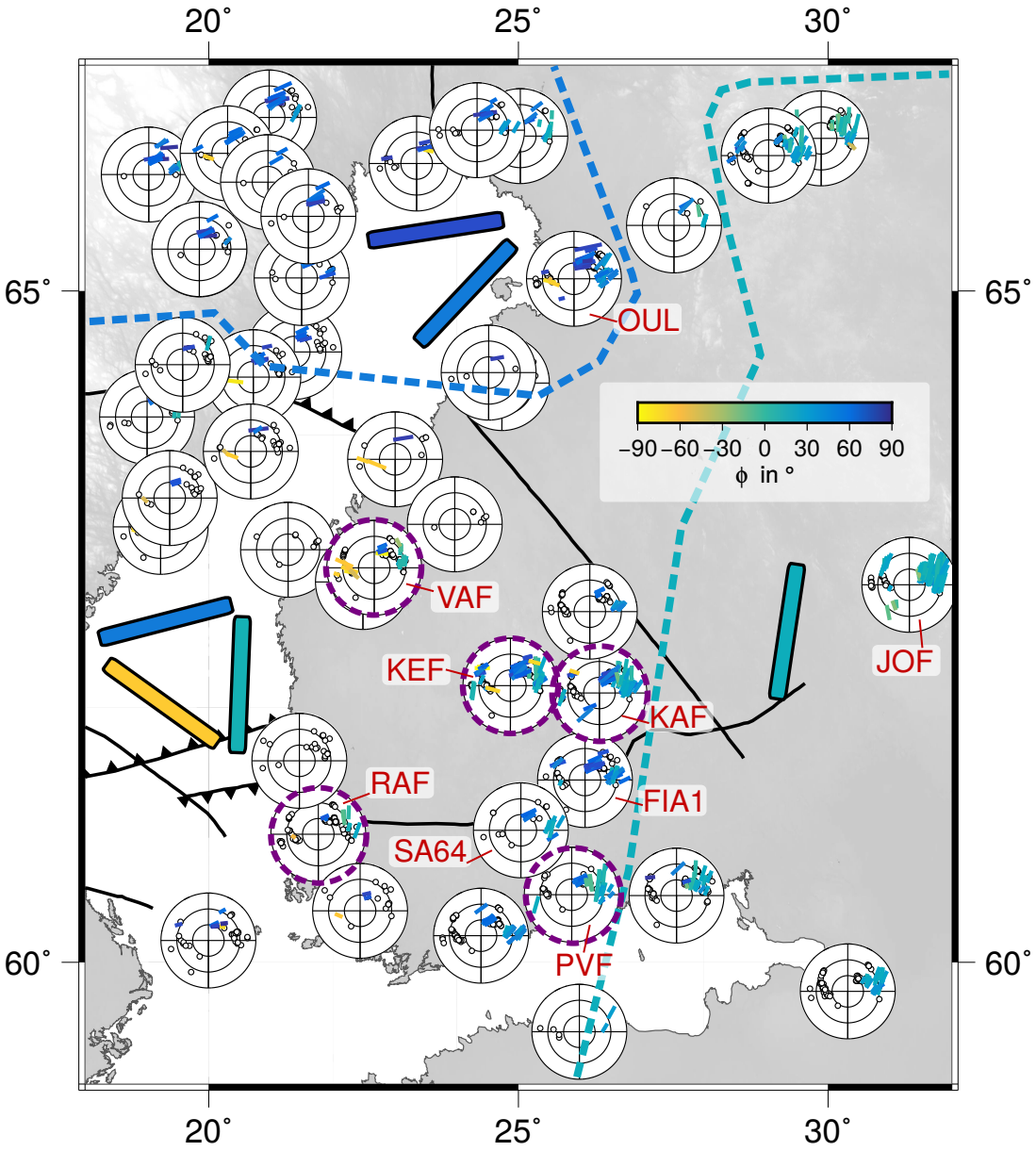

Figure 7.15: Distribution of stereoplots in southern and central Finland as well as surrounding areas. Purple dashed circles indicate stations for which only non-unique anisotropy models were found (see text). For plotting conventions see Fig. 7.12.

measurements related to South American events. Stations located in the northwestern region (Fig. 7.12) around OUL consistently offer two different directions for ϕ with $\sim 60°$ (darkblue) and $\sim 45°$ (light blue).

For stations at which no (or only negligible) backazimuthal variations were found (class 1), I calculated station averages for ϕ and δt using the WS method as implemented in StackSplit (see section 5.3.3). By this I get for each of the corresponding stations a single set of splitting parameters which characterize a single horizontal layer of anisotropy. However, due to back-azimuthal gaps in the data, I cannot fully rule out that a more complex anisotropic structure is located beneath the stations. For stations as belonging to the second group ("complex") I per-

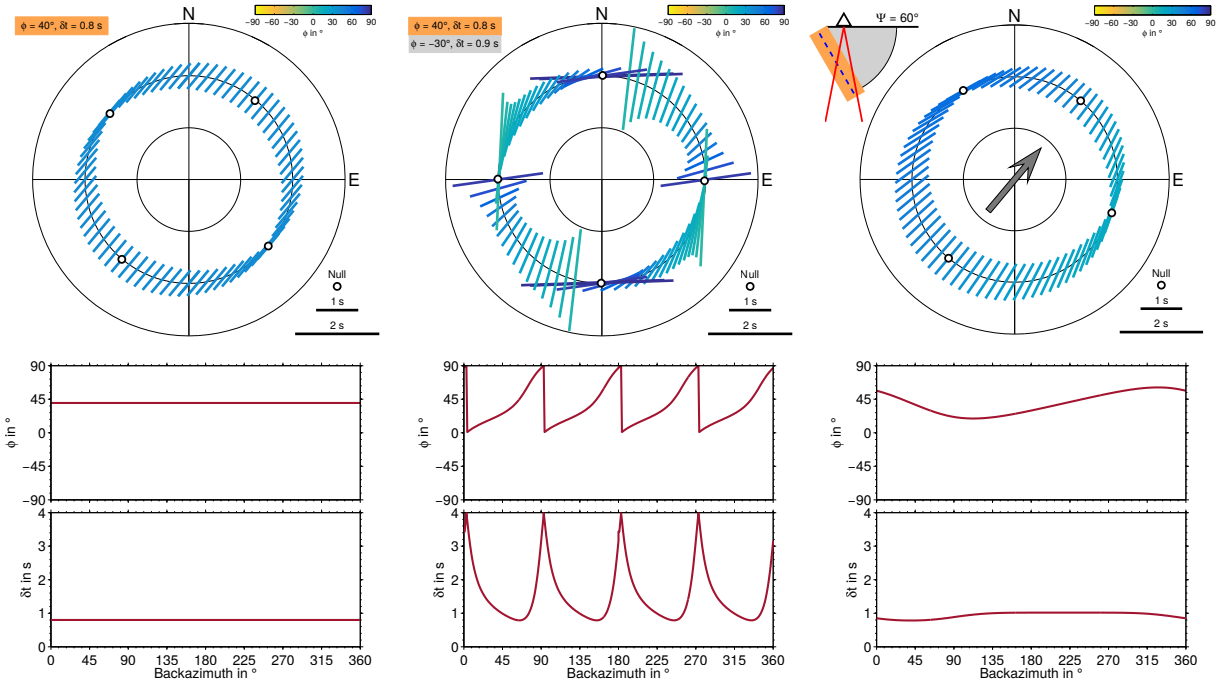

Figure 7.16: Synthetic splitting parameters for different model settings calculated using MSAT (*Walker and Wookey*, 2012). Parameters were computed for shear waves of 8 s dominant period which arrive at the station under incidence angles of 10° (as is typical for *SKS*). Left: Single-layer model with horizontal symmetry axis, a fast axis direction of $\phi = 40°$ and a delay time of $\delta t = 0.8$ s. The stereoplot shows the splitting parameters as function of backazimuth and incidence angle (radial axis). The orientation of ϕ is additionally color-coded. Delay time δt scales with the length of the single bars. Null measurements are shown as open circles. Note: There is a null split in the direction of the fast polarization direction (here 40°) although the blue bar indicates a delay time. Bottom panels show the same splitting parameters (red lines), separated into ϕ and δt over the backazimuth. Center: Splitting parameters for a two-layer model with $\phi = 40°$ and $\delta t = 0.8$ s for the upper layer (same as in the single-layer model) as well as $\phi = -30°$ and $\delta t = 0.9$ s for the lower layer. Note the 90° periodicity for both, ϕ and δt. Right: Splitting parameters for a model in which the fast axis ($\phi = 40°$) dips with $\Psi = 60°$ relative to the horizontal into the direction of ϕ (direction of gray arrow). 30% olivine crystal alignment is assumed for a layer thickness of 180 km. Note the smooth 360° periodicity for the two parameters.

formed detailed forward modeling which is discussed in the following section. Stations sorted into the last class (*poor*) were discarded for further analysis since the data availability does not allow an adequate modeling of anisotropic structure. Null stations were also not modeled but integrated in the final discussion and interpretation.

7.4 Modeling of complex splitting patterns

7.4.1 General considerations

Under the assumption of a single anisotropic layer with a horizontal symmetry axis, one would expect the same splitting parameters (ϕ and δt) for events from all directions (Fig. 7.16). Only waves arriving from backazimuths (nearly) parallel (or perpendicular) to the fast axis direction of the medium should indicate an absence of splitting (null measurement). However, a large portion of the stations in the data set does not offer such simple characteristics. Either the

splitting pattern show strong variations of ϕ and δt within narrow backazimuthal segments or null measurements appear for directions where they are not expected. Therefore, the clear variations of the splitting parameters with backazimuth indicate more complex anisotropy at depth (e.g. *Silver and Savage*, 1994; *Hartog and Schwartz*, 2000; *Marson-Pidgeon and Savage*, 2004).

For a system consisting of two or more anisotropic layers (each with a horizontal symmetry axis and $\phi_1 \neq \phi_2 \neq \phi_i$, with i representing the number of layers) the apparent splitting parameters would show a clear 90°-periodicity (Fig. 7.16). For multiple layers the splitting operators do not commute and therefore it is possible to distinguish in which order the different layers of anisotropy are stacked atop each other (*Silver and Savage*, 1994; *Silver and Long*, 2011). Furthermore, it was demonstrated that in the presence of multiple layers the uppermost layer may have a significant impact on the overall apparent orientation of ϕ measured at the station (*Saltzer et al.*, 2000).

In contrast, a dipping anisotropic layer would result in a smoothly 360°-periodic ϕ-δt pattern (e.g. *Chevrot and Van Der Hilst*, 2003, see Fig. 7.16). However, for dip angles < 30° the variations of ϕ and δt measured from field data (contaminated with seismic background noise of varying levels) are generally within the uncertainties (e.g. *Hartog and Schwartz*, 2000). Thus, it is difficult to clearly distinguish them from the splitting signature of a single horizontal layer. To map such variations good azimuthal data coverage is essential and, therefore, large backazimuthal gaps hamper a detailed modeling (and unique interpretation) for the full azimuthal range. Furthermore, especially at temporary stations the data coverage is often limited due to short recording periods and thus only few reliable splitting and null measurements from few backazimuths are available. In principal, I concentrate on the recording stations which offer good data coverage. This allows me to check whether slightly varying results for specific directions are stable for a bunch of events and therefore they are real indicators for complex structure, or whether the variations alternatively could be explained with, e.g., varying noise levels for different events.

7.4.2 Forward modeling approach

In order to constrain the underlying anisotropy system for stations sorted into class 2 (see section 7.3.3), I performed systematic forward modeling using the MATLAB Seismic Anisotropy Toolkit (MSAT, *Walker and Wookey*, 2012). For this purpose I first pre-computed synthetic splitting parameters for shear waves of 8 s dominant period (typical for the recorded *SKS*, *SKKS*, *PKS* and *sSKS* phases) that propagate through models consisting of two anisotropic layers or one layer with a dipping symmetry axis. Two-layer models, for instance, may represent a continental lithospheric layer dominated by fossil frozen-in seismic anisotropy atop an asthenospheric layer that reflects anisotropy induced by current horizontal mantle flow. Inclined structures re-

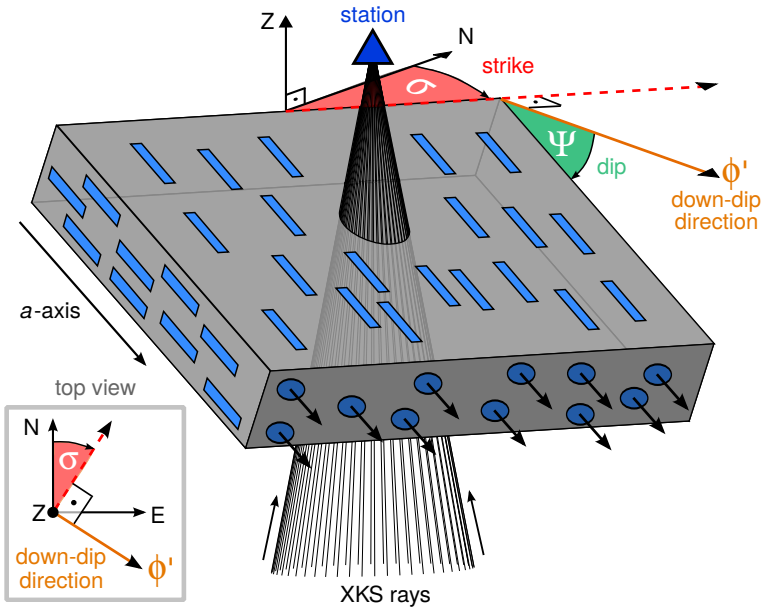

Figure 7.17: Simplified schematic to illustrate the parameter conventions used for the dipping symmetry axis modeling. The modeled olivine *a*-axis (blue bars within the layer) plunges with the dip angle Ψ (measured from the horizontal downwards, green) in down-dip direction ϕ' (orange) that is measured clockwise from geographic north (see also top view in lower left corner). ϕ' is perpendicular to the strike of the layer (σ, red), so $\phi' = \sigma + 90°$. Black lines indicate raypaths of core-refracted shear waves (XKS) which sample the layer from all backazimuth directions under an incidence angle of 10° before arriving at the recording station at the surface (blue triangle).

lated to relicts of paleo-subduction may be characterized by models with a dipping symmetry axis. Although this modeling approach is based on ray theory and generally ignores important seismic wave properties like finite-frequency effects, the results provide valuable information about potential first-order anisotropy characteristics beneath a seismic recording station (e.g. *Walker and Wookey*, 2012; *Aragon et al.*, 2017).

Two layer models were created by varying the fast axis in both layers (ϕ_1 and ϕ_2) in 5° increments between −90° and 90° and the delay time (δt_1 and δt_2) between 0 s and 4 s with increments of 0.2 s. Apparent splitting parameters for all possible combinations (ϕ_1, ϕ_2, δt_1, δt_2) were calculated using the equations outlined in *Silver and Savage* (1994) for backazimuths between 0° and 360°. If $\delta t_1 = \delta t_2 = 0$ s occurs, no splitting is measured. In contrast, if in only one of the two layers the delay time is zero ($\delta t_1 = 0$ s or $\delta t_2 = 0$ s) the corresponding setting is equal to a simple one-layer model.

The parameters used to set the dipping-layer models up are visualized in Fig. 7.17. For each model configuration the layer is assumed to consist of a synthetic aggregate of olivine (*Abramson et al.*, 1997). Since analyzed mantle xenoliths from the area partly consist of up to 70% olivine (*Kukkonen et al.*, 2003), such aggregate is a reasonable assumption for the modeling. The down-dip direction ϕ' of the layer is defined as clockwise rotation relative to North (0°-360°, varied in 5° increments) and the layer dip Ψ is measured from the horizontal downwards (0°-90°, in 5° increments). The orientation of the modeled fast axis (olivine *a*-axis) follows the same convention and therefore dips parallel to the down-dip direction (blue bars in Fig. 7.17). Together with the amount of aligned olivine crystals the layer thickness controls the accumulated delay time of each split wave along the slightly varying path lengths through the dipping layer (see schematic red raypaths in the right panel of Fig. 7.16) while the ϕ-pattern is fully insensitive to both parameters. Thus, a thick layer with a low percentage of crystal alignment can

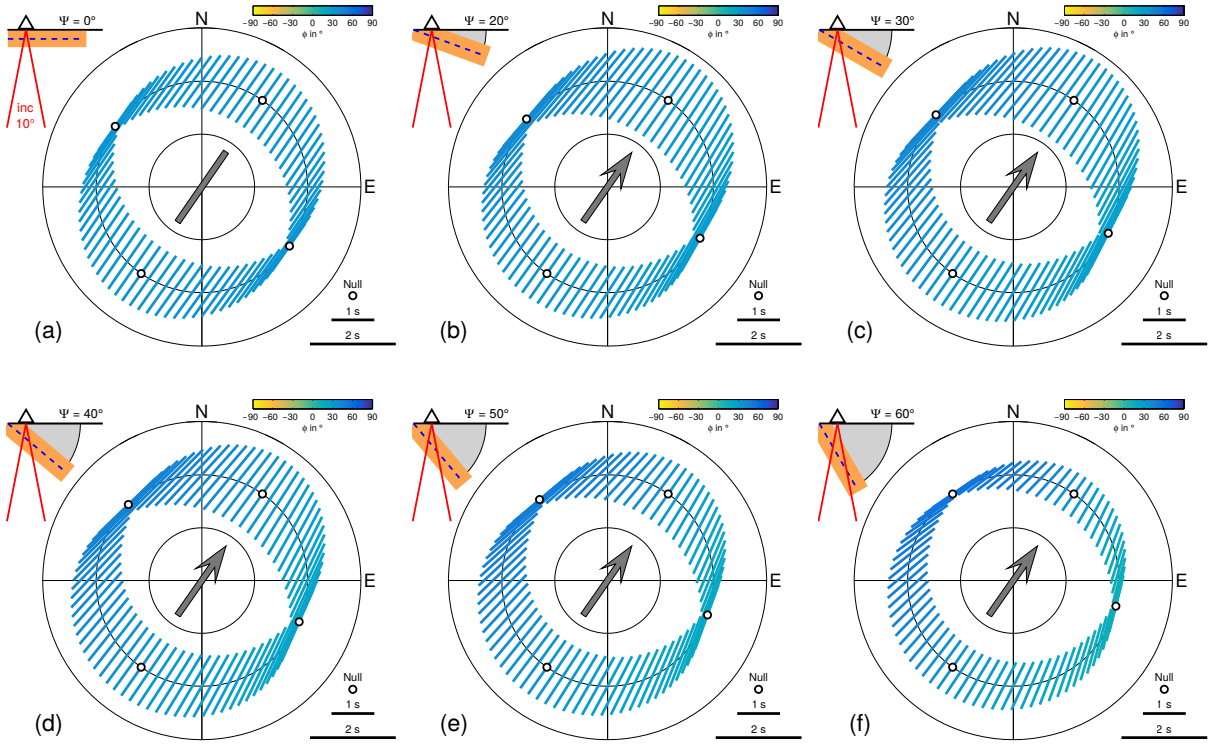

Figure 7.18: Overview about the influence of a dipping symmetry axis. (a) Standard horizontal symmetry axis with $\phi = 35°$ (small blue lines and gray bar). Seismic rays (red lines) are sampling the layer of the anisotropic fabric (brown) from all directions in 5° backazimuth steps, each with a typical incidence angle of 10° (see also Fig. 7.17), (b) symmetry axis is plunging 20° (Ψ) relative to the horizontal. The down-dip direction is 35°, corresponding to NW (gray arrow), (c)–(f) same for dip angles of 30°, 40°, 50° and 60°. Splitting parameters were calculated using MSAT (*Walker and Wookey*, 2012) for a 220 km-thick layer consisting of pure olivine with 30% crystal alignment. The incidence angles correspond to typical values observed for *SKS* phases. While in (a) and (b) only small changes are visible for measured apparent ϕ values, the delay times in (b) for arrivals from SW are slightly larger than from the other directions. Here the influence of a slightly longer raypath through the layer appears. For larger dips the influence of the longer raypath decreases since the raypath becomes more parallel to the symmetry axis which results in weaker anisotropic signatures.

generate the same δt like a thin layer with a high percentage of crystal alignment. This trade-off prevents me from making any reasonable assumptions about the layer thickness and the fraction of aligned crystals. Finally, the synthetic splitting parameters were determined by solving the Christoffel equation (*Hartog and Schwartz*, 2000; *Walker and Wookey*, 2012, see also section 2.2) for waves arriving from backazimuths between 0° and 360° with incidence angles of 10° as typical for XKS phases (black rays in Fig. 7.17). To highlight the impact of an increasing layer dip on the splitting parameters, in Fig. 7.18 stereoplots of synthetic data for six different dip angles are displayed. As mentioned before, for dip angles $< 30°$ the orientations of ϕ cannot be clearly distinguished. In contrast, the delay times already show larger variations. While for larger dips the delay times become more similar, the distributions of ϕ show a v-shaped pattern that can also be clearly identified from the color-coding.

In most cases the modeling was limited to a specific backazimuthal range, preferentially with a large number of observations. This allows to constrain a model even if the splitting pattern

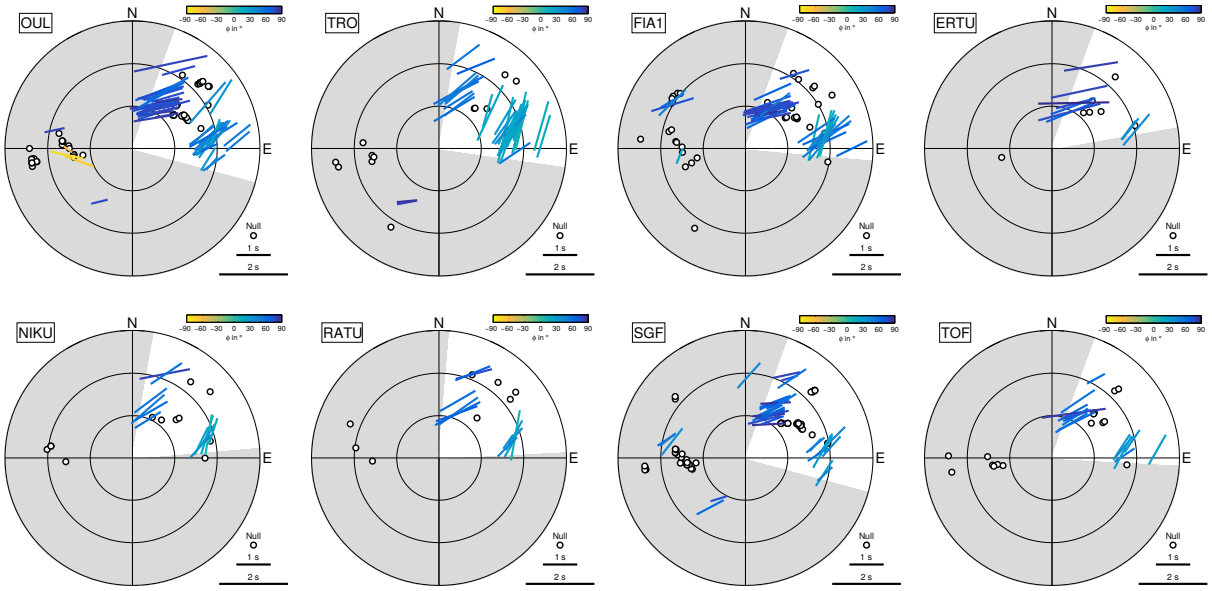

Figure 7.19: Exemplary stereoplots of stations which show a typical v-shaped pattern for the splitting parameters ϕ (orientation of bars and color-coding) and δt (length of bars). Black circles display null measurements. Adequate data coverage is mostly limited to the northeastern quadrant (white sector).

indicates additional lateral variations. To find for each station a model that best fits the data the minimum root-mean-square (RMS) misfit between the predicted splitting parameters and the measured values was determined using:

$$\mathrm{RMS} = \sqrt{\frac{1}{i}(x_1^2 + x_2^2 + \ldots + x_i^2)} \tag{7.1}$$

with i representing the number of measured data points and x the difference between model curve and each individual data point. Following *Liddell et al.* (2017) the misfits for ϕ (RMS_ϕ) and δt ($\mathrm{RMS}_{\delta t}$) were normalized separately by the maximum possible value of both parameters (90° for ϕ and 4 s for δt) to ensure that both RMS values equally contribute to the overall misfit (RMS_{tot}). Thus, RMS_{tot} is a dimensionless quantity. However, for some stations characterized by complex splitting patterns the models were constrained based on a fit of only the fast axis values (see below). Modeling results of selected stations are discussed in the following section.

7.4.3 Evidence for anisotropy with a dipping symmetry axis

As mentioned before, the data coverage at most recording stations in Fennoscandia is generally limited to events from the northeast or southwest (Fig.7.4) However, the fast axis patterns of several stations indicate slight variations which are consistent for a bunch of events from similar directions while the delay times are nearly constant within this range. Fig. 7.19 shows representative stereoplots of stations for which I observe such characteristics. Obviously, a horizontal layer of anisotropy cannot reliably explain the observations since the variation of ϕ is a robust

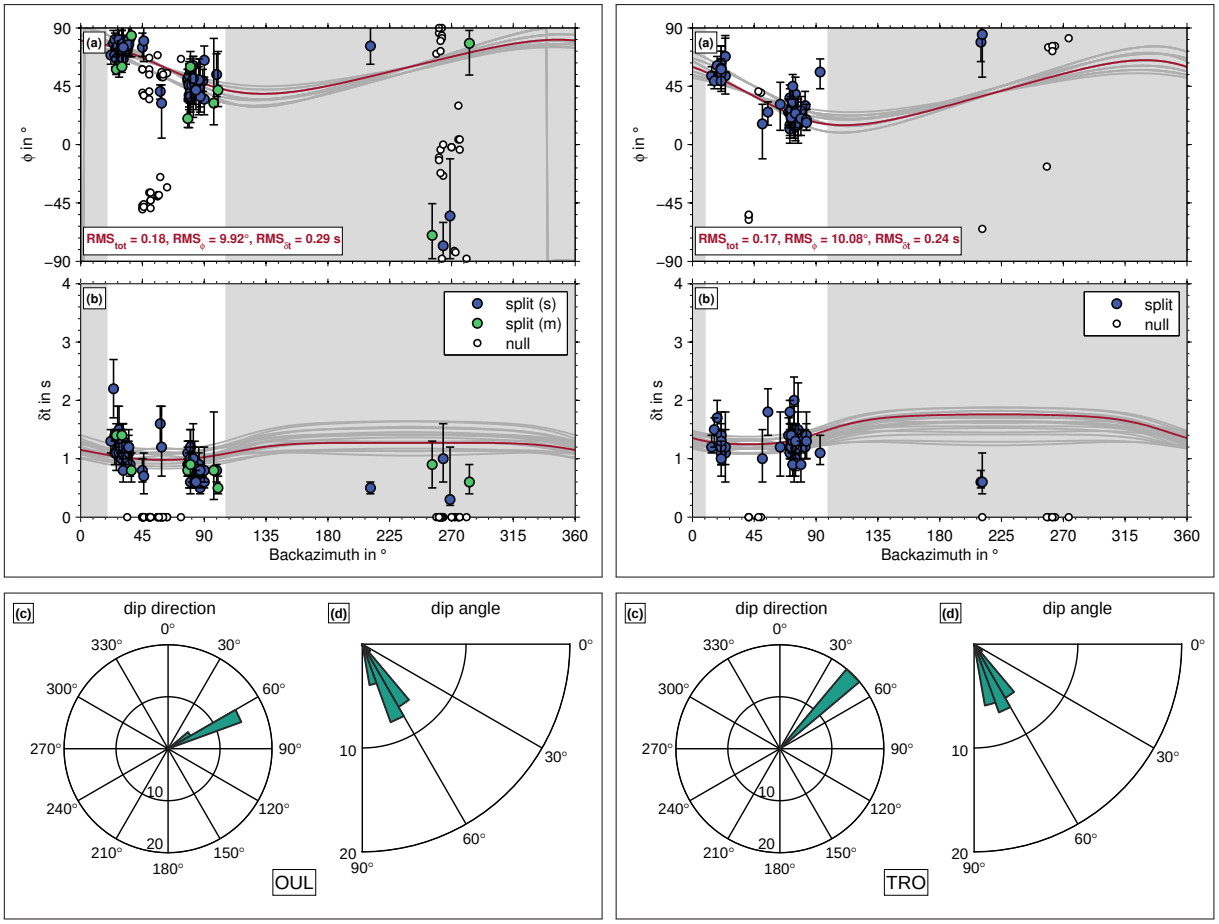

Figure 7.20: Modeling results for the two stations OUL (left column) and TRO (right column) assuming a dipping symmetry axis. (a) Distribution of apparent fast axis ϕ over backazimuth (BAZ). (b) Same for the delay time δt. Blue symbols with error bars (95% confidence interval) are single split measurements (only SC method shown), green ones show multi-splits based on surface stacking using the WS method (*Wolfe and Silver*, 1998, see section 5.3.3). Small dots filled white represent null measurements. The best-fit model is shown as red curve and the next 19 best models are shown as gray lines. Corresponding model parameters (dip direction and dip angle) are displayed in (c) and (d). Only the measurements included in the white sector are used for the modeling. Symbols in the gray backazimuthal range are only shown for the sake of completeness.

feature at all stations. A clear fast axis jump as well as significant delay time variation indicative for a two-layer model (Fig. 7.16) is also missing. Since I checked (and if necessary corrected) possible sensor misalignments, variations caused due to deviations of the initial polarization from the backazimuth for individual measurements can be ruled out as a primary reason. Furthermore, within the uncertainties ($\pm$ 10°), the measured initial polarizations of the arriving waves were aligned with the backazimuth direction of the corresponding event.

At all stations the consistent v-shaped pattern of splits with ϕ orientations separated into two clusters and nulls in the backazimuthal ranges in between represents the most striking characteristic. Therefore, I tested whether a dipping symmetry axis could explain these variations. In Fig. 7.20 I summarize the distribution of the models fitting best for the two stations OUL and TRO. Although the modeling was limited to a narrow backazimuthal range (white sectors), at

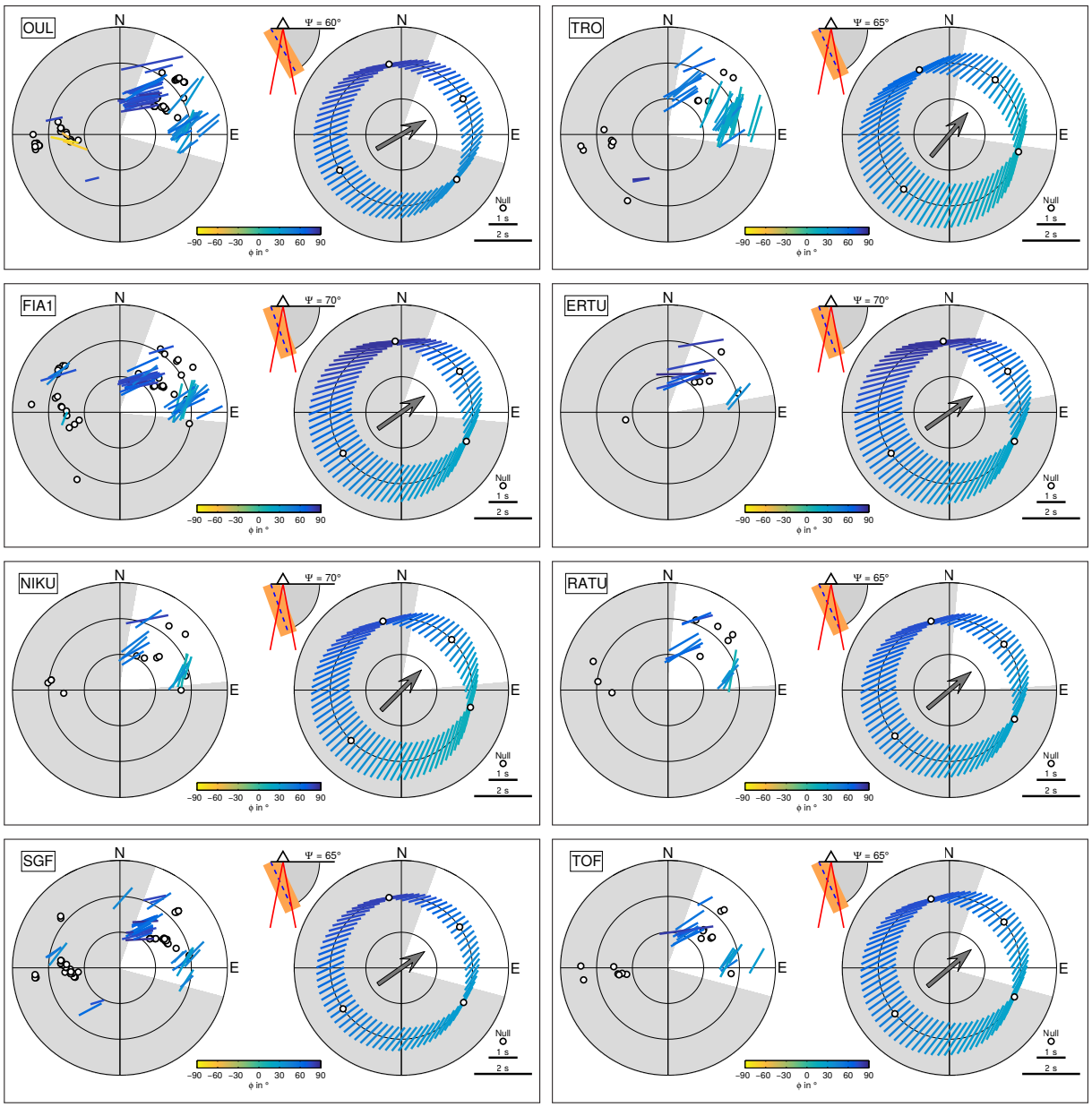

Figure 7.21: Comparison of observed (apparent) splitting parameters at eight seismic recording stations and theoretical parameters in stereoplot view computed based on the best-fit model for a dipping symmetry axis (see red curves in Fig. 7.20 for stations OUL and TRO). The gray arrow shows the down-dip direction (relative to geographic North) for the synthetics. Ψ indicates the dip angle of the symmetry axis (olivine *a*-axis, dashed blue line) relative to the horizontal (see also Fig. 7.17).

both stations the observations can be reasonably explained by models with a dipping symmetry axis. While the dip angles with $60° \pm 5°$ are similar for both stations, the down-dip directions slightly vary with $\phi' = 65°$ at OUL and $\phi' = 45°$ at TRO. This is not surprising since the overall pattern at both stations also shows variations between the two clusters of splitting observations. However, the down-dip directions for the 20 best models are well-constrained.

The success of the modeling becomes more obvious when comparing the measured splitting pattern of the stations shown in Fig. 7.19 with the synthetics of the best-fit model in stereoplot

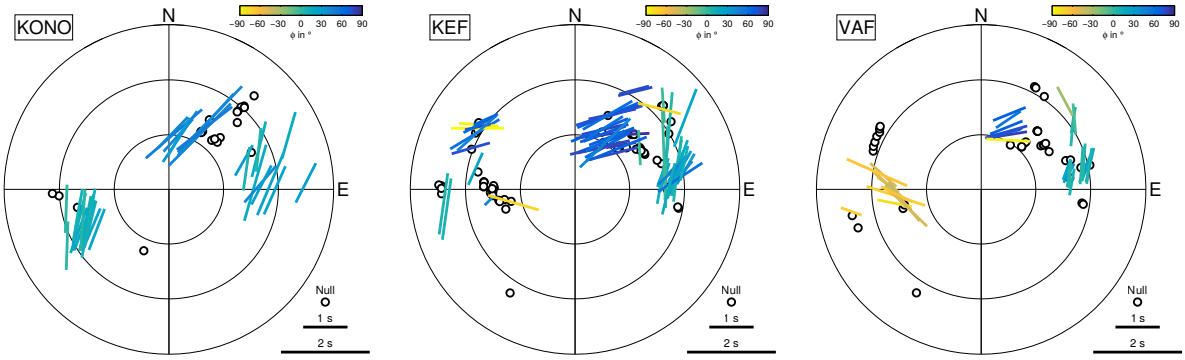

Figure 7.22: Stereoplots of the representative permanent recording stations KONO (left), KEF (center) and VAF (right) at which a complex pattern for the splitting parameters ϕ (orientation of bars and color-coding) and δt (length of bars) were found. Black circles display null measurements.

view (Fig. 7.21). Besides the reasonable reproduction of ϕ and δt, also the model predictions for nulls match very well with the splitting observations in areas between the split phases.

7.4.4 Non-uniqueness of models

The models discussed in the previous section are able to explain smooth variations of the splitting parameters within a limited backazimuthal range by a dipping symmetry axis. For other stations the data coverage is slightly better and therefore allows to test if two-layer models can also fit the observations, especially for wave arrivals from opposite directions. In the following I discuss representative examples of long-running permanent stations, each showing indications of anisotropy systems being more complex than a dipping symmetry axis.

KONO

At station KONO (Fig. 7.22, left) I observe a splitting pattern that is partly similar to those measured for the stations shown in the previous section. The northeastern quadrant is characterized by a v-shaped pattern with two sets of splits, each with consistent ϕ (averages $\sim 45°$ and $\sim 10°$) and δt as wells as nulls in between. Obviously, this splitting pattern is nearly identical to the pattern observed at station TRO (Fig. 7.19). However, additionally I measured a bunch of consistent splits in the southwestern quadrant for events from South America. With an average fast axis of $\sim 5°$-$10°$ these are very similar to the splits located between backazimuths of $\sim 75°$-$90°$ in the northeastern quadrant (greenish colors). Furthermore, these two groups are separated by nearly $180°$ with respect to the backazimuth. This allows to test the hypothesis of two anisotropic layers based on well-constrained observations from different backazimuthal ranges.

For the best-fit two-layer model shown in Fig. 7.23 the deviations of the predicted values from the measured ones are generally small for both, ϕ and δt, with a total normalized RMS misfit of 0.2. In order to explore the variability of models that explain the data adequately well,

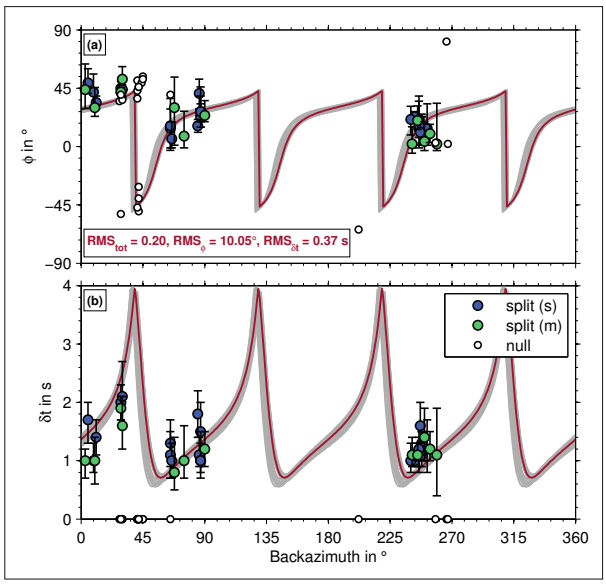

Figure 7.23: Modeling results for recording station KONO assuming a two-layer model of anisotropy. (a) Distribution of apparent fast axis ϕ over backazimuth (BAZ). (b) Same for the delay time δt. Blue symbols with error bars (95% confidence interval) are single split measurements (SC method shown), green ones show multi-splits based on surface stacking in bin steps with a maximum of 5° for BAZ and distance using the WS method (*Wolfe and Silver*, 1998). Small dots filled white represent null measurements. The best-fit model is shown as red curve and the next 19 best models are displayed as gray lines. The corresponding RMS misfit of the best model is shown in the upper panel.

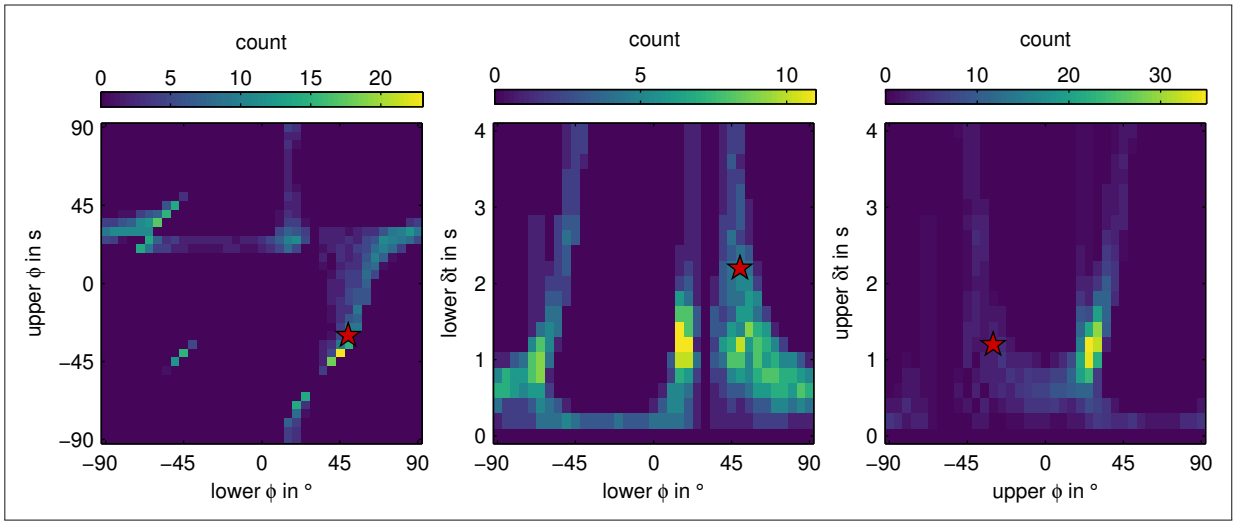

Figure 7.24: Characteristics of the 1000 best-fit two-layer models (out of 547600 totally tested models) for station KONO. The three subplots show individual 2D-projections of the whole model parameter space in which it is searched for the minimum RMS misfit. Color-coding of each cell represents the number of models which have the corresponding properties. The red stars indicate the characteristics of the best-fit model that is shown as red curve in Fig. 7.23.

in Fig. 7.24 the characteristics of the 1000 best-fit models (out of 547600 totally tested models) are displayed. With $\phi_{upp} = -30°$ and $\phi_{low} = 50°$ (Fig. 7.24, left panel, red star) the two fast axis orientations of the best-fit model are nearly perpendicular to each other. This parameter set is close to the global maximum with 23 counts ($\phi_{upp} = -40°$ and $\phi_{low} = 45°$, yellow square). However, there are also patches with increased numbers of counts which span from $-90°$ to $90°$ (ϕ), which means almost across the whole parameter range. The best-constrained parameter pair is the ϕ-δt combination of the upper layer (Fig. 7.24, right panel) but the best-fit model does not match with this value. Due to the variety of parameter sets that could explain the data, a two-layer model scenario is obviously not able to constrain the anisotropic signature with

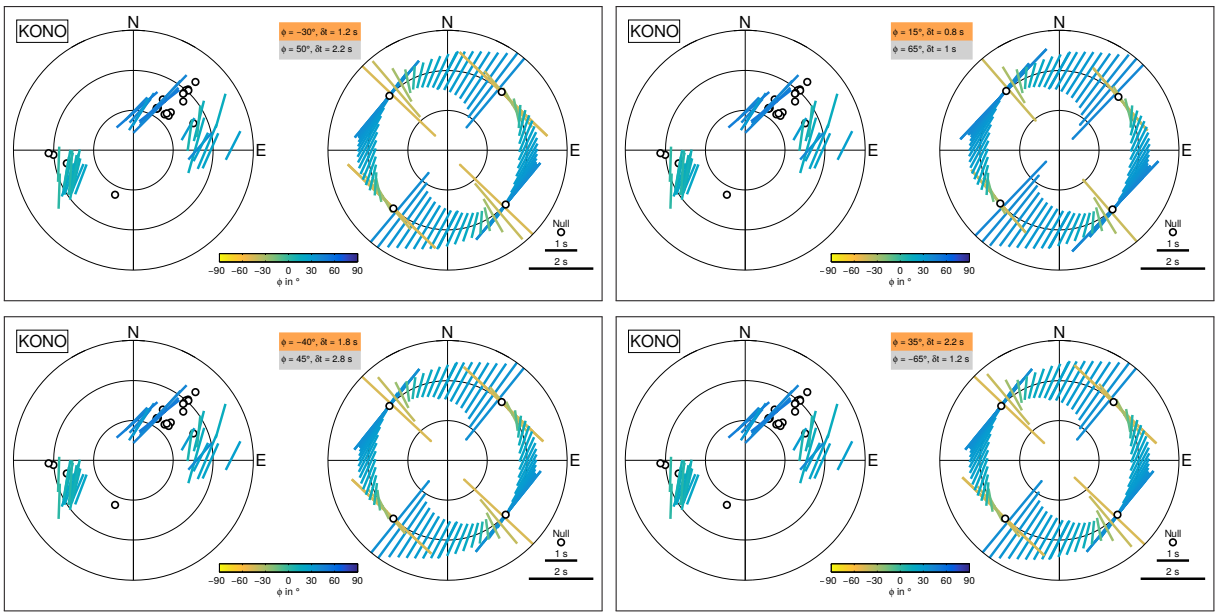

Figure 7.25: Comparison of observed (apparent) splitting parameters and theoretical parameters in stereoplot view computed based on the four best-fit two-layer models (see red Fig. 7.23) for station KONO. Note the almost identical splitting patterns, though the corresponding model parameters differ significantly.

high reliability. This becomes more obvious when comparing the corresponding stereoplot representations for the four best-fit models (Fig. 7.25). The individual splitting patterns are visually almost identical but the corresponding parameters for the upper and lower layer differ significantly. Furthermore, although the slight rotation of ϕ can be partly reproduced by all four models and the locations of nulls are adequately predicted, the delay times do not fit very well in this range.

Next, I searched for the best-fit model assuming a dipping symmetry axis. This approach was performed for two settings. First, for the whole backazimuthal range (as for the two-layer models) and secondly only for the northeastern quadrant (as in the previous section). In Fig. 7.26 the best-fit models with the variabilities of the corresponding parameters are shown. For both cases the models fit the observations sufficiently well, however, the determined parameters for the limited backazimuthal range (right column) performs better, especially for fitting ϕ. This is not surprising since if I compare the resulting stereoplots, the overall pattern (including the southwestern quadrant) does not show the splitting characteristics which would be expected for a dipping layer (Fig. 7.16). If only the northeastern quadrant is modeled, most aspects of the synthetic stereoplot match quite well with the observations (Fig. 7.27). Therefore, the splitting pattern at this station likely not only reflects a fast axis that dips by $45° \pm 10°$ toward the northeastern direction but also lateral variations of anisotropy around the seismic station. If I consider the stereoplots of stations that are located west of KONO (Fig. 7.13), the corresponding splitting patterns mostly show a similar trend as observed in the southwestern quadrant. Thus, waves arriving from this direction most likely sample an anisotropic volume west of the

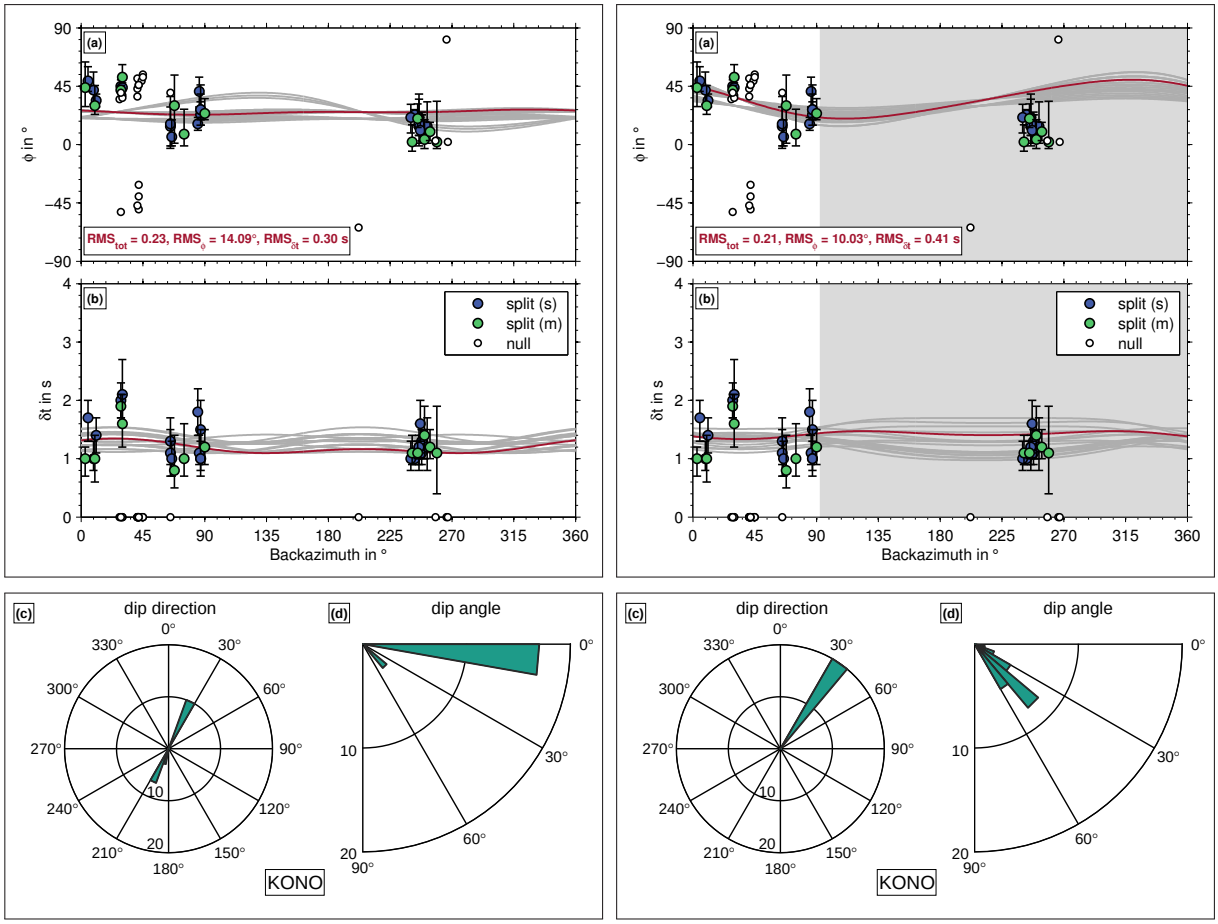

Figure 7.26: Modeling results within the full (left column) and only a limited backazimuthal range (right column) for recording station KONO assuming a dipping symmetry axis. Symbol conventions are as in Fig. 7.20. For the right column only the measurements included in the white sector are used for the modeling. Symbols in the gray range are only shown for the sake of completeness.

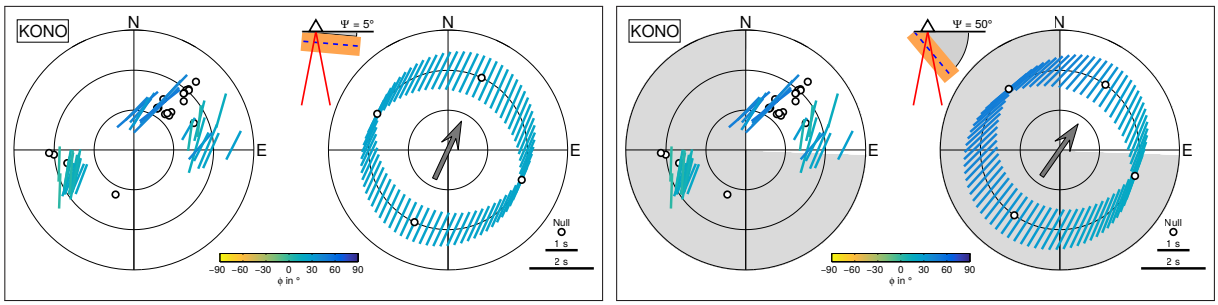

Figure 7.27: Comparison of observed (apparent) splitting parameters and theoretical parameters in stereoplot view computed based on the best-fit model for a dipping symmetry axis (see red curves in Fig. 7.26) at station KONO. Results for the full (left) and limited backazimuthal range (right) are displayed. The gray arrow shows the dip direction (relative to geographic north) for the synthetics. Ψ indicates the dip angle of the symmetry axis (olivine *a*-axis, dashed blue line) relative to the horizontal.

Oslo Graben while the measurements in the northeastern quadrant characterize an anisotropic fabric with a dipping symmetry axis, most probably related to the complex structure of the Oslo Graben itself.

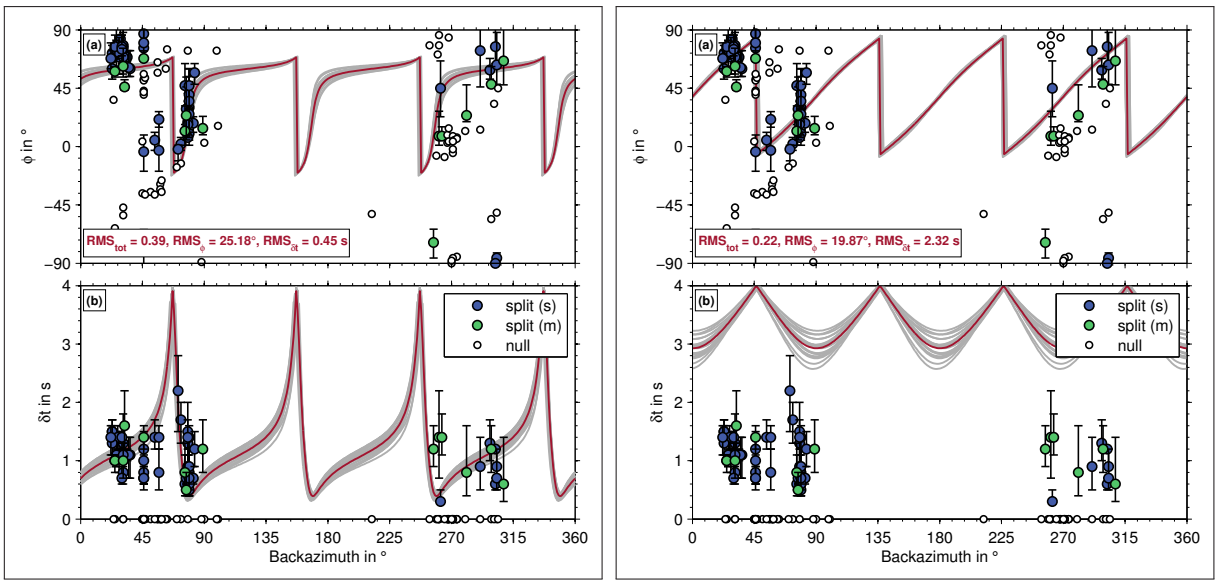

Figure 7.28: Modeling results for recording station KEF assuming a two-layer model of anisotropy. Left column shows models based on a combined minimum RMS misfit (ϕ and δt). Right column displays models only constrained by a minimum ϕ RMS misfit. Symbol conventions are as in Fig. 7.23. The total RMS misfit displayed in (a) in the right column is only calculated from the ϕ-fit.

KEF

As outlined before, in central and southern Finland some stations (KEF, KAF, PVF, RAF and VAF) show complex splitting patterns with strong variations over backazimuth. In the following I discuss the modeling for the representative permanent station KEF at which the splitting pattern has partly some similarity with the previously shown dipping layer characteristics (Fig 7.22). However, for ϕ there is no smooth transition visible but a relatively sharp flip from around $\phi = 60°$ to $\phi = 10°$ for backazimuths between 0° and 90°. Similar to the modeling for the previous section first the best-fit two-layer models for the full backazimuthal range were computed. If again the total (normalized) RMS misfit is taken, calculated from both, ϕ and δt deviations, the corresponding best-fit model has fast axes of 30° and 80° as well as delay times of 0.4 s and 1 s in the upper and lower layer, respectively (Fig. 7.28, left column). Although this ϕ_{upp}-ϕ_{low} combination is located within a patch of considerably increased numbers of counts in the parameter space distribution (Fig. 7.29, upper row, left panel), the highest counts are found for models with perpendicular fast axes in upper and lower layer (yellow cells). The individual ϕ-δt spaces for the two layers show different high-number counts with the best model pairs located close to the absolute maxima (Fig. 7.29, upper row, middle and right panel). Nevertheless, the ϕ values between backazimuths of 45°−60° cannot be explained by these models (Fig. 7.28). Furthermore, the delay times show no clear periodicity over backazimuth which would be expected for a two-layer model with horizontal symmetry axes.

Since the ϕ values indicate a distinct jump at a backazimuth of 45° next the best models for a fit of only the fast axis observations are explored. Thus, the RMS misfit calculated for

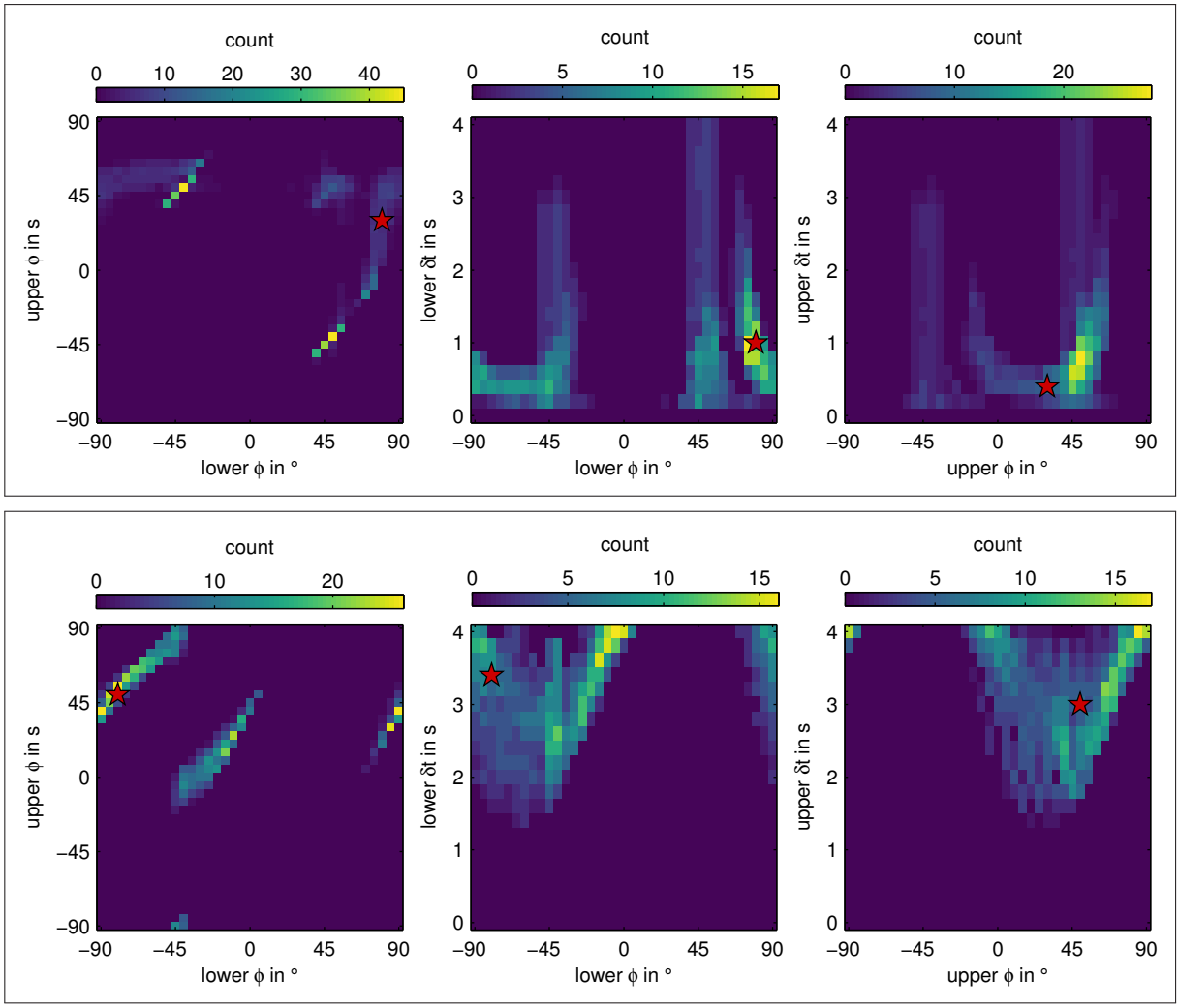

Figure 7.29: Characteristics of the 1000 best-fit two-layer models (out of 547600 totally tested models) for station KEF. Top row: combined ϕ-δt fit. Bottom row: ϕ-only-fit. Plotting conventions are as in Fig. 7.24. The red stars indicate the characteristics of the best-fit models that are shown as red curves in Fig. 7.28.

the delay times is not taken into account to find the best-fit models. A similar procedure was previously applied by *Marson-Pidgeon and Savage* (2004) for observations at station SNZO in New Zealand. Equally to my findings no significant variations of the delay times were measured while ϕ showed indications for a clear periodicity with respect to the incoming polarization directions. Using this criterion, the data is best explained by a two-layer model with fast axis directions of 50° in the upper and −80° in the lower layer (Fig 7.28, right column). As expected the model fits the ϕ pattern quite well but the corresponding predicted delay times are much too high (δt_{upp} = 3 s and δt_{low} = 3.4 s) and do not fit the data (with an average δt of $\sim$ 1.2 s) at all. Furthermore, the characteristics of the 1,000 best-fit two-layer models indicate that a variety of parameter sets could fit the data adequately well (Fig 7.29, lower row).

If the same modeling is performed for only a limited backazimuthal range between 20° and 95°, the best combined fit (ϕ and δt) offers no significant change (Fig 7.30, left column). Fur-

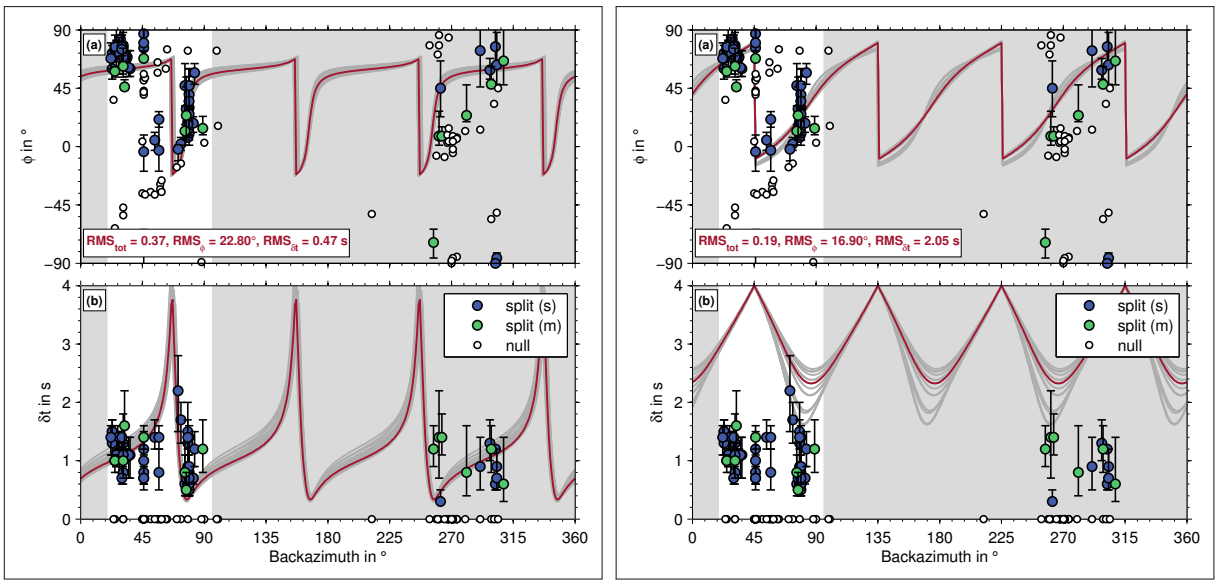

Figure 7.30: Modeling results for recording station KEF assuming a two-layer model of anisotropy within a limited backazimuthal range (white sectors). Left column shows models based on a combined minimum RMS misfit (ϕ and δt). Right column displays models only constrained by a minimum ϕ RMS misfit. Symbol conventions are as in Fig. 7.23. The total RMS displayed in (a) in the right column is only calculated from the ϕ-fit.

thermore, the model distributions in general are nearly identical showing different areas of high counts (Figs. 7.29 and 7.31, upper rows, red stars). When considering only ϕ in the misfit calculation, the characteristics of the best-fit model slightly change (Fig. 7.31, lower row). Nevertheless, as for the full backazimuthal range the ϕ pattern is reliably explained while δt again does not fit the data (Fig 7.30, right column).

The comparison of the stereoplots (for the full and limited backazimuthal range) show that the best-fit two-layer models obtained from the combined RMS misfit (ϕ and δt) generally cannot reproduce the pattern I observed (Fig. 7.32). As expected, for the ϕ-only fit the fast axis patterns match quite well, however, the delay times are not in scale since they would extend over the radial axis limits. Therefore, the fast axis can be fairly reconstructed but the delay times cannot be explained simultaneously at all. The delay times as predicted for the corresponding (fit) fast axes partly are three times higher than the observed values. In conclusion, although I have a sufficient data set based on long recording periods, the used modeling approach is not able to constrain the true characteristic of the anisotropy beneath KEF when assuming two horizontal layers.

In order to explore if the complex splitting pattern at KEF can be explained by a dipping symmetry axis (at least in parts), additionally I perform a model search in this parameter space for the limited backazimuthal range assuming lateral variations in anisotropy. The results are summarized in Fig. 7.33. The best model fits the observed δt values in principle quite well and also the locations of nulls show good agreement between synthetic and observed values. In contrast, ϕ can only be reconstructed in parts and the jump in the data between backazimuths

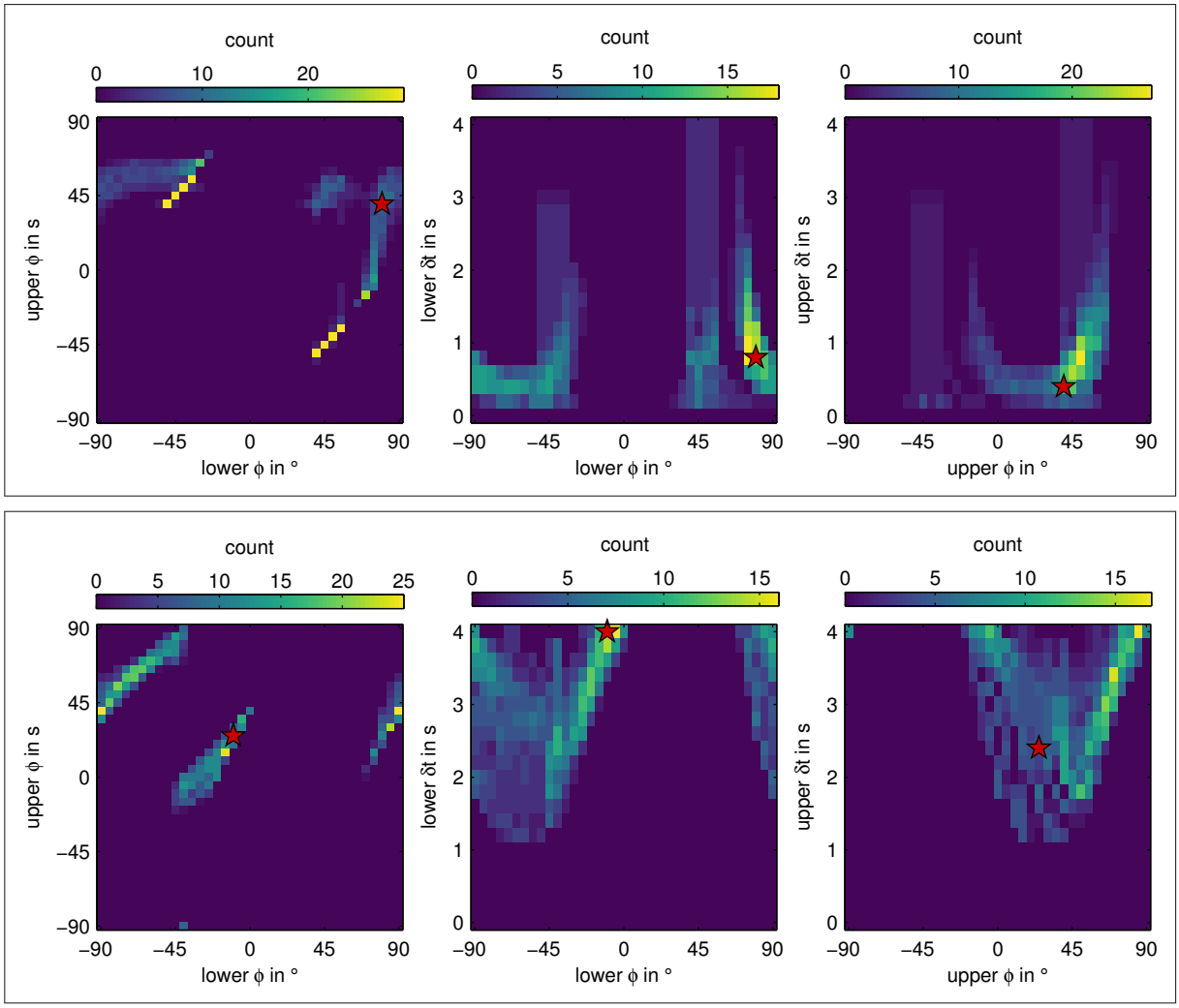

Figure 7.31: Characteristics of the 1000 best-fit two-layer models (out of 547600 totally tested models) for station KEF within a limited backazimuthal range (white sector). Top row: combined ϕ-δt-fit. Bottom row: ϕ-only-fit. Plotting conventions are as in Fig. 7.24. The red stars indicate the characteristics of the best-fit models that are shown as red curves in Fig. 7.30.

of 45° and 65° is not explained by the model at all. However, the down-dip direction and the dip angle are well-constrained based on the fits of the 20 best models.

VAF

With respect to the backazimuthal variations of ϕ and δt, VAF represents the station with the most complex splitting pattern across the ScanArray network (Fig. 7.22). As mentioned above, I observe three backazimuthal ranges with distinct differences for ϕ and partly δt. In general, the splitting pattern in the northeastern quadrant is nearly identical to that observed at station KEF. However, the delay times are much smaller with average values of ~ 0.75 s (compared to ~ 1.4 s at KEF). Obviously, a two-layer model for the full backazimuthal range cannot explain the measurements since the character of the splits for backazimuths of around $260° - 280°$ does not

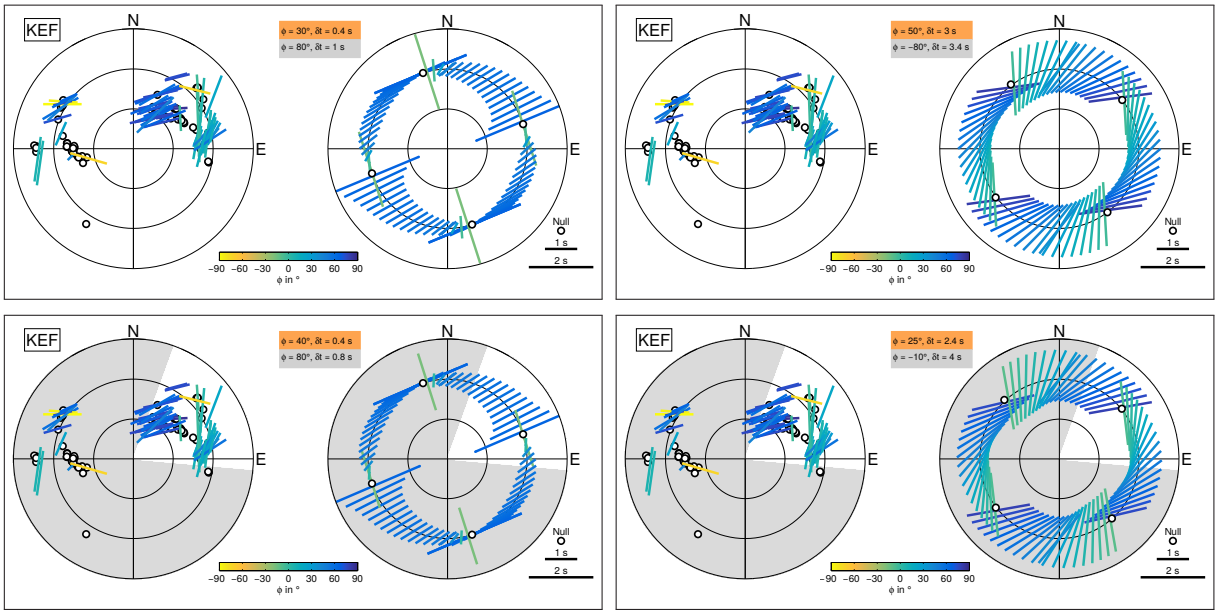

Figure 7.32: Comparison of observed (apparent) splitting parameters and theoretical parameters in stereoplot view computed based on the best-fit two-layer models for station KEF. Top row: full backazimuthal range, ϕ-δt-fit (left) and ϕ-only-fit (right), see red lines in Fig. 7.28. Bottom row: same for limited backazimuthal range (white sector, see also red lines in Fig. 7.30). Bar lengths in the right panels are uniformly scaled to 2 s and do not represent the true delay times of the models since they would extend over the radial axis limits.

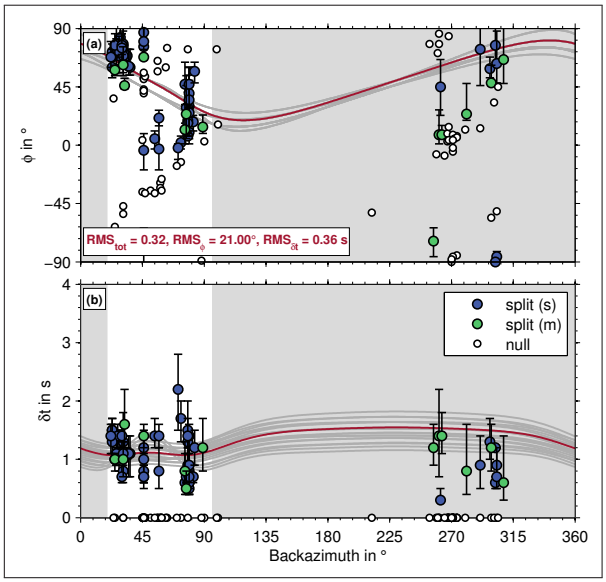

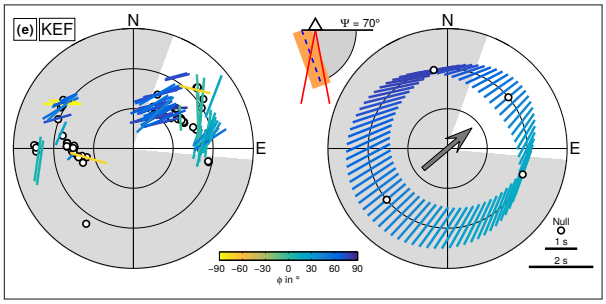

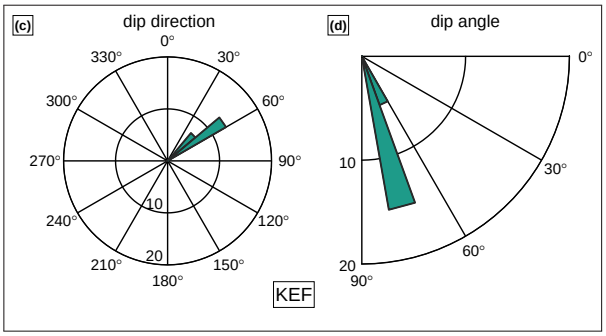

Figure 7.33: Modeling results within a limited backazimuthal range (white sector) for recording station KEF assuming a dipping symmetry axis. ← (a) Distribution of apparent fast axis ϕ over backazimuth (BAZ). (b) Same for the delay time δt. Symbol conventions are as in Fig. 7.20. Only the measurements included in the white sector are used for the modeling. Symbols in the gray range are only shown for the sake of completeness.
↑ Corresponding model parameters (dip direction and dip angle) are displayed in (c) and (d).
← (e) Comparison of observed (apparent) splitting parameters and theoretical parameters in stereoplot view. The shown pattern is based on the best-fit model highlighted by the red lines in (a) and (b).

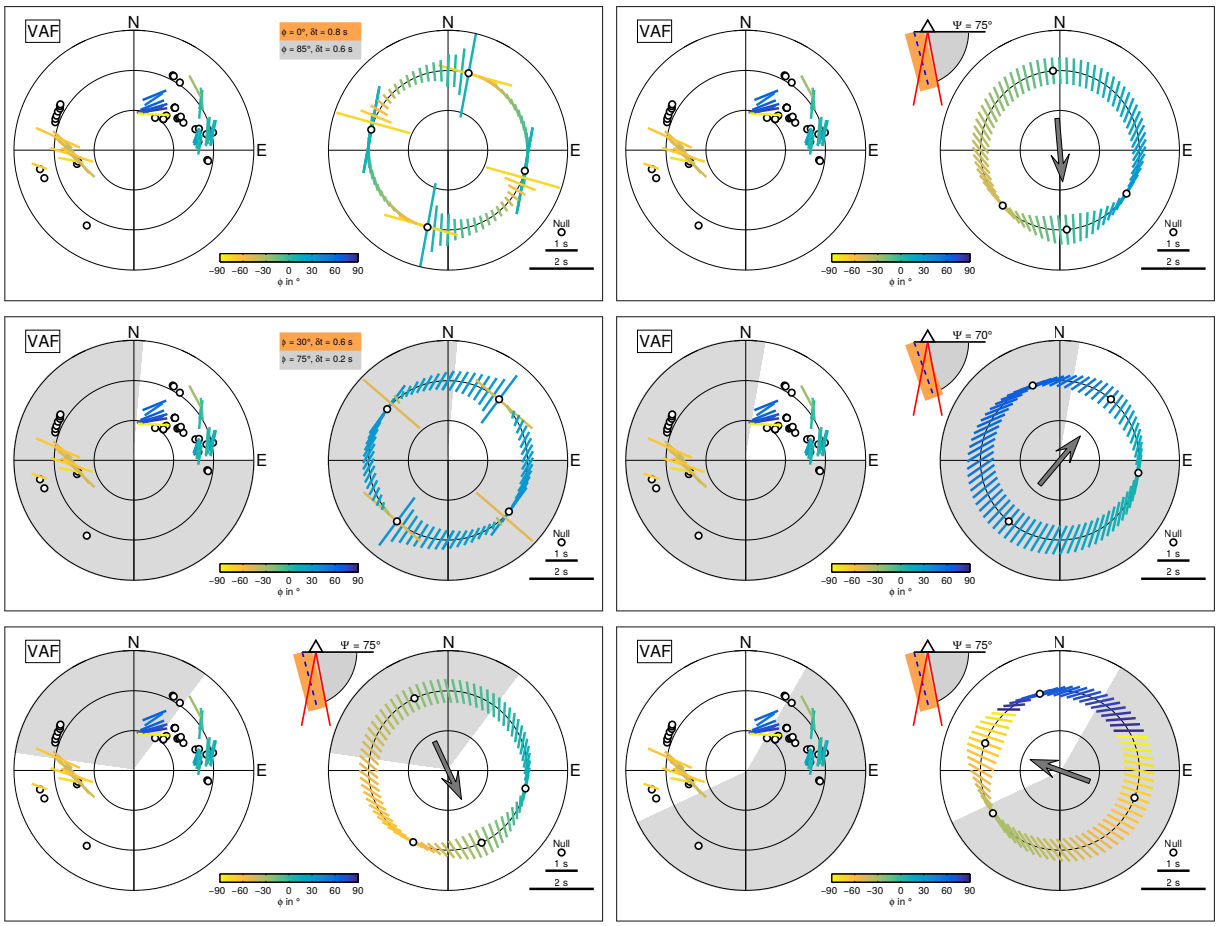

Figure 7.34: Comparison of observed (apparent) splitting parameters and theoretical parameters in stereoplot view computed based on different model settings for station VAF. Splitting parameters are robust estimates for each of the three clusters (blue, green and orange bars). However, none of the displayed models with two layers or a dipping layer of anisotropy can explain the splitting observations for the full backazimuthal range. Considering only limited ranges (white sectors) allows to fit the data sufficiently with individual models, all with different input parameters.

match with the values in the northeastern quadrant (BAZ $80° - 90°$) which would be expected for a $90°$ periodicity (compare Fig. 7.16). This is also seen in the corresponding stereoplot for the best-fit model where ϕ and δt do not fit at all for this setting (Fig. 7.34, left column, top panel). Similarly, a model with dipping symmetry axis is not able to reproduce the measured splitting characteristics (Fig. 7.34, right column, top panel).

The availability of three distinct groups of splitting estimates (each consistently robust) allows to explore also models based on different limited backazimuthal ranges. The central row of Fig. 7.34 displays stereoplots for the best-fit models (left panel: two-layers, right panel: dipping symmetry axis) based on data of only the northeastern quadrant (blue and greenish bars). While the two-layer model again cannot explain the splitting pattern, neither ϕ nor δt, the dipping layer model with a down-dip direction of $45°$ and a layer dip of $70°$ fits the data reasonably well. The locations of the measured null observations, however, scatter more than predicted from the model. If instead the group of splits with an average ϕ of $65°$ (blue bars) is excluded,

I receive a best-fit model with a down-dip direction of 150° and a layer dip of 75° (Fig. 7.34, bottom row, left panel). The modeled splitting parameters in general show good agreement with the observations, especially for ϕ, although the measured delay times for the arrivals from western backazimuths (orange bars) are slightly larger than the corresponding synthetics. Except for the southeastern quadrant, the distribution of observed nulls does not match the model predictions. Finally, only the groups of splits with fast axes of −60° (orange bars) and 65° (blue bars) are taken into account for calculating the RMS misfit. The synthetic stereoplot pattern of the corresponding best-fit model ($\phi' = 295°$ and $\Psi = 75°$) again shows substantial matching with the observations (Fig. 7.34, bottom row, right panel).

Therefore, based on these measurements alone it is quite difficult to constrain the true geometry and structure that causes the observed splitting pattern. Modeling the full backazimuthal range cannot recover splitting characteristics that explain all the observations. Thus, the interpretation is complicated by lateral anisotropy variations around some stations and the number of models which can explain the data with nearly the same reliability increases. Furthermore, observations from additional backazimuths, which could potentially help to rule out some of the presented model settings, are often not available.

7.5 Discussion and interpretation

While structural models with two stacked horizontal anisotropic layers are often used to explain variations of the splitting parameters with backazimuth (e.g. *Silver and Savage*, 1994; *Levin et al.*, 1999; *Currie et al.*, 2004; *Yang et al.*, 2014), the detection of systems with a dipping symmetry axis from shear wave splitting measurements alone is limited to only few studies (e.g. *Hartog and Schwartz*, 2000; *Hicks et al.*, 2012; *Liddell et al.*, 2017). There are many more cases in which a dip of the symmetry axis was inferred by the joint inversion of different body wave types, especially for some areas of the region studied in this thesis (e.g. *Babuška et al.*, 1993; *Plomerová et al.*, 2006; *Vecsey et al.*, 2007). The detailed modeling shown in the previous sections documents that the interpretation of the splitting measurements is not straightforward, although the data coverage at several stations in general allows to exclude a simple one-layer anisotropy due to the observations. In particular, one has to keep in mind that the splitting parameters can partly be explained by significantly different model parameters in the same way and with nearly identical RMS misfits. Furthermore, distinct lateral variations of the splitting patterns can be observed across the whole network. Therefore, it is quite important to discuss the individual station results not only as independent solutions but also in a broader context which enables to search for similarities (or discrepancies) over different scales.

7.5.1 Can the splitting patterns be associated with tectonic units and events?

Discussing the modeling results in the context of the tectonic and geological evolution of Fennoscandia allows to associate some of the splitting characteristics with past deformation events. In Fig. 7.35 I summarize the modeling results together with the major tectonic units of Fennoscandia.

The simple pattern for most stations located in southern Norway, northern Denmark and western Sweden allowed to calculate station averages for ϕ and δt, although the data coverage is mostly limited to two quadrants in stereoplot view (Fig. 7.13) and, therefore, more complex models cannot fully be ruled out. As indicated before, the orientation of ϕ smoothly rotates from around 0° to -20° in southern Norway to a -60° orientation further east (Sveconorwegian domain, orange) which is parallel to the dominant strike of the STZ. This suture zone is related to the collision of Avalonia and Baltica which caused large-scale deformation in the crust and mantle (e.g. *Torsvik and Rehnström*, 2003). Although the seismic properties constrained by tomographic images in general offer differences between the Proterozoic Europe and the Precambrian Baltic Shield (e.g. *Zielhuis and Nolet*, 1994), more recent regional studies (based on *P*- and *S*-waves) consistently show a sharp contrast for seismic velocities that separates southern Norway and northern Denmark from shield areas east of the Oslo Graben (*Medhus et al.*, 2009, 2012; *Wawerzinek et al.*, 2013). This transition zone roughly coincides with the observed rotation of ϕ and runs in nearly N-S direction through the Oslo Graben area. The anisotropic signatures at stations located on both sides of the STZ in Denmark and southwestern Sweden, however, do not differ significantly. The delay times observed for southern Norway (averages of 0.7 s to 1 s) are generally smaller than the previously reported values by *Roy and Ritter* (2013). However, for some stations δt is up to 1.5 s on average (Fig. 7.35). Since these values significantly exceed the typically observed magnitude for crustal anisotropy of 0.2 s to 0.3 s (*Crampin and Booth*, 1985; *Barruol and Mainprice*, 1993), a strong contribution from deeper structures such as the mantle lithosphere is necessary to explain the relatively large delay times. This is supported by a similar pattern (ϕ and δt) that was previously observed based on data of the temporary TOR experiment and associated with vertical coherent deformation of the lithosphere (*Wylegalla et al.*, 1999). With the increased data coverage being available this spatial correlation now becomes more obvious.

In contrast, the modeling at station KONO, based on robust measurements, indicates that the splitting pattern most likely reflects an anisotropic fabric that steeply dips towards NNE parallel to the dominant strike of the graben (Figs. 7.23–7.27). While generally similar orientations for ϕ were observed in the past (*Vinnik et al.*, 1992; *Wylegalla et al.*, 1999; *Roy and Ritter*, 2013), the characteristic v-shaped pattern in stereoplot form for the northeastern quadrant has not been documented so far. The formation of the Oslo Graben was accompanied by several epsiodes of

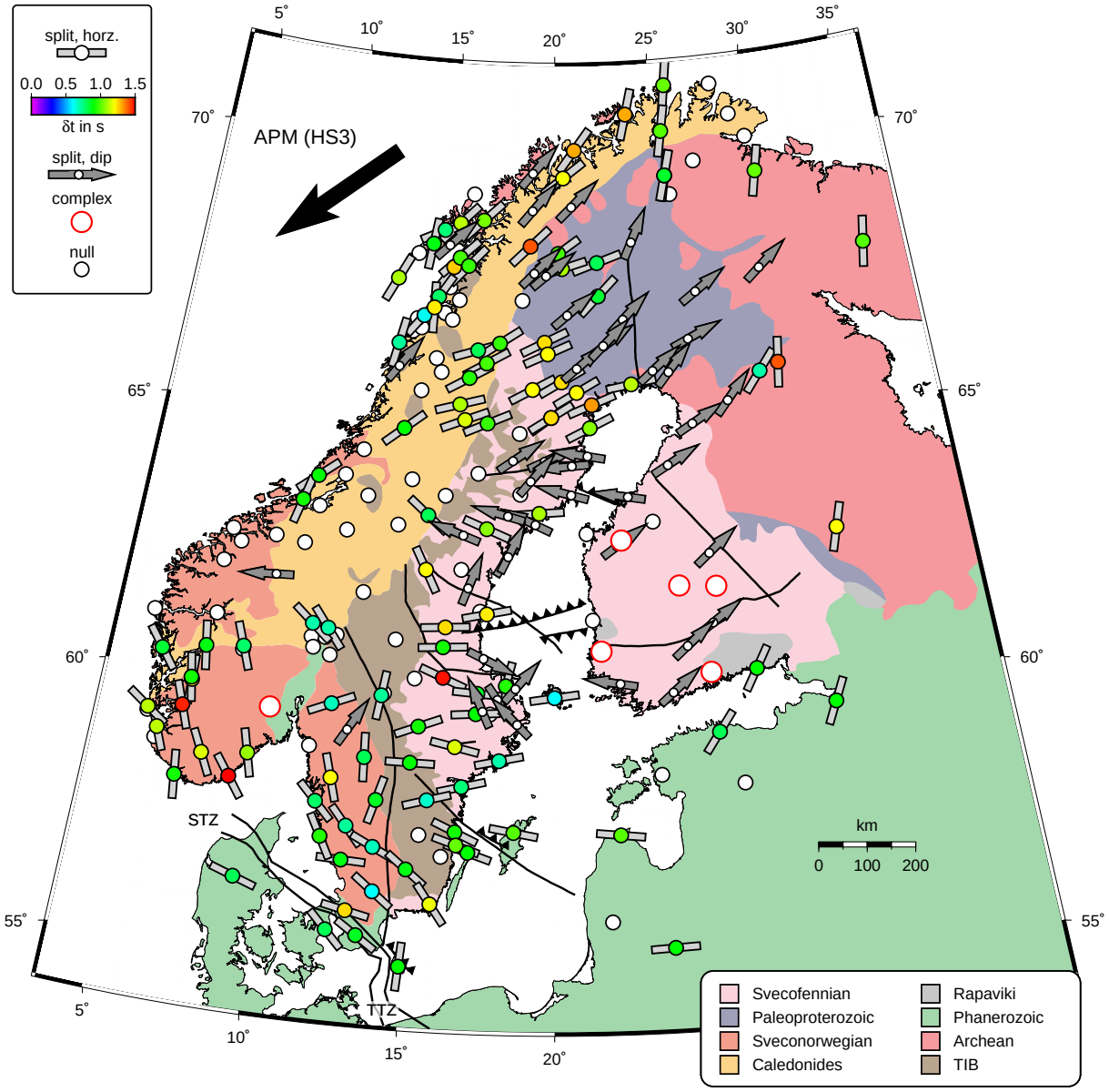

Figure 7.35: Map highlighting the modeling results together with the major tectonic units of Fennoscandia (background colors) after *Gorbatchev* (2004) and *Korja and Heikkinen* (2005). Stations with relatively simple splitting characteristics are shown as gray bars which indicate average values for ϕ and δt calculated with the WS method (*Wolfe and Silver*, 1998). The color fill of each circle represents the average delay time. Dark gray arrows indicate stations at which the data are best explained by a dipping layer of anisotropy with the arrow pointing into the down-dip direction. Stations at which the data-fit delivered non-unique models are shown as enlarged white dots with red edges. Null stations are displayed as white dots with black edges. The black arrow in the upper left corner indicates absolute plate motion direction (APM) in a hotspot reference frame (HS3-NUVEL 1A) after *Gripp and Gordon* (2002).

compressional and extensional deformation related to changing stress fields (*Heeremans et al.*, 1996). For vertically coherent deformation of the crust and upper mantle caused by rifting, ϕ would align parallel to the dominant extension direction of the graben in E-W direction (e.g. *Silver*, 1996). A compressional stress regime with the maximum horizontal stress component σ_1 aligned in nearly NW-SE direction would instead affect LPO-anisotropy with a ϕ orientation normal to the primary stress component in NNE-SSW direction. This correlates well with the down-dip direction of my observations. Therefore, the ϕ orientation may be related to the Caledonian orogeny whose assumed suture is nearly parallel to the modeled fast axis orientation and which is assumed to have caused a significant tectonic imprint in the Oslo Graben area (*Heeremans et al.*, 1996). An alternative explanation for a graben-parallel orientation of ϕ is that melt-filled pockets, fractures or dykes, aligned parallel to the strike of the rift, are located beneath the Oslo Graben. Although past magmatic activity is well documented (e.g. *Neumann et al.*, 1992), in comparison to other rift zones around the globe (e.g. *Gao et al.*, 1997; *Kendall et al.*, 2006) the Oslo Graben is not active anymore and therefore it is unlikely that partial melt plays a major role in this context. Nevertheless, the anisotropy may also characterize solidified oriented dykes. The dip of ϕ, however, cannot be explained by both scenarios alone.

For stations located east and west of the Sveconorwegian deformation zone (SNDF) the orientations of ϕ abruptly change from a nearly N-S direction on the Sveconorwegian domain (Fig. 7.35, orange) to an E-W alignment on the TIB (brown) and Svecofennian domain (pink). The western stations fit into the overall picture by representing a smooth rotation towards the STZ-parallel ϕ direction observed at stations further south. This pattern has not been documented in such detail before since previously analyzed stations of the SNSN (*Eken et al.*, 2010) were located only east of the deformation zone. The results of *Eken et al.* (2010) for the eastern part based on joint inversions of shear wave splitting measurements and *P*-wave residuals, however, are generally consistent with my findings based on more recent data. Furthermore, few observations of variations across the SNDF from a short-running temporary deployment were limited to a relatively small area at around 60°N (*Plomerová et al.*, 2001). Such abrupt changes of ϕ within short distances are strong indicators for fossil frozen-in anisotropy (e.g. *Chevrot et al.*, 2004) that was imprinted into individual mantle lithosphere fragments before their accretion onto the Baltic Shield (e.g. *Plomerová et al.*, 2001; *Plomerová et al.*, 2002a; *Eken et al.*, 2010). At this point it has to be mentioned that observed *P*-wave residuals may also be attributed to general velocity heterogeneities and, therefore, it is difficult to distinguish them from likely anisotropic contributions (*Plomerová et al.*, 2006).

A more complex picture appears for the Svecofennian domain in eastern Sweden up to around 65°N latitude. Although it was possible to calculate simple station averages with dominantly E-W orientations for ϕ and 0.7 s to 1.3 s for δt at several stations assuming one anisotropic layer with horizontal symmetry axis, observations of some sites in between were best fitted by a dipping layer geometry. As already pointed out by *Eken et al.* (2010) the varying splitting pat-

terns (different ϕ and dip angles) in the most southern part indicate complex anisotropy within short lengthscales. West of the Svecofennian domain atop the Caledonian nappes the recording stations are dominantly characterized by nulls. However, at this point it has to be mentioned that for some stations the azimuthal data coverage was worse compared to other stations across the study region. Therefore, this pattern may also reflect poor sampling of (potentially) anisotropic structure and does not necessarily mean that an isotropic rock volume is located beneath this area. Alternatively, the presence of two anisotropic layers with orthogonal symmetry axes but similar strengths would result in apparent null observations (e.g. *Silver and Savage*, 1994). For deformation related to the Caledonian orogeny one would expect a fast axis orientation that is nearly parallel to the strike of the present Scandinavian mountain chain (*Vauchez and Nicolas*, 1991; *Silver*, 1996, see also section 2.4.2). Only a few stations located along the western coast of Norway show such a NE-SW orientation for ϕ. In contrast, for stations north of 65°N, ϕ is consistently aligned in NE-SW direction across different tectonic domains from the Lofoten Islands in the northwest to the Bothnian Sea in the southeast. Although no clear orogen-parallel fast axis is measured for the southern region, an influence of the Caledonian collision (which represents the last major tectonic event) is most plausible to explain the splitting observations.

The most robust feature constrained by the modeling is a dipping symmetry axis geometry below stations mainly located on the Paleoproterozoic domain (purple area) with a dip towards NE by angles of 60° to 70° (Fig. 7.35). Some of the exemplary stations shown in Fig. 7.19 are located in this area. These findings are generally consistent with the results of *Eken et al.* (2010) for the most northern stations of the SNSN. Furthermore, anisotropy beneath the Paleoproterozoic domain was analyzed previously in the framework of the LAPNET project (*Plomerová et al.*, 2011; *Vinnik et al.*, 2014). While *Plomerová et al.* (2011) indicated spatial variability of anisotropic fabrics related to different tectonic blocks, *Vinnik et al.* (2014) found evidence for multi-layered anisotropy in different depths ranges. Since the consistent dip pattern from the modeling is observed across a widespread area, two scenarios are plausible to explain a dip of the fast axis. The first is based on the assumption that the measured anisotropic signature (with dipping symmetry axis) was already imprinted into the whole lithosphere long before the formation of the Baltic Shield during the phase of craton building. Alternatively, several episodes of subduction "transformed" the previously horizontal fast axis to a dipping one by inclining the orientation as a result of multiple underthrusting events (Fig. 7.36). Such model was proposed by *Babuška et al.* (1993) to explain the growing of cratons and continents. In the Gulf of Bothnia at around 64°N, a NE-dipping reflector was constrained from reflection seismic data in the framework of the BABEL project (*BABEL Working Group*, 1990; *Balling*, 2000). This inclined reflector was interpreted as a remnant of a paleo-subduction system (Fig. 7.37). However, the profile only enables a 2D view on this area and the lateral extension of the reflector and the average dip-angle are not well-resolved (*Balling*, 2000). Large-scale layering beneath Fennoscandia, indicative for several tectonic collision regimes, was inferred by

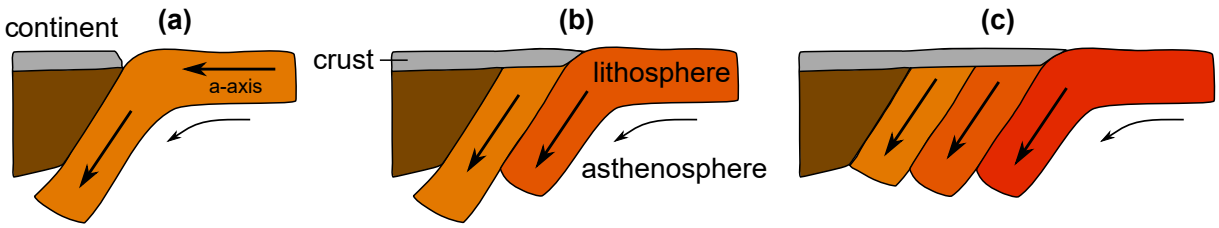

Figure 7.36: Schematic showing different stages of a continental growth. (a) An initially horizontal *a*-axis (e.g. frozen into the lithosphere) is inclined by initiated subduction and the lithospheric fragment is accreted on the continent. (b) and (c) Further episodes of subduction generate large anisotropic structures with characteristic dipping *a*-axes (modified after *Babuška et al.*, 1993).

receiver function analysis. Compared to other areas of (active) subduction processes like the Tibetan Plateau and the Himalayas, the likely signatures of ancient subduction zones beneath Fennoscandia cannot be clearly resolved so far (*Kind et al.*, 2013). Nevertheless, recent work based on *S*-wave receiver functions from the Canadian Shield supports this hypothesis and presumes that dipping mid-lithospheric layers may be a general characteristic of old shield areas (*Miller and Eaton*, 2010). Therefore, the steeply dipping symmetry axes, observed consistently within a widespread area, are a likely candidate to explain accretion due to several episodes of paleo-subduction. In contrast to previous studies in Fennoscandia (*Eken et al.*, 2010; *Plomerová et al.*, 2011), the dipping symmetry axes, however, can be clearly constrained from shear wave splitting measurements alone. Globally such observations are rare (*Hartog and Schwartz*, 2000; *Liddell et al.*, 2017) since the characterization of the indicative splitting pattern depends on sufficient data coverage.

The Paleoproterozoic domain is also traversed by the Baltic Bothnian megashear zone (BBZ) which runs in N-S direction nearly parallel to the national border between Sweden and Finland (*Berthelsen and Marker*, 1986). For a splitting signature related to deformation from the active episodes of the BBZ, a ϕ orientation parallel to the strike of the shear zone (roughly N-S) or at least a contrast to the surrounding areas would be expected (e.g. *Chevrot et al.*, 2004). Such a N-S oriented characteristic, however, is only found for stations located northeast and east of the BBZ, mainly on the Archean domain (red). Similar orientations for ϕ were also measured by *Vinnik et al.* (2014). The pattern observed for the region east of the BBZ is equivalent to the rest of the Paleoproterozoic domain and, therefore, the measured shear wave splitting is likely not related to the BBZ. In contrast, the consistent N-S orientation of ϕ at the sparse number of stations on the Archean domain is well constrained based on mostly long recording periods at the corresponding permanent stations (see Fig. 7.15, e.g. the most eastern station JOF). Therefore, this sharp contrast for the orientation of ϕ again indicates that laterally different fabrics (related to the different tectonic units) are responsible for the change in the observed splitting pattern.

The most complex area to interpret is the Finnish part of the Svecofennian domain (Fig. 7.35). In the past shear wave splitting was studied together with *P*-residuals in this area. The observations were mostly modeled with a dipping symmetry of anisotropy that varies between

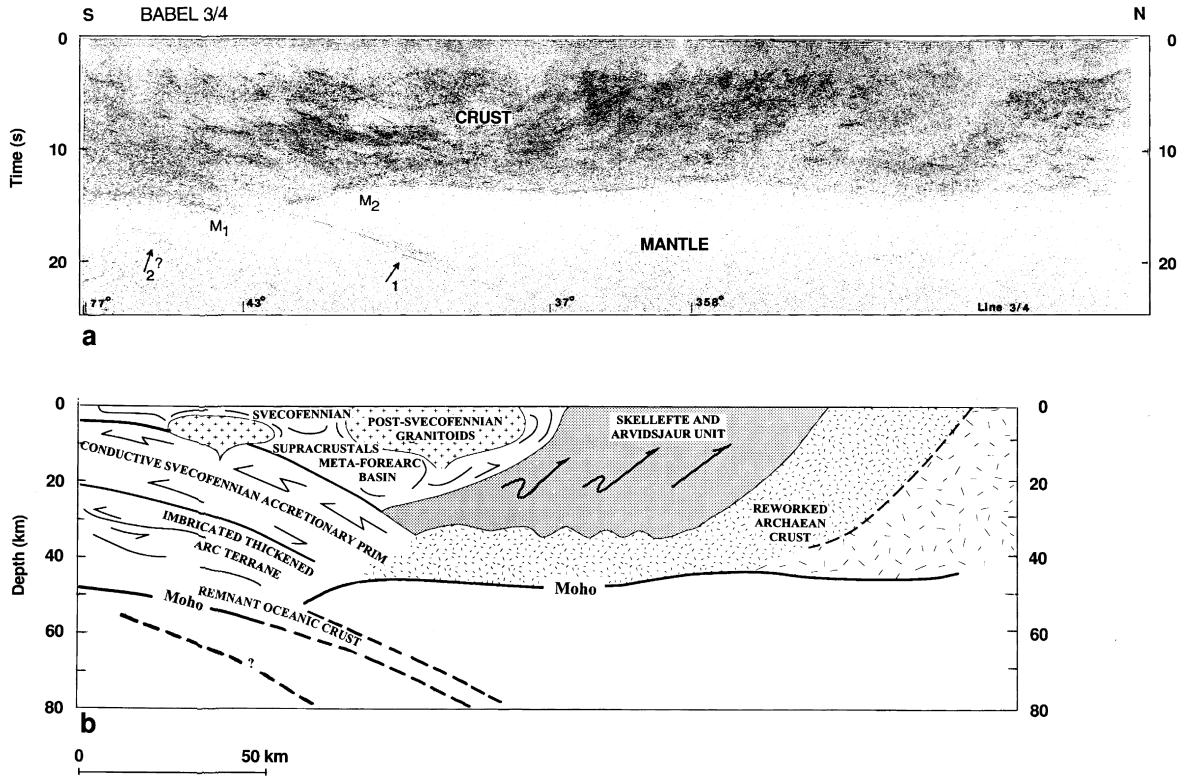

Figure 7.37: Findings and interpretation of reflection seismic data collected in the northern area of Fennoscandia in the framework of the BABEL project (*BABEL Working Group*, 1990; *Balling*, 2000). (a) Depth-migrated seismic section. (b) Associated integrated structural and tectonic interpretation. The dipping reflector was interpreted as a remnant of a paleo-subduction system (see *S1* in Fig. 7.1).

different tectonic blocks (*Plomerová et al.*, 2006; *Vecsey et al.*, 2007). Compared to my measurements at mostly long-running permanent stations, earlier studies were based on data of the dense temporary deployment SVEKALAPKO with only seven events of sufficient quality for a splitting analysis (*Vecsey et al.*, 2007). Although the lateral resolution here is worse than for the SVEKALAPKO array, at several stations I was able to analyze data of partly more than ten years of observation compared to a maximum of five months of data recorded during the temporary SVEKALAPKO deployment. In contrast to previous work, this allowed me to constrain the lateral anisotropic pattern with shear wave splitting measurements alone. While for the northern area the *a*-axis dip towards NE is similar, for the central part of Finland I partly observe more complex splitting characteristics (Fig. 7.35, red circles) which only in parts agree with the findings of *Plomerová et al.* (2006) and *Vecsey et al.* (2007). As representatively demonstrated for station KEF (see section 7.4.3), it is neither possible to fully explain the observations (ϕ and δt) with a dipping layer nor a two-layer scenario (Figs. 7.28-7.33). Similarly, for station VAF parts of the data can be explained by different models, each with a fast axis dipping into another direction (Fig. 7.34). However, few surrounding stations are robustly modeled with a dip of the *a*-axis that is similar to the observations north of 65°N (Fig. 7.35). This suggests that also

lateral variations around the individual stations may play a role. The previously documented lateral variations of the splitting parameters across the contact zone between the Paleoproterozoic Svecofennian domain and the Archean basement (*Vecsey et al.*, 2007) cannot be resolved with the current station distribution.

7.5.2 Comparison with surface wave data and absolute plate motion

The observation of split core-refracted shear waves indicates that anisotropy is located somewhere between the core-mantle boundary and the receiver at the surface. Thus, the depth estimation of the source of anisotropy cannot be determined from splitting measurements alone. In contrast to core-refracted shear waves, surface waves have a much better depth resolution, however, their lateral resolution is usually limited due to the long wavelengths (partly > 200 km). Therefore, estimates of azimuthal seismic anisotropy deduced by surface-wave analysis on a regional (e.g. *Zhu and Tromp*, 2013) or global scale (e.g. *Becker et al.*, 2012; *Schaeffer et al.*, 2016) mostly resolve smooth variations across different areas since the waves potentially sample portions of different anisotropic fabrics. Nevertheless, large-scale variations in anisotropy may also be resolved in shear wave splitting measurements, provided that a dense, large-aperture station network is available. Despite partly strong variations of the splitting parameters with backazimuth and indications for a dipping symmetry axis, a comparison of the observations obtained from both approaches can be used to find similarities and/or discrepancies and may finally help to constrain an approximate depth range for the anisotropy beneath Fennoscandia.

A recent azimuthally anisotropic model based on adjoint tomography impressively reveals high correlations between the observed anisotropy and large-scale tectonic features in Europe and the North Atlantic (*Zhu and Tromp*, 2013; *Zhu et al.*, 2015). Fig. 7.38 shows anisotropy fast axis orientations and strengths determined from surface wave data for Fennoscandia together with the best-fit models received from the splitting analysis in four different depth ranges. For depths of 100 km and beyond the fast axis directions (blue bars) are relatively constant for individual regions and provide only variations of the peak-to-peak amplitudes. The dominant trends from surface waves generally show high correlations with the splitting results, especially for the nearly NE-SW directions observed for parts of the Caledonides and the rotation of the fast axis towards a NW-SE direction parallel to the STZ in the most southern part of the study region. Weak anisotropy is consistently observed for all depth ranges in the area of the southern Caledonian nappes that is dominated by null splits (white circles with black edges) confirming the previously discussed possibility of partly isotropic fabrics in crust and lithosphere. Thus, an alternative scenario of two layers with orthogonal symmetry axes and similar strengths resulting in apparent null splits can also be ruled out with high probability.

Due to the high correlation of the fast axis orientations in the western part of the study region (west of $\sim 21^{\circ}$E), the peak in anisotropy strength allows to locate the main sources responsible

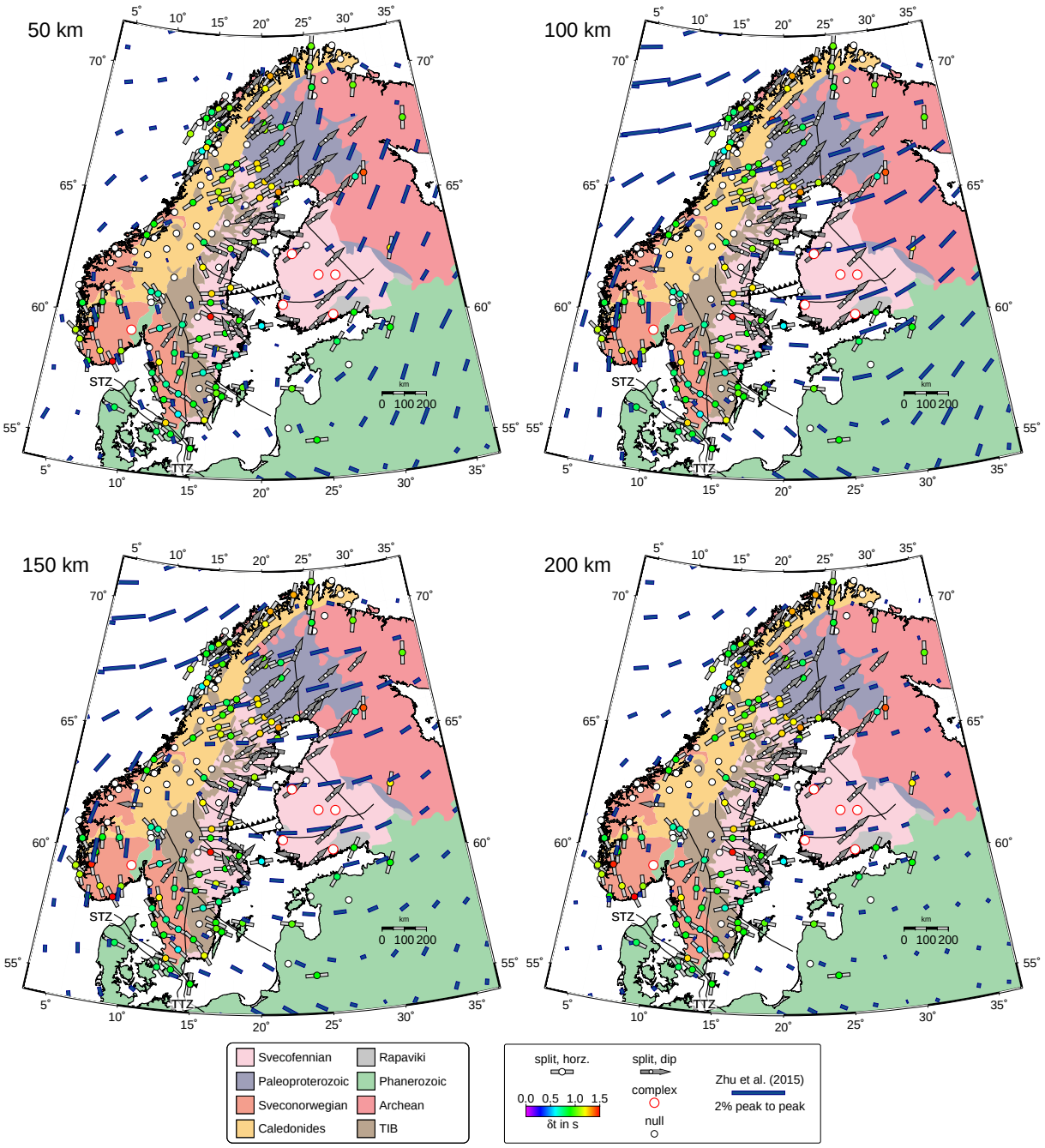

Figure 7.38: Same content as in Fig.7.35 together with the estimates of azimuthal anisotropy derived from surface-wave tomography (*Zhu and Tromp*, 2013; *Zhu et al.*, 2015) in different depths (50 km, 100 km, 150 km and 200 km). The directions and amplitudes of the fast axes are given by the orientations and lengths of the blue bars.

for the shear wave splitting in a depth interval of 70 km to 170 km (Fig. 7.38). Due to general agreement between splitting estimates from phases that were converted from *P*-to-*S* at the 410 km discontinuity (*Olsson*, 2007) and measurements from core-refracted phases, *Eken et al.* (2010) suggest that anisotropy beneath the SNSN stations is located shallower than 410 km. The lithosphere-asthenosphere boundary beneath Fennoscandia is located in depths of 200-250 km (e.g. *Plomerová et al.*, 2002b; *Artemieva*, 2006). Therefore, most of the anisotropy is likely located in the lithospheric lower crust and uppermost mantle which supports the idea of fossil frozen-in anisotropy.

Another component which can cause anisotropy is the LPO of mantle minerals like olivine due to asthenospheric mantle flow (e.g. *Zhang and Karato*, 1995; *Silver*, 1996). As already shown in the histogram distributions in Fig. 7.6 the fast axis orientations observed across Fennoscandia align only in parts with the absolute plate motion direction (APM) in a hotspot reference frame (HS3-NUVEL 1A, *Gripp and Gordon*, 2002). For a plate motion coupled to mantle flow one would expect a smoothly varying ϕ pattern across the network (e.g. *Fouch et al.*, 2000) and no abrupt changes in ϕ within relatively small scales. The plate motion of the Baltic Shield is only around 1 cm - 1.5 cm per year and thus too slow to generate a dominant APM-parallel fabric caused by the motion of the plate across a sub-lithospheric shearing layer (*Debayle and Ricard*, 2013). Furthermore, especially for the Caledonian area, APM direction and orientations of expected anisotropy imprints caused by the continent-continent collision are almost identical. Compared to other continental areas like North America (e.g. *Yang et al.*, 2014; *Chen et al.*, 2018) or the easternmost regions of the East European Platform (*Levin et al.*, 1999) I exclude asthenospheric flow as a primary cause for the observed anisotropy in the western part of the study region.

In contrast, based on a regional surface-wave study, asthenospheric flow not aligned with the APM direction was inferred for central and southern Finland below 200 km - 250 km depth while no strong indicators for lithospheric contributions were found (*Pedersen et al.*, 2006). The absence of a clear correlation with the APM was interpreted as complex flow pattern that cannot be explained by a scenario in which the Baltic Shield is coupled to the convecting mantle in a simple way. The derived fast axes orientations are N-NE (0° - 40°) and generally agree with previous body wave observations which located the anisotropy mainly in the lithospheric mantle (*Plomerová et al.*, 2006; *Vecsey et al.*, 2007). Furthermore, the fast axis orientations derived from the surface wave model of *Zhu and Tromp* (2013) show a similar pattern, although, only within the upper 70 km depth before the fast axes rotate to the previously mentioned E-W direction that is consistent for deeper layers (Fig. 7.38). This would be in clear contradiction with a nearly N-S aligned sub-lithospheric flow direction. In the analyzed shear wave splitting data of ScanArray such N-S orientation is only observed for the most eastern and northern parts of the study region (Archean domain). Although the delay times cannot be fitted, indications of two-layer anisotropy at KEF suggest that complex mantle flow may play a role and could

potentially cause a splitting pattern that cannot easily be explained by two layers with horizontal symmetry axis. Due to the limited depth sensitivity of the surface waves, the strength of anisotropy decreases below 200 km (*Zhu and Tromp*, 2013). Thus, another N-S oriented component, related to flow in the asthenosphere, beneath 200 km depth cannot be ruled out (*Pedersen et al.*, 2006). Nevertheless, although the lateral resolution of the surface-wave model of *Zhu and Tromp* (2013) is poor compared to the splitting measurements conducted at the individual stations, it supports the findings of complex anisotropic structure beneath that area. Dipping structures as found for several stations, however, cannot be resolved by the used model parameterization (*Zhu and Tromp*, 2013).

7.5.3 May lateral variations or deep anisotropy play a role?

In order to examine if lateral variations could be responsible for the complex backazimuthal pattern observed at some stations in southern Finland, I compare the locations of raypath pierce points in different intervals down to 600 km depth (Fig. 7.39). This allows to search for potential overlaps and areas in which all pierce points or raypaths sample the same volumes.

The six station stereoplots shown in Fig. 7.39 share the characteristic of a sharp rotation of ϕ from around 50° - 60° (blue) to 0° - 20° (greenish) within a narrow backazimuthal range of less than 5°. Measured delay times are almost constant except for station VAF and partly RAF at which significantly smaller values are observed. To explain such an abrupt change for shallow depths ($<$ 300 km) it would require that around each single station the same lateral variation is present for nearly the same azimuths. Stations KAF and KEF are located only 50 km apart from each other. Therefore, such small-scale variations (with almost identical splitting pattern) are quite unlikely. For larger depths ($\geq$ 400 km) the pierce point locations related to different stations partly overlap. In the presence of lateral variability in anisotropy one would therefore expect similar splitting characteristics for closely spaced pierce point locations, which is obviously not the case. Thus, the nearly identical ϕ-pattern at the six stations as well as the abrupt rotation of the fast axis are generally more indicative for a two-layer scenario than for laterally varying structure around each station (although the data coverage is mainly limited to the northeastern quadrant in a stereoplot view). At this point, in principal also the Fresnel zones of the different waves need to be considered to argue more about the finite-frequency sensitivity. However, the Fresnel zones of the individual waves (width $\sim$ 100 km - 200 km for dominant periods of 8 s) at a single station largely overlap down to 500 km depth (e.g. *Alsina and Snieder*, 1995; *Favier and Chevrot*, 2003). Therefore, the significant change in ϕ cannot be explained with finite-frequency considerations at all.

The main contributions to the anisotropy observations are most likely associated with fabrics in the lithosphere. However, the possibility that other sources of anisotropy, not related to the structure directly beneath Fennoscandia, can contribute to a complex splitting pattern has

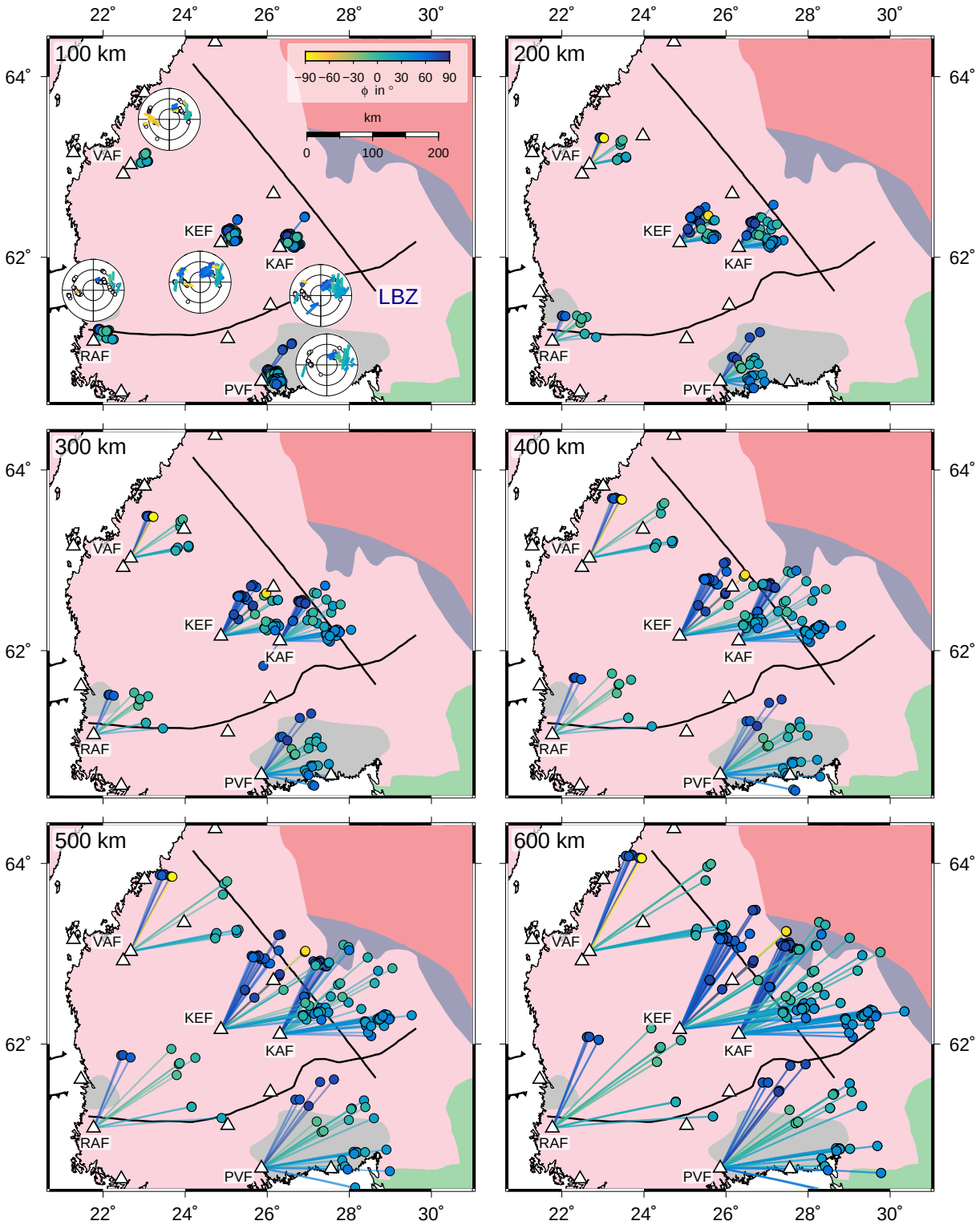

Figure 7.39: Pierce points (circles) in different depth ranges (100 km – −600 km) and raypaths (lines) from the corresponding depth to the recording station at the surface (triangles). Pierce points and raypaths are color-coded with respect to the observed fast axis direction (see stereoplots of the six stations in the upper left panel). Raypaths are only shown for events from northeast.

to be considered, too. Especially at the long-running permanent stations KAF, KEF and PVF clearly discrepant *SKS*-*SKKS* pairs were observed for the range in which the fast axes are almost differing by around 80° (*Grund and Ritter*, 2019). Therefore, I cannot rule out that further contributions from the lowermost mantle are included in the observations, although the discrepant pairs themselves were excluded before the modeling. In this case the poorly resolved orientation of ϕ from the lowermost mantle may contaminate the shallower signatures (e.g. *Lynner and Long*, 2012). This is also interesting since some surrounding stations show slightly different splitting patterns (e.g. FIA1, see Fig. 7.21) which can be modeled by a dipping symmetry axis.

In order to check if the observed delay times require an additional source beneath the lithosphere, following *Helffrich* (1995) a corresponding layer thickness can be estimated using

$$L \approx \frac{\delta t \cdot v_S}{\mathrm{d}v_S}, \tag{7.2}$$

where L is the layer thickness, δt is the observed delay time, v_S is the isotropic shear wave velocity and $\mathrm{d}v_S$ is the average percentage anisotropy. The observed delay times at KEF, for instance, vary between 1 and 1.5 s for the northeastern quadrant. In the mantle beneath stations in southern Finland, v_S is in the range of around 4.8 km/s (*Pedersen et al.*, 2006; *Vinnik et al.*, 2016). Taking these values and a $\mathrm{d}v_S$ of 4% as the upper limit for the strength of anisotropy prevalent in the upper 200 km of the Earth (*Savage*, 1999), the corresponding layer thickness varies between 120 and 180 km. However, a smaller percentage of anisotropy would result in an increased layer thickness. As already mentioned before, this trade-off cannot be modeled reliably and therefore a contribution from a deep source as inferred by discrepant *SKS* and *SKKS* phases is most likely. This is supported by the surface-wave model of *Zhu and Tromp* (2013) in which the strength of anisotropy below 180-200 km decreases significantly.

7.6 Summary

The shear wave splitting measurements conducted at the dense and large-aperture ScanArray network suggest a complex anisotropic structure beneath Fennoscandia that partly correlates well with past tectonic activity. The observed splitting characteristics at several stations can be modeled reliably only with a dipping symmetry axis. Indicative one- and two-layer model characteristics mostly cannot fit the variations of the splitting parameters with backazimuth equally well or the models have a non-unique character. However, it has to be mentioned that also the data coverage is partly limited due to the uneven distribution of global seismicity. In contrast to previous studies where few splitting observations were jointly inverted with *P*-wave residuals, at several stations I can clearly resolve a dipping symmetry axis from shear wave splitting measurements alone. Although the model constraints benefit from long recording

periods at several stations, also temporary stations (mostly in neighboring areas around the permanent ones) with shorter run times are robustly modeled by a dipping anisotropic fabric. Such dipping fabrics support assumptions that also old cratonic cores were formed by accretion as a consequence of repeated subduction events.

Although I had four years of new data of the SNSN available and most stations showed relatively simple splitting patterns I cannot rule out that the anisotropic structure is more complex beneath Sweden. Most results, however, are in good agreement with the splitting observations of *Eken et al.* (2010). They additionally used *P*-wave residuals to constrain self-consistent anisotropy models beneath the SNSN. The *P*-wave measurements can also be influenced by pure lateral heterogeneity while observations of clearly split shear waves are a strong argument for seismic anisotropy somewhere between the core-mantle boundary and the surface. Long-term observations (> 10 years of recording) at specific SNSN stations may therefore help to improve the resolution in future studies and probably rule out more complex geometries of anisotropy. For several SNSN stations this would already now be possible, however, the data is generally not open to the public.

The complex splitting pattern observed at several permanent stations in southern Finland could not be fully explained by the applied modeling strategy. Therefore, this area remains a highly interesting study region with respect to the observed anisotropic pattern. The combination of constraints received from shear wave splitting analysis with other techniques such as surface wave dispersion or anisotropic receiver functions would be a further step forward to better understand the lateral variability of anisotropy beneath Fennoscandia. The former is on the way and is studied by a group at GFZ Potsdam. However, previously observed clear discrepancies between *SKS-SKKS* phases of the same source-receiver pair indicate that also a contribution from the lowermost mantle may effect the non-compatibility with the two-layer and dipping layer models. Accurate modeling of the deep contributions is therefore essential to fully explain the observations at the surface.

Since new permanent stations will be installed in that area (*Kozlovskaya et al.*, 2016), in the future the characterization of anisotropy will hopefully be improved due to long recording periods. The use of dense station networks such as ScanArray, resulting from the combination of temporary and long-running permanent networks, is therefore highly recommended for future projects. Nevertheless, the run times of the temporary deployments in most cases are limited to around two years. In my opinion this is too short to guarantee a sufficient characterization of the anisotropic structure beneath a seismic recording station. Therefore, I recommend to extend temporary deployments to more than five years if possible (of course in most cases this depends on funding and equipment availability).

8 Conclusions and outlook

In this thesis I applied shear wave splitting analysis to examine the characteristics of seismic anisotropy in different depth ranges of the Earth's interior. For this purpose uniformly-processed recordings of teleseismic core-refracted shear waves (e.g. *SKS*, *SKKS* and *PKS*) were studied at a total of 266 seismic broadband receivers which are part of the international ScanArray project – the largest seismological field experiment conducted in northern Europe so far (chapter 3). Inter-station spacings of partly less than 50 km allowed me to characterize the anisotropic structure beneath the Fennoscandian peninsula with a high lateral resolution. The data set shows significant lateral and backazimuthal variations in shear wave splitting across the whole network even at individual stations themselves (section 7.3.1). Such clear variations were not resolved previously and this opens opportunities to explore so far unknown structures at depth. In order to increase data coverage by stacking single low-quality shear wave splitting measurements, I developed a flexible multi-event plugin, called StackSplit (chapter 5), for the widely applied SplitLab toolbox. A forward modeling approach was used to compare the observations with synthetic splitting calculations that were generated for different structural geometries (section 7.4.2). Although, the splitting observations in Fennoscandia can be explained by a relatively simple anisotropic structure with a horizontal axis of symmetry, for other areas more complex systems of anisotropy including dipping symmetry axes could be reliably modeled. Parts of the determined anisotropic signatures correlate well with features of past tectonic activity and show agreement with previous geophysical and geological studies. In contrast, non-unique models were found for a small number of seismic stations despite sufficient data coverage and recording quality. Furthermore, due to its nearly perfect position with respect to epicentral distance between source and receiver, the ScanArray experiment also allowed me to study two, so far unexplored regions in the Earth's lowermost mantle, far away from Fennoscandia in the so-called D" layer just atop the core-mantle boundary in $\sim$ 2700 km depth (chapter 6). Observations of distinct splitting discrepancies between *SKS* and *SKKS* phases for the same source-receiver configuration clearly indicate a contribution from anisotropy in D" that can be associated with two large-scale structural anomalies beneath the North Atlantic and northwestern Siberia. Since observations of D" anisotropy based on core-refracted shear waves are rare around the globe, these new findings provide important constraints for improved geodynamic modeling of mantle flow in the future. In the following I summarize the key results of this work in the framework of the questions formulated in the introductory chapter.

1. *What can we learn from shear wave splitting measurements conducted at long-running seismic recording stations compared to short-term deployments?*

In Fennoscandia appropriate teleseismic data coverage for shear wave splitting analysis is mainly limited to earthquakes from South America and the East Pacific region. Since only a fraction of the recorded events allows to perform high-quality splitting measurements, in principal long recording periods provide a better basis for a detailed splitting analysis. However, *Evans et al.* (2006) showed that even at permanent stations only 2% of the recorded events provide sufficient splitting estimates. Within the ScanArray project, neighboring and relatively densely spaced permanent and temporary stations allowed to compare the observed splitting patterns. As expected, for temporary stations in general only a few measurements are available mostly due to higher noise conditions and short recording periods, while the permanent stations deliver partly ten times more high-quality results. However, generally the same backazimuths are covered and therefore data coverage with respect to new source regions cannot be improved by permanent stations alone. Similarly, this was shown for one of the quietest and best performing stations around the globe, the Black Forest Observatory (BFO) in Germany (*Ritter et al.*, 2018). Nevertheless, permanent stations provide the advantage to compare multiple results for specific directions which allows to increase the confidence in the observations. In contrast, at a temporary station only few splits with potentially slightly varying characteristics might be incorrectly interpreted as a variation which, however, might be due to measurement uncertainties. Therefore, station run times of more than ten years seem to be necessary and sufficient to get a first-order overview of potentially complex splitting characteristics.

Furthermore, data coverage can be improved by including stacks of low-quality splitting measurements computed with the StackSplit plugin. However, for most temporary stations of ScanArray there were not enough measurements of poor quality available to significantly increase the data coverage. In contrast, for permanent stations several multi-event measurements show strong agreement with single high-quality measurements of the same source region. Therefore, such multi-event procedures can also help to improve the data coverage at permanent stations to achieve a higher confidence in individual splitting estimates for a specific backazimuthal range.

2. *Is there only a component from past lithospheric deformation included in the splitting signals or also a contribution from present-day dynamic processes and structures in the deep mantle?*

With respect to shear wave splitting analysis, I discussed two main aspects in this thesis. The first is the contribution of relatively shallow anisotropy to the observations which most likely is related to the tectonic history of Fennoscandia (see questions 3 and 4 below). In contrast, the second aspect is related to seismic anisotropy located deep in the Earth's interior. Although several previous studies partly analyzed shear wave splitting across Fennoscandia and generally

attributed the observations to relatively shallow anisotropy in the lithosphere and asthenosphere directly beneath the recording stations, the ScanArray network allowed for the first time to clearly decipher also a contribution from the lowermost mantle, namely the 250-300 km-thick D" layer in $\sim$ 2700 km depth. These contributions, however, are not related to Fennoscandia at all since the used seismic phases sample areas in D" far away from the network. The observed discrepancies between the phases *SKS* and *SKKS* (one is **null**, the other clearly **split**) are strong indicators for deep anisotropy beneath the North Atlantic and northwestern Siberia, since their raypaths and corresponding Fresnel zones overlap significantly in the upper mantle and crust (directly beneath the network) while in the lowermost mantle their raypath pierce points are separated by more than 800 km (chapter 6). Comparisons with lowermost mantle structures resolved by global tomography show a high correlation with two large-scale shear wave velocity anomalies. Beneath the North Atlantic the anisotropy partly mirrors the northern extensions of the African large low shear velocity province towards a meso-scale anomaly beneath Iceland. The detected anisotropic area beneath NW Siberia falls into a region in which remnants of a subducted slab are assumed to impinge on the core-mantle boundary, which results in strong strain-induced anisotropy. Therefore, it is important to keep in mind that in principle all conducted shear wave splitting measurements may be contaminated by contributions from deep anisotropy and not necessarily reflect only shallow anisotropic fabrics. However, the partly complex splitting patterns observed at individual ScanArray stations did not allow to derive the exact geometry and mechanism of the anisotropic fabrics in D" with splitting measurements alone.

3. *Do the splitting observations correlate with geological and tectonic features across Fennoscandia?*

The dense station spacing of ScanArray allowed to detect abrupt changes in the splitting characteristics within short distances. For some areas, these lateral variations partly correlate well within the boundaries of different tectonic units and, therefore, indicate a component of fossil anisotropy that was frozen into the lithosphere long before the corresponding terranes were accreted during the formation of Fennoscandia. In contrast, the measurements also indicate that especially in the southwestern part of the Baltic Shield (southern Noway and Sweden) and along the present Scandinavian Mountains anisotropy may reflect the signatures of collision events that coherently deformed the crust and lithosphere. Similar observations were previously made but mostly limited to selected smaller areas of interest. Based on comparisons with surface-wave observations, a depth range of 70 km to 170 km can be estimated for the location of the dominant anisotropic volume beneath the western part of the study region. For the most eastern part of the network in Finland, the station coverage was not sufficient to confirm previously found variations across the dominant contact zone of the Archean and Svecofennian domains. The absence of a clear match between the absolute plate motion direction and the

splitting observations does support earlier assumptions, namely either that asthenospheric mantle flow is too slow for generating anisotropic fabrics with a distinct splitting contribution or that the lithosphere is not coupled to the (horizontal) flow pattern in a simple way.

4. *Can complex anisotropic structure such as a dipping symmetry axis of anisotropic fabrics also be reliably constrained by splitting measurements alone?*

Constraining complex geometries of anisotropic fabrics like a dipping symmetry axis with shear wave splitting observations alone is quite challenging and only discussed by few studies. Based on consistent splitting characteristics at neighboring stations such a dipping system represents the most reliable model for an area in northern Sweden and Norway. These findings of a NE-dipping layer are mainly consistent with an inclined mantle reflector previously observed in reflection seismic data. Furthermore, they support the idea of ancient subduction due to a collision event. As mentioned above, data coverage with respect to the source regions is not perfect at ScanArray, neither for temporary nor permanent stations. The dense station spacing, however, allowed to constrain the dipping structure since neighboring stations show nearly identical characteristics. Although such a dip was reported previously based on joint inversions of sparse shear wave splitting observations and *P*-wave residuals, here it is demonstrated that such a fabric can also be reliably constrained by shear wave splitting measurements alone.

Despite long recording periods and highly consistent splitting measurements for several backazimuthal ranges, at a small number of stations not all observations can be explained with a unique-model. It is not possible to constrain the polarization direction and the strength of the underlying anisotropic fabric(s) simultaneously with the applied modeling approach by assuming models of two horizontal layers or a dipping symmetry axis. Lateral variations around each single station can be ruled out as a primary source since the individual station patterns show nearly identical characteristics. With the detected contributions of lowermost mantle anisotropy in mind, it is also possible that the splitting characteristics are distorted by a deeply located source of anisotropy that is not related to structures directly beneath Fennoscandia. Although anisotropy models exist for a lot of permanent observatories around the globe, anew analyses or the continuation of previously started shear wave splitting measurements are highly recommended to eventually constrain the possibility of potentially more complex structures that could yet not be determined with only few measurements, only from a very limited backazimuthal range.

Outlook and future directions

If we study a global map showing all seismological recording stations installed so far (permanent and temporary), Russia as well as oceans have always been areas that are poorly covered. Therefore, in the future analyses would be benefitting from expanding station deployments toward the Russian territory east of the ScanArray network. Such efforts would not only allow to

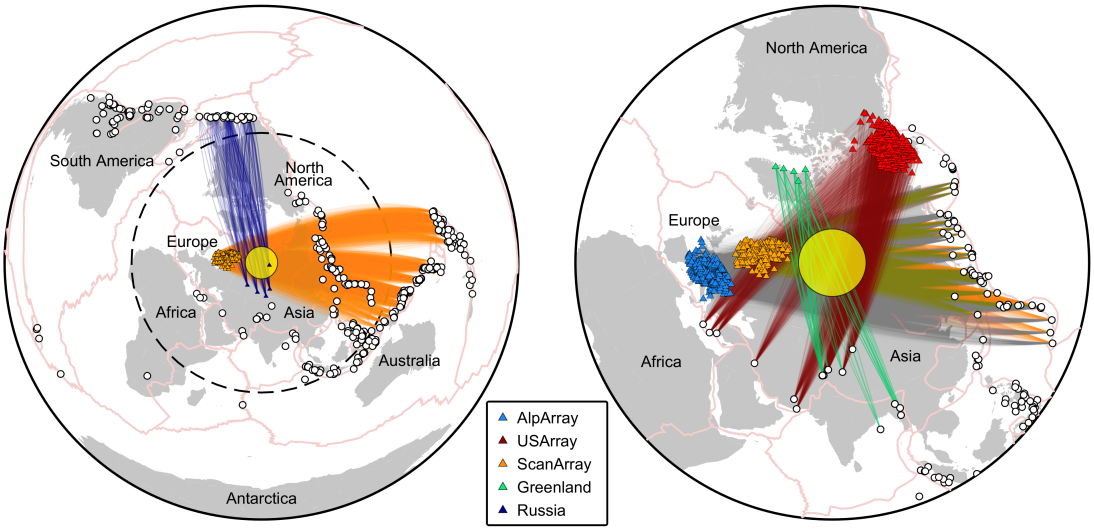

Figure 8.1: Potential future study areas beneath Siberia (yellow circle) using dense arrays for which data are available currently and in future. The map shows the distribution of earthquakes worldwide with magnitudes larger than M_W 6 and depth $>$ 20 km around each network within a distance range of 60°-140° that occurred between 2012 and summer 2018 based on the CMT catalog (white dots). Great-circle paths for event-station/network pairs that could be used for *SKS-SKKS* studies are shown on the left, for *S-ScS* and scattering studies on the right. Note, not all the shown stations were running the whole time period 2012-2018. However, this figure is only meant to demonstrate the potential raypaths with different crossing directions beneath Siberia that could be studied when using data of the shown large and dense seismic arrays and permanent stations, provided that sufficient seismicity occurs around the globe within the recording periods.

study (potential) lateral variations of relatively shallow anisotropic structures but also improve the knowledge about deep structures in the lowermost mantle beneath Siberia. Improving the backazimuthal coverage with direct *S*-waves is in principle possible (e.g. *Eken and Tilmann*, 2014). However, for this purpose a correction has to be applied which seems to be very challenging for some areas in Fennoscandia due to the complex splitting patterns partly observed. Furthermore, it were desirable if new permanent stations would be installed and operated in Fennoscandia. Especially in Finland there currently are some new sites in test operation (*Kozlovskaya et al.*, 2016), which may help to obtain a better data and raypath coverage. This effort ensures to increase the lateral resolution in this complex tectonic setting. With many more new, long-running stations the lateral change in the anisotropic fabric could be imaged in greater detail than possible so far. However, for this one needs around ten years of observation at these stations and, therefore, such an effort should be considered a long-term task for the future.

Since globally the trend is toward densely spaced seismic networks, the availability of massive seismological data sets will help to increase the resolution of the splitting patterns. Besides ScanArray such work has already started in recent years. Data of USArray stations still recording in Alaska[16] allow to study the lowermost mantle beneath Siberia with additional raypaths that cross the anomaly identified here using, e.g., differential splitting analysis of *S* and *ScS* phases (Fig. 8.1). Another raypath crossing the Siberian anomaly can be covered by the Al-

[16] USArray Alaska: http://www.usarray.org/alaska, last accessed 11 January 2019

pArray project in Europe that is still ongoing (*Hetényi et al.*, 2018) and may help to improve knowledge about the geometry and anisotropic fabric of the anomaly.

However, onshore the number of uncharted places for shear wave splitting is decreasing, although several blank spots still exist in several areas like, for instance, Africa. In the future it is necessary to deploy many of long-recording broadband stations across the oceans using ocean bottom seismometers (OBS) as done in previous studies on smaller and shorter scale (e.g. *Stähler et al.*, 2016). For Fennoscandia, OBS deployments in the Baltic Sea could contribute to resolve splitting variations between eastern Sweden and western Finland. Temporary OBS are well established but often only installed for less than two years due to power supply problems and with often weak data quality due to coupling problems and high noise. Permanent networks would be necessary to guarantee good backazimuthal coverage. Only then is it possible to map complex patterns of anisotropy. Of course, on the one hand this is an intensive and expensive effort but on the other hand nobody expected 30 years ago that collaborative projects like ScanArray, USArray or AlpArray would be possible today. Thus, it would be great to support growing ideas to power up installed OBS by autonomous wave gliders or collect their data (*Laske et al.*, 2014) or using new generations of Transoceanic Cables (*Tilmann et al.*, 2017; *Ranasinghe et al.*, 2018) in the oceans to map at least thousands of kilometers along specific lines. This would help to close large gaps in shear wave splitting measurements (provided the desired frequency band can be recorded with such upcoming techniques) which could then increase the structural resolution worldwide.

Additional work related to ScanArray data is currently on the way. Different 3D seismic tomography approaches are applied (e.g. *Grund et al.*, 2019) as well as imaging with receiver functions (*Makushkina et al.*, 2018), ambient noise, and surface-wave (*Mauerberger et al.*, 2018) analysis. Bringing all of them together will finally help to improve the understanding of the evolution and present-day shape of Fennoscandia.

Acknowledgements

Zum Abschluss möchte ich noch ein paar Worte des Danks aussprechen, insbesondere an die Personen, die mich während meiner gesamten Arbeit begleitet und unterstützt haben.

An allererster Stelle möchte ich mich bei **Prof. Dr. Joachim Ritter** für die Betreuung meiner Promotion, sowie die uneingeschränkte Unterstützung während meines gesamten Studiums in Karlsruhe bedanken. Insbesondere sein Engagement für das Schreiben von Gutachten und Bewerbungen um Förderungen und Preise, sowie das umfangreiche Korrekturlesen für Veröffentlichungen möchte ich hier hervorheben. Er hatte immer ein offenes Ohr für Fragen jeglicher Art und gab mir stets das Gefühl eine gute Arbeit zu machen. Danke auch für die Möglichkeit, an vielen nationalen und internationalen Tagungen und Workshops teilzunehmen und dadurch wertvolle Kontakte knüpfen zu können.

Prof. Dr. Andreas Rietbrock danke ich für die Übernahme des Korreferats, sowie seinem Interesse an meiner Arbeit und der damit verbundenen Unterstützung. Viele gewinnbringende Anmerkungen und Diskussionen haben maßgeblich zu der Fertigstellung dieser Arbeit beigetragen.

I would like to thank all participants of the **ScanArray working group** for the fruitful discussions and suggestions on conferences, workshops and during PhD schools. It was a pleasure for me to contribute to such a great seismological data set. In particular, I thank **Alexandra Mauerberger** and **Prof. Dr. Frederik Tilmann** from GFZ Potsdam for the successful and uncomplicated collaboration in the fieldwork. Many thanks also to the **Geophysical Instrument Pool Potsdam (GIPP)** for providing the seismic instruments and equipment we installed in Finland and Sweden as well as the great support during the individual service trips. Furthermore, I thank our Finnish and Swedish field teams, namely **Hanna Silvennoinen**, **Jouni Nevalainen**, **Henrik Jänkavarra**, **Andreas Björk** and **Sara Andersson**. The University of Oulu is thanked for the provision of the Azimuth Pointing System (especially **Elena Kozlovskaya**).

Ich danke dem **Karlsruhe House of Young Scientists (KHYS)** für die Finanzierung des Networking Grants. Die dadurch ermöglichte Reise an die Yale University in die Arbeitsgruppe von Prof. Dr. Maureen Long hat zu einer Vertiefung meiner Anisotropiekenntnisse und darüber hinaus beigetragen.

A big thanks goes to **Prof. Dr. Maureen Long** and her working group for hosting me ten days at Yale in March 2018 in the framework of my Networking Grant trip. The discussions regarding

seismic anisotropy in the lowermost mantle had an profound impact on my research and the interpretation.

I would like to thank the **European Geosciences Union (EGU)** for selecting my picture *Symbiosis of fire, ice and water*, taken during a service trip in Sweden, as one of three winners in the EGU photo contest 2017. The associated grant allowed me to visit the EGU General Assembly 2018 with a free registration.

Several people helped me out with various things that I used to prepare this thesis. At this point I want to thank **Caroline Eakin** for providing the original file to generate the circular color scale that I used in several figures for visualization. Furthermore, I thank **Ed Garnero** for the permission to use some of his descriptive visualizations of content related to anisotropy and shear wave splitting in the theory chapter of this thesis. The figures helped me a lot to understand more complex relationships, especially related to lowermost mantle anisotropy.

Ein großer Dank geht auch an alle Mitglieder des **GPI**, sowie der **Arbeitsgruppe Seismologie**. Die kontinuierlichen und konstruktiven Anmerkungen und Diskussionen während Arbeitsgruppentreffen haben ebenfalls zu dieser Arbeit beigetragen. **Petra Knopf**, **Claudia Payne**, **Kerstin Dick**, **Rainer Plokarz** und **Thomas Nadolny** danke ich für die immerwährende Unterstützung und Hilfe bei formellen sowie technischen Problemen. **Thomas Forbriger** möchte ich für die Beantwortung jeglicher Fragen bezüglich Seismometern und seismischen Daten danken. **Franz Lutz** danke ich für die Digitalisierung von geologischen Karten und Störungszonen, sowie für seine gewinnbringende Mitarbeit am ScanArray Projekt. Zu guter Letzt möchte ich mich bei **Thomas Hertweck** für das umfangreiche Korrekturlesen dieser Arbeit bedanken. Weiterhin danke ich ihm für viele konstruktive Diskussionen zu meiner Arbeit und Manuskripten, sowie für seine kontinuierliche Bereitschaft bei Fragen und Problemen aller Art zur Verfügung zu stehen.

Ein besonderer Dank gebührt **Werner Scherer** für seine großartige Unterstützung und Hilfsbereitschaft während den Feldarbeiten in Finnland und Schweden. Danke auch für all die Erklärungen bezüglich technischer Fragen. Ich habe sehr viel über Seismometer und die Installation von Geräten gelernt, insbesondere auch, dass man bei der Standortsuche/auswahl manchmal etwas energischer vorgehen muss ☺. Die teilweise abenteuerlichen nächtlichen Unternehmungen um Polarlichter zu beobachten, sowie die vielen geselligen Abende in Schweden, Finnland und auf den Fährfahrten werden mir immer in guter Erinnerung bleiben. Für deinen wohlverdienten Ruhestand wünsche ich dir alles Gute!

Besonders danken möchte ich **Alexander Gerst**, der mich durch seinen Vortrag an meiner ehemaligen Schule nicht nur auf das Gebiet der Geophysik gebracht hat, sondern mir auch gezeigt hat, was alles möglich ist, wenn man nur an seine Träume glaubt.

Für das freundschaftliche und angenehme Arbeitsklima in unserem Büro möchte ich **Sarah**, **Toni** und **Mohsen** danken. Die vielen Diskussionen haben sich immer positiv auf meinen Arbeitsalltag ausgewirkt, auch wenn Seismologie und Geophysik nicht immer im Fokus standen.

Für die schöne Zeit in Karlsruhe danke ich meinen Freunden und ehemaligen Kommilitonen, **Michael**, **Jens**, **Tobi**, **Christopher**, **Tommy**, **Laura**, **Matthias**, **Anne**, **Niklas**, **Markus** und all den anderen zu denen der Kontakt ein Glück auch nie ganz abgerissen ist. Meinen Freunden aus der Heimat danke ich insbesondere für die anhaltende Freundschaft und die regelmäßigen gemeinsamen Unternehmungen über all die Jahre die ich nun schon in der "Ferne" wohne. Meinem Schulkumpel **Consi** danke ich für das Korrekturlesen von Teilen dieser Arbeit.

Zum Schluss möchte ich meiner **Familie** für jegliche Unterstützung während meiner nun mehr als zehnjährigen Studien- und Promotionszeit in Karlsruhe danken. Ich bin sehr froh solch eine Familie im Hintergrund zu wissen, die mich bei all meinen bisherigen Träumen und Wünschen unterstützt hat. Ohne euch wäre ich nie an diesem Punkt angelangt. Ganz besonders möchte ich **Carina** für ihre immerwährende Unterstützung und Motivierung danken und viel mehr noch dafür, mir ab und zu klar zu machen, dass das Leben nicht nur aus Arbeit besteht!

Funding

This work was carried out in the framework of the LITHOS-CAPP (LITHOspheric Structure of Caledonian, Archaean and Proterozoic Provinces) project funded by the **Deutsche Forschungsgemeinschaft** (grant numbers **RI1333/11-1** and **RI1333/11-2**).

The author was supported by the *Networking Grant* of the **Karlsruhe House of Young Scientists (KHYS)** to visit Yale University in March 2018.

Appendix

A Used hardware and software

The following hardware and software was used to prepare this dissertation:

- The whole analysis work was done on a computer with Linux **openSUSE** operating system (version 13.1).
- Most figures were prepared using **MATLAB** version 2014a (*MATLAB*, 2014).
- The free MATLAB toolboxes **SplitLab** (*Wüstefeld et al.*, 2008), **StackSplit** (*Grund*, 2017), **MSAT** (*Walker and Wookey*, 2012) and **MatTaup**[17] were used for the analysis and modeling.
- Several freely available MATLAB tools were used to prepare specific figure content like circle segments[18], fancy arrows (the free "arrow" component of **DaVinci Draw**[19]) and 3D planes (the free **drawLA** toolbox[20]).
- Maps were prepared using the **Generic Mapping Tools (GMT)** version 5.1.3 (*Wessel et al.*, 2013).
- Some graphics were prepared using the free and open-source vector graphics editor **Inkscape** version 0.92[21].
- This thesis was written and typeset with **LaTeX** using **TeXnicCenter**[22] on Windows 7 and 10 and **Kile** on Linux. **BibTeX** was used to organize the huge amount of references and to ensure consistency in the reference style.

[17] MatTaup by Qin Li is a MATLAB toolkit that contains the functionality of the original Taup seismic travel time calculator (*Crotwell et al.*, 1999)
[18] secdraw by Laine B. Kahsay from MathWorks file exchange, https://de.mathworks.com/matlabcentral/fileexchange/4503, last accessed 11 January 2019
[19] DaVinci Draw by Leonard R. Wayne, http://davinci-draw.com/, last accessed 11 January 2019
[20] drawLA - Draw Toolbox for Linear Algebra by Vladimir Bondarenko from MathWorks file exchange, https://de.mathworks.com/matlabcentral/fileexchange/23608, last accessed 11 January 2019
[21] Inkscape, https://inkscape.org/en/, last accessed 11 January 2019
[22] TeXnicCenter, http://www.texniccenter.org/, last accessed 11 January 2019

B Station information

Table B.1 lists all seismic recording stations (first column) used in this study together with the corresponding FDSN network code (second column) and the location coordinates (third and fourth column).

Table B.1: Information of seismic recording stations for which data were analyzed in this work. LITHOSCAPP stations described in section 3.2 are also listed.

Station name	Network code	Lat. in °	Lon. in °
AAL	UP	60.178	19.994
AKN	NO	62.178	6.997
ARA0	NO	69.535	25.506
ARBE	EE	59.437	25.984
ARE0	NO	69.535	25.506
ARJ	UP	66.242	16.973
ARNU	UP	61.692	17.378
ASKU	UP	58.895	14.829
ASPU	UP	57.419	16.599
BACU	UP	59.854	17.108
BER	NS	60.384	5.335
BJO	UP	63.970	17.101
BJUU	UP	56.074	13.023
BLEU	UP	56.304	15.815
BLS5	NS	59.423	6.456
BORU	UP	57.635	12.770
BREU	UP	63.891	18.578
BSD	DK	55.114	14.915
BURU	UP	64.584	21.377
BYXU	UP	57.290	17.008
COP	DK	55.685	12.432
DEL	UP	56.470	13.870
DOMB	NS	62.073	9.112
DUNU	UP	67.121	20.569
EKSU	UP	57.573	15.302

(continued)

Station name	Network code	Lat. in °	Lon. in °
ERTU	UP	66.554	22.189
ESKU	UP	59.231	16.394
FABU	UP	57.001	12.718
FALU	UP	60.494	15.832
FAUS	NS	67.930	15.240
FIA1	HE	61.445	26.076
FIBU	UP	59.901	17.352
FINU	UP	59.403	12.479
FKPU	UP	58.159	13.724
FLYU	UP	60.128	17.885
FOO	NS	61.597	5.042
FORU	UP	60.387	18.180
GNOU	UP	57.290	13.756
GOTU	UP	57.685	18.570
GRAU	UP	60.334	18.540
HAMF	NS	70.642	23.684
HARU	UP	66.163	20.975
HASU	UP	62.153	16.614
HEF	HE	68.392	23.657
HEMU	UP	62.676	18.036
HFC2	HF	60.133	13.694
HOMB	NS	58.270	8.505
HUDU	UP	61.736	17.119
HUSU	UP	63.342	19.218
IGGU	UP	60.873	17.316
JETT	NO	69.556	20.410
JOF	HE	62.918	31.312
JOK	UP	66.638	19.543
KAF	HE	62.111	26.309

(continued)

Station name	Network code	Lat. in °	Lon. in °
KALU	UP	65.860	23.357
KEF	HE	62.166	24.871
KEV	HE	69.757	27.004
KIF	HE	69.043	20.804
KMY	NS	59.212	5.247
KONO	IU	59.649	9.598
KOVU	UP	68.223	20.161
KU6	HE	66.025	29.891
KUA	UP	67.954	20.337
LANU	UP	68.049	21.988
LILU	UP	65.286	19.848
LNKU	UP	58.223	15.505
LOF	NS	68.131	13.542
LUNU	UP	55.632	13.446
LVZ	II	67.898	34.651
MASU	UP	67.457	21.998
MEF	HE	60.217	24.396
MOL	NS	62.570	7.547
MOR	NS	66.286	14.735
MOS	UP	65.787	19.029
MSF	FN	65.911	29.040
MTSE	EE	58.714	23.815
MUD	DK	56.455	9.173
N1301	ZR	66.095	13.116
N1302	ZR	66.141	14.056
N1303	ZR	66.042	14.995
N1304	ZR	66.876	14.655
N1305	ZR	66.383	14.068
N1306	ZR	66.742	15.738
N1307	ZR	67.103	14.969
N1308	ZR	67.120	16.096
N1309	ZR	66.472	16.561
N1311	ZR	66.607	17.529
N1312	ZR	65.629	13.442
N1313	ZR	65.688	14.171
N1314	ZR	65.758	15.482
N1315	ZR	65.967	16.245
N1316	ZR	65.207	16.144
N1317	ZR	64.797	16.956
N1318	ZR	64.966	17.613
N1319	ZR	65.163	17.114
N1320	ZR	65.744	16.192
N1321	ZR	65.648	17.729
N2AN	2D	69.237	16.035
N2BR	2D	68.579	14.707
N2DI	2D	68.313	14.986

(continued)

Station name	Network code	Lat. in °	Lon. in °
N2HA	2D	68.784	16.561
N2HS	2D	68.103	15.514
N2IH	2D	67.966	15.937
N2LO	2D	68.400	15.953
N2NF	2D	67.761	15.228
N2RO	2D	67.517	12.116
N2SO	2D	68.714	15.438
N2ST	2D	67.349	15.596
N2SV	2D	67.891	13.010
N2TV	2D	67.567	15.125
N2VA	2D	67.664	12.694
N2VG	2D	66.709	13.269
N2VI	2D	68.321	14.198
NAO01	NO	60.844	10.887
NASU	UP	58.928	13.186
NB201	NO	61.050	11.294
NBB03	2D	67.103	14.968
NBB05	2D	67.037	14.031
NBB08	2D	67.387	14.636
NBB12	2D	66.388	13.120
NBB13	2D	66.627	13.327
NBB14	2D	66.303	13.559
NBB15	2D	66.743	13.578
NBB17	2D	66.816	13.958
NBB28	2D	67.191	14.462
NBB29	2D	66.992	15.329
NBB30	2D	66.973	13.735
NBB40	2D	66.513	13.010
NBO00	NO	61.031	10.777
NC204	NO	61.276	10.763
NC303	NO	61.225	11.369
NC405	NO	61.113	11.715
NC602	NO	60.735	11.541
NIKU	UP	67.867	19.035
NOD	UP	63.443	14.857
NRAU	UP	59.570	15.040
NRTU	UP	59.677	18.631
NSS	NS	64.531	11.967
NWG01	Z6	63.495	9.736
NWG03	Z6	62.782	7.152
NWG04	Z6	62.784	8.878
NWG05	Z6	62.720	10.043
NWG09	Z6	62.029	7.534
NWG13	Z6	61.198	7.101
NWG15	Z6	60.576	6.924
NWG16	Z6	60.618	8.291

(continued)

Station name	Network code	Lat. in °	Lon. in °
NWG19	Z6	59.853	11.815
NWG20	Z6	59.643	8.030
NWG21	Z6	59.953	6.594
NWG22	Z6	59.268	5.241
NWG27	Z6	58.749	9.036
NWG28	Z6	58.620	7.419
NWG29	Z6	58.742	5.682
NWG30	Z6	58.131	6.620
NWG35	Z6	59.495	7.386
NYNU	UP	59.005	18.004
ODD	NS	59.912	6.628
ODEU	UP	64.409	20.716
ONAU	UP	57.397	11.918
ONSU	UP	57.397	11.926
OSKU	UP	57.195	16.099
OSTU	UP	60.230	17.134
OUF	HE	64.367	24.731
OUL	FN	65.085	25.896
PABE	GE	55.505	23.968
PAJU	UP	67.024	23.113
PBUR	GE	56.024	21.929
PUL	GE	59.767	30.317
PVF	HE	60.545	25.859
RAF	HE	61.023	21.768
RATU	UP	67.823	19.591
RNF	FN	66.609	26.014
ROTU	UP	61.420	15.814
SA01	1G	71.111	25.817
SA02	1G	71.064	28.242
SA03	1G	70.503	29.067
SA04	1G	70.319	25.477
SA05	1G	70.284	31.008
SA05A	1G	70.371	31.099
SA06	1G	70.134	20.760
SA06A	1G	70.038	20.973
SA07	1G	70.127	23.374
SA08	1G	69.764	22.062
SA09	1G	69.454	30.039
SA10	1G	69.201	25.692
SA11	1G	69.132	18.049
SA12	1G	68.973	18.914
SA13	1G	68.349	18.837
SA14	1G	67.696	21.624
SA15	1G	67.475	18.365
SA15A	1G	67.475	18.365
SA16	1G	67.152	21.078

(continued)

Station name	Network code	Lat. in °	Lon. in °
SA17	1G	66.953	17.726
SA18	1G	66.739	23.564
SA19	1G	66.565	22.179
SA20	1G	66.430	19.686
SA21	1G	66.041	25.030
SA21A	1G	66.040	25.029
SA22	1G	66.038	17.859
SA23	1G	65.926	20.301
SA24	1G	65.736	20.954
SA25	1G	65.672	14.225
SA26	1G	65.699	12.438
SA27	1G	65.482	15.896
SA28	1G	65.447	27.511
SA29	1G	65.288	19.845
SA30	1G	65.092	21.498
SA31	1G	64.991	18.501
SA32	1G	64.988	13.581
SA33	1G	64.903	10.850
SA34	1G	64.832	15.031
SA35	1G	64.534	12.401
SA36	1G	64.440	24.517
SA37	1G	64.247	16.818
SA38	1G	64.129	19.000
SA39	1G	64.072	14.091
SA40	1G	64.043	11.335
SA41	1G	63.967	10.232
SA42	1G	63.827	23.008
SA43	1G	63.816	15.515
SA44	1G	63.705	12.348
SA45	1G	63.549	19.366
SA46	1G	63.490	18.095
SA47	1G	63.360	23.973
SA48	1G	63.230	13.678
SA49	1G	63.175	21.279
SA50	1G	63.114	16.322
SA51	1G	63.044	11.644
SA52	1G	62.938	22.488
SA53	1G	62.800	13.053
SA54	1G	62.750	18.149
SA55	1G	62.719	10.040
SA55A	1G	63.298	10.058
SA56	1G	62.486	16.309
SA57	1G	62.449	14.921
SA58	1G	61.945	12.553
SA59	1G	61.865	14.120
SA60	1G	61.693	17.379

(continued)

Station name	Network code	Lat. in °	Lon. in °
SA61	1G	61.593	21.462
SA62	1G	61.384	15.512
SA63	1G	61.134	13.957
SA64	1G	61.054	25.040
SA65	1G	61.053	15.770
SA66	1G	60.447	14.781
SA67	1G	60.416	22.444
SALU	UP	67.380	18.507
SGF	FN	67.442	26.526
SJUU	UP	65.508	21.605
SKAR	NS	60.680	8.304
SLIT	GE	57.629	22.291
SOLU	UP	63.247	17.258
STAV	NS	58.935	5.702
STEI	NS	67.930	15.242
STRU	UP	59.035	11.182
SUE	NS	61.057	4.761
SUF	HE	62.719	26.151
SVAU	UP	64.494	19.575
TBLU	UP	63.420	10.434
TJOU	UP	58.032	11.625
TOF	HE	66.080	24.330
TRO	NS	69.635	18.908
UDD	UP	60.090	13.607
UMAU	UP	63.883	20.678
UPP	UP	59.858	17.627
VADS	NS	70.080	29.760
VAF	HE	63.042	22.672
VAG	UP	64.497	18.249
VANU	UP	58.492	12.073
VIKU	UP	58.502	16.699
VJF	HE	60.539	27.555
VOR	UP	64.431	16.013
VRF	HE	67.748	29.609
VSTU	UP	57.660	16.536
VSU	EE	58.462	26.735
VXJU	UP	56.921	14.939

C Sensor misorientations of the extended ScanArray network

Table C.1 lists the sensor misorientations (relative to true North) of the extended ScanArray network (except LITHOS-CAPP stations) determined by comparing the SC (*Silver and Chan*, 1991) and RC (*Bowman and Ando*, 1987) methods. See section 4.1.5 for a detailed description.

Table C.1: Sensor misorientations (relative to true North) of the extended ScanArray network (except LITHOS-CAPP stations, see Table 3.3).

Station	Orientation relative to true north in °
HARU	10
SA44	-10
STEI	18
MEF	10
SALU	-15
SA11	25
SA44	-10
SA34	+27
SA40	-55
SA41	-90
SA45	+7
SA50	-20
SA51	-30
SA20	+20
N2AN	-10
NBB29	-10
NBB30	+30

D Lowermost mantle anisotropy (*SKS-SKKS*) – Supporting content

D.1 Results of individual *SKS-SKKS* pairs

Due to the massive amount of measurements, results for all *SKS-SKKS* are available in the electronic appendix (see F). Table D.1 shows an exemplary subset of these data.

D.2 Further discrepant *SKS-SKKS* waveform examples

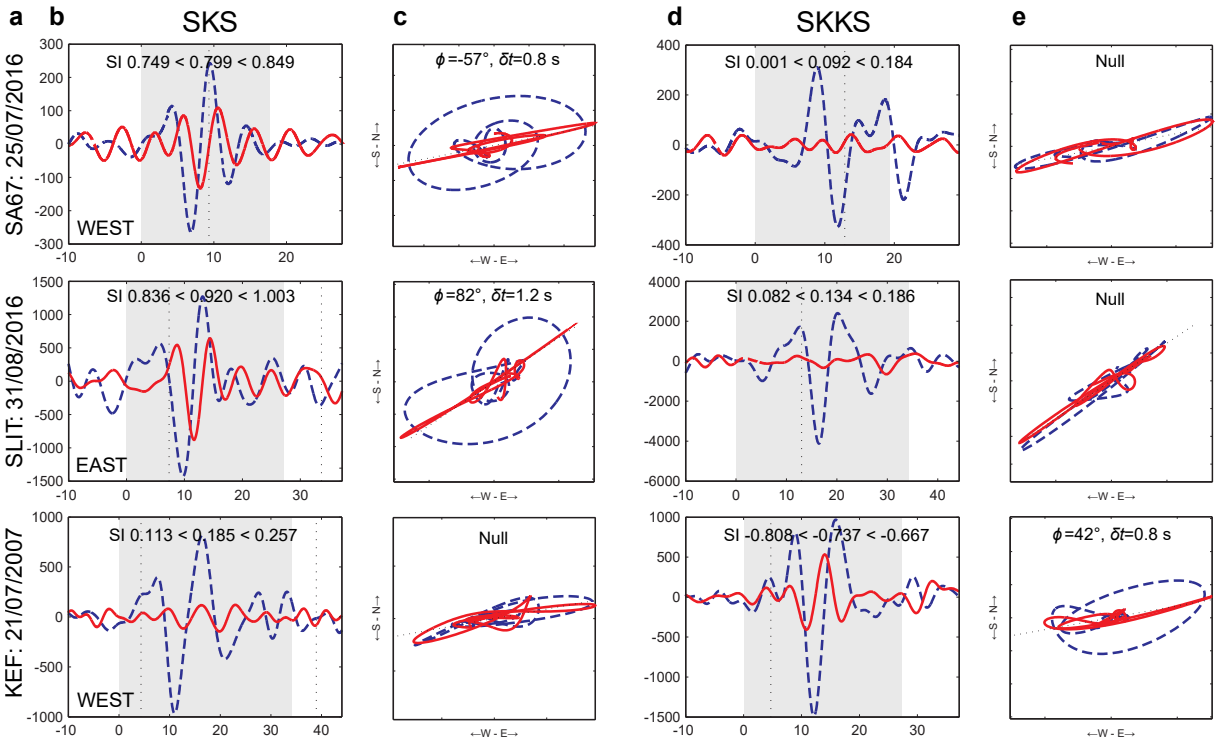

Figure D.1: (a) Station and earthquake information for anomalous *SKS-SKKS* waveforms. (b) Original (uncorrected) radial (blue dashed) and transverse (solid red) component seismograms for the *SKS* phase. At the top the corresponding SI value along with its uncertainty (95% confidence interval) is shown and at the bottom the direction from which the wave arrived (east or west). (c) Corresponding particle motions in the horizontal plane before (blue dashed) and after (solid red) correcting the splitting using the SC method *Silver and Chan* (1991). Splitting parameters ϕ and δt or nulls are indicated at the top of each panel. (d) and (e) Corresponding content for the *SKKS* phase of the same event.

Table D.1: Subset of the *SKS-SKKS* splitting discrepancy analysis results. Discrepant pairs are indicated by yes/no in column **Disc**. Furthermore the corresponding table entries are highlighted in bold **red**. Latitude (**Lat PP**) and longitude (**Lon PP**) values represent the locations of the *SKS* and *SKKS* pierce points in 2700 km depth based on the *iasp91* earth model (*Kennett*, 1991). These can be used for easy plotting the pierce points with e.g. GMT (*Wessel et al.*, 2013).

Sta	Date ev yyyy-mm-dd	Lat ev in °	Lon ev in °	Phase	ϕ_{SC} err - in °	ϕ_{SC} in °	ϕ_{SC} err + in °	δt_{SC} err - in s	δt_{SC} in s	δt_{SC} err + in s	SI err -	SI	SI err +	ΔSI	Disc	Mis in °	Lat PP in °	Lon PP in °
AAL	04-Mar-2010	-22.23	-68.33	*SKKS*	NULL	NULL	NULL	NULL	NULL	NULL	0.15	0.18	0.22	-	no	-	47.05	-18.69
AAL	04-Mar-2010	-22.23	-68.33	*SKS*	NULL	NULL	NULL	NULL	NULL	NULL	0.09	0.13	0.18	-	no	-	55.14	-2.51
AAL	21-Sep-2013	-7.26	119.96	*SKKS*	NULL	NULL	NULL	NULL	NULL	NULL	-0.15	-0.06	0.02	-	no	-	52.42	67.98
AAL	21-Sep-2013	-7.26	119.96	*SKS*	NULL	NULL	NULL	NULL	NULL	NULL	-0.16	-0.08	-0.00	-	no	-	58.21	48.83
AAL	28-May-2016	-56.20	-26.89	*SKKS*	NULL	NULL	NULL	NULL	NULL	NULL	-0.01	0.08	0.18	-	no	-	38.88	6.05
AAL	28-May-2016	-56.20	-26.89	*SKS*	NULL	NULL	NULL	NULL	NULL	NULL	-0.21	-0.16	-0.10	-	no	-	51.31	12.48
ARA0	07-May-2015	-7.23	154.55	*SKKS*	-7.08	4.90	19.21	0.85	1.10	1.40	-0.63	-0.52	-0.41	-	no	-	68.66	102.55
ARA0	07-May-2015	-7.23	154.55	*SKS*	-7.08	16.90	33.37	0.55	0.80	1.10	-0.70	-0.66	-0.61	-	no	-	73.37	64.32
ARA0	25-Jul-2016	-26.11	-70.65	*SKKS*	NULL	NULL	NULL	NULL	NULL	NULL	-0.10	-0.07	-0.04	-	no	-	57.59	-24.26
ARA0	25-Jul-2016	-26.11	-70.65	*SKS*	NULL	NULL	NULL	NULL	NULL	NULL	-0.15	-0.11	-0.07	-	no	-	66.21	-2.58
ARA0	31-Aug-2016	-3.69	152.79	*SKKS*	-3.03	9.59	21.24	0.85	1.05	1.25	-1.05	-0.99	-0.93	-	no	-	68.12	103.09
ARA0	31-Aug-2016	-3.69	152.79	*SKS*	-7.08	1.59	11.12	0.90	1.05	1.25	-1.00	-0.95	-0.91	-	no	-	73.16	67.12
ARA0	15-Apr-2017	-23.24	-67.65	*SKKS*	NULL	NULL	NULL	NULL	NULL	NULL	-0.28	-0.12	0.03	-	no	-	56.60	-24.23
ARA0	15-Apr-2017	-23.24	-67.65	*SKS*	NULL	NULL	NULL	NULL	NULL	NULL	-0.21	-0.06	0.09	-	no	-	65.50	-3.97
ARBE	24-Aug-2011	-7.64	-74.53	*SKKS*	NULL	NULL	NULL	NULL	NULL	NULL	-0.23	-0.16	-0.10	-	no	-	51.90	-21.52
ARBE	24-Aug-2011	-7.64	-74.53	*SKS*	NULL	NULL	NULL	NULL	NULL	NULL	-0.23	-0.16	-0.09	-	no	-	57.58	-2.39
ARBE	**02-Sep-2011**	**-28.40**	**-63.07**	***SKKS***	**33.37**	**43.87**	**49.55**	**0.80**	**1.00**	**1.20**	**-0.90**	**-0.85**	**-0.80**	**0.61**	**yes**	**-**	**46.47**	**-9.34**
ARBE	**02-Sep-2011**	**-28.40**	**-63.07**	***SKS***	**NULL**	**NULL**	**NULL**	**NULL**	**NULL**	**NULL**	**-0.19**	**-0.09**	**0.00**	**0.61**	**yes**	**-**	**54.68**	**6.74**
ARBE	**22-Nov-2011**	**-15.36**	**-65.09**	***SKKS***	**45.51**	**56.96**	**63.71**	**0.80**	**1.10**	**1.40**	**-0.68**	**-0.61**	**-0.54**	**0.35**	**yes**	**-**	**47.96**	**-15.44**
ARBE	**22-Nov-2011**	**-15.36**	**-65.09**	***SKS***	**NULL**	**NULL**	**NULL**	**NULL**	**NULL**	**NULL**	**-0.19**	**-0.12**	**-0.06**	**0.35**	**yes**	**-**	**55.11**	**1.11**
ARE0	01-Jul-2001	-4.31	152.96	*SKKS*	1.01	11.61	21.24	1.05	1.25	1.50	-1.18	-1.09	-1.01	-	no	-	68.01	103.39
ARE0	01-Jul-2001	-4.31	152.96	*SKS*	1.01	9.61	17.19	0.75	0.85	0.95	-0.98	-0.96	-0.94	-	no	-	73.15	67.35
ARE0	21-Mar-2005	-24.98	-63.47	*SKKS*	NULL	NULL	NULL	NULL	NULL	NULL	-0.21	-0.15	-0.08	-	no	-	55.66	-21.19
ARE0	21-Mar-2005	-24.98	-63.47	*SKS*	NULL	NULL	NULL	NULL	NULL	NULL	0.09	0.20	0.30	-	no	-	64.86	-2.28
ARE0	21-May-2005	-3.29	-80.99	*SKKS*	NULL	NULL	NULL	NULL	NULL	NULL	-0.02	-0.01	0.01	-	no	-	60.37	-40.54
ARE0	21-May-2005	-3.29	-80.99	*SKS*	NULL	NULL	NULL	NULL	NULL	NULL	-0.01	0.02	0.05	-	no	-	67.63	-18.81
ARE0	03-Jul-2008	-23.37	-179.78	*SKKS*	NULL	NULL	NULL	NULL	NULL	NULL	0.11	0.18	0.24	-	no	-	78.93	103.73
ARE0	03-Jul-2008	-23.37	-179.78	*SKS*	NULL	NULL	NULL	NULL	NULL	NULL	-0.10	-0.01	0.08	-	no	-	75.73	42.61

D.3 Observations of *SKS-SKKS-sSKS*

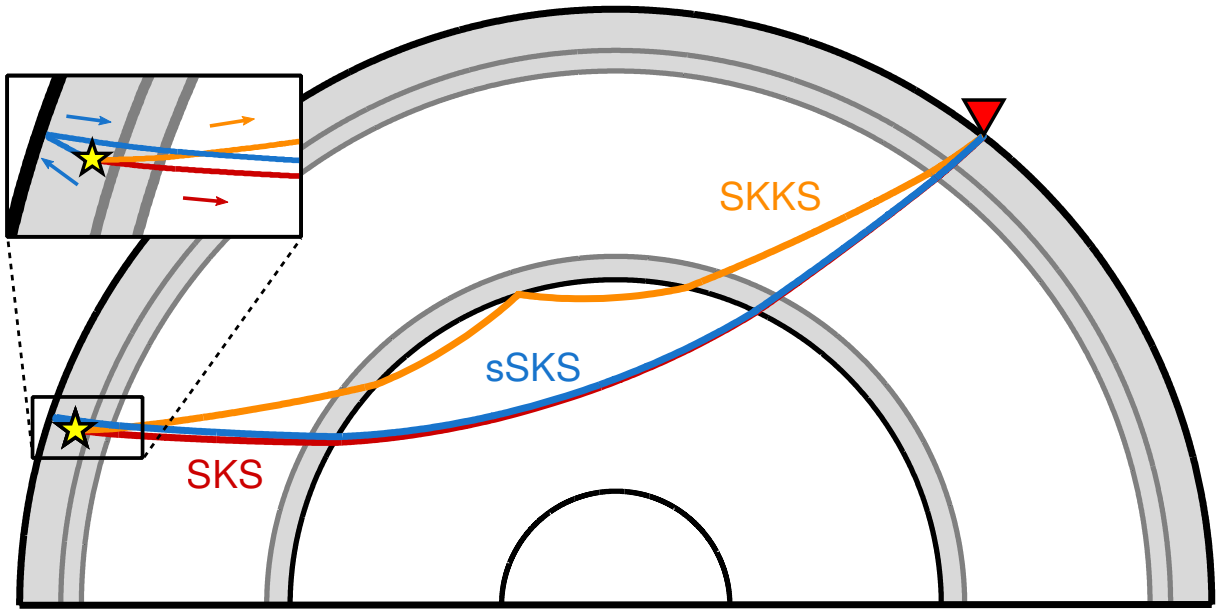

Figure D.2: Raypaths of *SKS*, *SKKS* and *sSKS* from hypocenter (star) to receiver (500 km depth, $\Delta \sim 100°$). In comparison to *SKS* the raypath for *sSKS* contains an additional leg that results from a reflection of an upgoing shear wave at the free surface (small blue arrow in inset). Since both phases have nearly identical incidence angles (within $\sim 0.3°$) and raypaths, they also sample the same region in D". Therefore, both raypaths lie almost atop each other after the *P*-to-*S* conversion at the core-mantle boundary on the receiver side. (*Fig. continued on next page*)

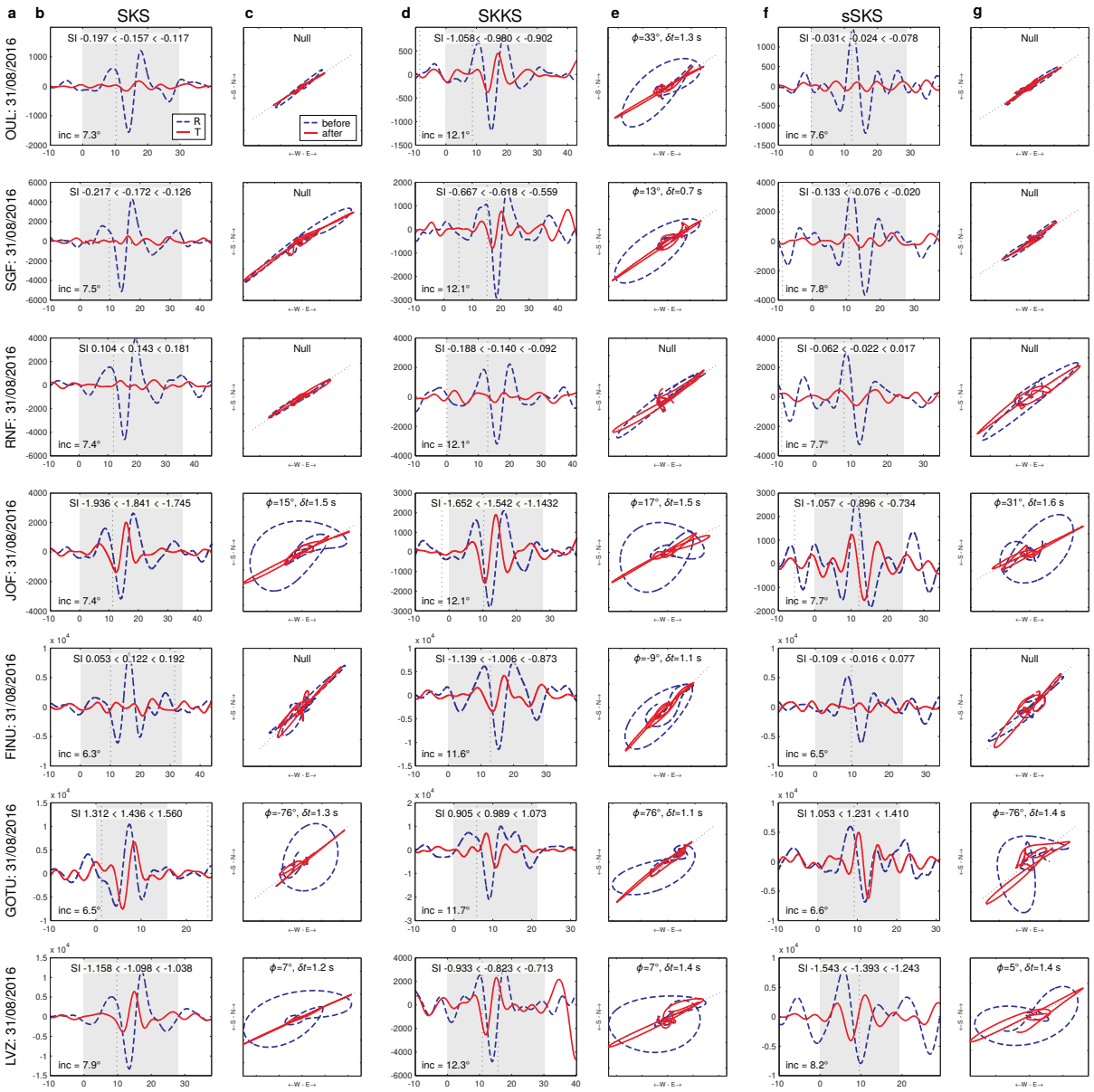

Figure D.2 (Cont.): Waveform examples for *SKS*, *SKKS* and *sSKS* phases. (a) Station and event date. (b) Original (uncorrected) radial (blue dashed) and transverse (solid red) components for the *SKS* phase. On top the corresponding SI along with its uncertainty (95% confidence interval) is shown. The incidence angle is given in the lower left corner. The gray shaded area indicates the analysis window. (c) Corresponding particle motions before (blue dashed) and after (solid red) the correction for splitting using the SC method *Silver and Chan* (1991). Splitting parameters or nulls are indicated at the top of each panel. (d) and (e) Corresponding content for the *SKKS* phase of the same event. (f) and (g) Corresponding content for the *sSKS* phase of the same event.

D.4 Exemplary 3D-raypaths of *SKS* and *SKKS*

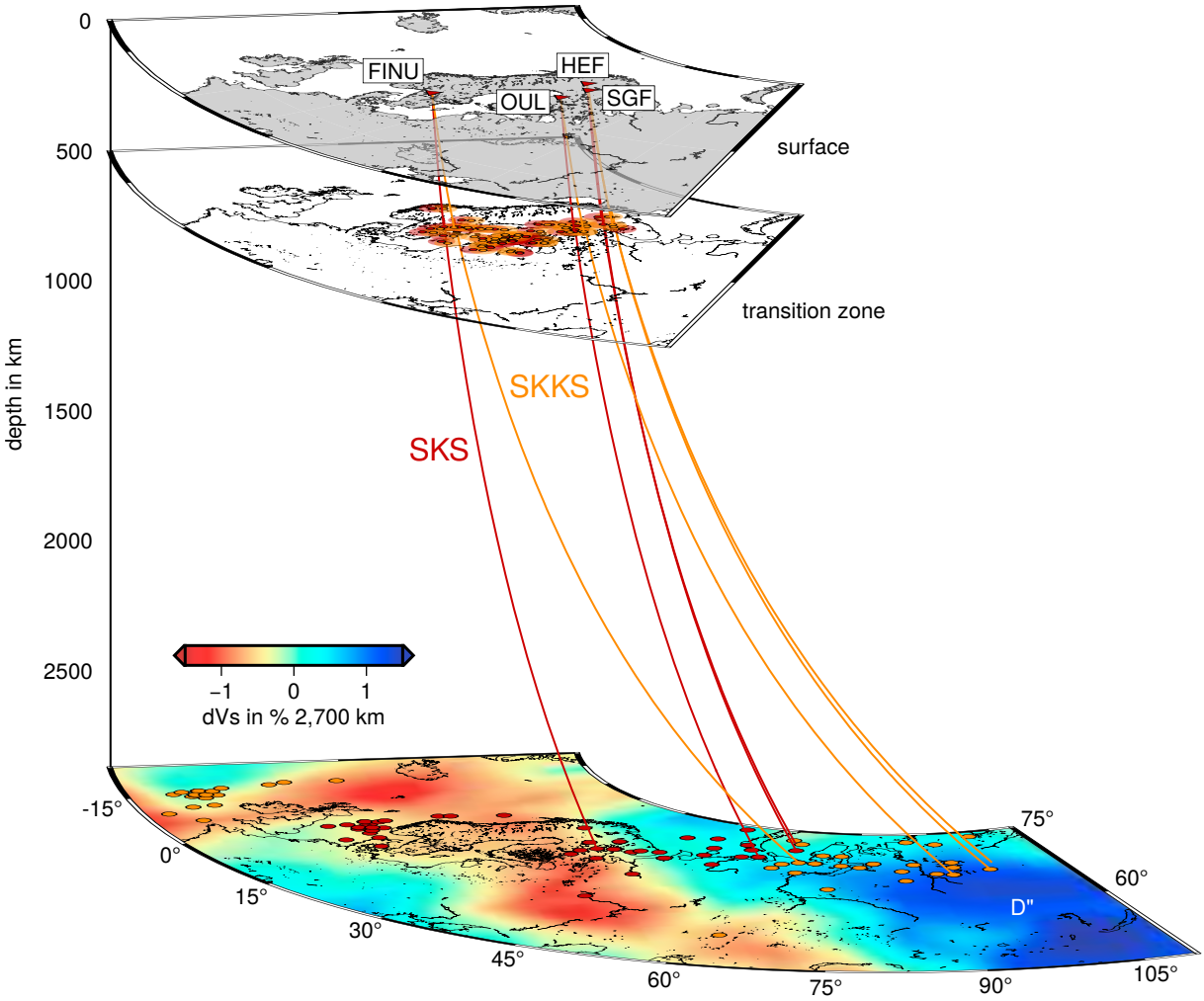

Figure D.3: Simplified 3D visualization of the raypaths of *SKS* (red) and *SKKS* (orange) for an event on 31/08/2016, recorded at four stations in Finland and Sweden (red triangles at surface). Raypaths are calculated with the tauP toolkit (*Crotwell et al.*, 1999) and the iasp91 Earth model (*Kennett*, 1991). All recorded *SKS*-*SKKS* pairs are discrepant with the *SKS* null and the *SKKS* phase clearly split. While the raypaths are similar above the transition zone, they differ significantly in the lowermost mantle. Please note that the figure is not in scale regarding the spherical shape of the Earth since the different depths are only shown as flat planes.

D.5 Map showing split-split *SKS-SKKS* pairs

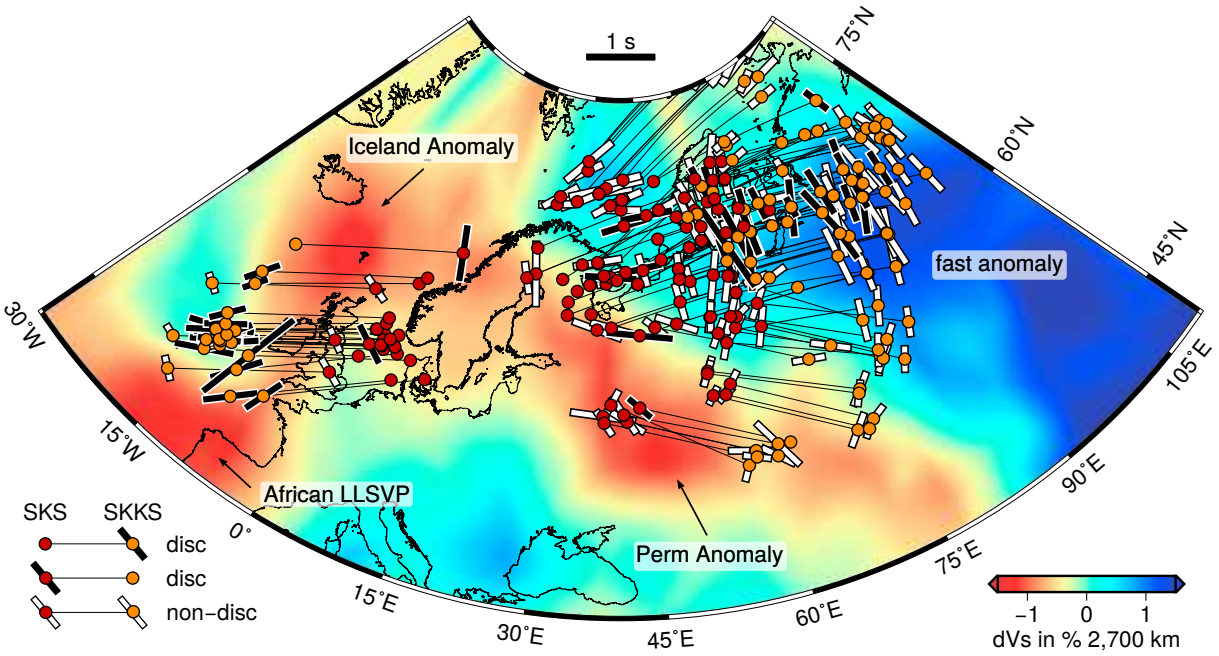

Figure D.4: *SKS-SKKS* pierce points at 2700 km depth, calculated with the tauP toolkit (*Crotwell et al.*, 1999) and the iasp91 earth model (*Kennett*, 1991), atop of the GyPSuM model (*Simmons et al.*, 2010) in the lower mantle. Pairs are marked with red (*SKS*) and orange (*SKKS*) dots. For discrepant pairs the split phase is indicated with a white bordered black bar oriented in the direction of the fast axis ϕ. Non-discrpeant pairs (only split-split) are marked with a black bordered white bar at the *SKS* and *SKKS* pierce points (also oriented in the direction of the fast axis ϕ).

E Anisotropy beneath Fennoscandia – Supporting content

E.1 Single-event shear wave splitting results

Due to the massive amount of measurements, single-event results of all stations rated as *good* or *fair* (1772 splits and 4695 nulls) are available in the electronic appendix (see F). Discrepant *SKS-SKKS* pairs are not included in this list (see appendix D). Table E.1 shows an exemplary subset of these data (split phases).

Table E.1: Subset of shear wave splitting results for the extended ScanArray network. Only splits ranked as *good/fair* are shown. Nulls can be found in the electronic appendix (see F).

Sta	Lat	Lon	Date ev	Lat ev	Lon ev	BAZ	Phase	ϕ_{RC}	δt_{RC}	ϕ_{SC}	δt_{SC}	Null	Qual
	in °	in °	yyyy-mm-dd	in °	in °	in °		in °	in s	in °	in s		
AAL	60.18	19.99	2010-08-10	-17.54	168.07	42.40	*PKS*	87.40	0.58	84.40	0.60	No	fair
AAL	60.18	19.99	2011-08-20	-18.31	168.22	42.58	*PKS*	89.58	0.58	-77.42	0.68	No	fair
AAL	60.18	19.99	2014-04-26	-20.71	-174.72	21.31	*PKS*	60.31	0.42	75.31	0.44	No	fair
AAL	60.18	19.99	2014-07-19	-15.80	-174.40	19.56	*PKS*	67.56	0.80	63.56	0.84	No	fair
AAL	60.18	19.99	2014-07-21	-19.78	-178.44	26.14	*PKS*	76.14	0.58	88.14	0.72	No	fair
AAL	60.18	19.99	2014-11-01	-19.70	-177.79	25.23	*SKS*	67.23	0.62	61.23	0.64	No	good
AAL	60.18	19.99	2015-07-17	-18.08	-178.20	25.26	*PKS*	65.26	0.58	77.26	0.60	No	fair
AAL	60.18	19.99	2015-12-17	15.88	-93.46	297.95	*SKS*	80.95	0.60	75.95	0.60	No	fair
AAL	60.18	19.99	2016-04-28	-16.07	167.39	42.52	*PKS*	79.52	0.50	86.52	0.48	No	fair
AKN	62.18	7.00	2013-05-14	18.73	145.29	39.11	*SKS*	2.11	0.62	5.11	0.65	No	fair
ARA0	69.53	25.51	2015-04-30	-5.39	151.82	57.07	*SKS*	-6.93	1.25	5.07	1.10	No	fair
ARA0	69.53	25.51	2015-05-07	-7.23	154.55	54.90	*SKS*	15.90	1.10	4.90	1.10	No	fair
ARA0	69.53	25.51	2015-05-07	-7.23	154.55	54.90	*SKS*	6.90	0.75	16.90	0.80	No	fair
ARA0	69.53	25.51	2016-06-05	-4.58	125.62	82.10	*SKS*	35.10	0.75	26.10	0.80	No	good
ARA0	69.53	25.51	2016-08-31	-3.69	152.79	55.59	*SKS*	19.59	1.07	9.59	1.05	No	good
ARA0	69.53	25.51	2016-08-31	-3.69	152.79	55.59	*SKS*	9.59	1.00	1.59	1.05	No	good
ARA0	69.53	25.51	2016-08-31	-3.69	152.79	55.59	*sSKS*	22.59	1.07	19.59	1.05	No	fair
ARA0	69.53	25.51	2017-07-13	-4.79	153.16	55.55	*SKS*	18.55	0.75	1.55	0.80	No	fair
ARBE	59.44	25.98	2012-12-10	-6.53	129.82	81.35	*SKS*	37.35	0.75	31.35	0.80	No	fair
ARBE	59.44	25.98	2016-08-31	-3.69	152.79	58.90	*SKS*	21.90	1.00	28.90	1.10	No	fair
ARE0	69.53	25.51	2000-02-06	-5.84	150.88	58.15	*SKS*	12.15	1.05	10.15	1.05	No	fair
ARE0	69.53	25.51	2001-07-01	-4.31	152.96	55.61	*SKS*	-0.39	0.90	9.61	0.85	No	good
ARE0	69.53	25.51	2001-07-01	-4.31	152.96	55.61	*SKS*	24.61	1.33	11.61	1.25	No	fair
ARE0	69.53	25.51	2002-06-10	10.98	140.69	62.73	*SKS*	17.73	1.05	4.73	1.25	No	fair

E.2 Multi-event shear wave splitting results

Multi-event splitting results (Table E.2) were calculated for individual recording stations using single-event measurements ranked as *poor*. For this purpose, the surface stacking approach of *Wolfe and Silver* (1998) as implemented in StackSplit (*Grund*, 2017) was applied (see section 5.3.3). Fig. E.1 displays the results of four exemplary multi-event measurements. The rows in Table E.2 corresponding to these measurements are highlighted in red.

Since several stations showed significant backazimuthal variations of the splitting parameters, single-event results were only stacked in bins covering a maximum range of 5° with respect to backazimuth and epicentral distance. Fig. E.2 schematically displays the lower and upper bin limits for backazimuth (**min BAZ**, **max BAZ**) and epicentral distance (**min dist**, **max dist**) that are listed in Table E.2. If upper and lower limits are the same, the stack consists of multiple phases of the same event. Parameters **mean BAZ** and **mean dist** represent simple averages calculated of the individual BAZ and distance values.

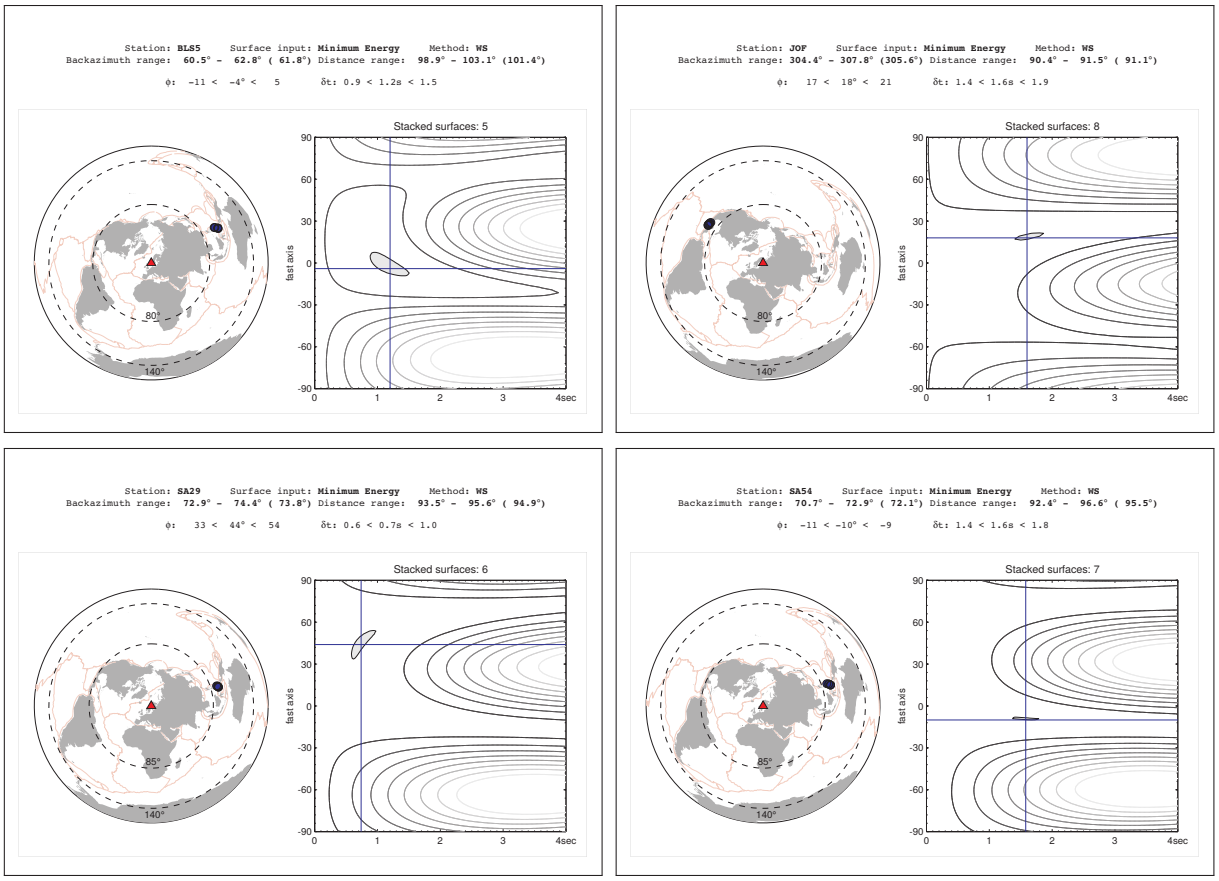

Figure E.1: StackSplit diagnostic plots showing exemplary multi-event measurements using the surface stacking method of *Wolfe and Silver* (1998) at the recording stations BLS5, JOF (both permanent stations, top row), SA29 and SA54 (temporary, bottom row).

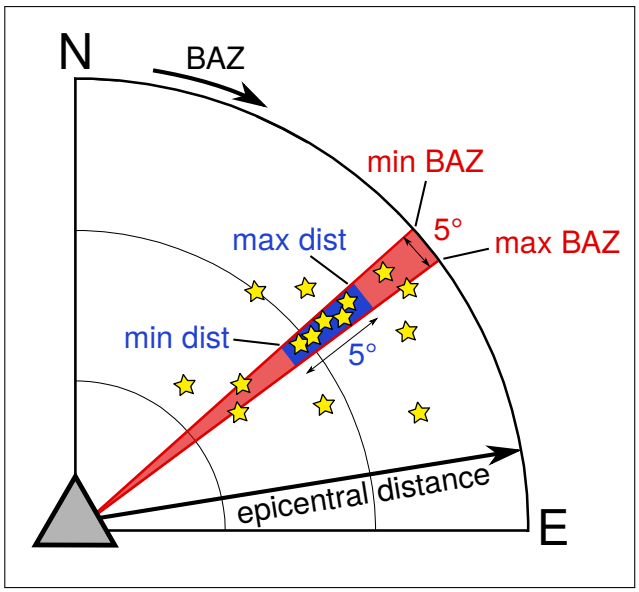

Figure E.2: Schematic to visualize the parameter definitions of **min BAZ**, **max BAZ**, **min dist** and **max dist** listed in Table E.2. The gray triangle indicates an exemplary recording station. Splitting results of the exemplary events (stars) located within the selected bin limits (blue area) are considered in the multi-event measurement using the method of *Wolfe and Silver* (1998). Backazimuth is measured clockwise from north and epicentral distance in radial direction.

Table E.2: Multi-event shear wave splitting results – **Sta**: station name, **# surf**: number of stacked surfaces, **min BAZ**: lower backazimuthal bin bound (see Fig. E.2), **max BAZ**: upper backazimuthal bin bound, **min dist**: lower distance bin bound, **max dist**: upper distance bin bound, ϕ_{WS}: fast axis direction (including errors, 95% confidence interval) based on method of *Wolfe and Silver* (1998), δt_{WS}: delay time (including errors, 95% confidence interval).

Sta	# surf	min BAZ in °	max BAZ in °	mean BAZ in °	min dist in °	max dist in °	mean dist in °	ϕ_{WS} in °	δt_{WS} in s
BLS5	2	200.4	200.4	200.4	118.6	118.6	118.6	-43 < -34 < -27	1.4 < 1.7 < 2.0
BLS5	2	24.5	24.9	24.7	135.6	139.4	137.5	-41 < -26 < -11	1.0 < 1.5 < 1.9
BLS5	2	44.6	46.1	45.3	118.2	118.9	118.6	-19 < -6 < 7	0.9 < 1.2 < 1.5
BLS5	**5**	**60.5**	**62.8**	**61.8**	**98.9**	**103.1**	**101.4**	**-11 < -4 < 5**	**0.9 < 1.2 < 1.5**
BLS5	6	25.6	26.5	26.1	131.9	134.5	132.7	-25 < -16 < -11	1.3 < 1.4 < 1.6
FIA1	2	301.8	302.3	302.0	89.8	90.4	90.1	43 < 46 < 56	0.8 < 1.1 < 1.4
FIA1	2	74.6	76.9	75.8	97.7	101.8	99.8	41 < 56 < 66	0.7 < 1.3 < 2.0
FIA1	2	78.1	78.6	78.4	85.5	89.9	87.7	35 < 48 < 62	0.9 < 1.3 < 1.7
FIA1	2	79.2	79.5	79.4	93.2	93.2	93.2	9 < 14 < 21	1.1 < 1.4 < 1.7
FIA1	3	80.3	82.1	80.9	90.3	94.5	92.8	13 < 34 < 58	0.6 < 0.8 < 1.1
FIA1	4	33.9	33.9	33.9	135.4	136.3	136.1	48 < 52 < 62	0.8 < 1.1 < 1.5
FIA1	4	34.2	37.6	35.4	135.4	138.3	136.5	68 < 74 < 86	0.9 < 1.1 < 1.3
GRAU	2	16.1	16.3	16.2	134.0	134.1	134.0	50 < 60 < 74	0.8 < 1.0 < 1.3
GRAU	2	207.8	207.8	207.8	121.9	121.9	121.9	-13 < -2 < 5	1.2 < 1.7 < 2.1
GRAU	2	24.4	24.4	24.4	139.0	139.9	139.5	-92 < -82 < -78	0.6 < 0.9 < 1.3
GRAU	3	275.2	277.4	276.1	90.7	93.6	92.1	-9 < -6 < -5	1.2 < 1.5 < 2.1
GRAU	3	73.3	74.3	73.6	97.1	98.2	97.5	-5 < 32 < 64	0.2 < 0.4 < 1.0
JOF	2	216.3	216.5	216.4	127.3	127.5	127.4	-39 < -20 < 5	0.5 < 0.8 < 1.3
JOF	2	32.8	34.2	33.5	129.6	132.3	130.9	-5 < 16 < 27	0.4 < 0.8 < 1.4
JOF	2	40.7	40.8	40.8	137.9	138.5	138.2	7 < 14 < 23	0.8 < 1.1 < 1.4
JOF	2	52.9	53.0	52.9	122.5	125.4	124.0	7 < 14 < 21	1.5 < 1.8 < 2.1
JOF	3	314.9	319.7	316.5	90.4	92.4	91.5	13 < 24 < 31	1.0 < 1.5 < 2.0

continued on next page ...

... continued from previous page

Sta	# surf	min BAZ in °	max BAZ in °	mean BAZ in °	min dist in °	max dist in °	mean dist in °	ϕ_{WS} in °	δt_{WS} in s
JOF	3	43.7	45.3	44.8	134.9	136.3	135.8	-3 < 10 < 23	0.8 < 1.0 < 1.4
JOF	3	62.1	62.8	62.5	108.9	111.1	110.2	11 < 16 < 21	1.5 < 1.7 < 2.0
JOF	3	85.7	87.6	86.5	96.2	100.2	98.7	13 < 18 < 27	1.1 < 1.4 < 1.7
JOF	4	63.3	66.1	64.8	106.6	108.4	107.9	1 < 6 < 13	1.7 < 2.0 < 2.3
JOF	7	38.2	40.1	39.4	130.2	134.5	132.1	11 < 16 < 21	0.8 < 0.9 < 1.1
JOF	**8**	**304.4**	**307.8**	**305.6**	**90.4**	**91.5**	**91.1**	**17 < 18 < 21**	**1.4 < 1.6 < 1.9**
JOF	8	83.3	84.3	83.7	88.3	91.2	89.6	11 < 16 < 27	0.7 < 1.0 < 1.3
KAF	2	213.1	213.9	213.5	125.4	125.5	125.4	46 < 48 < 56	1.1 < 1.6 < 2.1
KAF	2	260.8	263.0	261.9	113.0	116.1	114.5	11 < 48 < 68	0.4 < 0.6 < 1.1
KAF	2	263.1	263.3	263.2	111.2	111.5	111.4	1 < 12 < 60	0.3 < 0.8 < 1.6
KAF	2	309.3	311.1	310.2	89.0	89.3	89.2	-84 < -72 < -66	0.6 < 0.8 < 1.1
KAF	2	83.2	83.3	83.3	98.5	102.0	100.3	9 < 20 < 43	0.7 < 1.1 < 1.6
KAF	3	32.6	33.8	33.3	134.3	134.8	134.5	43 < 48 < 60	0.8 < 1.2 < 1.7
KAF	3	38.7	40.3	39.4	137.7	139.7	139.0	58 < 62 < 70	1.1 < 1.4 < 1.8
KAF	5	58.4	60.4	59.1	110.5	110.8	110.6	-3 < 10 < 23	0.7 < 0.8 < 1.0
KAF	6	25.6	30.5	27.9	130.9	134.2	132.6	46 < 50 < 58	1.4 < 1.7 < 2.1
KAF	6	48.0	48.8	48.4	129.5	133.4	130.7	-27 < -14 < 11	0.5 < 0.8 < 1.2
KAF	6	78.0	79.7	79.0	88.9	93.6	91.7	17 < 28 < 41	0.7 < 0.8 < 1.0
KAF	6	81.0	82.7	81.9	89.2	94.2	91.7	19 < 28 < 46	0.8 < 1.0 < 1.2
KAF	7	299.9	303.4	301.9	88.9	90.6	89.8	46 < 60 < 74	0.3 < 0.3 < 0.6
KEF	2	257.2	258.4	257.8	121.4	123.3	122.3	-86 < -74 < -64	0.9 < 1.2 < 1.6
KEF	2	260.8	261.8	261.3	111.6	115.4	113.5	1 < 8 < 27	0.7 < 1.4 < 2.2
KEF	2	261.9	265.7	263.8	107.1	110.9	109.0	5 < 8 < 15	1.1 < 1.4 < 1.8
KEF	2	46.5	46.6	46.6	124.4	125.8	125.1	66 < 68 < 74	1.2 < 1.4 < 1.6
KEF	2	88.9	90.4	89.6	98.8	100.1	99.5	9 < 14 < 23	0.8 < 1.2 < 1.7
KEF	3	24.8	26.4	25.5	131.1	134.4	133.2	54 < 58 < 62	1.0 < 1.0 < 1.1
KEF	3	32.4	33.7	32.9	132.4	136.1	134.2	43 < 46 < 52	1.2 < 1.6 < 2.2
KEF	3	76.2	76.7	76.5	88.5	91.1	89.7	1 < 12 < 31	0.5 < 0.8 < 1.3
KEF	4	77.3	77.6	77.5	90.6	93.3	92.0	5 < 24 < 54	0.4 < 0.5 < 0.8
KEF	5	280.2	283.2	281.7	93.3	97.9	95.2	19 < 24 < 48	0.4 < 0.8 < 1.6
KEF	5	298.6	301.1	299.8	89.2	89.4	89.3	46 < 48 < 62	0.8 < 1.2 < 1.6
KEF	5	31.6	32.2	32.0	134.6	136.9	135.6	54 < 62 < 76	0.7 < 1.0 < 1.3
KEF	6	306.1	309.2	308.1	88.4	89.9	89.3	48 < 66 < -76	0.3 < 0.6 < 1.4
KONO	2	2.3	5.3 3	.8 13	6.9	137.1	137.0	29 < 44 < 64	0.7 < 1.0 < 1.2
KONO	2	30.0	30.3	30.2	131.3	134.9	133.1	48 < 52 < 62	1.2 < 1.6 < 2.1
KONO	2	68.4	69.4	68.9	106.9	109.1	108.0	1 < 30 < 54	0.5 < 0.8 < 1.4
KONO	3	240.9	241.2	241.1	105.8	106.1	105.9	-5 < 2 < 15	0.9 < 1.1 < 1.4
KONO	3	249.1	251.9	250.4	99.9	102.0	101.2	-3 < 4 < 19	1.0 < 1.4 < 1.9
KONO	3	258.4	261.0	259.3	92.2	93.6	92.9	-3 < 2 < 33	0.4 < 1.1 < 1.9
KONO	3	29.6	29.7	29.7	129.7	132.6	131.1	41 < 42 < 46	1.7 < 1.9 < 2.1
KONO	3	73.6	77.4	75.1	107.7	109.7	108.4	-1 < 8 < 27	0.7 < 1.0 < 1.6
KONO	3	9.2	11.8	10.8	136.6	139.8	138.1	23 < 30 < 46	0.6 < 1.0 < 1.4
KONO	4	243.2	246.6	245.6	103.1	104.5	103.8	13 < 20 < 31	1.0 < 1.1 < 1.3
KONO	6	252.4	255.9	254.3	97.8	100.7	99.3	3 < 10 < 17	1.0 < 1.2 < 1.5
KONO	7	90.1	90.8	90.5	90.8	94.3	93.1	19 < 24 < 35	0.9 < 1.2 < 1.5
KU6	2	40.2	40.9	40.5	135.7	139.3	137.5	-39 < -16 < 23	0.3 < 0.5 < 1.0

continued on next page ...

... continued from previous page

Sta	# surf	min BAZ in °	max BAZ in °	mean BAZ in °	min dist in °	max dist in °	mean dist in °	ϕ_{WS} in °	δt_{WS} in s
KU6	2	49.5	49.5	49.5	128.8	128.8	128.8	-23 < -16 < -9	1.1 < 1.4 < 1.7
KU6	3	88.6	90.6	90.0	97.7	98.7	98.0	19 < 28 < 41	0.6 < 0.8 < 1.1
KU6	4	54.4	54.9	54.6	115.4	116.7	116.1	-1 < 10 < 23	1.0 < 1.2 < 1.4
KU6	4	59.4	63.3	61.5	106.2	109.4	107.7	-5 < 4 < 13	1.3 < 1.6 < 1.9
KU6	7	81.2	83.6	82.7	90.4	94.0	91.5	9 < 12 < 17	0.7 < 0.9 < 1.0
MSF	10	58.9	62.9	60.7	107.1	110.5	108.3	25 < 40 < 48	0.5 < 0.7 < 1.0
MSF	2	295.3	295.4	295.3	89.8	90.1	90.0	33 < 42 < 78	0.4 < 1.0 < 1.8
MSF	2	34.9	35.2	35.1	131.2	131.9	131.5	41 < 48 < 72	0.3 < 0.6 < 1.1
MSF	2	47.4	48.6	48.0	130.0	130.2	130.1	-23 < -14 < -5	0.7 < 0.9 < 1.2
MSF	2	82.2	82.4	82.3	95.2	99.9	97.6	11 < 28 < 56	0.6 < 1.0 < 1.5
MSF	3	262.9	264.9	264.2	111.1	113.9	112.4	52 < 58 < 66	0.6 < 0.8 < 0.9
MSF	3	283.2	284.6	284.1	97.8	101.4	99.3	27 < 44 < 82	0.3 < 0.4 < 0.9
MSF	3	286.8	287.4	287.2	94.1	97.2	96.1	33 < 38 < 50	0.9 < 1.2 < 1.6
MSF	3	92.0	94.9	93.5	95.3	98.4	96.9	25 < 32 < 41	0.8 < 1.0 < 1.3
MSF	4	28.9	30.0	29.7	130.3	133.5	131.7	41 < 50 < 76	0.4 < 0.6 < 0.9
MSF	4	30.6	32.4	31.8	131.3	132.2	131.7	41 < 42 < 46	0.8 < 1.0 < 1.2
MSF	4	53.5	54.1	53.9	113.9	117.0	115.7	-3 < 26 < 39	0.4 < 0.6 < 1.0
MSF	4	63.1	66.4	65.4	106.1	107.5	106.8	-5 < 2 < 15	0.7 < 0.9 < 1.2
MSF	5	49.2	49.5	49.3	121.2	122.1	121.7	-23 < 16 < 33	0.3 < 0.4 < 0.6
MSF	6	81.3	82.1	81.7	89.0	91.8	90.1	3 < 6 < 15	0.9 < 1.4 < 1.9
OUL	12	77.5	80.0	78.7	89.5	93.2	91.4	13 < 20 < 33	0.7 < 0.8 < 0.9
OUL	2	100.4	101.1	100.7	93.5	94.0	93.7	29 < 42 < 72	0.4 < 0.5 < 0.7
OUL	2	256.3	256.5	256.4	114.8	115.1	115.0	-88 < -70 < -46	0.5 < 0.9 < 1.3
OUL	2	96.8	99.1	97.9	97.0	97.0	97.0	15 < 32 < 82	0.3 < 0.8 < 1.8
OUL	3	30.7	30.9	30.8	129.8	130.0	129.9	56 < 60 < 70	1.1 < 1.4 < 1.6
OUL	3	80.0	80.1	80.1	93.2	95.8	94.1	35 < 60 < 72	0.5 < 0.9 < 1.5
OUL	4	281.9	284.3	283.2	93.1	96.0	94.3	54 < 78 < 88	0.4 < 0.6 < 0.9
OUL	5	25.5	26.5	26.2	131.1	133.2	131.8	56 < 58 < 68	1.2 < 1.4 < 1.5
OUL	5	36.5	37.8	37.2	136.2	139.2	137.3	68 < 84 < -80	0.6 < 0.8 < 1.1
PVF	2	37.9	39.2	38.6	139.0	139.6	139.3	54 < 60 < 72	0.7 < 1.0 < 1.4
PVF	3	49.4	49.6	49.4	131.8	132.2	132.0	-13 < -8 < -5	0.7 < 0.7 < 0.8
PVF	3	77.7	79.0	78.4	91.8	93.4	92.8	7 < 12 < 21	0.8 < 1.0 < 1.3
PVF	3	79.5	79.9	79.7	93.0	94.5	93.7	19 < 30 < 46	0.6 < 0.7 < 0.8
PVF	3	80.4	81.6	81.0	102.2	102.8	102.5	9 < 8 < 11	1.6 < 1.8 < 1.9
PVF	3	83.6	87.8	85.0	98.8	100.9	99.8	11 < 22 < 46	0.5 < 0.7 < 1.1
PVF	4	25.4	28.4	26.7	132.6	135.6	133.9	54 < 58 < 66	1.1 < 1.3 < 1.6
PVF	4	33.9	34.1	34.1	136.2	136.4	136.3	60 < 68 < 82	0.7 < 0.8 < 1.0
SA19	2	26.4	26.7	26.6	132.3	133.6	133.0	48 < 54 < 68	1.1 < 1.5 < 1.8
SA19	2	281.1	281.1	281.1	94.2	94.3	94.3	21 < 26 < 43	0.8 < 1.6 < 2.4
SA19	2	76.0	76.0	76.0	93.8	93.9	93.9	5 < 24 < 52	0.4 < 0.5 < 0.9
SA19	2	97.6	99.1	98.4	91.6	95.6	93.6	48 < 68 < 84	0.5 < 0.8 < 1.2
SA19	3	20.5	23.0	22.0	130.3	131.4	131.0	41 < 46 < 52	1.3 < 1.6 < 1.9
SA19	3	83.4	83.5	83.4	100.8	100.8	100.8	5 < 10 < 25	0.5 < 0.9 < 1.2
SA21	2	261.7	262.1	261.9	120.6	121.4	121.0	19 < 40 < 62	0.7 < 1.0 < 1.4
SA21	3	82.2	86.1	84.8	98.5	99.7	99.3	13 < 18 < 27	1.1 < 1.4 < 1.8
SA21	4	29.7	30.5	29.9	131.4	132.3	131.6	46 < 52 < 62	0.9 < 1.2 < 1.6

continued on next page ...

... continued from previous page

Sta	# surf	min BAZ in °	max BAZ in °	mean BAZ in °	min dist in °	max dist in °	mean dist in °	ϕ_{WS} in °	δt_{WS} in s
SA21	4	77.6	78.7	78.3	91.2	92.9	92.4	3 < 6 < 13	1.0 < 1.3 < 1.6
SA23	2	279.3	279.4	279.3	93.6	93.7	93.7	52 < 62 < 74	0.7 < 0.9 < 1.1
SA23	3	23.3	24.7	24.1	133.3	136.2	134.7	58 < 62 < 72	1.3 < 1.6 < 1.9
SA23	4	74.3	75.1	74.7	91.8	95.3	94.2	56 < 60 < 64	1.0 < 1.3 < 1.6
SA23	5	18.4	23.3	20.7	129.6	132.3	131.5	56 < 60 < 70	1.1 < 1.3 < 1.4
SA28	2	80.4	81.0	80.7	91.9	92.0	91.9	11 < 18 < 29	0.8 < 1.0 < 1.3
SA28	5	29.4	33.3	32.0	129.7	131.9	131.1	46 < 44 < 46	1.5 < 1.7 < 1.8
SA28	5	58.2	60.2	59.2	108.3	111.3	109.6	-17 < -8 < 3	0.7 < 1.0 < 1.4
SA29	4	22.9	24.0	23.2	131.3	135.2	133.1	56 < 64 < 76	1.0 < 1.3 < 1.5
SA29	**6**	**72.9**	**74.4**	**73.8**	**93.5**	**95.6**	**94.9**	**33 < 44 < 54**	**0.6 < 0.7 < 1.0**
SA30	2	20.1	25.1	22.6	131.8	132.8	132.3	48 < 56 < 72	1.0 < 1.4 < 1.8
SA30	3	83.0	86.9	84.4	101.2	102.0	101.5	72 < 72 < 78	1.0 < 1.3 < 1.8
SA30	5	75.5	75.9	75.6	94.5	95.0	94.6	48 < 58 < 64	0.5 < 0.8 < 1.2
SA38	2	17.2	17.2	17.2	131.4	133.1	132.3	50 < 72 < -92	0.5 < 0.8 < 1.3
SA38	2	73.0	73.5	73.2	93.5	96.0	94.8	1 < 8 < 21	1.1 < 1.6 < 2.1
SA38	2	81.0	81.0	81.0	102.4	102.4	102.4	-1 < 4 < 15	0.5 < 1.0 < 1.5
SA38	3	22.4	23.4	23.0	132.5	136.4	134.6	39 < 56 < 88	0.5 < 0.8 < 1.4
SA42	2	268.8	269.1	269.0	100.8	101.2	101.0	-86 < -70 < -29	0.4 < 1.0 < 1.9
SA46	3	21.3	22.3	21.9	134.9	135.6	135.1	64 < 78 < -92	0.7 < 0.9 < 1.3
SA52	2	77.8	80.3	79.1	100.0	104.2	102.1	29 < 36 < 46	1.9 < 2.4 < 2.8
SA54	2	49.7	50.1	49.9	112.2	116.2	114.2	-33 < -14 < 27	0.3 < 0.6 < 1.3
SA54	4	21.7	22.8	22.2	135.6	137.8	136.3	35 < 42 < 62	0.6 < 1.0 < 1.4
SA54	**7**	**70.7**	**72.9**	**72.1**	**92.4**	**96.6**	**95.5**	**-11 < -10 < -9**	**1.4 < 1.6 < 1.8**
SA60	2	71.7	73.2	72.4	92.0	94.9	93.4	82 < 82 < 88	1.2 < 1.5 < 1.9
SA60	3	49.3	51.3	50.1	113.2	117.1	114.8	66 < 68 < 74	1.3 < 1.6 < 2.0
SA64	2	78.4	79.1	78.7	93.8	93.9	93.8	9 < 22 < 43	0.6 < 0.9 < 1.2
SA64	3	31.4	32.2	31.9	134.0	135.7	135.1	52 < 62 < 82	0.4 < 0.5 < 0.8
SA64	3	87.0	90.9	88.3	100.0	100.5	100.1	5 < 14 < 43	0.5 < 1.4 < 2.8
VAF	12	75.6	77.3	76.5	92.6	97.6	94.5	3 < 4 < 7	0.8 < 0.9 < 1.0
VAF	2	252.7	252.9	252.8	112.9	113.2	113.1	-68 < -46 < -37	0.6 < 1.0 < 1.4
VAF	2	266.3	267.1	266.7	104.6	106.4	105.5	-82 < -64 < -35	0.5 < 0.8 < 1.3
VAF	2	278.9	279.5	279.2	92.4	93.5	92.9	-72 < -66 < -62	1.1 < 1.5 < 1.9
VAF	2	43.5	43.6	43.6	125.6	125.8	125.7	-39 < -28 < 1	0.4 < 0.7 < 1.2
VAF	2	77.6	77.9	77.8	88.9	89.2	89.1	5 < 8 < 17	0.6 < 0.8 < 1.0
VAF	2	79.9	80.5	80.2	99.9	103.1	101.5	-1 < 4 < 15	0.4 < 0.6 < 1.3
VAF	3	20.8	21.9	21.2	130.9	132.9	131.6	41 < 56 < 82	0.5 < 0.7 < 1.0
VAF	3	23.8	26.1	25.1	131.5	136.0	133.3	56 < 72 < -92	0.5 < 0.7 < 0.9
VAF	3	260.3	260.6	260.4	109.6	110.2	109.9	-88 < -70 < -41	0.3 < 0.5 < 0.9
VAF	3	84.5	86.8	85.3	99.8	101.0	100.5	5 < 10 < 27	0.3 < 0.6 < 1.0
VAF	4	74.7	75.5	75.1	91.4	94.2	92.9	-1 < 4 < 13	0.6 < 0.8 < 1.1

E.3 Backazimuth-dependent splitting parameters

Figs. E.3-E.6 show individual splitting measurements color-coded with respect to the source regions. These figures are complements to the plots shown in section 7.3.1 (Figs. 7.7-7.10).

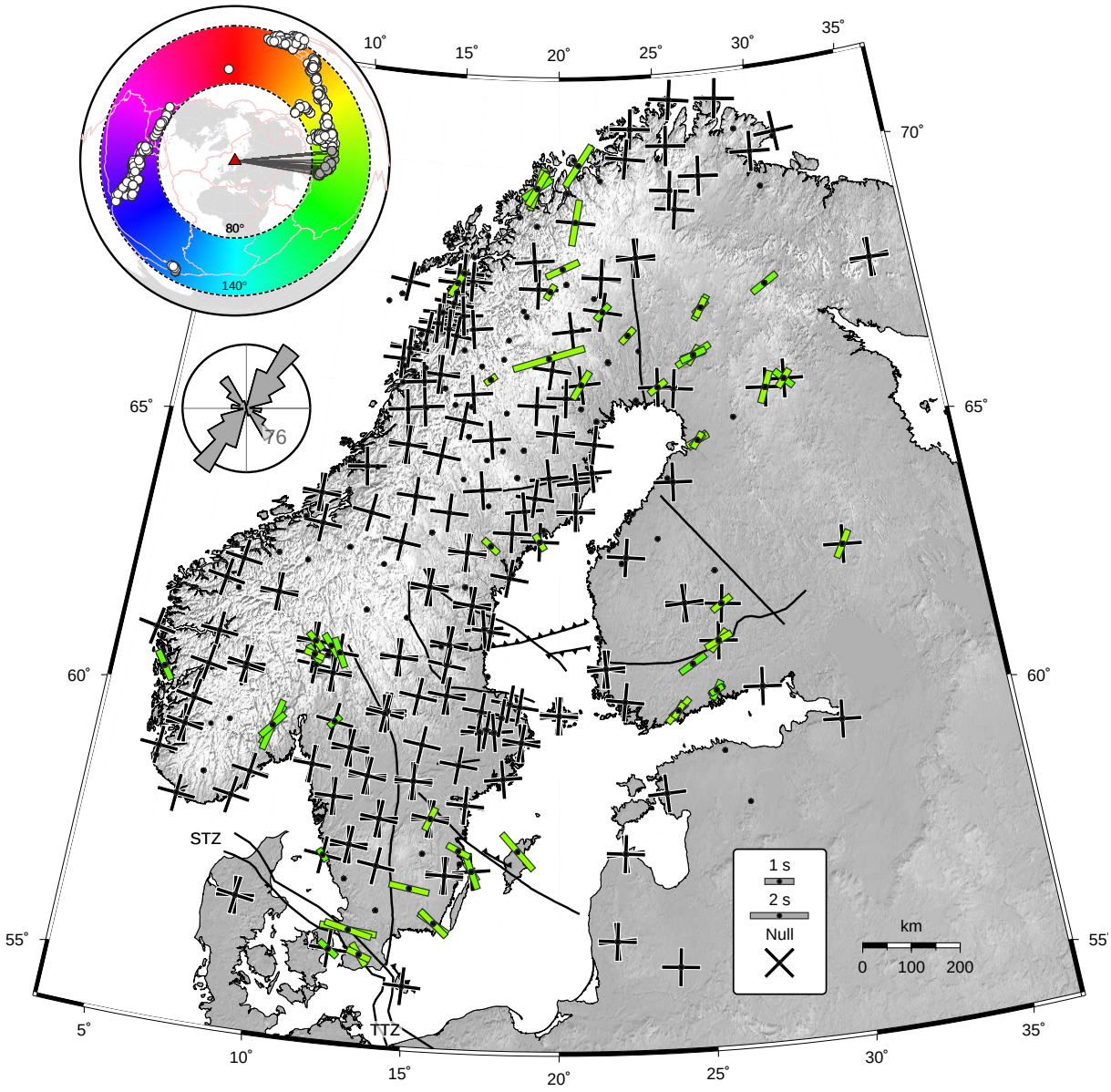

Figure E.3: Backazimuth-dependent individual shear wave splitting measurements color-coded with respect to the source region of the corresponding seismic event (see color-wheel). Individual null measurements are shown with black bars parallel and perpendicular to the backazimuth of the event.

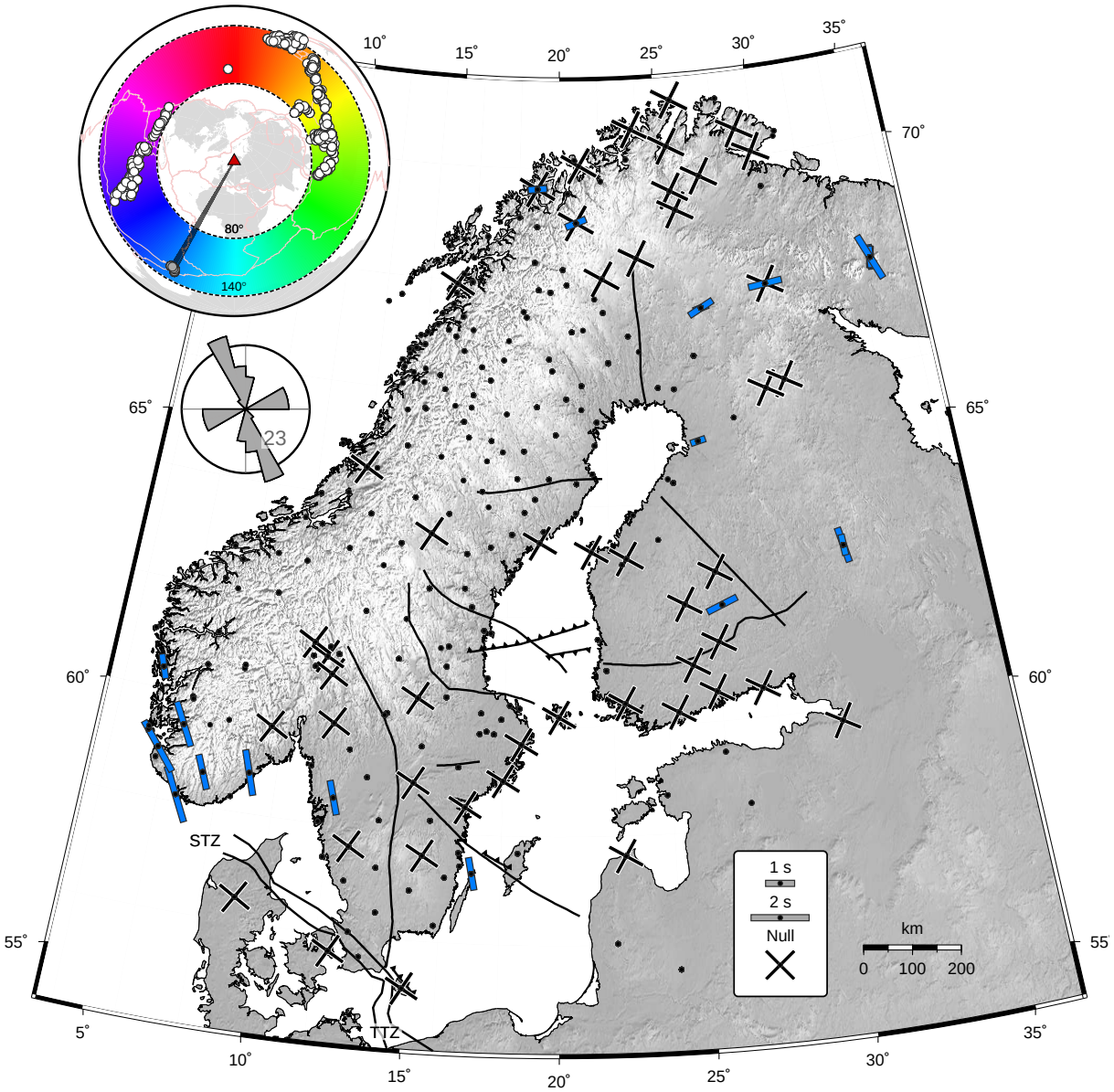

Figure E.4: Backazimuth-dependent individual shear wave splitting measurements color-coded with respect to the source region of the corresponding seismic event (see color-wheel). Individual null measurements are shown with black bars parallel and perpendicular to the backazimuth of the event.

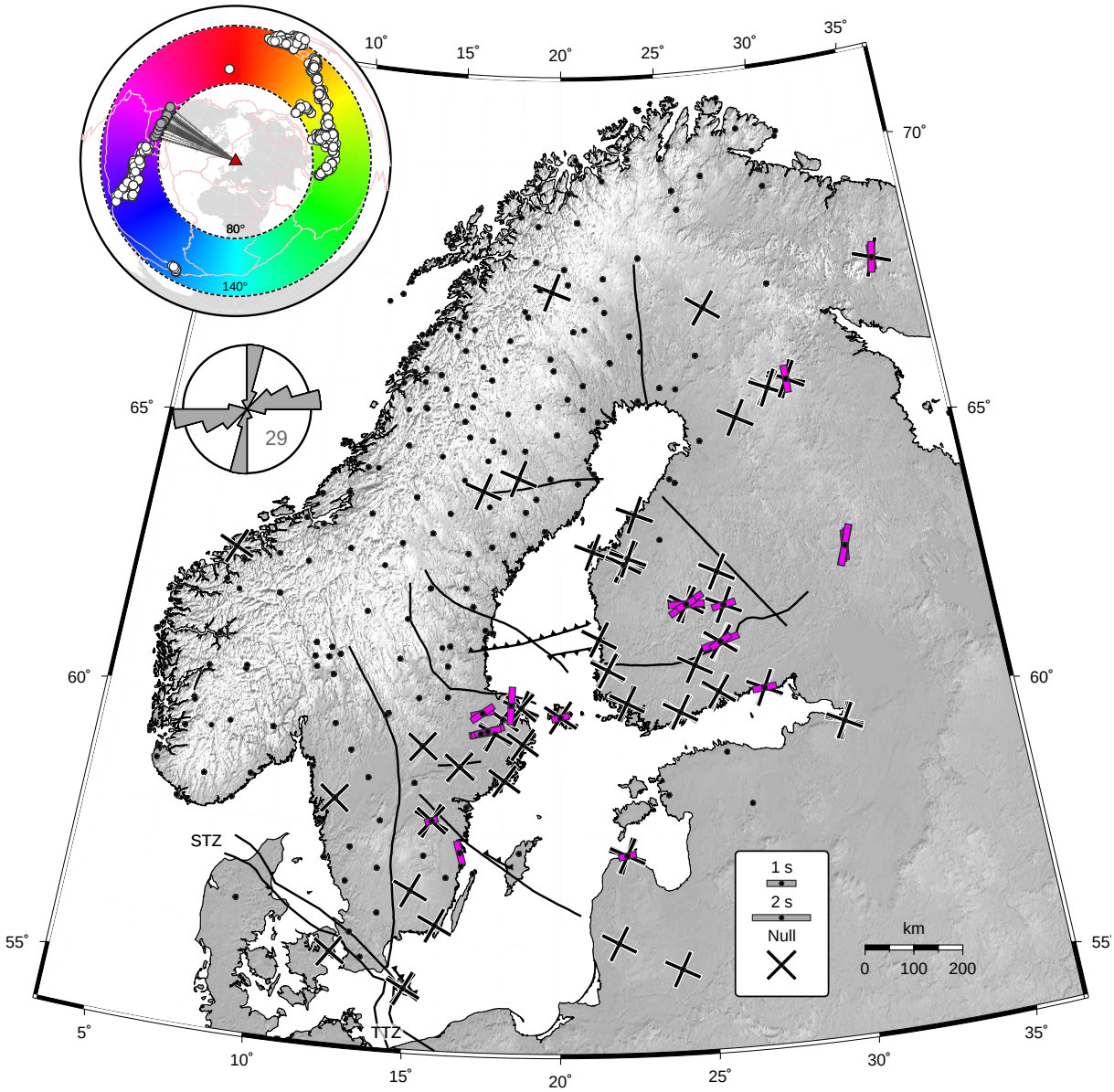

Figure E.5: Backazimuth-dependent individual shear wave splitting measurements color-coded with respect to the source region of the corresponding seismic event (see color-wheel). Individual null measurements are shown with black bars parallel and perpendicular to the backazimuth of the event.

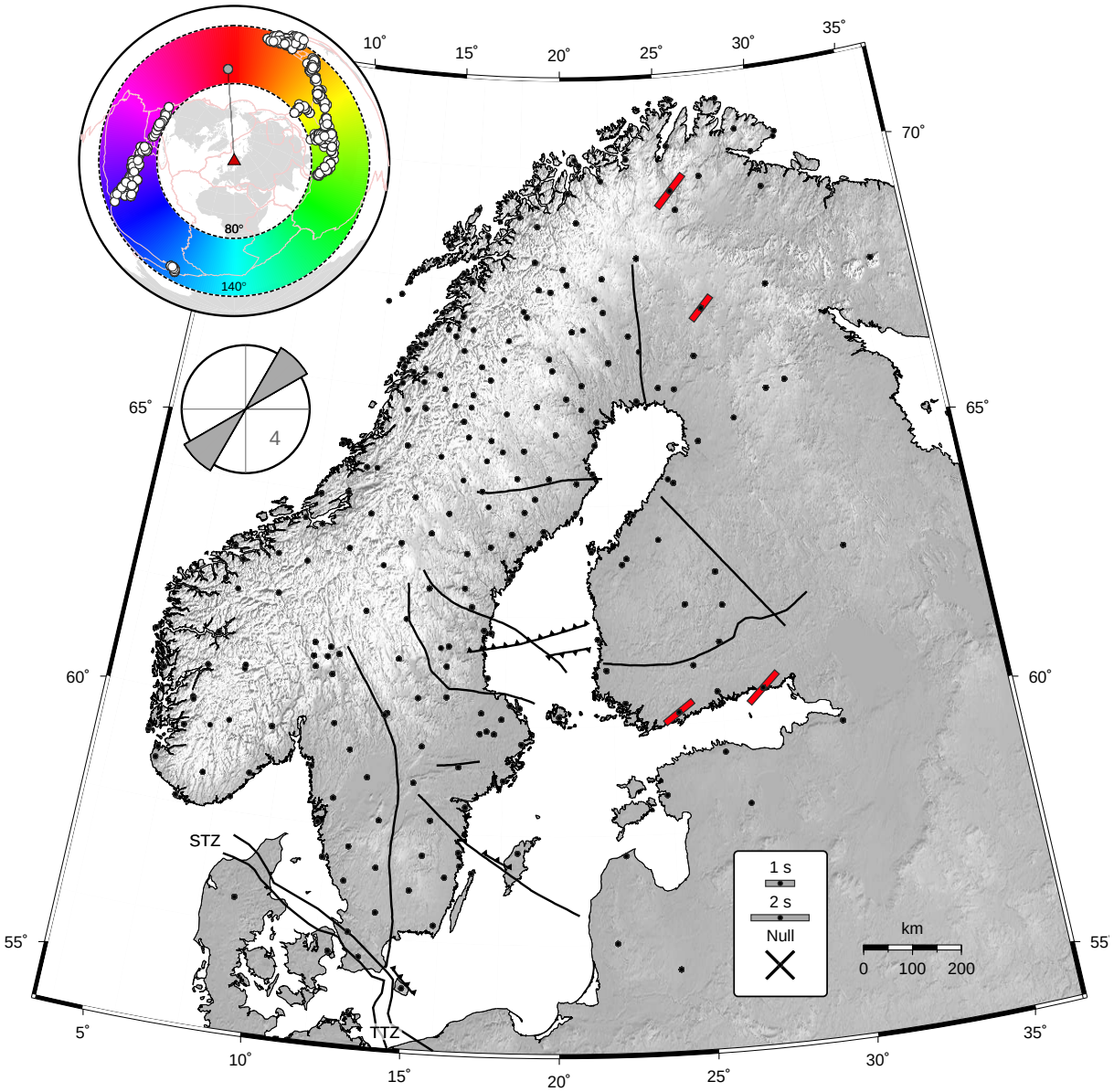

Figure E.6: Backazimuth-dependent individual shear wave splitting measurements color-coded with respect to the source region of the corresponding seismic event (see color-wheel). Individual null measurements are shown with black bars parallel and perpendicular to the backazimuth of the event.

E.4 Stereoplots of individual recording stations

In the following, splitting results (ϕ and δt) are shown for each individual station (total 266) in stereoplot form, plotted as a function of backazimuth (clockwise direction from North) and incidence angle (radial axis). Fast axis ϕ is additionally color-coded. Bar length scales with the delay time δt. Black open circles indicate nulls. Single and multi-event (see Table E.2) splits are displayed. Discrepant pairs of *SKS-SKKS* as found by *Grund and Ritter* (2019) are not shown. Stations are sorted in alphabetical order.

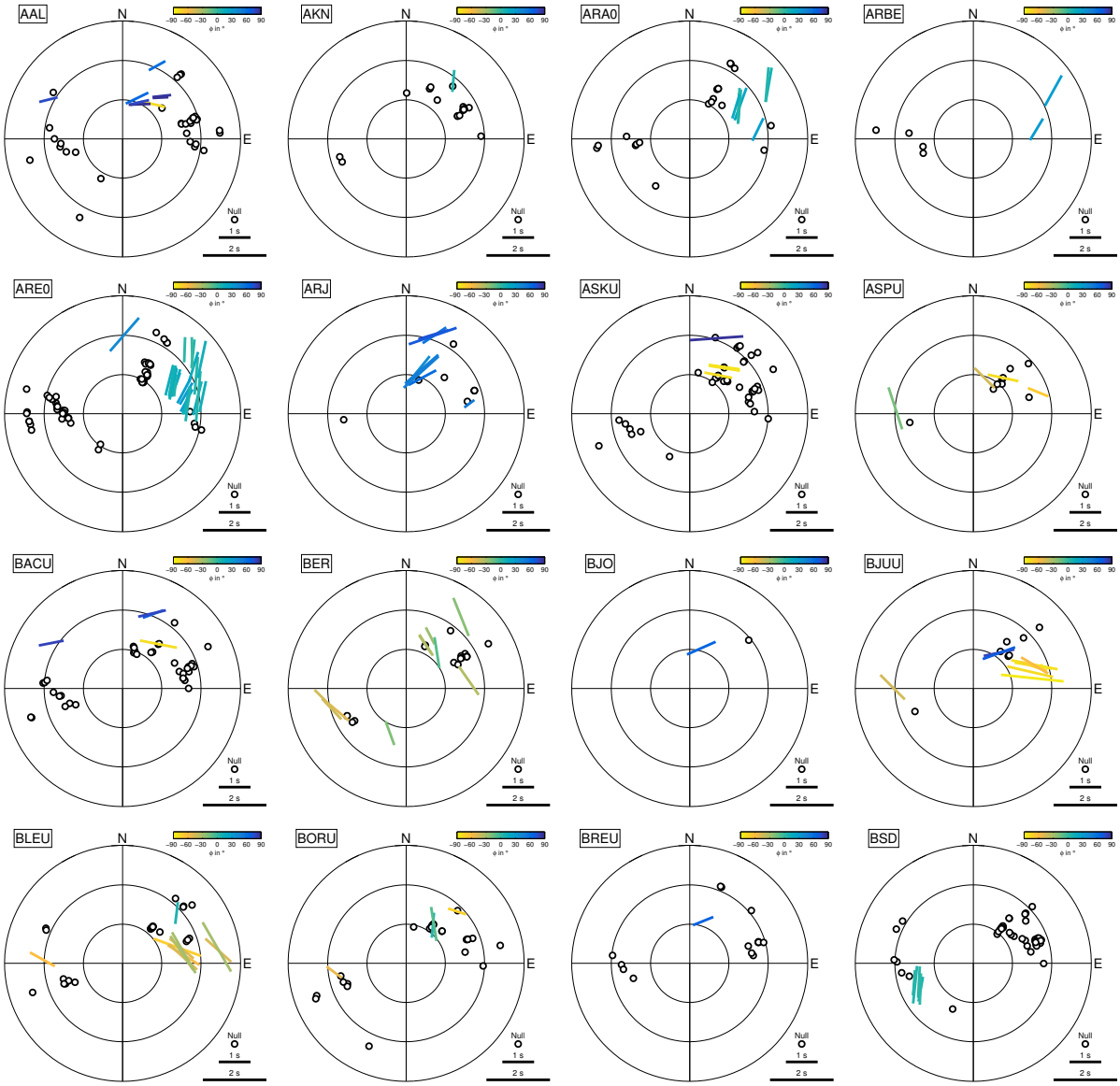

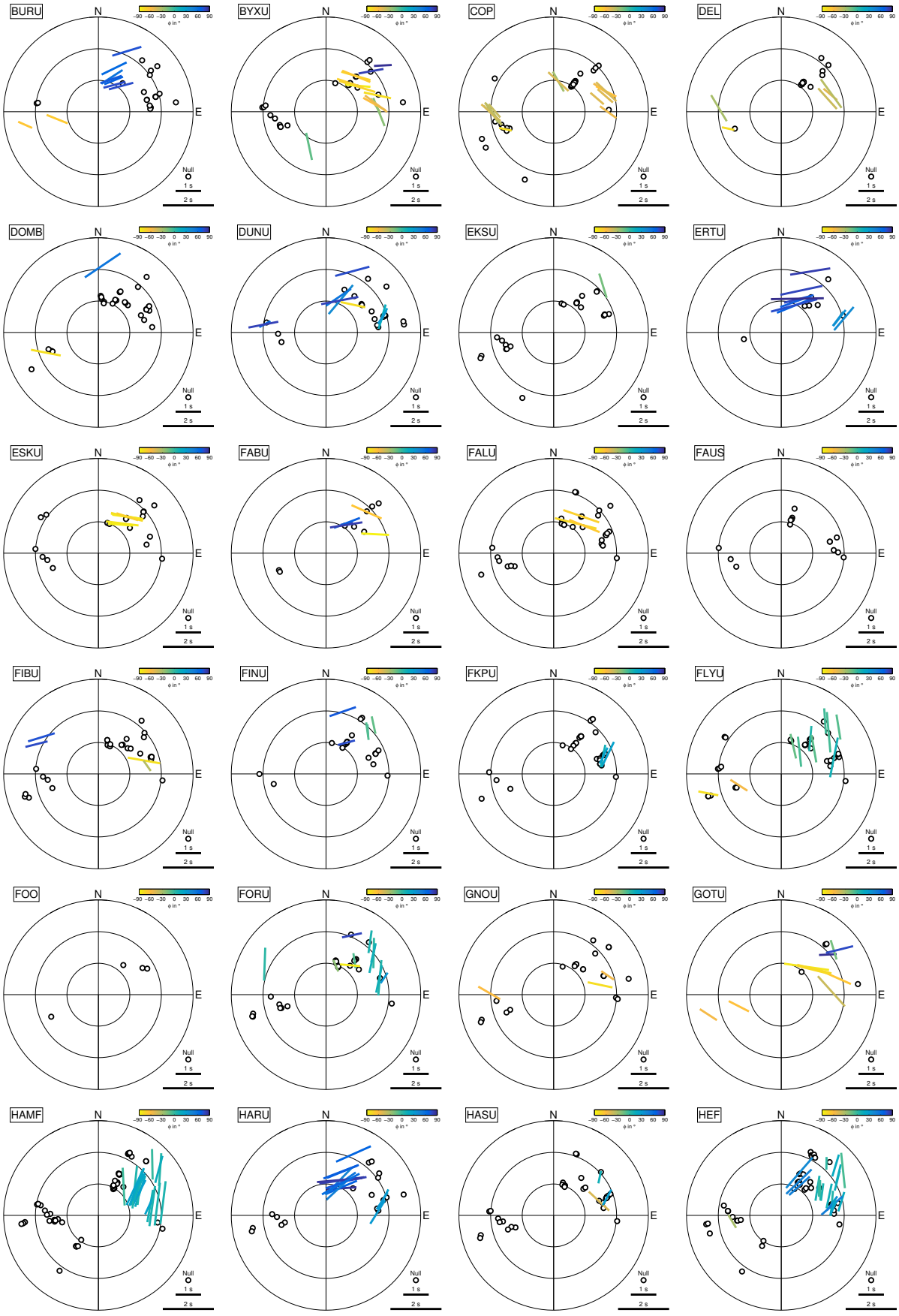
BURU
BYXU
COP
DEL
DOMB
DUNU
EKSU
ERTU
ESKU
FABU
FALU
FAUS
FIBU
FINU
FKPU
FLYU
FOO
FORU
GNOU
GOTU
HAMF
HARU
HASU
HEF
N
E
Null
1 s
2 s

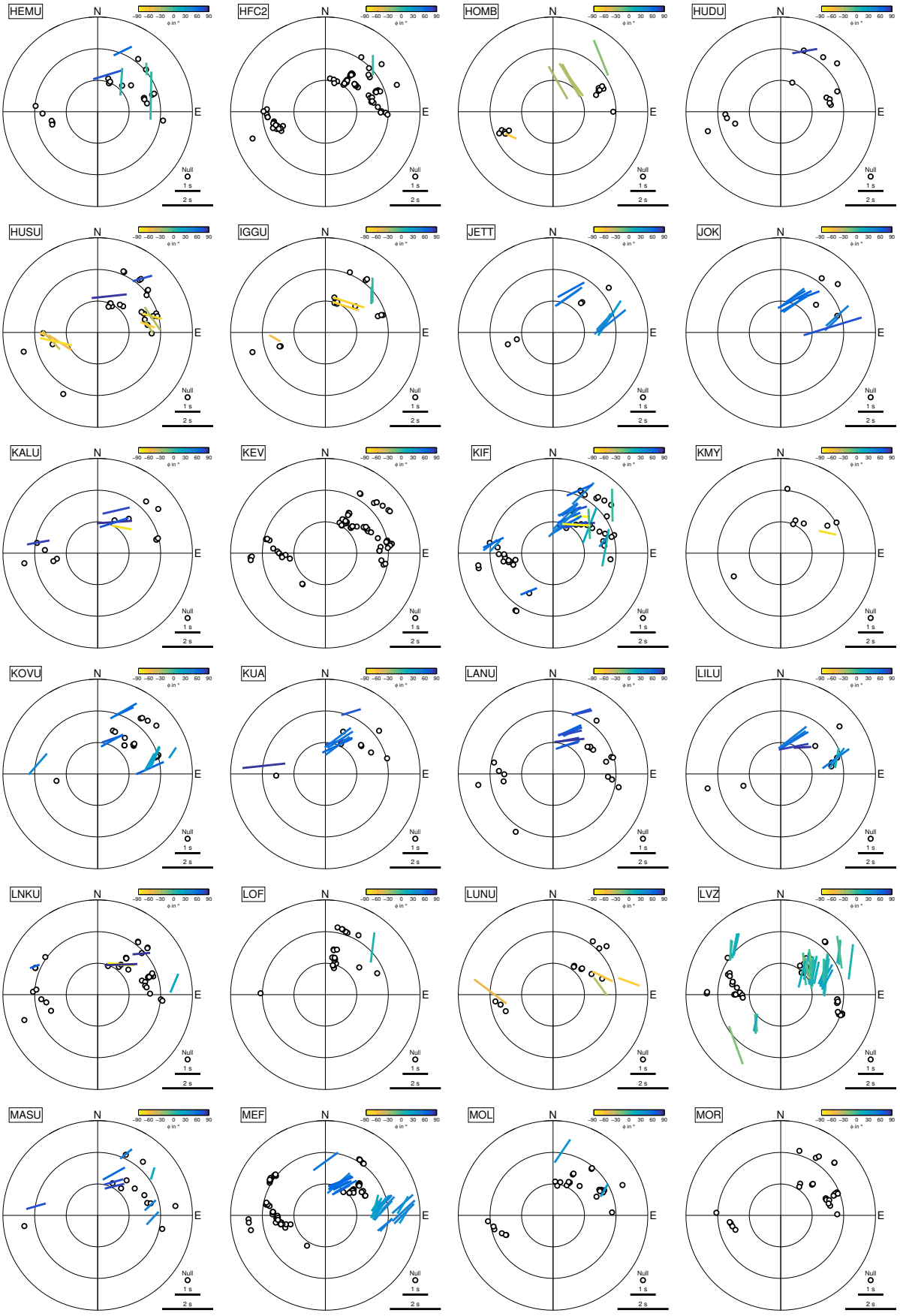
HEMU
HFC2
HOMB
HUDU
HUSU
IGGU
JETT
JOK
KALU
KEV
KIF
KMY
KOVU
KUA
LANU
LILU
LNKU
LOF
LUNU
LVZ
MASU
MEF
MOL
MOR
N
E
Null
1 s
2 s

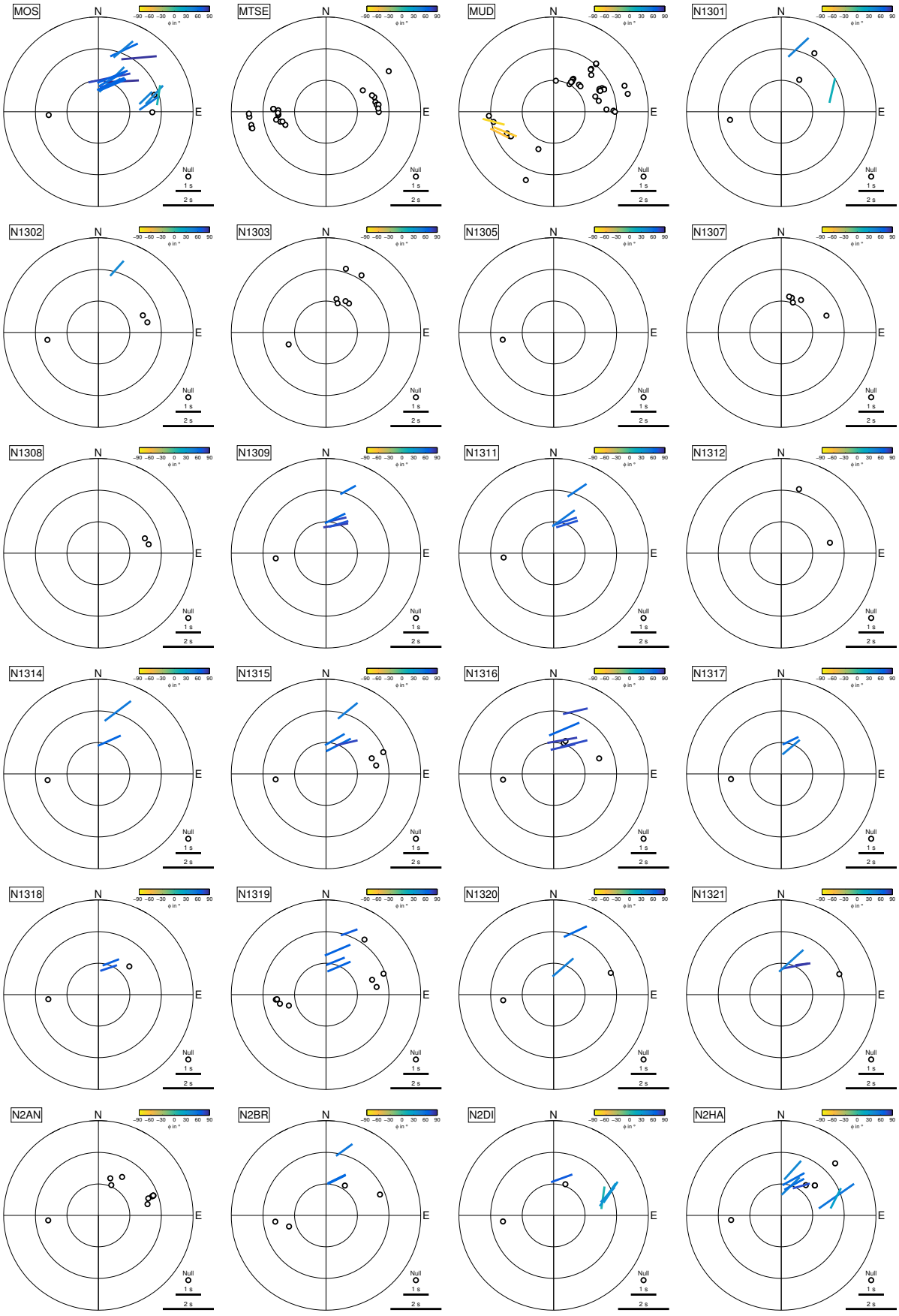
MOS
MTSE
MUD
N1301
N1302
N1303
N1305
N1307
N1308
N1309
N1311
N1312
N1314
N1315
N1316
N1317
N1318
N1319
N1320
N1321
N2AN
N2BR
N2DI
N2HA
N
E
Null
1 s
2 s

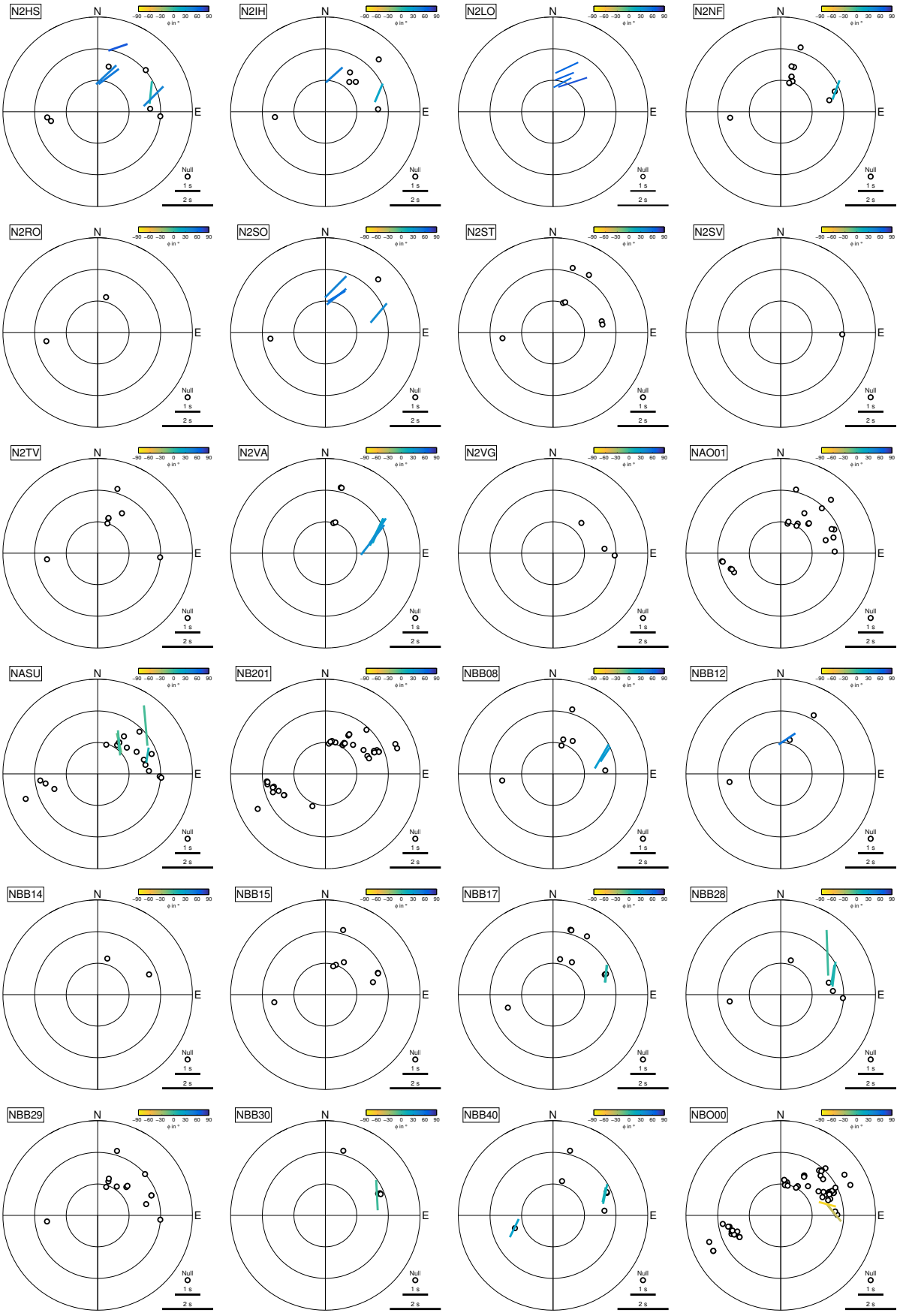
N2HS
N2IH
N2LO
N2NF
N2RO
N2SO
N2ST
N2SV
N2TV
N2VA
N2VG
NAO01
NASU
NB201
NBB08
NBB12
NBB14
NBB15
NBB17
NBB28
NBB29
NBB30
NBB40
NBO00
N
E
Null
1 s
2 s

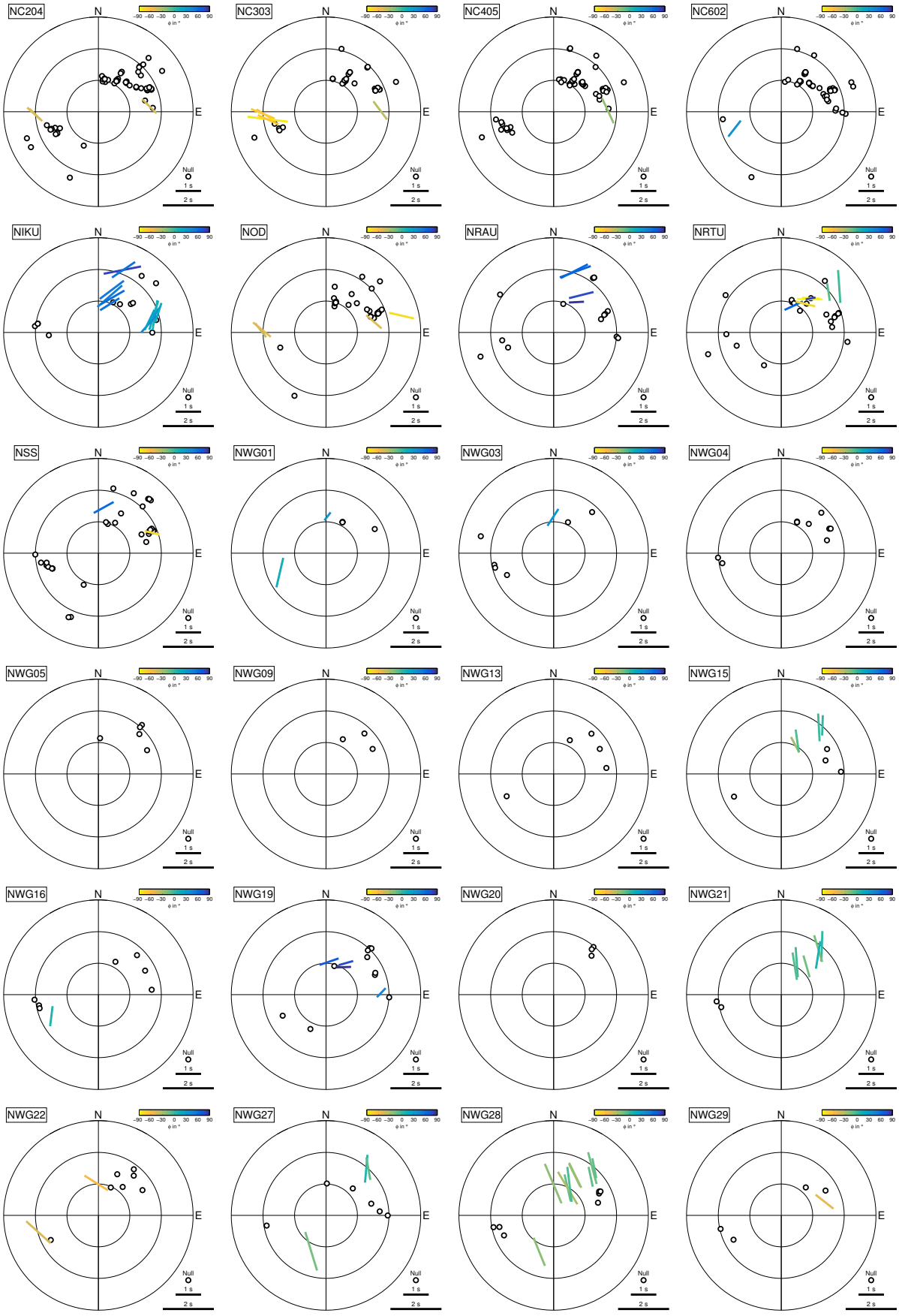
NC204
NC303
NC405
NC602
NIKU
NOD
NRAU
NRTU
NSS
NWG01
NWG03
NWG04
NWG05
NWG09
NWG13
NWG15
NWG16
NWG19
NWG20
NWG21
NWG22
NWG27
NWG28
NWG29
N
E
Null
1 s
2 s

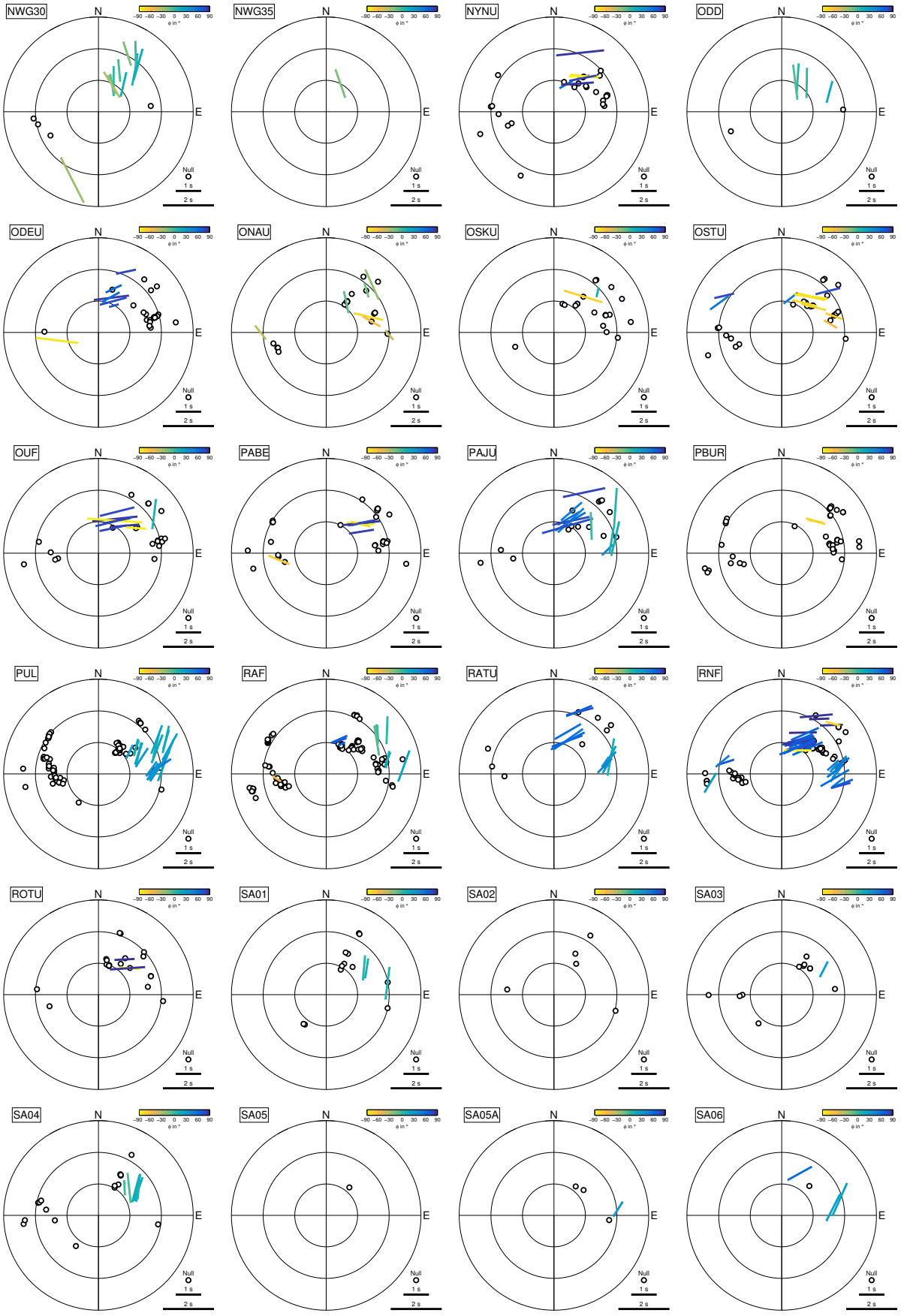
NWG30
NWG35
NYNU
ODD
ODEU
ONAU
OSKU
OSTU
OUF
PABE
PAJU
PBUR
PUL
RAF
RATU
RNF
ROTU
SA01
SA02
SA03
SA04
SA05
SA05A
SA06
N
E
Null
1 s
2 s

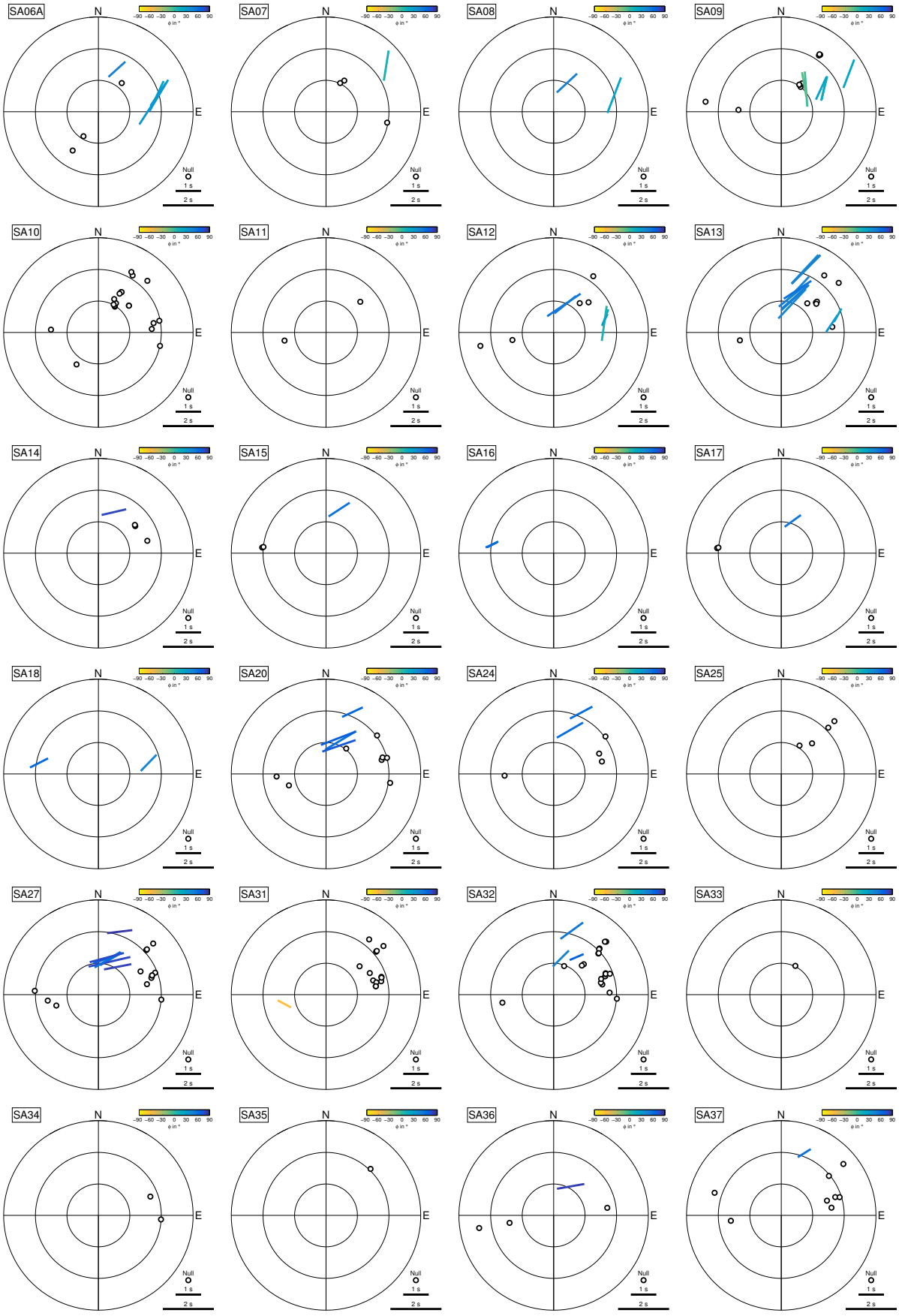
SA06A
SA07
SA08
SA09
SA10
SA11
SA12
SA13
SA14
SA15
SA16
SA17
SA18
SA20
SA24
SA25
SA27
SA31
SA32
SA33
SA34
SA35
SA36
SA37
N
E
Null
1 s
2 s

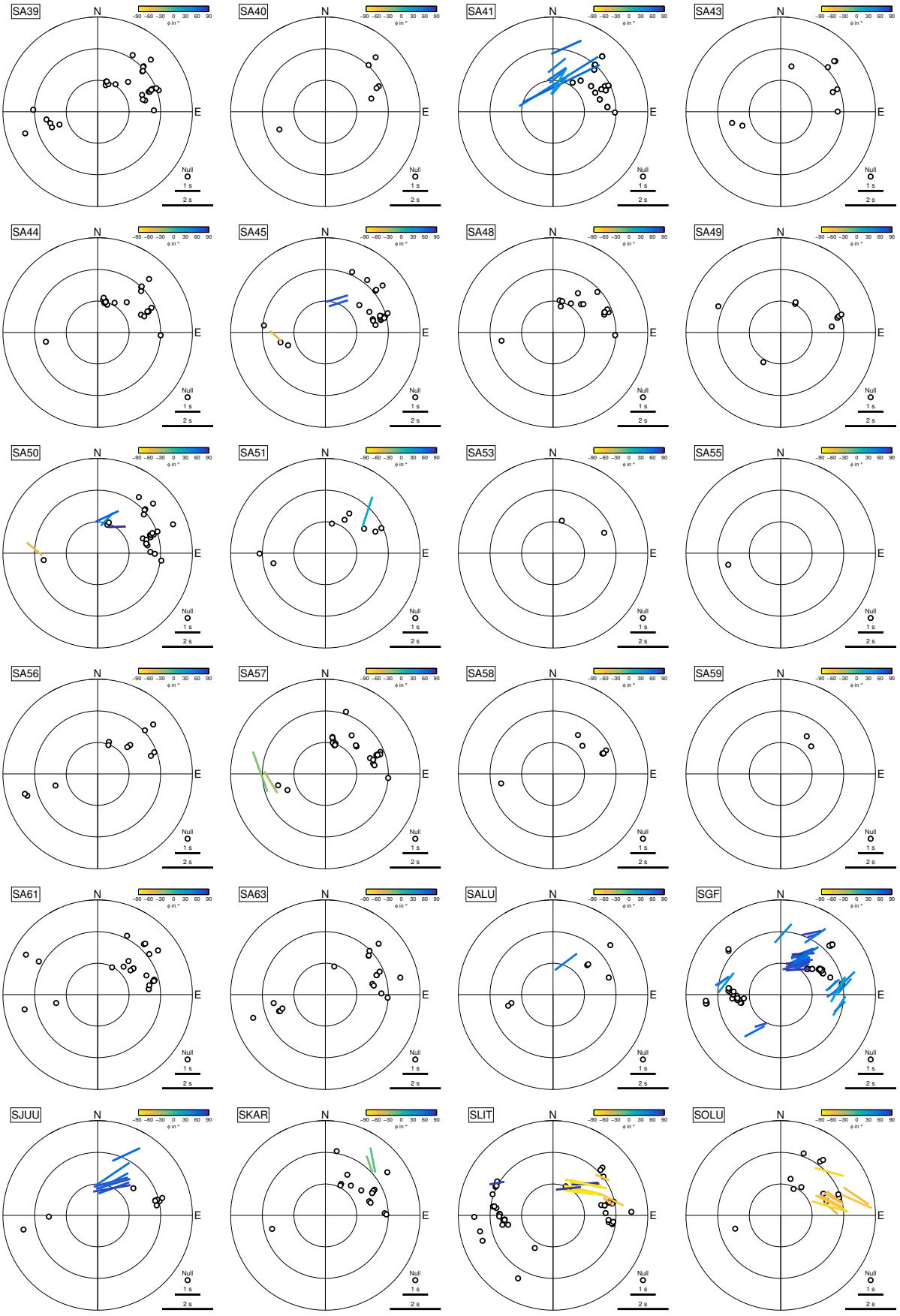
SA39
SA40
SA41
SA43
SA44
SA45
SA48
SA49
SA50
SA51
SA53
SA55
SA56
SA57
SA58
SA59
SA61
SA63
SALU
SGF
SJUU
SKAR
SLIT
SOLU
N
E
Null
1 s
2 s

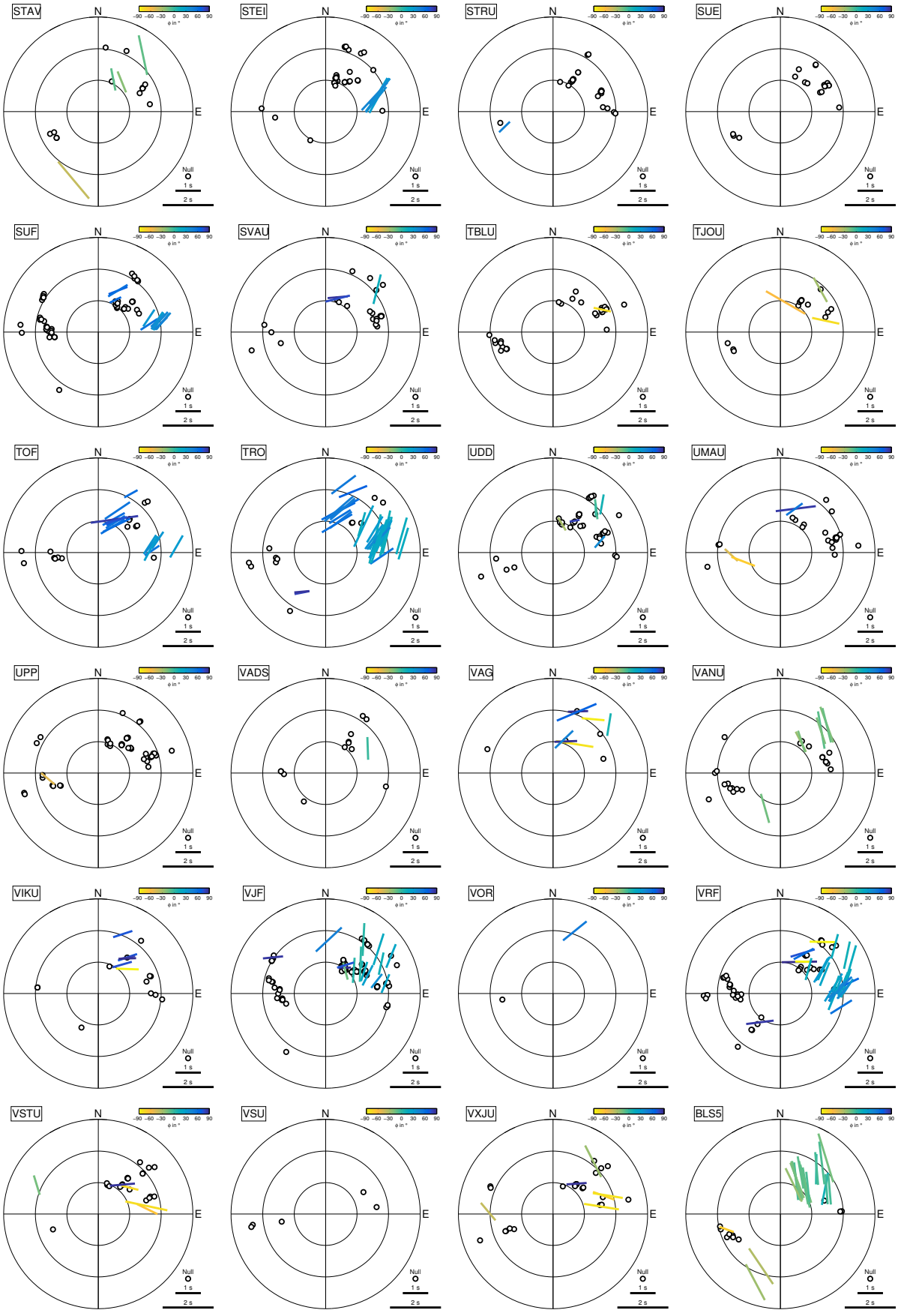
STAV
STEI
STRU
SUE
SUF
SVAU
TBLU
TJOU
TOF
TRO
UDD
UMAU
UPP
VADS
VAG
VANU
VIKU
VJF
VOR
VRF
VSTU
VSU
VXJU
BLS5
N
E
Null
1 s
2 s

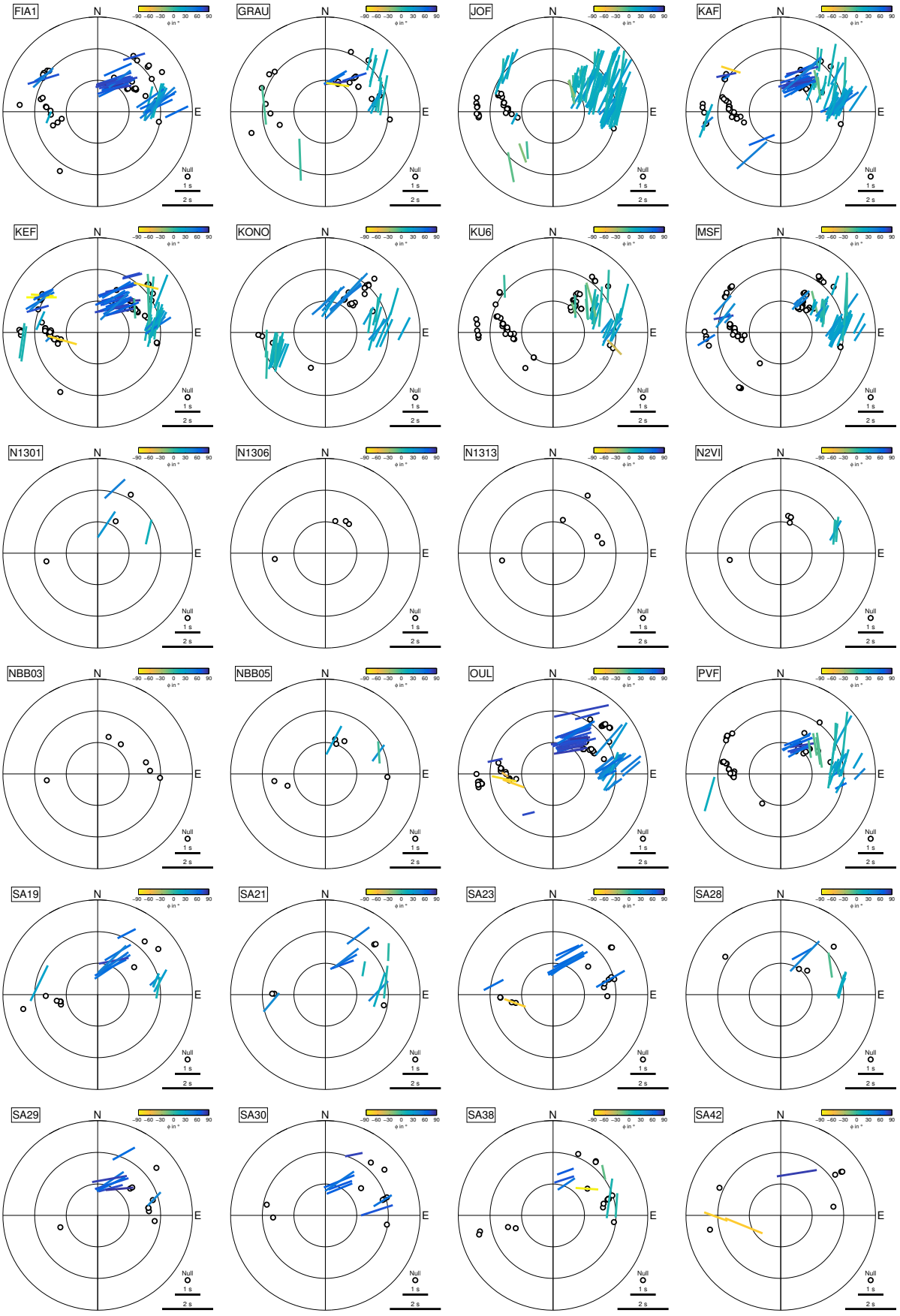
FIA1
GRAU
JOF
KAF
KEF
KONO
KU6
MSF
N1301
N1306
N1313
N2VI
NBB03
NBB05
OUL
PVF
SA19
SA21
SA23
SA28
SA29
SA30
SA38
SA42
N
E
Null
1 s
2 s

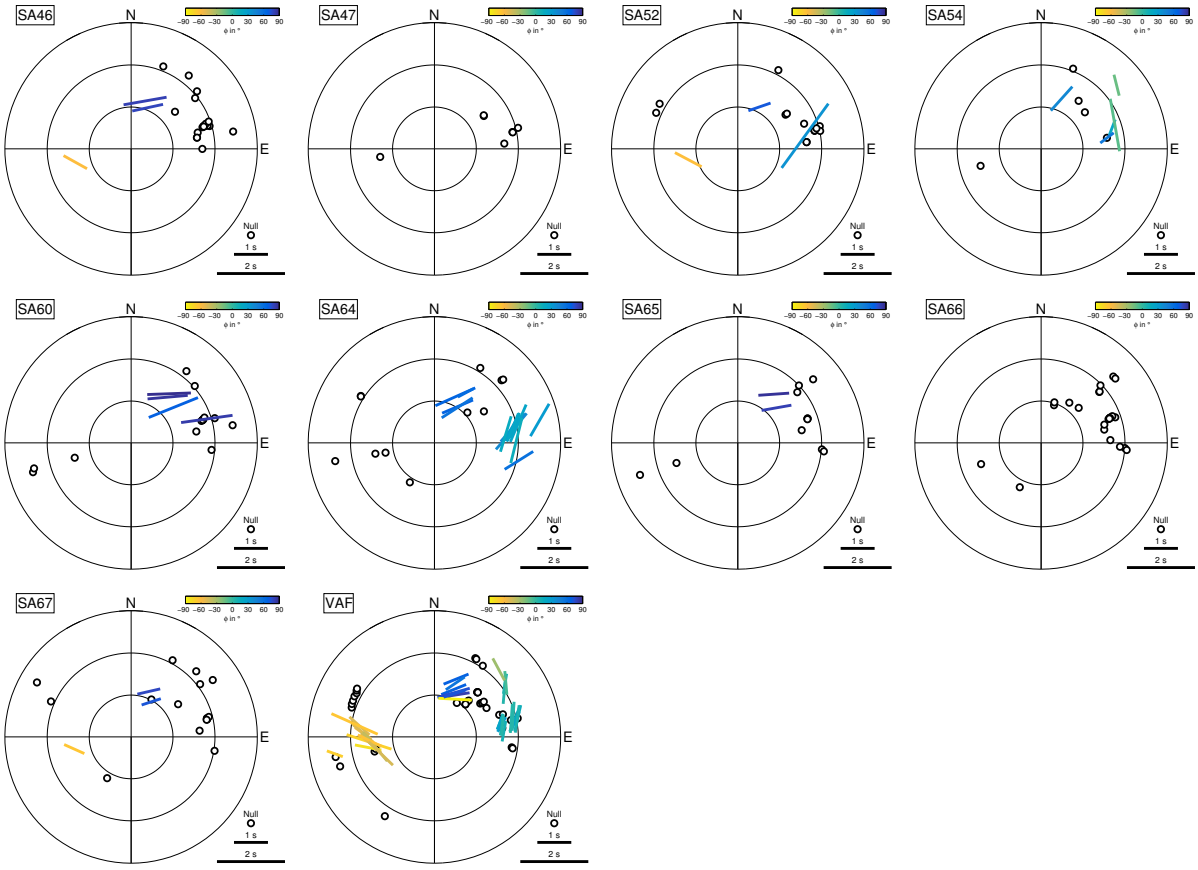
SA46
SA47
SA52
SA54
SA60
SA64
SA65
SA66
SA67
VAF
N
E
Null
1 s
2 s

F Electronic appendix

Table F.1 lists the content of the electronic appendix that is available from KITopenData via https://doi.org/10.5445/IR/1000091427.

Table F.1: Content of electronic appendix

Directory	File name	Description
01_SWS_SKS_SKKS	01_SWS_SKS_SKKS.pdf	listing of all *SKS-SKKS* splitting measurements in pdf format (same convention as in the subset shown in Table D.1)
	02_2019049_Table DR1.xlsx	listing of all *SKS-SKKS* splitting measurements in an Excel spreadsheet (as published in the electronic supporting information of *Grund and Ritter* (2019))
02_SWS_splits	01_SWS_SA_splits.pdf	listing of all non-null splitting measurements of *good/fair* quality in pdf format (same convention as in the subset shown in Table E.1)
	02_SWS_SA_splits.dat	listing of all non-null splitting measurements of *good/fair* quality in text format
	03_SWS_SA_splits_full.mat	listing of all non-null splitting measurements of *good/fair* quality in a MATLAB struct including full information on processing, data, error surfaces etc.
03_SWS_nulls	01_SWS_SA_nulls.pdf	listing of all null measurements of *good/fair* quality in pdf format
	02_SWS_SA_nulls.dat	listing of all null splitting measurements of *good/fair* quality in text format
	03_SWS_SA_nulls_full.mat	listing of all null splitting measurements of *good/fair* quality in a MATLAB struct including full information on processing, data, error surfaces etc.
04_SUPP_PLOTS	01_SAmap_STE_full_raw.pdf	all stereoplots in map view atop tectonic units, a slightly modified version of this map was presented in poster format during the DGG conference 2018 in Leoben (*Grund and Ritter*, 2018)
	02_SAmap_STE_full.pdf	all stereoplots in map view (including zones I-IV)
	03_SAmap_STE_I_SW.pdf	stereoplots in map view, zone I (southwest)
	04_SAmap_STE_II_SE.pdf	stereoplots in map view, zone II (southeast)
	05_SAmap_STE_III_NE.pdf	stereoplots in map view, zone III (northeast)
	06_SAmap_STE_IV_NW.pdf	stereoplots in map view, zone IV (northwest)

Bibliography

Abramson, E. H., Brown, J. M., Slutsky, L. J., and Zaug, J. (1997). The elastic constants of San Carlos olivine to 17 GPa. *J. Geophys. Res.*, 102:12253–12263.

Alsina, D. and Snieder, R. (1995). Small-scale sublithospheric continental mantle deformation: Constraints from SKS splitting observations. *Geophys. J. Int.*, 123:431–448.

Ando, M. and Ishikawa, Y. (1982). Observations of shear-wave velocity polarization anisotropy beneath Honshu, Japan. *J. Phys. Earth*, 30:191–199.

Ando, M., Ishikawa, Y., and Wada, H. (1980). S-wave anisotropy in the upper mantle under a volcanic area in Japan. *Nature*, 286:43.

Aragon, J. C., Long, M. D., and Benoit, M. H. (2017). Lateral variations in SKS splitting across the MAGIC array, central Appalachians. *Geochem. Geophys. Geosyst.*, 18:4136–4155, doi:10.1002/2017GC007169.

Artemieva, I. M. (2006). Global 1×1 thermal model TC1 for the continental lithosphere: implications for lithosphere secular evolution. *Tectonophysics*, 416:245–277.

BABEL Working Group (1990). Evidence for early Proterozoic plate tectonics from seismic reflection profiles in the Baltic shield. *Nature*, 348:34.

Babuška, V., Plomerova, J., and Šílenỳ, J. (1993). Models of seismic anisotropy in the deep continental lithosphere. *Phys. Earth Planet. In.*, 78:167–191.

Babuška, V. and Cara, M. (1991). *Seismic anisotropy in the Earth*, volume 10. Kluwer Academic Publishers, Dordrecht, The Netherlands.

Backus, G. E. (1962). Long-wave elastic anisotropy produced by horizontal layering. *J. Geophys. Res.*, 67:4427–4440.

Balling, N. (2000). Deep seismic reflection evidence for ancient subduction and collision zones within the continental lithosphere of northwestern Europe. *Tectonophysics*, 329:269–300.

Barruol, G. and Hoffmann, R. (1999). Upper mantle anisotropy beneath the Geoscope stations. *J. Geophys. Res.*, 104:10757–10773.

Barruol, G. and Mainprice, D. (1993). A quantitative evaluation of the contribution of crustal rocks to the shear-wave splitting of teleseismic SKS waves. *Phys. Earth Planet. In.*, 78:281–300.

Barruol, G., Silver, P. G., and Vauchez, A. (1997). Seismic anisotropy in the eastern US: Deep structure of a complex continental plate. *J. Geophys. Res.*, 102:8329–8348.

Barruol, G., Souriau, A., Vauchez, A., Diaz, J., Gallart, J., Tubia, J., and Cuevas, J. (1998). Lithospheric anisotropy beneath the Pyrenees from shear wave splitting. *J. Geophys. Res.*, 103:30039–30053.

Bastow, I. D., Pilidou, S., Kendall, J.-M., and Stuart, G. W. (2010). Melt-induced seismic anisotropy and magma assisted rifting in Ethiopia: Evidence from surface waves. *Geochem. Geophys. Geosyst.*, 11.

Becker, T. W., Lebedev, S., and Long, M. D. (2012). On the relationship between azimuthal anisotropy from shear wave splitting and surface wave tomography. *J. Geophys. Res.*, 117:B01306, doi:10.1029/2011JB008705.

Beghein, C., Resovsky, J., and Van Der Hilst, R. D. (2008). The signal of mantle anisotropy in the coupling of normal modes. *Geophys. J. Int.*, 175:1209–1234.

Berthelsen, A. (1992). Mobile Europe. In *A Continent Revealed, The European Geotraverse*, pages 11–32. Cambridge University Press.

Berthelsen, A. and Marker, M. (1986). 1.9-1.8 Ga old strike-slip megashears in the Baltic Shield, and their plate tectonic implications. *Tectonophysics*, 128:163–181.

Billings, S. D., Sambridge, M. S., and Kennett, B. L. N. (1994). Errors in hypocenter location: picking, model, and magnitude dependence. *Bull. Seismol. Soc. Am.*, 84:1978–1990.

Bird, P. (2003). An updated digital model of plate boundaries. *Geochem. Geophys. Geosyst.*, 4:1027, doi:10.1029/2001GC000252.

Bodmer, M., Toomey, D., Hooft, E. E., Nábělek, J., and Braunmiller, J. (2015). Seismic anisotropy beneath the Juan de Fuca plate system: Evidence for heterogeneous mantle flow. *Geology*, 43(12):1095–1098.

Bowman, J. and Ando, M. (1987). Shear-wave splitting in the upper-mantle wedge above the Tonga subduction zone. *Geophys. J. Roy. Astron. Soc.*, 88:25–41.

Braun, M. G., Hirth, G., and Parmentier, E. M. (2000). The effects of deep damp melting on mantle flow and melt generation beneath mid-ocean ridges. *Earth Planet. Sci. Lett.*, 176:339–356.

Brisbourne, A. (2012). How to store and share geophysical data. *Astron. Geophys.*, 53:19–20.

Bullen, K. E. (1940). The problem of the Earth's density variation. *Bull. Seismol. Soc. Am.*, 30:235–250.

Bullen, K. E. (1949). Compressibility-pressure hypothesis and the Earth's interior. *Geophys. J. Int.*, 5:335–368.

Burke, K., Steinberger, B., Torsvik, T. H., and Smethurst, M. A. (2008). Plume Generation Zones at the margins of Large Low Shear Velocity Provinces on the core-mantle boundary. *Earth Planet. Sci. Lett.*, 265:49–60.

Chen, X., Li, Y., and Levin, V. (2018). Shear wave splitting beneath eastern North American continent: evidence for a multi-layered and laterally variable anisotropic structure. *Geochem. Geophys. Geosyst.*, 19:2857–2871.

Chevrot, S. (2000). Multichannel analysis of shear wave splitting. *J. Geophys. Res.*, 105:21579–21590.

Chevrot, S., Favier, N., and Komatitsch, D. (2004). Shear wave splitting in three-dimensional anisotropic media. *Geophys. J. Int.*, 159:711–720.

Chevrot, S. and Van Der Hilst, R. D. (2003). On the effects of a dipping axis of symmetry on shear wave splitting measurements in a transversely isotropic medium. *Geophys. J. Int.*, 152:497–505.

Christoffel, E. B. (1877). Über die Fortpflanzung von Stössen durch elastische feste Körper. *Annali di Matematica Pura ed Applicata (1867-1897)*, 8:193–243.

Clauser, C. (2014). *Einführung in die Geophysik*. Springer, Berlin Heidelberg, Germany.

Cottaar, S. and Lekic, V. (2016). Morphology of seismically slow lower-mantle structures. *Geophys. J. Int.*, 207:1122–1136, doi:10.1093/gji/ggw324.

Cottaar, S., Li, M., McNamara, A. K., Romanowicz, B., and Wenk, H.-R. (2014). Synthetic seismic anisotropy models within a slab impinging on the core–mantle boundary. *Geophys. J. Int.*, 199:164–177.

Cottaar, S. and Romanowicz, B. (2013). Observations of changing anisotropy across the southern margin of the African LLSVP. *Geophys. J. Int.*, 195:1184–1195, doi:10.1093/gji/ggt285.

Crampin, S. (1984). Effective anisotropic elastic constants for wave propagation through cracked solids. *Geophys. J. Int.*, 76:135–145.

Crampin, S. and Booth, D. C. (1985). Shear-wave polarizations near the North Anatolian Fault-II. Interpretation in terms of crack-induced anisotropy. *Geophys. J. Roy. Astron. Soc.*, 83:75–92.

Crampin, S. and Chastin, S. (2003). A review of shear wave splitting in the crack-critical crust. *Geophys. J. Int.*, 155:221–240.

Crampin, S. and Lovell, J. H. (1991). A decade of shear-wave splitting in the Earth's crust: what does it mean? what use can we make of it? and what should we do next? *Geophys. J. Int.*, 107:387–407.

Creasy, N., Long, M. D., and Ford, H. A. (2017). Deformation in the lowermost mantle beneath Australia from observations and models of seismic anisotropy. *J. Geophys. Res.*, 122:5243–5267, doi:10.1002/2016JB013901.

Crotwell, H. P., Owens, T. J., and Ritsema, J. (1999). The TauP toolkit: Flexible seismic travel-time and ray-path utilities. *Seismol. Res. Lett.*, 70:154–160.

Currie, C. A., Cassidy, J. F., Hyndman, R. D., and Bostock, M. G. (2004). Shear wave anisotropy beneath the Cascadia subduction zone and western North American craton. *Geophys. J. Int.*, 157:341–353.

Dahm, C. G. (1934). *A Study of Dilational Wave Velocity in the Earth as a Function of Depth, Based on a Comparison of the P, P1, and PcP Phases*. PhD thesis, Saint Louis University.

Debayle, E., Kennett, B., and Priestley, K. (2005). Global azimuthal seismic anisotropy and the unique plate-motion deformation of Australia. *Nature*, 433:509.

Debayle, E. and Ricard, Y. (2013). Seismic observations of large-scale deformation at the bottom of fast-moving plates. *Earth Planet. Sci. Lett.*, 376:165–177.

Deng, J., Long, M. D., Creasy, N., Wagner, L., Beck, S., Zandt, G., Tavera, H., and Minaya, E. (2017). Lowermost mantle anisotropy near the eastern edge of the Pacific LLSVP: constraints from SKS-SKKS splitting intensity measurements. *Geophys. J. Int.*, 210:774–786.

Deuss, A. (2014). Heterogeneity and anisotropy of Earth's inner core. *Annu. Rev. Earth Planet. Sci.*, 42:103–126.

Dimech, J. L., Weber, R. C., and Savage, M. K. (2017). Shear-wave splitting and moonquakes (DI21A-0389). In *AGU Fall Meeting 2017*, New Orleans, United States.

Dost, B. (1994). The ORFEUS Data Center. *Annals of Geophysics*, 37.

Dziewoński, A. M., Chou, T.-A., and Woodhouse, J. H. (1981). Determination of earthquake source parameters from waveform data for studies of global and regional seismicity. *J. Geophys. Res.*, 86(B4):2825–2852, doi:10.1029/JB086iB04p02825.

Eakin, C. M. and Long, M. D. (2013). Complex anisotropy beneath the Peruvian flat slab from frequency-dependent, multiple-phase shear wave splitting analysis. *J. Geophys. Res.*, 118:4794–4813, doi:10.1002/jgrb.50349.

Eakin, C. M., Long, M. D., Scire, A., Beck, S. L., Wagner, L. S., Zandt, G., and Tavera, H. (2016). Internal deformation of the subducted Nazca slab inferred from seismic anisotropy. *Nature Geosci.*, 9:56–59.

Eakin, C. M., Obrebski, M., Allen, R. M., Boyarko, D. C., Brudzinski, M. R., and Porritt, R. (2010). Seismic anisotropy beneath Cascadia and the Mendocino triple junction: Interaction of the subducting slab with mantle flow. *Earth Planet. Sci. Lett.*, 297:627–632.

Eakin, C. M., Rychert, C. A., and Harmon, N. (2018). The role of oceanic transform faults in seafloor spreading: A global perspective from seismic anisotropy. *J. Geophys. Res.*, 123:1736–1751, doi:10.1002/2017JB015176.

Einstein, A. (1916). Die Grundlage der allgemeinen Relativitätstheorie. *Annalen der Physik*, 354:769–822.

Eken, T., Plomerová, J., Roberts, R., Vecsey, L., Babuška, V., Shomali, H., and Bodvarsson, R. (2010). Seismic anisotropy of the mantle lithosphere beneath the Swedish National Seismological Network (SNSN). *Tectonophysics*, 480:241–258.

Eken, T. and Tilmann, F. (2014). The use of direct shear waves in quantifying seismic anisotropy: Exploiting regional arrays. *Bull. Seismol. Soc. Am.*, 104:2644–2661.

Ekström, G., Nettles, M., and Dziewoński, A. M. (2012). The global CMT project 2004-2010: Centroid-moment tensors for 13,017 earthquakes. *Phys. Earth Planet. In.*, 200:1–9, doi:10.1016/j.pepi.2012.04.002.

England, R. W., Ebbing, J., and Ben Mansour, W. (2015). SCANLIPS3D - SCANdinavian LIthosphere P and S wave experiment 3 D. Scientific report 959, NERC Geophysical Equipment Facility.

Evans, M. S., Kendall, J.-M., and Willemann, R. J. (2006). Automated SKS splitting and upper-mantle anisotropy beneath Canadian seismic stations. *Geophys. J . Int.*, 165:931–942.

Favier, N. and Chevrot, S. (2003). Sensitivity kernels for shear wave splitting in transverse isotropic media. *Geophys. J. Int.*, 153:213–228.

Flament, N., Williams, S., Müller, R. D., Gurnis, M., and Bower, D. J. (2017). Origin and evolution of the deep thermochemical structure beneath Eurasia. *Nat. Commun.*, 8:14164, doi:10.1038/ncomms14164.

Ford, H. A., Long, M. D., He, X., and Lynner, C. (2015). Lowermost mantle flow at the eastern edge of the African Large Low Shear Velocity Province. *Earth Planet. Sci. Lett.*, 420:1–10.

Fouch, M. J. and Fischer, K. M. (1996). Mantle anisotropy beneath northwest Pacific subduction zones. *J. Geophys. Res.*, 101:15987–16002.

Fouch, M. J., Fischer, K. M., Parmentier, E. M., Wysession, M. E., and Clarke, T. J. (2000). Shear wave splitting, continental keels, and patterns of mantle flow. *J. Geophys. Res.*, 105:6255–6275.

Fouch, M. J. and Rondenay, S. (2006). Seismic anisotropy beneath stable continental interiors. *Phys. Earth Planet. In.*, 158:292–320.

Frietsch, M., Groos, J. C., and Ritter, J. R. R. (2015). Detection and delineation of a fracture zone with observation of seismic shear wave anisotropy in the Upper Rhine Graben, SW Germany. *Pure Appl. Geophys.*, 172:267–282.

Frost, D. A. and Romanowicz, B. (2017). Constraints on inner core anisotropy using array observations of P'P'. *Geophys. Res. Lett.*, 44.

Fukao, Y. (1984). Evidence from core-reflected shear waves for anisotropy in the Earth's mantle. *Nature*, 309:695.

Gaál, G. (1986). 2200 million years of crustal evolution: the Baltic Shield. *Bull. Geol. Soc. Finland*, 58:149–168.

Gaál, G. and Gorbatschev, R. (1987). An outline of the Precambrian evolution of the Baltic Shield. *Precambrian Res.*, 35:15–52.

Gao, S., Davis, P. M., Liu, H., Slack, P. D., Rigor, A. W., Zorin, Y. A., Mordvinova, V. V., Kozhevnikov, V. M., and Logatchev, N. A. (1997). SKS splitting beneath continental rift zones. *J. Geophys. Res.*, 102:22781–22797.

Gao, S., Davis, P. M., Liu, H., Slack, P. D., Zorin, Y. A., Mordvinova, V. V., Kozhevnikov, V. M., and Meyer, R. P. (1994). Seismic anisotropy and mantle flow beneath the Baikal rift zone. *Nature*, 371:149.

Garnero, E. J., Maupin, V., Lay, T., and Fouch, M. J. (2004). Variable azimuthal anisotropy in Earth's lowermost mantle. *Science*, 306:259–261.

Garnero, E. J. and McNamara, A. (2008). Structure and dynamics of Earth's lower mantle. *Science*, 320:626–628.

Garnero, E. J., McNamara, A. K., and Shim, S.-H. (2016). Continent-sized anomalous zones with low seismic velocity at the base of Earth's mantle. *Nature Geosci.*, 9:481–489.

Gee, D. G., Fossen, H., Henriksen, N., and Higgins, A. K. (2008). From the early Paleozoic platforms of Baltica and Laurentia to the Caledonide Orogen of Scandinavia and Greenland. *Episodes*, 31:44–51.

GEOFON Data Centre (1993). GEOFON (GeoForschungsNetz). Seismic Network, Deutsches GeoForschungsZentrum GFZ, doi:10.14470/TR560404.

Gerst, A. and Savage, M. K. (2004). Seismic anisotropy beneath Ruapehu volcano: a possible eruption forecasting tool. *Science*, 306:1543–1547.

Gorbatchev, R. (2004). The Transscandinavian Igneous Belt – introduction and background. In Högdahl, K., Andersson, U., and Eklund, O., editors, *The Transscandinavian Igneous Belt (TIB) in Sweden: a Review of Its Character and Evolution. Geological Survey of Finland, Special Paper*, volume 37, pages 9–15. Geological Survey of Finland.

Gradmann, S., Keiding, M., Olesen, O., and Maystrenko, Y. (2014). NEONOR2-Neotectonics in Nordland, NW Norway. In *Eighth Symposium on Structure, Composition and Evolution of the Lithosphere in Fennoscandia*, page 17.

Gripp, A. E. and Gordon, R. G. (2002). Young tracks of hotspots and current plate velocities. *Geophys. J. Int.*, 150:321–361.

Grund, M. (2017). StackSplit - a plugin for multi-event shear wave splitting analyses in SplitLab. *Comput. Geosci.*, 105:43–50, doi:10.1016/j.cageo.2017.04.015.

Grund, M., Groos, J. C., and Ritter, J. R. R. (2016a). Fault reactivation analysis using microearthquake clustering based on signal-to-noise weighted waveform similarity. *Pure Appl. Geophys.*, 173:2325–2355, doi:10.1007/s00024–016–1281–4.

Grund, M., Lutz, F., Ritter, J., and Weidle, C. (2019). 3D-shear wave velocity anomalies underneath Fennoscandia deduced from global travel time tomography. In *Geophys. Res. Abstr. Vol. 21, EGU2019-8556*, EGU, Vienna, Austria.

Grund, M., Mauerberger, A., Ritter, J. R. R., and Tilmann, F. (2017a). Broadband Recordings for LITHOS-CAPP: LITHOspheric Structure of Caledonian, Archaean and Proterozoic Provinces Sep. 2014 - Oct. 2016, Sweden and Finland. Scientific Technical Report STR-Data 17/02, GIPP Experiment and Data Archive, Potsdam: GFZ German Research Centre for Geosciences, doi:10.2312/GFZ.b103-17029.

Grund, M., Mauerberger, A., Ritter, J. R. R., and Tilmann, F. (2017b). Broadband Recordings for LITHOS-CAPP: LITHOspheric Structure of Caledonian, Archaean and Proterozoic Provinces Sep. 2014 - Oct. 2016, Sweden and Finland. Recorder log-file - Datasets, GFZ Data Services. doi:10.5880/GIPP.201417.1.

Grund, M. and Ritter, J. (2018). Teleseismic shear wave splitting observations across Scandinavia: signatures of multi-layered and laterally varying anisotropy. In *Proceedings of the annual meeting of the German Geophysical Society (DGG)*, Leoben, Austria.

Grund, M. and Ritter, J. R. R. (2019). Widespread seismic anisotropy in Earth's lowermost mantle beneath the Atlantic and Siberia. *Geology*, 47(2), doi:10.1130/G45514.1:123–126.

Grund, M., Ritter, J. R. R., and Gehrig, M. (2016b). Ground motion relations while TBM drilling in unconsolidated sediments. *Rock Mech. Rock Eng.*, 49:1773–1787, doi:10.1007/s00603–015–0887–7.

Hall, S. A., Kendall, J.-M., and van der Baan, M. (2004). Some comments on the effects of lower-mantle anisotropy on SKS and SKKS phases. *Phys. Earth Planet. In.*, 146:469–481.

Hammond, J. O. S., Kendall, J.-M., Wookey, J., Stuart, G. W., Keir, D., and Ayele, A. (2014). Differentiating flow, melt, or fossil seismic anisotropy beneath Ethiopia. *Geochem. Geophys. Geosyst.*, 15:1878–1894.

Hanka, W. and Kind, R. (1994). The GEOFON Program. *Annals of Geophysics*, 37(5):1061–1065, doi:10.4401/ag–4196.

Hanna, J. and Long, M. D. (2012). SKS splitting beneath Alaska: Regional variability and implications for subduction processes at a slab edge. *Tectonophysics*, 530-531:272–285.

Hartog, R. and Schwartz, S. Y. (2000). Subduction-induced strain in the upper mantle east of the Mendocino triple junction, California. *J. Geophys. Res.*, 105:7909–7930.

He, X. and Long, M. D. (2011). Lowermost mantle anisotropy beneath the northwestern Pacific: Evidence from ScS, PcS, SKS, and SKKS phases. *Geochem. Geophys. Geosyst.*, 12:Q12012, doi:10.1029/2011GC003779.

He, Y., Wen, L., Capdeville, Y., and Zhao, L. (2015). Seismic evidence for an Iceland thermo-chemical plume in the Earth's lowermost mantle. *Earth Planet. Sci. Lett.*, 417:19–27.

Heeremans, M., Larsen, B. T., and Stel, H. (1996). Paleostress reconstruction from kinematic indicators in the Oslo Graben, southern Norway: new constraints on the mode of rifting. *Tectonophysics*, 266:55–79.

Helffrich, G. (1995). Lithospheric deformation inferred from teleseismic shear wave splitting observations in the United Kingdom. *J. Geophys. Res.*, 100:18195–18204.

Helmberger, D. V., Wen, L., and Ding, X. (1998). Seismic evidence that the source of the Iceland hotspot lies at the core-mantle boundary. *Nature*, 396:251–255.

Hetényi, G., Molinari, I., Clinton, J., Bokelmann, G., Bondár, I., Crawford, W. C., Dessa, J.-X., Doubre, C., Friederich, W., Fuchs, F., Giardini, D., Gráczer, Z., Handy, M. R., Herak, M., Jia, Y., Kissling, E., Kopp, H., Korn, M., Margheriti, L., Meier, T., Mucciarelli, M., Paul, A., Pesaresi, D., Piromallo, C., Plenefisch, T., Plomerová, J., Ritter, J., Rümpker, G., Šipka, V., Spallarossa, D., Thomas, C., Tilmann, F., Wassermann, J., Weber, M., Wéber, Z., Wesztergom, V., and Živčić, M. (2018). The AlpArray Seismic Network: A Large-Scale European Experiment to Image the Alpine Orogen. *Surv. Geophys.*, 39:1009–1033, doi:10.1007/s10712–018–9472–4.

Hicks, S. P., Nippress, S. E. J., and Rietbrock, A. (2012). Sub-slab mantle anisotropy beneath south-central Chile. *Earth Planet. Sci. Lett.*, 357:203–213.

Howell Jr., B. F. and Kisslinger, C. (2000). That "Dahm" layer: Comments on renaming the D". *Eos Trans. AGU*, 81:210–210.

Hutko, A. R., Lay, T., Garnero, E. J., and Revenaugh, J. (2006). Seismic detection of folded, subducted lithosphere at the core-mantle boundary. *Nature*, 441:333–336.

IRIS DMC (2012). Data Services Products: SWS-DBs Shear-wave splitting databases, doi:10.17611/DP/SWS.1.

Ismaïl, W. B. and Mainprice, D. (1998). An olivine fabric database: an overview of upper mantle fabrics and seismic anisotropy. *Tectonophysics*, 296:145–157.

Jung, H., Katayama, I., Jiang, Z., Hiraga, T., and Karato, S. (2006). Effect of water and stress on the lattice-preferred orientation of olivine. *Tectonophysics*, 421:1–22.

Karato, S. (2008). *Deformation of Earth Materials: An Introduction to the Rheology of Solid Earth*. Cambridge Univ. Press.

Karato, S., Jung, H., Katayama, I., and Skemer, P. (2008). Geodynamic significance of seismic anisotropy of the upper mantle: new insights from laboratory studies. *Annu. Rev. Earth Planet. Sci.*, 36:59–95.

Karato, S.-I. and Wu, P. (1993). Rheology of the upper mantle: A synthesis. *Science*, 260:771–778.

Katayama, I., Jung, H., and Karato, S.-I. (2004). New type of olivine fabric from deformation experiments at modest water content and low stress. *Geology*, 32:1045–1048.

Kendall, J.-M. (1994). Teleseismic arrivals at a mid-ocean ridge: Effects of mantle melt and anisotropy. *Geophys. Res. Lett.*, 21:301–304.

Kendall, J.-M., Pilidou, S., Keir, D., Bastow, I. D., Stuart, G. W., and Ayele, A. (2006). Mantle upwellings, melt migration and the rifting of Africa: Insights from seismic anisotropy. *Geological Society, London, Special Publications*, 259:55–72.

Kendall, J.-M. and Silver, P. G. (1996). Constraints from seismic anisotropy on the nature of the lowermost mantle. *Nature*, 381:409–412, doi:10.1038/381409a0.

Kennett, B. L. N. (1991). IASPEI 1991 seismological tables. *Terra Nova*, 3(2):122.

Kind, R., Sodoudi, F., Yuan, X., Shomali, H., Roberts, R., Gee, D., Eken, T., Bianchi, M., Tilmann, F., and Balling, N. (2013). Scandinavia: a former Tibet? *Geochem. Geophys. Geosyst.*, 14:4479–4487.

Kong, F., Gao, S. S., and Liu, K. H. (2015). Applicability of the multiple-event stacking technique for shear-wave splitting analysis. *Bull. Seismol. Soc. Am.*, 105:3156–3166.

Kong, F., Wu, J., Liu, K. H., and Gao, S. S. (2016). Crustal anisotropy and ductile flow beneath the eastern Tibetan Plateau and adjacent areas. *Earth Planet. Sci. Lett.*, 442:72–79.

Korja, A. and Heikkinen, P. (2005). The accretionary Svecofennian orogen-insight from the BABEL profiles. *Precambrian Res.*, 136:241–268.

Korja, A., Lahtinen, R., and Nironen, M. (2006). The Svecofennian orogen: a collage of microcontinents and island arcs. *Geological Society, London, Memoirs*, 32:561–578, doi:10.1144/GSL.MEM.2006.032.01.34.

Kozlovskaya, E., Narkilahti, J., Nevalainen, J., Hurskainen, R., and Silvennoinen, H. (2016). Seismic observations at the Sodankylä Geophysical Observatory: history, present, and the future. *Geosci. Instrum. Method. Data Syst.*, 5:365–382, doi:10.5194/gi–5–365–2016.

Krogh, E. J. (1977). Evidence of Precambrian continent-continent collision in Western Norway. *Nature*, 267:17.

Kukkonen, I. T., Kinnunen, K. A., and Peltonen, P. (2003). Mantle xenoliths and thick lithosphere in the Fennoscandian Shield. *Phys. Chem. Earth*, 28:349–360.

Kustowski, B., Ekström, G., and Dziewoński, A. (2008). Anisotropic shear-wave velocity structure of the Earth's mantle: A global model. *J. Geophys. Res.*, 113:B06306, doi:10.1029/2007JB005169.

Lahtinen, R., Korja, A., and Nironen, M. (2005). Paleoproterozoic tectonic evolution. In *Developments in Precambrian Geology*, volume 14, pages 481–531.

Laske, G., Berger, J., Orcutt, J., and Babcock, J. (2014). ADDOSS: Autonomously Deployed Deep-ocean SEismic System-Communications Gateway for Ocean Observatories. In *Geophys. Res. Abstr. Vol. 16, EGU2014-4707*, EGU, Vienna, Austria.

Latifi, K., Kaviani, A., Rümpker, G., Mahmoodabadi, M., Ghassemi, M. R., and Sadidkhouy, A. (2018). The effect of crustal anisotropy on SKS splitting analysis synthetic models and real-data observations. *Geophys. J. Int.*, 213:1426–1447.

Lay, T. and Wallace, T. C. (1995). *Modern Global Seismology*. Academic Press, San Diego, CA, USA.

Lekic, V., Cottaar, S., Dziewonski, A., and Romanowicz, B. (2012). Cluster analysis of global lower mantle tomography: A new class of structure and implications for chemical heterogeneity. *Earth Planet. Sci. Lett.*, 357-358:68–77.

Levin, V., Menke, W., and Park, J. (1999). Shear wave splitting in the Appalachians and the Urals: a case for multilayered anisotropy. *J. Geophys. Res.*, 104:17975–17993.

Liddell, M. V., Bastow, I., Darbyshire, F., Gilligan, A., and Pugh, S. (2017). The formation of Laurentia: Evidence from shear wave splitting. *Earth Planet. Sci. Lett.*, 479:170–178.

Lin, Y.-P., Zhao, L., and Hung, S.-H. (2014). Full-wave effects on shear wave splitting. *Geophys. Res. Lett.*, 41:799–804, doi:10.1002/2013GL058742.

Liu, K. H. and Gao, S. S. (2013). Making reliable shear-wave splitting measurements. *Bull. Seismol. Soc. Am.*, 103:2680–2693.

Liu, K. H., Gao, S. S., Gao, Y., and Wu, J. (2008). Shear wave splitting and mantle flow associated with the deflected Pacific slab beneath northeast Asia. *J. Geophys. Res.*, 113:B01305, doi:10.1029/2007JB005178.

Long, M. D. (2009). Complex anisotropy in D" beneath the eastern Pacific from SKS-SKKS splitting discrepancies. *Earth Planet. Sci. Lett.*, 283:181–189.

Long, M. D. (2010). Frequency-dependent shear wave splitting and heterogeneous anisotropic structure beneath the Gulf of California region. *Phys. Earth Planet. In.*, 182:59–72.

Long, M. D. and Becker, T. W. (2010). Mantle dynamics and seismic anisotropy. *Earth Planet. Sci. Lett.*, 297:341–354.

Long, M. D., Jackson, K. G., and McNamara, J. F. (2016). SKS splitting beneath Transportable Array stations in eastern North America and the signature of past lithospheric deformation. *Geochem. Geophys. Geosyst.*, 17:2–15.

Long, M. D. and Lynner, C. (2015). Seismic anisotropy in the lowermost mantle near the Perm Anomaly. *Geophys. Res. Lett.*, 42:7073–7080, doi:10.1002/2015GL065506.

Long, M. D. and Silver, P. G. (2009). Shear wave splitting and mantle anisotropy: Measurements, interpretations, and new directions. *Surv. Geophys.*, 30:407–461.

Love, A. E. H. (1927). *A treatise on the mathematical theory of elasticity*. Dover publ., New York, USA.

Lynner, C., Anderson, M. L., Portner, D. E., Beck, S. L., and Gilbert, H. (2017). Mantle flow through a tear in the Nazca slab inferred from shear wave splitting. *Geophys. Res. Lett.*, 44:6735–6742.

Lynner, C. and Bodmer, M. (2017). Mantle flow along the eastern North American margin inferred from shear wave splitting. *Geology*, 45:867–870, doi:10.1130/G38980.1.

Lynner, C. and Long, M. D. (2012). Evaluating contributions to SK(K)S splitting from lower mantle anisotropy: A case study from station DBIC, Côte D'Ivoire. *Bull. Seismol. Soc. Am.*, 102(3):1030–1040.

Lynner, C. and Long, M. D. (2014). Lowermost mantle anisotropy and deformation along the boundary of the African LLSVP. *Geophys. Res. Lett.*, 41:3447–3454, doi:10.1002/2014GL059875.

Mainprice, D. and Silver, P. G. (1993). Interpretation of SKS-waves using samples from the subcontinental lithosphere. *Phys. Earth Planet. In.*, 78:257–280.

Makushkina, A., Tauzin, B., Tkalcic, H., Thybo, H., and Artemieva, I. (2018). Topography and thickness of the mantle transition zone beneath Scandinavia. In *Geophys. Res. Abstr. Vol. 20, EGU2018-10856-1*, EGU, Vienna, Austria.

Marson-Pidgeon, K. and Savage, M. K. (1997). Frequency-dependent anisotropy in Wellington, New Zealand. *Geophys. Res. Lett.*, 24:3297–3300.

Marson-Pidgeon, K. and Savage, M. K. (2004). Modelling shear wave splitting observations from Wellington, New Zealand. *Geophys. J. Int.*, 157:853–864.

Martin-Short, R., Allen, R. M., Bastow, I. D., Totten, E., and Richards, M. A. (2015). Mantle flow geometry from ridge to trench beneath the Gorda-Juan de Fuca plate system. *Nature Geosci.*, 8:965–969.

Matcham, I., Savage, M. K., and Gledhill, K. R. (2000). Distribution of seismic anisotropy in the subduction zone beneath the Wellington region, New Zealand. *Geophys. J. Int.*, 140:1–10.

MATLAB (2014). *version R2014a*. The MathWorks Inc., Natick, Massachusetts, USA.

Mauerberger, A., Sadeghisorkhani, H., Tilmann, F. J., Gudmundsson, O., and Maupin, V. (2018). Lithospheric structure of Scandinavia derived from ambient noise and surface waves (T43G-0500). In *AGU Fall Meeting 2018*, Washington, D.C., United States.

Maupin, V., Agostini, A., Artemieva, I., Balling, N., Beekman, F., Ebbing, J., England, R. W., Frassetto, A., Gradman, S., Jacobsen, B. H., Köhler, A., Kvarnen, T., Medhus, A. B., Mjelde, R., Ritter, J., Sokoutis, D., Stratford, W., Thybo, H., Wawerzinek, B., and Weidle, C. (2013). The deep structure of the Scandes and its relation to tectonic history and present-day topography. *Tectonophysics*, 602:15–37.

Maupin, V., Garnero, E. J., Lay, T., and Fouch, M. J. (2005). Azimuthal anisotropy in the D" layer beneath the Caribbean. *J. Geophys. Res.*, 110.

McKerrow, W. S., Mac Niocaill, C., and Dewey, J. F. (2000). The Caledonian orogeny redefined. *Geological Society of London*, 157:1149–1154.

McNamara, A. K., Karato, S., and Van Keken, P. E. (2001). Localization of dislocation creep in the lower mantle: implications for the origin of seismic anisotropy. *Earth Planet. Sci. Lett.*, 191:85–99.

McNamara, A. K., van Keken, P. E., and Karato, S. (2002). Development of anisotropic structure in the Earth's lower mantle by solid-state convection. *Nature*, 416:310–314.

McNamara, D. E., Owens, T. J., Silver, P. G., and Wu, F. T. (1994). Shear wave anisotropy beneath the Tibetan Plateau. *J. Geophys. Res.*, 99:13655–13665.

Meade, C., Silver, P. G., and Kaneshima, S. (1995). Laboratory and seismological observations of lower mantle isotropy. *Geophys. Res. Lett.*, 22:1293–1296, doi:10.1029/95GL01091.

Medhus, A. B., Balling, N., Jacobsen, B. H., Kind, R., and England, R. W. (2009). Deep-structural differences in southwestern Scandinavia revealed by P-wave travel time residuals. *Norw. J. Geol.*, 89.

Medhus, A. B., Balling, N., Jacobsen, B. H., Weidle, C., England, R. W., Kind, R., Thybo, H., and Voss, P. (2012). Upper-mantle structure beneath the Southern Scandes Mountains and the Northern Tornquist Zone revealed by P-wave traveltime tomography. *Geophys. J. Int.*, 189:1315–1334.

Merkel, S., McNamara, A. K., Kubo, A., Speziale, S., Miyagi, L., Meng, Y., Duffy, T. S., and Wenk, H.-R. (2007). Deformation of (Mg,Fe)SiO3 post-perovskite and D" anisotropy. *Science*, 316:1729–1732.

Miller, M. S. and Eaton, D. W. (2010). Formation of cratonic mantle keels by arc accretion: Evidence from S receiver functions. *Geophys. Res. Lett.*, 37:1–5, doi:10.1029/2010GL044366.

Monteiller, V. and Chevrot, S. (2010). How to make robust splitting measurements for single-station analysis and three-dimensional imaging of seismic anisotropy. *Geophys. J. Int.*, 182:311–328.

Moore, M. M., Garnero, E. J., Lay, T., and Williams, Q. (2004). Shear wave splitting and waveform complexity for lowermost mantle structures with low-velocity lamellae and transverse isotropy. *J. Geophys. Res.*, 109:1–26, doi:10.1029/2003JB002546.

Munzarová, H., Plomerová, J., Kissling, E., Vecsey, L., and Babuška, V. (2018). Novel anisotropic teleseismic body-wave tomography code AniTomo to illuminate heterogeneous anisotropic upper mantle: Part II - Application to data of passive seismic experiment LAPNET in northern Fennoscandia. *Geophys. J. Int.*, 215:1388–1409, doi:10.1093/gji/ggy327.

Murakami, M., Hirose, K., Kawamura, K., Sata, N., and Ohishi, Y. (2004). Post-perovskite phase transition in MgSiO3. *Science*, 304:855–858.

Neumann, E.-R., Olsen, K. H., Baldridge, W. S., and Sundvoll, B. (1992). The Oslo rift: A review. *Tectonophysics*, 208:1–18.

Nicolas, A. and Christensen, N. I. (1987). Formation of anisotropy in upper mantle peridotites - A review. *Composition, structure and dynamics of the lithosphere-asthenosphere system*, 16:111–123.

Nielsen, S. B., Gallagher, K., Leighton, C., Balling, N., Svenningsen, L., Jacobsen, B. H., Thomsen, E., Nielsen, O. B., Heilmann-Clausen, C., Egholm, D. L., Sunmmerfield, M. A., Clausen, O. R., Piotrowski, J. A., Thorsen, M. R., Huuse, M., Abrahamsen, N., King, C., and Lykke-Andersen, H. (2009). The evolution of western Scandinavian topography: a review of Neogene uplift versus the ICE (isostasy-climate-erosion) hypothesis. *J. Geodynamics*, 47:72–95.

Niu, F. and Perez, A. M. (2004). Seismic anisotropy in the lower mantle: A comparison of waveform splitting of SKS and SKKS. *Geophys. Res. Lett.*, 31:L24612, doi:10.1029/2004GL021196.

Nowacki, A., Wookey, J., and Kendall, J.-M. (2010). Deformation of the lowermost mantle from seismic anisotropy. *Nature*, 467:1091–1096.

Nowacki, A., Wookey, J., and Kendall, J.-M. (2011). New advances in using seismic anisotropy, mineral physics and geodynamics to understand deformation in the lowermost mantle. *J. Geodynamics*, 52:205–228.

Olsson, S. (2007). *Analyses of seismic wave conversion in the crust and upper mantle beneath the Baltic Shield*. PhD thesis, Acta Universitatis Upsaliensis.

Özalaybey, S. and Chen, W.-P. (1999). Frequency-dependent analysis of SKS/SKKS waveforms observed in Australia: evidence for null birefringence. *Phys. Earth Planet. Int.*, 114:197–210.

Panning, M. and Romanowicz, B. (2006). A three-dimensional radially anisotropic model of shear velocity in the whole mantle. *Geophys. J. Int.*, 167:361–379.

Pedersen, H. A., Bruneton, M., and Maupin, V. (2006). Lithospheric and sublithospheric anisotropy beneath the Baltic shield from surface-wave array analysis. *Earth Planet. Sci. Lett.*, 244:590–605.

Peterson, J. (1993). Observations and modelling of background seismic noise. Open-file report 93-322, https://pubs.usgs.gov/of/1993/0322/ofr93-322.pdf, U.S. Geological Survey, Albuquerque, New Mexico, doi:10.3133/ofr93322, last accessed 11 January 2019.

Pharaoh, T. C. (1999). Palaeozoic terranes and their lithospheric boundaries within the Trans-European Suture Zone (TESZ): a review. *Tectonophysics*, 314:17–41.

Plesinger, A., Hellweg, M., and Seidl, D. (1986). Interactive high-resolution polarization analysis of broad-band seismograms. *J. Geophys.*, 59:129–139.

Plomerová, J., Arvidsson, R., Babuška, V., Granet, M., Kulhánek, O., Poupinet, G., and Šılenỳ, J. (2001). An array study of lithospheric structure across the Protogine zone, Värmland, south-central Sweden - signs of a paleocontinental collision. *Tectonophysics*, 332:1–21.

Plomerová, J., Babuška, V., Vecsey, L., Kozlovskaya, E., and Raita, T. (2006). Proterozoic-Archean boundary in the mantle lithosphere of eastern Fennoscandia as seen by seismic anisotropy. *J. Geodynamics*, 41:400–410.

Plomerová, J., Babuška, V., Vecsey, L., and Kouba, D. (2002a). Seismic anisotropy of the lithosphere around the Trans-European Suture Zone (TESZ) based on teleseismic body-wave data of the TOR experiment. *Tectonophysics*, 360:89–114.

Plomerová, J., Kouba, D., and Babuška, V. (2002b). Mapping the lithosphere-asthenosphere boundary through changes in surface-wave anisotropy. *Tectonophysics*, 358:175–185.

Plomerová, J., Vecsey, L., Babuška, V., Heikkinen, P., and Komminaho, K. (2011). Domains of Archean mantle lithosphere deciphered by seismic anisotropy-initial results from the LAPNET array in northern Fennoscandia. *Solid Earth*, 2:303–313, doi:10.5194/se–2–303–2011.

Porritt, R. W. (2014). SplitLab version 1.2.1. Changelog, https://robporritt.wordpress.com/, last accessed 11 January 2019.

Ranasinghe, N., Rowe, C., Syracuse, E., Larmat, C., and Begnaud, M. (2018). Enhanced Global Seismic Resolution Using Transoceanic SMART Cables. *Seismol. Res. Lett.*, 89:77–85.

Restivo, A. and Helffrich, G. (1999). Teleseismic shear wave splitting measurements in noisy environments. *Geophys. J. Int.*, 137:821–830.

Ritter, J., Grund, M., and Sanz Alonso, Y. (2018). Laterally varying deep seismic anisotropy around the Black Forest Observatory, Germany. In *Geophys. Res. Abstr. Vol. 20, EGU2018-3403*, EGU, Vienna, Austria.

Ritter, J. R. R., Jordan, M., Christensen, U. R., and Achauer, U. (2001). A mantle plume below the Eifel volcanic fields, Germany. *Earth Planet. Sci. Lett.*, 186:7–14.

Roberts, D. (2003). The Scandinavian Caledonides: event chronology, palaeogeographic settings and likely modern analogues. *Tectonophysics*, 365:283–299.

Roy, C. and Ritter, J. R. R. (2013). Complex deep seismic anisotropy below the Scandinavian Mountains. *J. Seism.*, 17:361–384.

Roy, C., Winter, A., Ritter, J. R. R., and Schweitzer, J. (2017). On the improvement of SKS splitting measurements by the Simultaneous Inversion of Multiple Waveforms (SIMW). *Geophys. J. Int.*, 208:1508–1523, doi:10.1093/gji/ggw470.

Rümpker, G. and Ryberg, T. (2000). New "Fresnel-zone" estimates for shear-wave splitting observations from finite-difference modeling. *Geophys. Res. Lett.*, 27:2005–2008.

Rümpker, G. and Silver, P. G. (1998). Apparent shear-wave splitting parameters in the presence of vertically varying anisotropy. *Geophys. J. Int.*, 135:790–800.

Saltzer, R. L., Gaherty, J. B., and Jordan, T. H. (2000). How are vertical shear wave splitting measurements affected by variations in the orientation of azimuthal anisotropy with depth? *Geophys. J. Int.*, 141:374–390.

Savage, M. K. (1999). Seismic anisotropy and mantle deformation: what have we learned from shear wave splitting. *Rev. Geophys.*, 37:69–106.

Schaeffer, A. J. and Lebedev, S. (2013). Global shear speed structure of the upper mantle and transition zone. *Geophys. J. Int.*, 194:417–449.

Schaeffer, A. J., Lebedev, S., and Becker, T. W. (2016). Azimuthal seismic anisotropy in the Earth's upper mantle and the thickness of tectonic plates. *Geophys. J. Int.*, 207:901–933, doi:10.1093/gji/ggw309.

Shepard, G. E., Matthews, K. J., Hosseini, K., and Domeier, M. (2017). On the consistency of seismically imaged lower mantle slabs. *Sci. Rep.*, 7:10976.

Silver, P. G. (1996). Seismic anisotropy beneath the continents: Probing the depths of geology. *Annu. Rev. Earth Planet. Sci.*, 24:385–432.

Silver, P. G. and Chan, W. W. (1988). Implications for continental structure and evolution from seismic anisotropy. *Nature*, 335:34.

Silver, P. G. and Chan, W. W. (1991). Shear wave splitting and subcontinental mantle deformation. *J. Geophys. Res.*, 96:16429–16454.

Silver, P. G. and Long, M. D. (2011). The non-commutivity of shear wave splitting operators at low frequencies and implications for anisotropy tomography. *Geophys. J. Int.*, 184:1415–1427.

Silver, P. G. and Savage, M. K. (1994). The interpretation of shear-wave splitting parameters in the presence of two anisotropic layers. *Geophys. J. Int.*, 119:949–963.

Simmons, N. A., Forte, A., Boschi, L., and Grand, S. (2010). GyPSuM: A joint tomographic model of mantle density and seismic wave speeds. *Geophys. Res. Lett.*, 115:B12310, doi:10.1029/2010JB007631.

Simmons, N. A., Myers, S. C., Johannesson, G., Matzel, E., and Grand, S. P. (2015). Evidence for long-lived subduction of an ancient tectonic plate beneath the southern Indian Ocean. *Geophys. Res. Lett.*, 42:9270–9278, doi:10.1002/2015GL066237.

SNSN (1904). SNSN (Swedish National Seismic Network). Seismic Network, Uppsala University, Uppsala, Sweden, doi:10.18159/SNSN.

Stähler, S. C., Sigloch, K., Hosseini, K., Crawford, W. C., Barruol, G., Schmidt-Aursch, M. C., Tsekhmistrenko, M., Scholz, J.-R., Mazzullo, A., and Deen, M. (2016). Performance report of the RHUM-RUM ocean bottom seismometer network around La Réunion, western Indian Ocean. *Adv. Geosc.*, 41:43–63, doi:10.5194/adgeo–41–43–2016.

Stein, S. and Wysession, M. (2009). *An Introduction to Seismology, Earthquakes and Earth Structure*. Blackwell Publishing, Malden, MA, USA.

Steinberger, B. and Torsvik, T. H. (2012). A geodynamic model of plumes from the margins of Large Low Shear Velocity Provinces. *Geochem. Geophys. Geosyst.*, 13:Q01W09, doi:10.1029/2011GC003808.

Storchak, D. A., Schweitzer, J., and Bormann, P. (2011). Seismic phase names: IASPEI standard. In *Encyclopedia of Solid Earth Geophysics*, pages 1162–1173. Springer.

Su, W. and Dziewonski, A. M. (1995). Inner core anisotropy in three dimensions. *J. Geophys. Res.*, 100:9831–9852.

Tesoniero, A., Leng, K., Long, M. D., and Nissen-Meyer, T. (2017). Insight on the anisotropic nature of the D" layer through the analysis of SKS-SKKS splitting obtained via 3D spectral element modeling (DI43B-0364). In *AGU Fall Meeting 2017*, New Orleans, United States.

Thomas, C. and Kendall, J.-M. (2002). The lowermost mantle beneath northern Asia-II. Evidence for lower-mantle anisotropy. *Geophys. J. Int.*, 151:296–308.

Thomsen, L. (1986). Weak elastic anisotropy. *Geophysics*, 51:1954–1966.

Thorne, M. S., Garnero, E. J., and Grand, S. P. (2004). Geographic correlation between hot spots and deep mantle lateral shear-wave velocity gradients. *Phys. Earth Planet. In.*, 146:47–63.

Thybo, H., Balling, N., Maupin, V., Ritter, J., and Tilmann, F. (2012). ScanArray Core (1G 2012-2017). Seismic Network, The ScanArray consortium, doi:10.14470/6T569239.

Tian, X., Zhang, J., Si, S., Wang, J., Chen, Y., and Zhang, Z. (2011). SKS splitting measurements with horizontal component misalignment. *Geophys. J. Int.*, 185:329–340.

Tilmann, F., Rowe, C., and Butler, R. (2017). Commercial underwater cable systems could reduce disaster impact. *Eos Trans. AGU*, 98:https://doi.org/10.1029/2017EO069575.

Torsvik, T. H. and Cocks, L. R. M. (2005). Norway in space and time: A Centennial cavalcade. *Norw. J. Geol.*, 85.

Torsvik, T. H. and Rehnström, E. F. (2003). The Tornquist Sea and Baltica-Avalonia docking. *Tectonophysics*, 362:67–82.

Trabant, C., Hutko, A. R., Bahavar, M., Karstens, R., Ahern, T., and Aster, R. (2012). Data products at the IRIS DMC: Stepping stones for research and other applications. *Seism. Res. Lett.*, 83:846–854.

Trampert, J. and van Heijst, H. J. (2002). Global azimuthal anisotropy in the transition zone. *Science*, 296:1297–1299.

Van der Hilst, R. D., Widiyantoro, S., and Engdahl, E. R. (1997). Evidence for deep mantle circulation from global tomography. *Nature*, 386:578.

Van der Voo, R., Spakman, W., and Bijwaard, H. (1999). Mesozoic subducted slabs under Siberia. *Nature*, 397:246–249.

Vauchez, A. and Nicolas, A. (1991). Mountain building: strike-parallel motion and mantle anisotropy. *Tectonophysics*, 185:183–201.

Vecsey, L., Plomerová, J., and Babuška, V. (2008). Shear-wave splitting measurements-problems and solutions. *Tectonophysics*, 462:178–196.

Vecsey, L., Plomerová, J., Kozlovskaya, E., and Babuška, V. (2007). Shear wave splitting as a diagnostic of variable anisotropic structure of the upper mantle beneath central Fennoscandia. *Tectonophysics*, 438:57–77.

Vinnik, L., Kozlovskaya, E., Oreshin, S., Kosarev, G., Piiponen, K., and Silvennoinen, H. (2016). The lithosphere, LAB, LVZ and Lehmann discontinuity under central Fennoscandia from receiver functions. *Tectonophysics*, 667:189–198.

Vinnik, L., Makeyeva, L. I., Milev, A., , and Usenko, A. Y. (1992). Global patterns of azimuthal anisotropy and deformations in the continental mantle. *Geophys. J. Int.*, 111:433–447.

Vinnik, L., Oreshin, S., Makeyeva, L., Peregoudov, D., and Kozlovskaya, E. (2014). Anisotropic lithosphere under the Fennoscandian shield from P receiver functions and SKS waveforms of the POLENET/LAPNET array. *Tectonophysics*, 628:45–54.

Vinnik, L. P., Kosarev, G. L., and Makeyeva, L. I. (1984). Anisotropiya litosfery po nablyudeniyam voln SKS and SKKS. In *Dokl. Akad. Nauk USSR*, volume 278, pages 1335–1339.

Voigt, W. (1928). *Lehrbuch der Kristallphysik (mit Ausschluss der Kristalloptik)*. Teubner, Leipzig, Germany.

Walker, A. M. and Wookey, J. (2012). MSAT - a new toolkit for the analysis of elastic and seismic anisotropy. *Comput. Geosci.*, 49:81–90.

Walker, K. T., Bokelmann, G. H. R., Klemperer, S. L., and Bock, G. (2005). Shear-wave splitting around the Eifel hotspot: evidence for a mantle upwelling. *Geophys. J. Int.*, 163:962–980.

Walsh, E., Arnold, R., and Savage, M. K. (2013). Silver and Chan revisited. *J. Geophys. Res.*, 118:5500–5515.

Wang, Y. and Wen, L. (2007). Complex seismic anisotropy at the border of a very low velocity province at the base of the Earth's mantle. *J. Geophys. Res.*, 112:B09305, doi:10.1029/2006JB004719.

Wawerzinek, B. (2012). *Untersuchung der elastischen Scherwellenstruktur unter dem Südskandinavischen Gebirge*. PhD thesis, Karlsruhe Institute of Technology (KIT).

Wawerzinek, B., Ritter, J. R. R., and Roy, C. (2013). New constraints on the 3D shear wave velocity structure of the upper mantle underneath Southern Scandinavia revealed from non-linear tomography. *Tectonophysics*, 602:38–54.

Weber, M. (1993). P- and S-wave reflections from anomalies in the lowermost mantle. *Geophys. J . Int.*, 115:183–210.

Weber, M. (1994). Lamellae in D"?: An alternative model for lower mantle anomalies. *Geophys. Res. Lett.*, 21:2531–2534.

Weber, M. and Körnig, M. (1992). A search for anomalies in the lowermost mantle using seismic bulletins. *Phys. Earth Planet. In.*, 73:1–28.

Wegener, A. (1920). *Die Entstehung der Kontinente und Ozeane*. Friedrich Vieweg und Sohn, Braunschweig, Germany.

Weidle, C., Maupin, V., Ritter, J., Kværna, T., Schweitzer, J., Balling, N., Thybo, H., Faleide, J. I., and Wenzel, F. (2010). MAGNUS-A Seismological Broadband Experiment to Resolve Crustal and Upper Mantle Structure beneath the Southern Scandes Mountains in Norway. *Seism. Res. Lett.*, 81(1):76–84, doi:10.1785/gssrl.81.1.76.

Wessel, P., Smith, W. H. F., Scharroo, R., Luis, J., and Wobbe, F. (2013). Generic Mapping Tools: Improved version released. *Eos Trans. AGU*, 94(45):409–420.

Wirth, E. and Long, M. D. (2010). Frequency-dependent shear wave splitting beneath the Japan and Izu-Bonin subduction zones. *Phys. Earth Planet. In.*, 181:141–154.

Wolfe, C. J. and Silver, P. G. (1998). Seismic anisotropy of oceanic upper mantle: Shear wave splitting methodologies and observations. *J. Geophys. Res.*, 103:749–771.

Wolfe, C. J. and Solomon, S. C. (1998). Shear-wave splitting and implications for mantle flow beneath the MELT region of the East Pacific Rise. *Science*, 280:1230–1232.

Woodhouse, J. H., Giardini, D., and Li, X.-D. (1986). Evidence for inner core anisotropy from free oscillations. *Geophys. Res. Lett.*, 13:1549–1552.

Wookey, J. and Helffrich, G. (2008). Inner-core shear-wave anisotropy and texture from an observation of PKJKP waves. *Nature*, 454:873–876.

Wookey, J. and Kendall, J.-M. (2004). Evidence of midmantle anisotropy from shear wave splitting and the influence of shear-coupled P waves. *J. Geophys. Res.*, 109:1–16, doi:10.1029/2003JB002871.

Wookey, J. and Kendall, J.-M. (2008). Constraints on lowermost mantle mineralogy and fabric beneath Siberia from seismic anisotropy. *Earth Planet. Sci. Lett.*, 275:32–42.

Wüstefeld, A. (2007). *Methods and applications of shear wave splitting: The East European Craton*. PhD thesis, Univ. de Montpellier, France, http://splitting.gm.univ-montp2.fr/, last accessed 11 January 2019.

Wüstefeld, A. and Bokelmann, G. (2007). Null detection in shear-wave splitting measurements. *Bull. Seismol. Soc. Am.*, 97(4):1204–1211.

Wüstefeld, A., Bokelmann, G., and Barruol, G. (2010). Evidence for ancient lithospheric deformation in the East European Craton based on mantle seismic anisotropy and crustal magnetics. *Tectonophysics*, 481:16–28.

Wüstefeld, A., Bokelmann, G., Zaroli, C., and Barruol, G. (2008). SplitLab: A shear-wave splitting environment in Matlab. *Comput. Geosci.*, 34:515–528.

Wüstefeld, A., Bokelmann, G. H. R., Barruol, G., and Montagner, J.-P. (2009). Identifying global seismic anisotropy patterns by correlating shear-wave splitting and surface waves data. *Phys. Earth Planet. Int.*, 176:198–212.

Wylegalla, K., Bock, G., Gossler, J., and Hanka, W. (1999). Anisotropy across the Sorgenfrei-Tornquist Zone from shear wave splitting. *Tectonophysics*, 314:335–350.

Yang, B. B., Gao, S. S., Liu, K. H., Elsheikh, A. A., Lemnifi, A. A., Refayee, H. A., and Yu, Y. (2014). Seismic anisotropy and mantle flow beneath the northern Great Plains of North America. *J. Geophys. Res.*, 119:1971–1985.

Yuan, K. and Beghein, C. (2013). Seismic anisotropy changes across upper mantle phase transitions. *Earth Planet. Sci. Lett.*, 374:132–144.

Yuan, K. and Beghein, C. (2014). Three-dimensional variations in Love and Rayleigh wave azimuthal anisotropy for the upper 800 km of the mantle. *J. Geophys. Res.*, 119:3232–3255.

Zhang, S. and Karato, S.-I. (1995). Lattice preferred orientation of olivine aggregates deformed in simple shear. *Nature*, 375:774.

Zhu, H., Bozdağ, E., and Tromp, J. (2015). Seismic structure of the European upper mantle based on adjoint tomography. *Geophys. J. Int.*, 201:18–52.

Zhu, H. and Tromp, J. (2013). Mapping tectonic deformation in the crust and upper mantle beneath Europe and the North Atlantic Ocean. *Science*, 341:871–875.

Zieger, T. and Ritter, J. R. R. (2018). Influence of wind turbines on seismic stations in the Upper Rhine Graben, SW Germany. *J. Seism.*, 22:105–122.

Zielhuis, A. and Nolet, G. (1994). Deep seismic expression of an ancient plate boundary in Europe. *Science*, 265:79–81.

Zietlow, D. W., Sheehan, A. F., Molnar, P. H., Savage, M. K., Hirth, G., A., C. J., and Hager, B. H. (2013). Upper mantle seismic anisotropy at a strike-slip boundary: South Island, New Zealand. *J. Geophys. Res.*, 119:1020–1040.

Index

Abramson et al. (1997), 109
Alsina and Snieder (1995), 20, 134
Ando and Ishikawa (1982), 2
Ando et al. (1980), 2
Aragon et al. (2017), 109
Artemieva (2006), 133
BABEL Working Group (1990), 89, 128, 130
Babuška and Cara (1991), 7–13, 16, 17, 85
Babuška et al. (1993), 124, 128, 129
Backus (1962), 1, 12, 21, 85
Balling (2000), 89, 128, 130
Barruol and Hoffmann (1999), 96
Barruol and Mainprice (1993), 21, 125
Barruol et al. (1997), 62
Barruol et al. (1998), 2
Bastow et al. (2010), 14
Becker et al. (2012), 131
Beghein et al. (2008), 23
Berthelsen and Marker (1986), 129
Berthelsen (1992), 89
Billings et al. (1994), 45
Bird (2003), 3, 92
Bodmer et al. (2015), 55
Bowman and Ando (1987), 18, 42, 43, 54, 72, 92, 157
Braun et al. (2000), 23
Brisbourne (2012), 41
Bullen (1940), 23
Bullen (1949), 1, 23
Burke et al. (2008), 68
Chen et al. (2018), 133
Chevrot and Van Der Hilst (2003), 108
Chevrot et al. (2004), 127, 129
Chevrot (2000), 18, 19, 43, 72
Christoffel (1877), 11
Clauser (2014), 7
Cottaar and Lekic (2016), 68
Cottaar and Romanowicz (2013), 24, 68, 70, 81
Cottaar et al. (2014), 78
Crampin and Booth (1985), 1, 21, 85, 125
Crampin and Chastin (2003), 20
Crampin and Lovell (1991), 20
Crampin (1984), 20
Creasy et al. (2017), 15, 68
Crotwell et al. (1999), 17, 19, 73, 77, 80–82, 151, 163, 164
Currie et al. (2004), 124
Dahm (1934), 1, 23
Debayle and Ricard (2013), 133
Debayle et al. (2005), 21
Deng et al. (2017), 19, 24, 43, 68, 70, 72, 73, 75, 81
Deuss (2014), 20
Dimech et al. (2017), 2
Dost (1994), 41
Dziewoński et al. (1981), 91, 92
Eakin and Long (2013), 56
Eakin et al. (2010), 55
Eakin et al. (2016), 2, 20, 56, 63, 92

Eakin et al. (2018), 20, 23
Einstein (1916), 7
Eken and Tilmann (2014), 143
Eken et al. (2010), 4, 88, 89, 91, 127–129, 133, 137
Ekström et al. (2012), 91, 92
England et al. (2015), 26, 27, 90, 91
Evans et al. (2006), 140
Favier and Chevrot (2003), 20, 72, 73, 134
Flament et al. (2017), 68
Ford et al. (2015), 68
Fouch and Fischer (1996), 23
Fouch and Rondenay (2006), 20, 85, 94, 95
Fouch et al. (2000), 133
Frietsch et al. (2015), 20
Frost and Romanowicz (2017), 20
Fukao (1984), 42, 43
GEOFON Data Centre (1993), 41
Gao et al. (1994), 2, 22
Gao et al. (1997), 23, 127
Garnero and McNamara (2008), 68
Garnero et al. (2004), 24
Garnero et al. (2016), 68
Gaál and Gorbatschev (1987), 75, 76, 80, 86, 89
Gaál (1986), 86
Gee et al. (2008), 86
Gerst and Savage (2004), 2, 20, 56
Gorbatchev (2004), 75, 76, 80, 87, 126
Gradmann et al. (2014), 90, 91
Gripp and Gordon (2002), 23, 95, 126, 133
Grund and Ritter (2018), 187
Grund and Ritter (2019), 6, 86, 92, 93, 136, 175, 187
Grund et al. (2016a), 1
Grund et al. (2016b), 1
Grund et al. (2017a), 5, 27, 38, 66, 71, 90, 91, 93
Grund et al. (2017b), 40
Grund et al. (2019), 144
Grund (2017), 5, 72, 92, 93, 151, 166
Hall et al. (2004), 70, 86
Hammond et al. (2014), 2, 23
Hanka and Kind (1994), 41
Hanna and Long (2012), 46
Hartog and Schwartz (2000), 86, 108, 110, 124, 129
He and Long (2011), 24, 70
He et al. (2015), 79, 81, 82
Heeremans et al. (1996), 127
Helffrich (1995), 136
Helmberger et al. (1998), 79, 81, 82
Hetényi et al. (2018), 2, 83, 144
Hicks et al. (2012), 20, 124
Howell Jr. and Kisslinger (2000), 23
Hutko et al. (2006), 68
IRIS DMC (2012), 89
Ismaïl and Mainprice (1998), 9, 21, 22
Jung et al. (2006), 23
Karato and Wu (1993), 14
Karato et al. (2008), 2, 22, 85
Karato (2008), 14
Katayama et al. (2004), 23
Kendall and Silver (1996), 2, 24, 85
Kendall et al. (2006), 127
Kendall (1994), 23
Kennett (1991), 17, 19, 28, 43, 73, 75, 76, 80–82, 160, 163, 164
Kind et al. (2013), 129
Kong et al. (2015), 55, 93
Kong et al. (2016), 21
Korja and Heikkinen (2005), 87, 126
Korja et al. (2006), 89
Kozlovskaya et al. (2016), 137, 143
Krogh (1977), 86
Kukkonen et al. (2003), 109

Kustowski et al. (2008), 68
Lahtinen et al. (2005), 89
Laske et al. (2014), 144
Latifi et al. (2018), 21
Lay and Wallace (1995), 7
Lekic et al. (2012), 68, 79, 81
Levin et al. (1999), 124, 133
Liddell et al. (2017), 111, 124, 129
Lin et al. (2014), 73
Liu and Gao (2013), 44
Liu et al. (2008), 46
Long and Becker (2010), 2, 20, 22, 23, 85
Long and Lynner (2015), 2, 24, 68, 70, 72, 73, 75, 81, 82
Long and Silver (2009), 4, 7, 18, 54, 58, 69, 85, 93
Long et al. (2016), 2, 22
Long (2009), 24, 68, 70, 72, 75
Long (2010), 45
Love (1927), 8
Lynner and Bodmer (2017), 23
Lynner and Long (2012), 24, 46, 86, 92, 136
Lynner and Long (2014), 24, 58, 68, 70, 74
Lynner et al. (2017), 20
MATLAB (2014), 151
Mainprice and Silver (1993), 22
Makushkina et al. (2018), 144
Marson-Pidgeon and Savage (1997), 45
Marson-Pidgeon and Savage (2004), 86, 108, 119
Martin-Short et al. (2015), 55
Matcham et al. (2000), 2
Mauerberger et al. (2018), 144
Maupin et al. (2005), 24
Maupin et al. (2013), 86
McKerrow et al. (2000), 86
McNamara et al. (1994), 21
McNamara et al. (2001), 15, 68
McNamara et al. (2002), 78
Meade et al. (1995), 21, 23, 70, 85
Medhus et al. (2009), 125
Medhus et al. (2012), 125
Merkel et al. (2007), 2, 78, 85
Miller and Eaton (2010), 129
Monteiller and Chevrot (2010), 19, 44, 54
Moore et al. (2004), 23, 24
Munzarová et al. (2018), 89
Murakami et al. (2004), 2, 85
Neumann et al. (1992), 127
Nicolas and Christensen (1987), 2, 14
Nielsen et al. (2009), 86
Niu and Perez (2004), 2, 68, 70
Nowacki et al. (2010), 15, 24, 78
Nowacki et al. (2011), 1, 7, 15, 23, 24, 70
Olsson (2007), 133
Panning and Romanowicz (2006), 23
Pedersen et al. (2006), 89, 133, 134, 136
Peterson (1993), 39, 40
Pharaoh (1999), 89
Plesinger et al. (1986), 35, 42
Plomerová et al. (2002a), 4, 88, 89, 127
Plomerová et al. (2002b), 89, 133
Plomerová et al. (2001), 89, 127
Plomerová et al. (2006), 4, 89, 124, 127, 130, 133
Plomerová et al. (2011), 4, 89, 128, 129
Porritt (2014), 55, 66
Ranasinghe et al. (2018), 144
Restivo and Helffrich (1999), 44, 48, 49, 54, 59, 60
Ritter et al. (2001), 1
Ritter et al. (2018), 140
Roberts (2003), 86
Roy and Ritter (2013), 88, 89, 91, 101, 125
Roy et al. (2017), 41, 48, 54, 60, 64
Rümpker and Ryberg (2000), 20

Rümpker and Silver (1998), 59
SNSN (1904), 41, 91
Saltzer et al. (2000), 108
Savage (1999), 2, 4, 7, 9, 15, 18, 21, 22, 54, 69, 85, 86, 136
Schaeffer and Lebedev (2013), 1
Schaeffer et al. (2016), 131
Shepard et al. (2017), 68, 78–80
Silver and Chan (1988), 18, 21
Silver and Chan (1991), 2, 7, 17, 18, 42, 43, 45, 54, 56, 57, 69, 71, 72, 85, 92, 157, 159, 162
Silver and Long (2011), 108
Silver and Savage (1994), 59, 86, 103, 108, 109, 124, 128
Silver (1996), 2, 14, 22, 23, 85, 94, 95, 127, 128, 133
Simmons et al. (2010), 68, 74, 77, 164
Simmons et al. (2015), 68
Stein and Wysession (2009), 7, 8, 10, 14
Steinberger and Torsvik (2012), 68
Storchak et al. (2011), 16
Stähler et al. (2016), 144
Su and Dziewonski (1995), 20
Tesoniero et al. (2017), 76
Thomas and Kendall (2002), 82
Thomsen (1986), 12
Thorne et al. (2004), 68
Thybo et al. (2012), 25, 27, 71, 90, 91
Tian et al. (2011), 46, 92
Tilmann et al. (2017), 144
Torsvik and Cocks (2005), 86
Torsvik and Rehnström (2003), 89, 125
Trabant et al. (2012), 89
Trampert and van Heijst (2002), 23
Van der Hilst et al. (1997), 1
Van der Voo et al. (1999), 68, 78
Vauchez and Nicolas (1991), 128
Vecsey et al. (2007), 4, 20, 23, 62, 88, 89, 124, 130, 131, 133
Vecsey et al. (2008), 44, 54
Vinnik et al. (1984), 2
Vinnik et al. (1992), 21, 88, 89, 125
Vinnik et al. (2014), 4, 88, 89, 128, 129
Vinnik et al. (2016), 136
Voigt (1928), 7
Walker and Wookey (2012), 60, 107–110, 151
Walker et al. (2005), 20
Walsh et al. (2013), 45, 56, 72, 93
Wang and Wen (2007), 58, 68
Wawerzinek et al. (2013), 125
Wawerzinek (2012), 93
Weber and Körnig (1992), 76
Weber (1993), 76, 82
Weber (1994), 24
Wegener (1920), 1
Weidle et al. (2010), 90, 91, 101
Wessel et al. (2013), 60, 83, 151, 160
Wirth and Long (2010), 45
Wolfe and Silver (1998), 54, 58, 59, 93, 112, 115, 126, 166, 167
Wolfe and Solomon (1998), 23
Woodhouse et al. (1986), 20
Wookey and Helffrich (2008), 20
Wookey and Kendall (2004), 56
Wookey and Kendall (2008), 15, 24, 78, 79, 82, 83
Wylegalla et al. (1999), 88–90, 105, 125
Wüstefeld and Bokelmann (2007), 7, 18, 43, 45, 48, 49, 52, 54, 60, 62, 93, 101
Wüstefeld et al. (2008), 41, 45, 54, 55, 57, 62, 65, 71, 92, 151
Wüstefeld et al. (2009), 89
Wüstefeld et al. (2010), 20, 88, 89
Wüstefeld (2007), 59, 97

Yang et al. (2014), 23, 124, 133
Yuan and Beghein (2013), 21
Yuan and Beghein (2014), 86
Zhang and Karato (1995), 2, 85, 133
Zhu and Tromp (2013), 86, 89, 131–134, 136
Zhu et al. (2015), 89, 131, 132
Zieger and Ritter (2018), 1, 40
Zielhuis and Nolet (1994), 89, 125
Zietlow et al. (2013), 55
Özalaybey and Chen (1999), 45